Hierarchical Graphene Supercapacitors

A thesis submitted to the University of Manchester for the degree of Doctor of Philosophy in the Faculty of Science and Engineering.

2017

Ralph Hick

School of Materials

1.1 Contents

1.2 List of Figures

1.3 List of Tables

1.4 Abstract

Electrochemical supercapacitors are promising devices for energy storage applications. However, their uptake is currently limited by their relatively low energy density. The recent discovery of graphene has strengthened supercapacitor research, due to graphene’s high surface area, conductivity, strength, and flexibility. However, the synthesis of large quantities of defect-free graphene and its subsequent incorporation into supercapacitors has proved difficult due to aggregation and restacking of the graphene. Hence, in order to retain the high surface area of graphene, it needs to be incorporated into hierarchical structures. Given these issues, this thesis aimed to produce high quality graphene flakes via electrochemical exfoliation. These flakes were then processed into hierarchical structures (foams and fibres) for supercapacitor devices. The graphene was exfoliated using a reductive process, with two different cells designs explored. The influence of the microstructure of the initial graphite on the exfoliation process was also studied. The hierarchical foams were produced by depositing the graphene onto nickel foam. It was found that the degree of exfoliation has a marginal effect on the capacitance of the device. This electrochemically exfoliated graphite was also wet-spun with polyacrylonitrile (PAN) and carbonised to produce carbon fibre-graphene composites. It was found that the carbonised materials had a higher capacitance than the precursor material (33 F g^{-1} and 47 F g^{-1} respectively). As a comparison, wet-spun graphene oxide fibres were synthesised with polyvinyl alcohol and were subsequently carbonised and reduced. These fibres gave comparable capacitance results to the carbonised polyacrylonitrile fibres (47 F g^{-1} and 40 F g^{-1} respectively).

1.5 Declaration

No portion of the work referred to in the thesis has been submitted in support of an application for another degree or qualification of this or any other university or other institute of learning

1.6 Copyright

The author of this thesis (including any appendices and/or schedules to this thesis) owns certain copyright or related rights in it (the “Copyright”) and s/he has given The University of Manchester certain rights to use such Copyright, including for administrative purposes.

Copies of this thesis, either in full or in extracts and whether in hard or electronic copy, may be made only in accordance with the Copyright, Designs and Patents Act 1988 (as amended) and regulations issued under it or, where appropriate, in accordance with licensing agreements which the University has from time to time. This page must form part of any such copies made.

The ownership of certain Copyright, patents, designs, trademarks and other intellectual property (the “Intellectual Property”) and any reproductions of copyright works in the thesis, for example graphs and tables (“Reproductions”), which may be described in this thesis, may not be owned by the author and may be owned by third parties. Such Intellectual Property and Reproductions cannot and must not be made available for use without the prior written permission of the owner(s) of the relevant Intellectual Property and/or Reproductions.

Further information on the conditions under which disclosure, publication and commercialisation of this thesis, the Copyright and any Intellectual Property and/or Reproductions described in it may take place is available in the University IP Policy (see http://documents.manchester.ac.uk/DocuInfo.aspx?DocID=2442 0), in any relevant Thesis restriction declarations deposited in the University Library, The University Library’s regulations (see http://www.library.manchester.ac.uk/about/regulations/) and in The University’s policy on Presentation of Theses

1.7 Abbreviations

1D: 1 Dimensional

2D: 2 Dimensional

3D: 3 Dimensional

AFM: Atomic Force Microscopy

CNT: Carbon Nanotube

CV: Cyclic Voltammetry

EDL: Electrical Double Layer

EDLC: Electrical Double Layer Capacitor

ESR: Equivalent Series Resistance

FLG: Few Layer Graphene

FTIR: Fourier-Transform Infra-Red

FWHM: Full Width Half Maximum

GO: Graphene Oxide

MWCNT: Multi-Walled Carbon Nanotube

PAN: Polyacrylonitrile

PVA: Polyvinyl Alcohol

rGO: Reduced Graphene Oxide

SEM: Scanning Electron Microscopy

SWCNT: Single-Walled Carbon Nanotube

TGA: Thermogravimetric Analysis

vdW: van der Waals

XRD: X-Ray Diffraction

1.8 Acknowledgements

I would like to give special thanks to my main supervisor Prof. Ian Kinloch and my co-supervisor Prof. Robert Dryfe. I would also like to show my gratitude for the EPSRC who without their funding I would not have been able to do this PhD project.

I would like to give thanks to members of the Carbon group who significantly aided me during the project: Dr. Amor Abdelkadar, Dr. Cristina Valles, Dr. Fei Liu, Dr. Jinyuan Cao, Dr. Oana Istrate, and Dr. Mark Bissett.

I would also like to acknowledge the help of instrumental technicians and give thanks to: Mr Michael Faulkner, Dr. Christopher Wilkins, Mrs Polly Greensmith, Miss Jasmine Fernley, Mr Andrij Zadoroshnyj, Mr Andy Wallwork, Dr. John Warren, and Dr. Ben Spencer.

Finally, I could not have completed this PhD without support from my mother and brother, Sezgin and Mark, and my partner Tom.

Words: 72,486

2 Introduction and Objectives

Renewable power is projected to be the key growth area in the world power market growth by 2020.[1] A challenge to these green technologies is the variability in their supply of the energy with time, and thus there is a need for quick and efficient ways to store the energy. There is also a demand for smaller, more efficient, and faster energy storage devices for the portable market. Batteries, including the lithium-ion (Li^+) battery, are popular due to their high energy density; however they are relatively quick to degrade (low cycle life) and have low power densities. Capacitors traditionally have lower energy densities, however they can be charged / discharged very quickly and are stable over many cycles. The discovery of graphene in the late 2000’s has shown light on a new material for supercapacitor research. Graphene has a high specific surface area (2630 m^2 g^{-1}), high carrier mobility, is lightweight, and is stable to degradation. These unique electrical and physical properties of monolayer graphene are apt for supercapacitor devices. In order utilise the unique features of graphene, the high specific surface area must be maintained, with few defects which could interrupt the carrier mobility. This makes super-capacitor construction difficult, as building up a material from the nanoscale to the macroscale can introduce re-stacking and defects, which will inhibit the ultimate performance of the super-capacitor. Some research groups are pursuing fibre spinning as a method for supercapacitor manufacture, due to the continuous synthesis method, allowing for high-throughput capacitor synthesis and ease of transferability. Another challenge is the synthesis of graphene itself, due to the need for the product to be thin and defect free. This is especially hard for commercial applications as many current synthesis methods which produce high amounts of graphene are either defect prevalent and/or costly. The electrochemical exfoliation of graphite and the reduction of GO have been shown to be highly efficient methods of graphene synthesis, with bulk quantities of relatively defect and impurity free graphene synthesised.

The main objective of this research project is to move graphene from nanoscale graphene particles to macroscale devices, while retaining the super-capacitor performance.

The aims were:

1. To investigate the role of graphite microstructure on the electrochemical exfoliation process, and characterise the electrochemical behaviour of the resultant flakes.
2. To optimise the wet-spinning of graphene-polyacrylonitrile composite fibres and their subsequent carbonisation, and determine the capacitance of the carbon fibre composites, relating it to their microstructure.
3. To optimise the wet-spinning of graphene oxide-polyvinyl alcohol fibres and their subsequent reduction, and analyse the capacitance of the reduced graphene oxide fibres.

This thesis explores the electrochemical exfoliation of graphite using two methods on four different graphite samples, and the application of this exfoliated graphite to nickel foam to analyse the capacitance; the synthesis of exfoliated graphite-carbon fibre composites from the electrochemically exfoliated graphite and capacitance analysis; and synthesis of graphene oxide and spinning into fibres, with subsequent reduction and capacitive analysis.

3 Literature Survey

To determine where this PhD project lies within the scientific landscape, the literature around the use of carbon materials within supercapacitors will be reviewed. The key areas of specific interest are: graphene related materials (particularly their structure, properties, and synthesis), the electrochemical exfoliation of graphite, energy storage capacity, and graphene-based supercapacitors.

3.1 Introduction

Different materials confer different properties to capacitors. Early capacitors utilised metal electrodes, usually with air as the medium between the two plates. These capacitors have an extremely low energy density. The rise of electrochemical capacitors, which use electrolyte as the conductive medium between the plates, gave rise to higher energy density capacitors, with two prominent types, pseudo- and super-capacitor. Metal oxides and conductive polymers can form pseudocapacitors, which store charge through Faradic (redox) reactions. This storage method reduces their stability but affords them a higher energy density. Carbonaceous materials can form electrical double-layer capacitors (EDLC), which store charge on their surface. These have high power densities and are more stable to degradation. These carbonaceous capacitors are also referred to as supercapacitors and are gaining popularity due to their ease of use, and potential to store high amounts of energy.[2]

Figure 3.1 is a Ragone plot displaying the range of specific power and energy that different energy storage devices can deliver. While fuel cells will always have a higher energy density than other devices, they deliver power slowly, and these reactions cannot be reversed. In general, batteries have higher energy densities than electrochemical capacitors and fuel cells, however there is some overlap. This could mean there becomes a point when electrochemical capacitors could replace batteries for applications that also require a quick delivery of energy. Electrochemical capacitors cover the largest energy density and power density window of all the energy storage mechanisms. This potential could be used in a wide range of applications in the energy storage market.

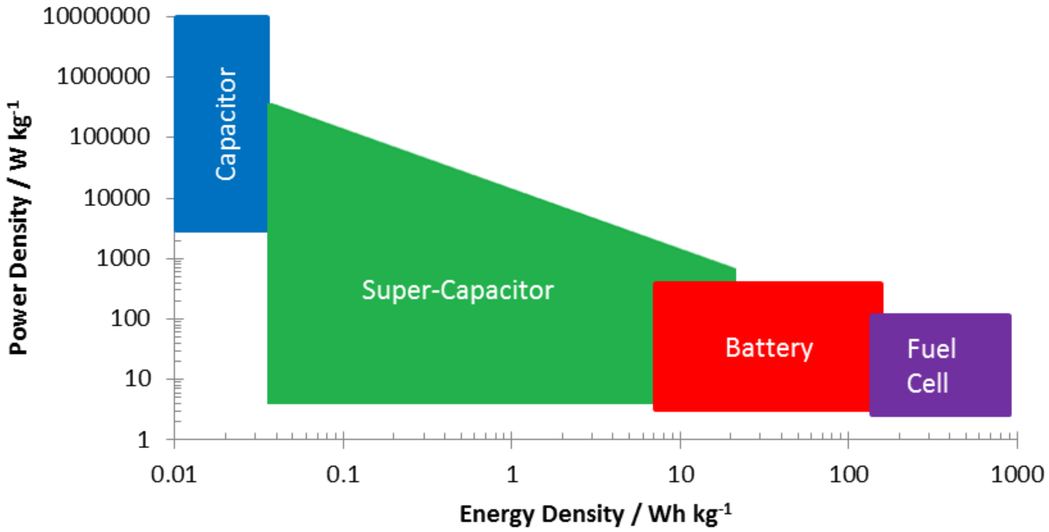

Figure 3.1: A Ragone Plot, showing the range of power and energy densities certain energy storage devices can achieve using current technology. Electrochemical capacitors occupy the largest window of both energy and power densities, allowing for a wide range of potential energy storage applications.[3]

Early carbonaceous capacitors utilised activated carbon as the electrode material, due to the ease of synthesis and large surface area. However, it is not electrically conductive and has dead mass in the form of inaccessible pores, making it unsuitable for high powered capacitor applications. Currently a significant percentage of supercapacitor research is directed towards graphene due to its high specific surface area, speed of charge carriers, and electrical conductivity, making it ideal for energy storage applications. **Figure 3.2** shows a timeline of the discovery of carbon materials and capacitor breakthroughs.

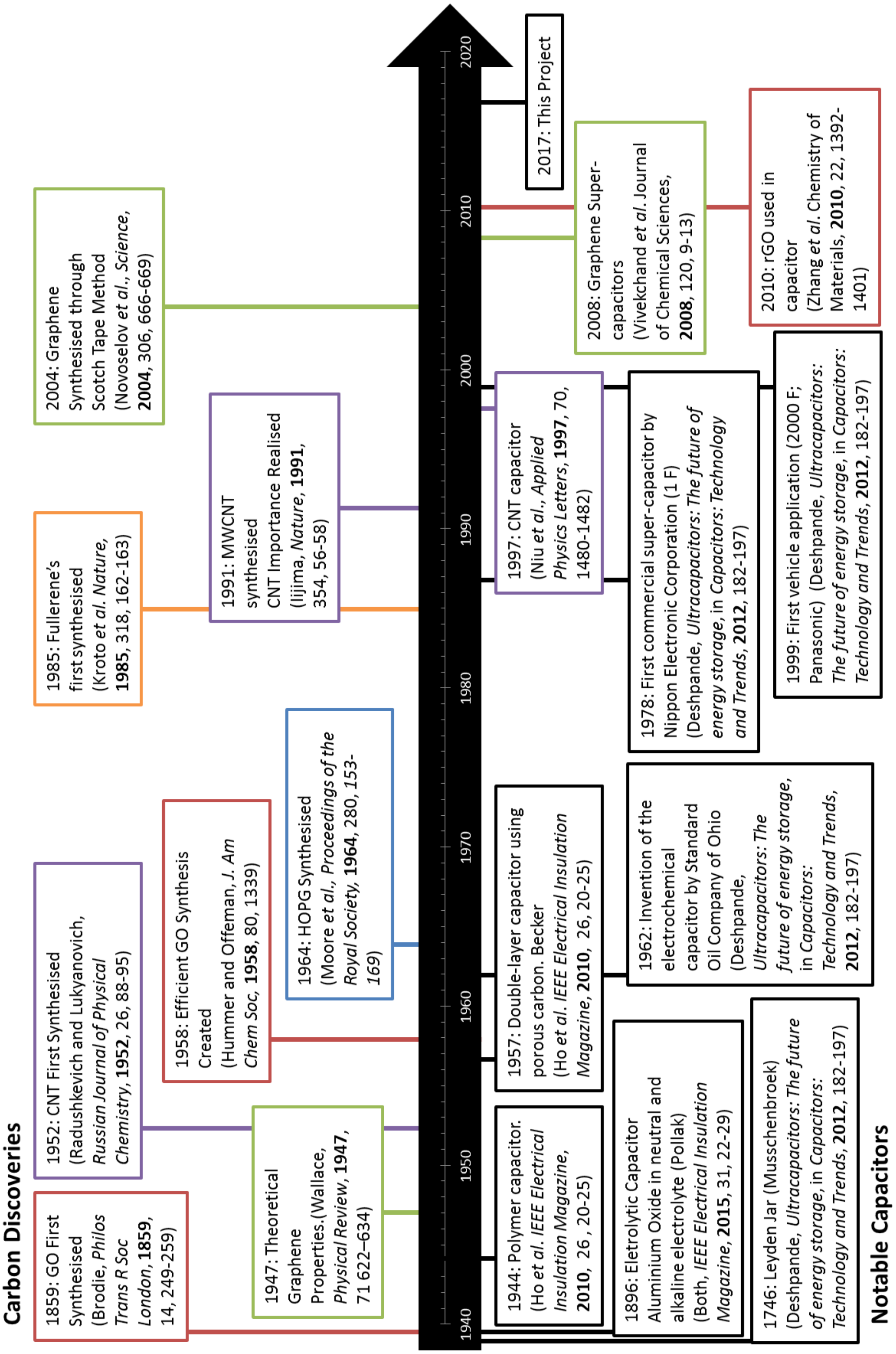

Figure 3.2: A timeline showing when a range of carbon materials were first discovered and their first use within energy storage applications.

In a study by *marketsandmarkets,* the graphene market was predicted to be worth \$278.47 Million by 2020, with a growth rate of 42.8 % from 2015 to 2020. They predicted that graphene oxide will be the biggest segment of this graphene market, in part due to its stability in aqueous solvents. They also report that the largest application for graphene is in energy.[4] Meanwhile, the global market for all types supercapacitors is \$2.0 Billion, and it is expected to grow at a 5 year compound rate of 19.1 % to \$4.8 Billion in 2020.[5] These two markets are of course intertwined, with each having a synergistic effect on the other, given the current focus on graphene enabled supercapacitors.

Graphene has recently gained interest in some parts of the scientific community ever since Geim and Novoselov won the 2010 Nobel Prize in Physics for research into the electrical properties of mechanically exfoliated graphene.[6] Their research highlighted graphene as having a unique combination of properties, which has encouraged a push towards further research into 2D materials, including metal dichalcogenides (*eg*. MoS_2) and boron nitride. The graphene research landscape is very large, with 25,000 papers written on graphene in 2016 alone.[7] **Figure 3.3** is a report made on Web of Science™ displaying two plots; one showing the number of papers produced per year containing the word '*graphene'* and the other containing two words '*graphene*' and '*capacitor'*. The general trend in both areas is a sharp increase in the number of papers published. This is particularly prominent in both plots, where after 2010, there is an increase of interest in the field. This interest of graphene has a synergistic effect on the graphene capacitor research field, with both receiving an increase in interest due to new discoveries.

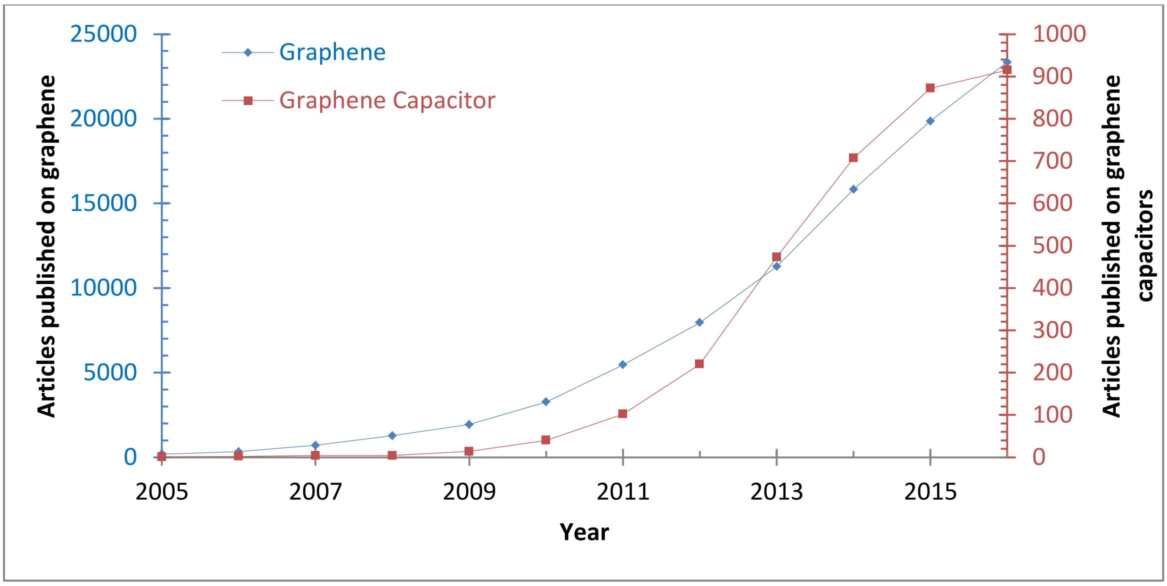

Figure 3.3: Two plots of the number of publications containing the words 'graphene' and 'graphene capacitor' per year, made using Web of Science™. Both fields have gained a considerable momentum since 2009, due to the discovery of the important niche 2D materials have. (Search term: graphene; graphene capacitor).

3.2 Graphene-Related Materials

This section of the thesis will explore the structure, properties, and synthesis of the graphene-related materials, graphene, graphene oxide, and reduced graphene oxide. Also featured is a detailed review on the electrochemical exfoliation of graphene from graphite, due to its extensive use in this PhD project.

3.2.1 Graphene

Structure and Properties

Graphene is a one atom thick hexagonal lattice of sp^2 carbon atoms. When more layers of graphene are added, the structure can be referred to as bi-layer, tri-layer, and few layer graphene (FLG), after which it becomes many layer graphene (MLG). Past 10 – 20 layers of graphitic sheets, the structure is commonly thought of as bulk graphite, due to many of the desired graphene properties only occurring at low (< 10) amounts of graphitic sheets.[8] **Figure 3.4** shows how graphene can be considered as the theoretical basis to all other sp^2 carbon allotropes (namely Buckminster fullerene, carbon nanotubes, and graphite).

Graphite is an anisotropic material, where the electrical and thermal conductivities are 1000 times higher in-plane than out-of-plane, and was the first indication of the unique properties of graphene. The distance between the layers in graphite is 3.35 Å,[9] while the nearest neighbour carbon-carbon bonds in a graphitic sheet is 1.42 Å. As a result the inter-layer interactions (mainly vdW and π-π stacking) are far weaker than intra-layer interactions, allowing for the separation of graphitic sheets. However the sheets in graphite have a high cohesive vdW energy of 5.9 kJ mol^{-1} (61 meV / atom)[10], which is strong enough to cause the re-stacking of graphene sheets to graphite. The stacking of graphitic layers in graphite mainly follows ABA stacking, although random (turbostratic) and ABC stacking can also occur.[11]

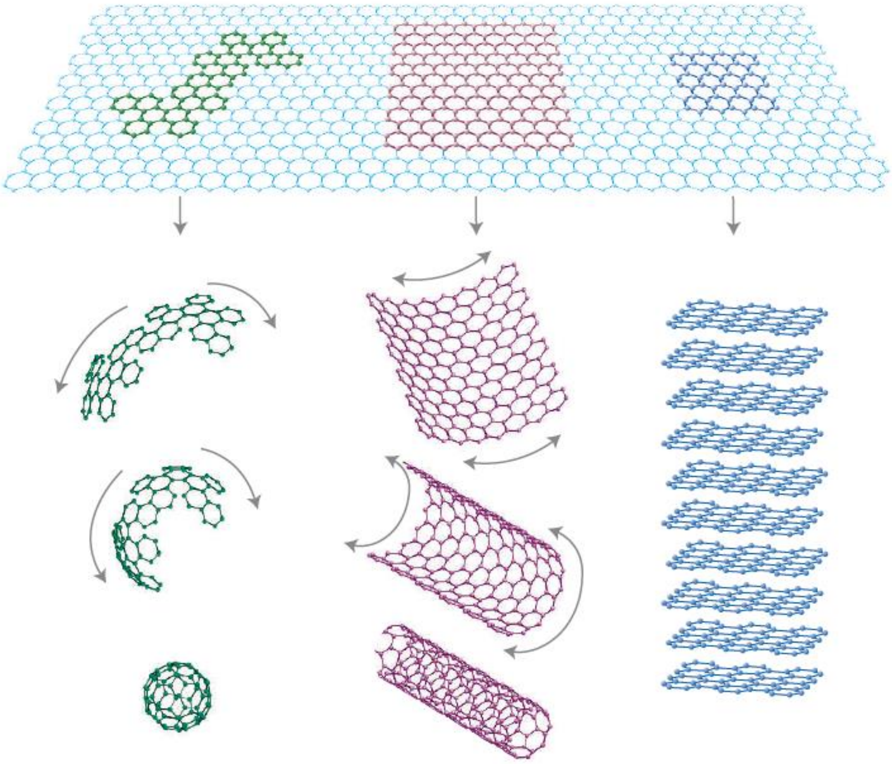

Figure 3.4: Graphene as the base for other carbon materials. (Top) Graphene; (Left) 0D Buckminster Fullerene; (Centre) 1D Nanotube; (Right) 3D Graphite. Buckminster Fullerene, CNTs, and graphite can be described in terms of graphene, by shaping it into a sphere, rolling it into a tube, or stacking it, respectively.[12]

In hexagonal sp^2 carbon structures a carbon atom has four orbital electrons, three of which are used for sp^2 bonding to three carbon atoms filling up the s, p$_x$ and p$_y$ (σ) orbitals, leaving the p_z (π) orbital half filled with one electron. Like all orbitals this is split into bonding and anti-bonding orbitals which appear above and below the graphene molecule, with the electron firmly in the valence band. The aromaticity of graphene is different to benzene and its derivatives, as graphene has two π-electrons over each ring, making it local aromaticity.[13]

In graphene, the hexagonal lattice can be broken down into two sub-lattices denoted by A and B in (**Figure 3.5**), with the unit cell consisting of two carbon atoms. The bonding (valance band) and anti-bonding (conduction band) meet at the K (corner) points of the Brillouin zone (**Figure 3.6**).[14] These are called the Dirac points due to the presence of Dirac fermions, where the electrons require no excitation energy in order to be promoted to the conduction band.

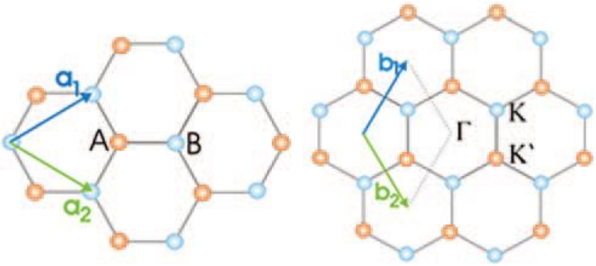

Figure 3.5: (Left) The crystal lattice; and (Right) the reciprocal lattice of graphene. The crystal lattice has two atoms in the unit cell, while the reciprocal lattice shows the location of the Γ and K points (where the valance and conduction bands meet).[14]

The unit cell in graphene has two atoms, with the 2D lattice vectors:

$$\boldsymbol{A_0} = (\frac{a}{2})(3, \sqrt{3})$$

$$\boldsymbol{B_0} = (\frac{a}{2})(3, -\sqrt{3})$$

Where *a* ≈ 0.142 nm, the distance between nearest neighbour carbon atoms. The K points appear at the inequivalent corners of the Brillouin zone, with the vectors:

$$\boldsymbol{K} = (\frac{2\pi}{(3a)}, \frac{2\pi}{(3\sqrt{3a})})$$

$$\boldsymbol{K'} = (\frac{2\pi}{(3a)}, -\frac{2\pi}{(3\sqrt{3a})})$$

The Dirac points (similar to *Γ* points in semi-conductors), are where the electron transport physics are the most important.. At these points there is a linear energy-momentum dispersion of electrons, making graphene a zero band-gap semiconductor. As there are two Dirac points (at K and K') there is a valley degeneracy of two ($g_v = 2$), which will be explored further in the section on Raman spectroscopy. At these Dirac points the electrons travel at the Fermi velocity. **Equation 1** shows that the Fermi velocity does not depend on energy or momentum, unlike in all other cases in different molecules.[15]

$$E_{\pm}(\boldsymbol{q}) \approx \pm v_F|\boldsymbol{q}| + O[\left(\frac{q}{K}\right)^2] \qquad \textbf{Equation 1}$$

Where q is the electron momentum relative to the Dirac points and v_F is the Fermi velocity. Electron mass does not appear in the equation.[16]

In graphene, the carrier dispersion depends on the Fermi velocity, v_F. This constant for graphene is ≈ 10^8 cm s^{-1} without any carriers. This is only 1/300th of the velocity of light, which leads to the unique electrical properties of graphene, which are sought for electrical applications.[17] The chemical potential of graphene crosses at the exact Dirac point, meaning that it shows aspects of quantum electrodynamics, explaining how the Dirac fermions have such a high velocity. These Dirac ferimons are also importantly massless, chiral, and unaffected by electrostatic potentials (which can occur from dissorder in the graphene).[18] The Dirac fermions can also insensitive to scattering over micron ranges.[19] **Equation 2** shows that Dirac fermions near the speed of light can be described by the quasi-particles showing a linear dispersion relation.[12] The electronic structure in graphene is influenced by doping (p and n), the curvature of the sheets, and the addition of more graphitic sheets. With additional graphitic sheets the bandstucture of the graphene become far more complicated, and is not covered here.

$$E = \hbar v_F|k| \qquad \textbf{Equation 2}$$

Where E is the energy, ħ is Hamiltonian's constant, v_F the Fermi velocity (10^6 m s^{-1}), and |k| is the quasi-particle momentum.[12]

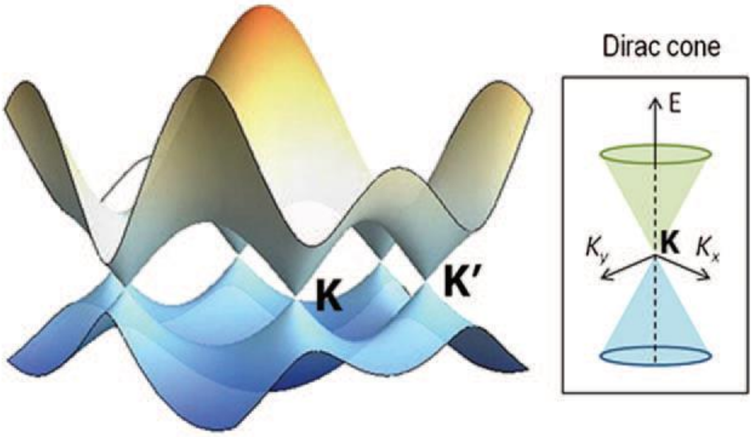

Figure 3.6: The Brillouin zone of Graphene. The Dirac cones meet at the K points, with the cones half filled (blue), which is why graphene can be described as a zero band-gap semiconductor.

Concerning physical properties, graphene boasts ultra-high strength and stress, with a tensile strength of 130 GPa and a Young's modulus of 1 TPa,[20] both of which are superior to other materials. The high strength and flexibility are due to the rigid hexagonal lattice and thinness.[21] Graphene also boasts an impressive surface area of 2630 m^2 g^{-1}, due to its nature has a lightweight thin 2D material with a very low density.[22]

In addition to the extraordinary mobility of the charge carriers graphene exhibits the chiral quantum Hall effect at room temperature,[12] meaning it could be used in circuit devices. It has unusual magnetic properties, can perform charge transfer reactions, has great electrical and thermal conductivity, and exhibits the ambipolar electric field effect. The optical transparency of graphene is a high 97.7% at visible wavelengths,[23] making it desirable as a replacement for indium tin oxide (ITO) photovoltaic devices, display screens, and touch screens.[24, 25] Graphene is also chemically and thermally stable, owing to the rigid hexagonal lattice, however it will oxidise via strong oxidisers and high temperatures in air.

Stacking more graphene sheets together will alter the properties of the material, though there are no defined values due to the varying nature of FLG. For FLG there is an increase in sheet resistance to hundreds of Ω sq^{-1} (< 3 nm thick) and more commonly kΩ sq^{-1}.[19, 26].

The optical transmittance is about 90%. For graphite the resistance can be in the MΩ (10^6) region.[27]

The high carrier mobility and surface area, combined with the strength and flexibility makes graphene ideal for energy storage research, which will be reviewed in **Section 3.4.**

Synthesis of Graphene

Synthesising high quality mono- / few-layer graphene is difficult due to the nature of creating such a small and thin material. Two important considerations are preventing the re-stacking of graphene sheets (counteracting the strong vdW and π-π stacking forces between the sheets), and reducing the number of defects in the 2D lattice. Extra concerns when developing graphene for capacitance applications are retaining the high surface area for double-layer capacitance, and using a substrate that is transferable to create the electrode.

Broadly there are two general techniques used to synthesise nanomaterials: bottom-up and top-down. Bottom-up approaches create graphene by stitching together smaller carbon molecules; techniques include CVD, epitaxial growth,[28] and organic coupling reactions. Top-down techniques separate the graphitic sheets in graphite by mechanical, thermal, or chemical means; methods include ion exfoliation, microwave plasma,[29] arc discharge,[30] mechanical exfoliation, and graphene oxide reduction. The most important techniques for the synthesis of graphene will be examined below, though as the electrochemical exfoliation is the key synthesise method in this thesis, this topic will be reviewed more in-depth.

The synthesis method used for graphene production will depend on the most important aspect of the produced graphene. **Figure 3.7** shows various methods to synthesise graphene on an axis of production cost against quality. For instance, mechanical exfoliation can produce high quality graphene, useful for scientific analysis, but it would not be suitable for applications which require large amounts of graphene, like commercial devices, due to the high synthesis cost.

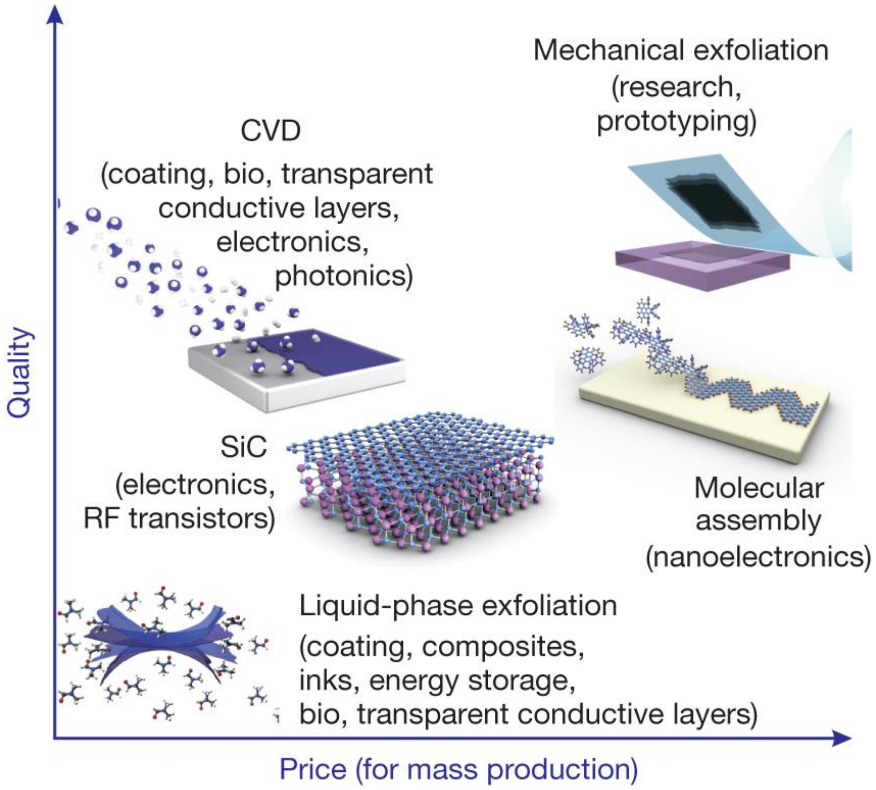

Figure 3.7: A graph showing how graphene synthesis techniques vary in terms of the cost of production and quality of the graphene synthesised.[31]

Chemical Vapour Deposition

CVD is a reproducible and scalable method for the synthesis of high-quality and defect-free, monolayer graphene, making it a popular method for the synthesis of graphene films and coatings. However the high costs, low yield, and transfer problems inhibit the use of CVD grown graphene for certain applications.

In a typical CVD experiment, graphene is produced by the decomposition of small hydrocarbons over a metal substrate at high temperatures. The most common carbon precursor and substrate is methane and copper (111) respectively as they synthesise mono-layer graphene reproducibly. During the synthesis, the substrate is first annealed at 1000 °C using hydrogen to remove surface impurities like oxides and possibly reconstruct the surface. Methane (with additional hydrogen) is then added, which decomposes on the substrate to form nuclei which then grow laterally. **Figure 3.8** shows a schematic of how this process broadly occurs. Li *et al*. have shown the mechanism of growth depends on the metal substrate, with growth by surface absorption on copper, and carbon diffusion combined with precipitation on nickel.[32] Though, the synthesis of consistent mono-layer graphene on nickel is more difficult than on copper, with FLG dominating the product composition.[33]

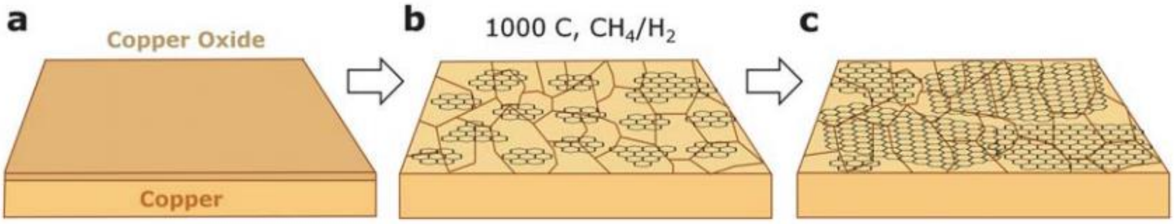

Figure 3.8: Schematic representation of CVD graphene growth on copper. First the copper is annealed at 1000 °C (a), then the graphene grows via island formation (b), and finally the flakes grow large enough to form a graphene sheet with a variety of grain orientations (c).[34]

The main challenges with the CVD production of graphene are low yields, the process of transferring the graphene to other substrates tends to induce defects and impurities, multilayer graphene can form, and incomplete coverage is common. However Bea *et al*. have shown that they can synthesise large areas (30 inch diagonal length) of high quality monolayer graphene on copper, through multiple transfer and chemical doping. [35] This quickly gown graphene is ideal for use in transparent conductive films for electronic screens or photo-voltaic devices.[36] Conversely Wei *et al*. have doped graphene with nitrogen by using ammonia and methane as the reactants. It was found that though monolayer graphene was present, FLG was most prevalent.[37] This is not useful for the synthesis of graphene, as CVD is a costly and time-consuming technique to synthesise graphene, thus anything product other than mono-layer graphene is non-ideal. Additionally, if functionalisation is wanted, other methods, such as the reduction of GO, are more useful for the synthesis of functionalised graphene.

Liquid Phase Exfoliation

Liquid phase exfoliation arose from earlier work which investigated the dispersion of CNTs in a suitable solvents.[38] It was found that when the surface energy of a liquid matches the surface energy of the material dispersed in it, the material can be stabilised in solution. The key intellectual step was to then realise that suitable solvents could not only disperse carbon nanomaterials, but also facilitate its cleaving from graphitic sheets. In general, graphite is dispersed in a solvent and shear force is applied via sonication for many hours, which will separate the graphitic sheets into solution. Centrifugation follows to separate the sheets based on size and thickness.[39] Typically, graphene made from liquid exfoliation is small in diameter (<1 μm) , with larger flakes being defect prevalent, due to the long sonication times which can damage the graphene sheets. This prohibits liquid exfoliated graphene from use in electronic applications, and especially as a transparent electrode. For example, Sukanta *et al*. aqueously exfoliated graphene with surfactants and determined that the resultant material could not be used for transparent conductors, as the optical transmittance was only 76% and sheet resistance was 4 kΩ sq^{-1}.[40] However the exfoliated materials can be used as a nano-filler in composites and coatings, despite its fine size.[41]

Graphene has a surface energy of 68 mJ m^{-2}, which corresponds to a surface tension of 40 mJ m^{-2}.[38] For the enthalpy of mixing to be at a minimum in order to ensure spontaneous mixing, the solvent's energies need to be similar in value. Reducing the potential energy between the graphitic sheets stabilises the graphene against re-stacking by reducing the strong vdW attractions between the sheets. Hildebrand and Hansen solubility parameters also need to be similar to ensure adequate exfoliation. Appropriate solvents have been found to include NMP, DMF, DMSO, and *ortho*-dichlorobenzene.[42, 43] Graphene can form stable concentrations in NMP up to 63 mg mL^{-1}, although only 27 mg mL^{-1} is indefinitely stable.[44] Graphene is particularly stable at high concentrations (20 mg mL^{-1}) in chlorosulphonic acid. This super acid protonates graphite, and stabilises the negatively charged graphene. Additionally liquid crystals are readily formed.[38]

Coleman *et al.* used liquid exfoliation to produce a product in NMP which was largely less than 5 layers thick and 25% of this was monolayer graphene, in a concentration of 1 mg ml^{-1}. However long sonication times produced defects in the basal planes and reduced the size of the graphene flakes to less than 1 μm in diameter. DMSO was also used as the solvent with 1 % monolayer graphene produced.[45] Chih-Jen Shih *et al*. have corroborated these results when looking at the stabilisation of graphene in DMSO. DMSO also showed promise for other synthesis techniques due to its wide electrochemical window. Using simulations, they have found that the correct solvent can efficiently reduce the vdW energy and increase the barrier to restacking.[46] In this PhD project, DMSO was used as the electrolyte for electrochemical exfoliation, for its wide electrochemical window and stabilisation of graphene in solution.

Adding a surfactant will help stabilise graphene in less favourable solvents, through steric or electrostatic stabilisation. This approach means that solvents such as water can then be used. For electrostatic stabilised graphene, an electrical double layer is formed, which counteracts the vdW and π–π forces between neighbouring sheets, keeping graphene from re-stacking. Surfactants also open non-covalent functionalization routes for functionalising graphene. Colman *et al*. showed that sodium chlorate stabilised individual sheets of graphene through Coulomb repulsion from the electric double layers.[47] Flake quality was good, but the product had a lower concentration of monolayer graphene compared to NMP exfoliated graphene. It took 400 hours of sonication get 0.3 mg mL^{-1} graphene.[48] Though surfactants are useful for stabilising the graphene, they add dead weight for capacitance, which makes them undesirable for use in this PhD research.

Microwave

There are many different microwave synthesis methods for graphene, making microwave synthesis a wide and varied route. For instance, some mechanisms of graphene synthesis are completely different, and in some cases the product can be functionalised. All however use a microwave to assist in the synthesis of graphene.

For example, Dato *et al*. synthesised graphene via dropping ethanol into argon plasma in a quartz tube located within a microwave. In the one second the droplets were in the system they evaporated and dissociated, forming a solid. The product was collected after rapid cooling with 2 mg of material made per minute of reaction time. Un-functionalised mono- and bi-layer graphene could be synthesised routinely with 250 W of microwave power.[29] This synthesis technique has the advantage that it is extremely quick at production good quality graphene, however the resultant graphene is small and unable to be used in supercapacitor applications due to many defect edges.

Xu *et al*. have used graphite prepared from microwave synthesised metal phthalocyanine at a high temperature to synthesis graphene. The graphite is obtained after 20 minutes at 450 °C, with subsequent rapid cooling. The cooling causes thermal stress, breaking the graphite sheets into graphene. The process was fast, taking 30 minutes, and when liquid nitrogen was used as a coolant the product was 1 – 2 layers thick. Microwave synthesis of graphene is a scalable way to create graphene, however the resultant graphene is highly functionalised, with 24% oxygen.[49] This product would need to be reduced in order to gain the important aspects of graphene in supercapacitor applications (like high conductivity and ability to form multiple EDL sites), making the synthesis of GO via chemical methods more ideal due to the large quantities of high quality large flake GO produced. This is why in this PhD project the chemical synthesis of GO was used.

Arc-Discharge

In this method, two graphite electrodes are held close together and charged at a very high current. Discharge will occur, resulting in plasma, which causes the anode to vaporise, and produce a product of FLG. The reaction takes place in a cooled stainless steel chamber and buffer atmosphere.

In work by Wu *et al*. they successfully synthesised FLG using arc discharge in a range of conditions. They found the optimum conditions were a buffer gas of carbon dioxide and helium at high pressures (> 1270 Torr), with the electrodes having a low voltage (< 35 V) and high current (150 A). The products have few-defects and little-functionality, with a resistance of 670 kΩ sq^{-1} and conductivity of 11 S cm^{-1} (thickness: ~ 25 nm). The products were 4 – 5 layers thick with tens of grams synthesised in minutes.[30] Conversely Li *et al*. used ammonium and helium as buffer gases at 760 Torr to synthesise N-doped FLG sheets using arc-discharge. The graphite rod anode was consumed producing sheets between 2 – 6 layers thick with a nitrogen content of 1%.[50] The arc-discharge method requires a lot of expensive equipment not readily available and thus unsuitable for creating graphene at low cost.

GO Reduction

GO can also be synthesised via the reduction of graphene oxide; however this will be covered in more detail in **Section 3.2.4** which discusses graphene oxide in detail.

3.2.2 Electrochemically Exfoliated Graphite

The electrochemical exfoliation of graphite is a versatile technique, in which the properties and structure of the resultant graphene product is dependent on many factors, including the initial graphite used, whether it is a reductive or oxidative process, the power supplied during exfoliation, the electrolyte used, the length of exfoliation, and subsequent washing techniques.

Typically a two-electrode electrochemical cell is used with graphite as the working electrode (**Figure 3.9**). A potential is applied which forces the ions in the electrolyte intercalate between the graphitic sheets, disrupting the vdW and π-π stacking forces, separating them producing free-standing graphene. The electrolyte can also decompose and form *in-situ* compounds with the graphite, physically expanding the electrode, allowing the graphitic sheets to be separated. The graphite working electrode can be either the anode or cathode, depending on what product compound is desired. Anodic oxidation often results in a functionalised material similar to graphene oxide requiring further reduction, although after reduction the product is often monolayer graphene. Cathodic reduction can produce pure monolayer graphene; however the process is more likely to produce few-layer graphene than its oxidative counterpart. **Figure 3.10** shows the difference in these electrochemical synthesis techniques.

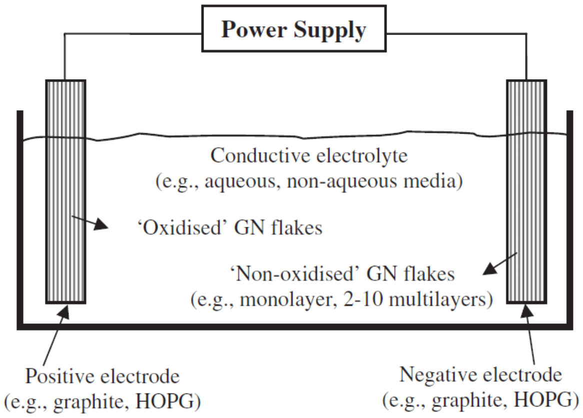

Figure 3.9: A schematic showing the set-up used for the electrochemical exfoliation of graphene. An applied potential forces ions to intercalate between the graphitic sheets of graphite separating them, forming graphene. The positive electrode can undergo oxidation, while the negative electrode can go through reduction, depending on the electrolyte used and power supplied.[51]

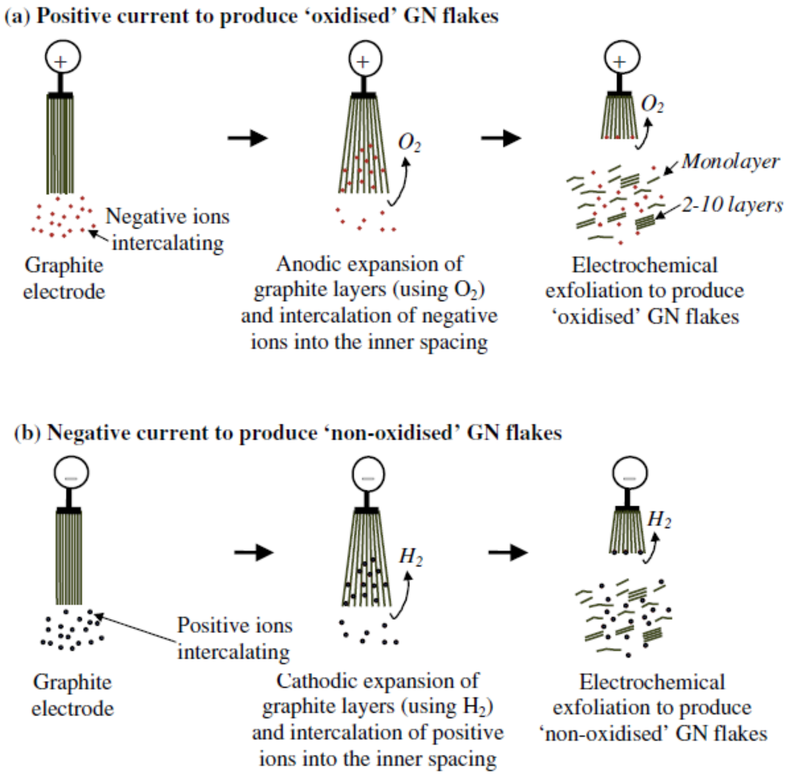

Figure 3.10: A representation of the difference between (a) anodic oxidation and (b) cathodic reduction. Due to potentials applied, only certain ions or anions will intercalate into the graphite (anode or cathode respectively), changing the resultant product. [51]

Electrochemical exfoliation has been shown to produce graphene quickly and efficiently, but it also uses relatively cheap materials and equipment. In some cases the intercalation is single step, quick (can be performed in hours, unlike chemical / liquid exfoliation methods taking days), performed at ambient conditions, and produce gram quantities,[52] which makes them ideal for industrial applications. However, as no substrate is used, re-stacking of the sheets can occur, limiting the unique properties of graphene, including the surface area and conductivity. It has been shown that using HOPG with a grain size of < 20 µm often grants a higher concentration of graphene in the product.[53]

A key advantage of electrochemical exfoliation route is that the structure of the product can be tuned through the operating parameters (voltage, electrolyte, initial graphite, *etc*.). The majority of exfoliation processes in the literature are potential controlled with varying current (chrono-amperometry). A potential difference of 5 – 20 V is typical in a two electrode system, which will likely cause the breakdown of most electrolytes. Recently, there has been a shift to current controlled practices (chrono-potentiometry) as these will not cause the breakdown of electrolyte.

In electrochemical exfoliation, the pH can control the kinetics. With very acidic electrolytes the reaction is so facile that graphite flakes will drop from the electrode without complete exfoliation, giving a low yield of graphene. In addition the products are occasionally extremely oxidised and viscous. When using alkaline electrolyte the product is primarily graphene oxide, due to the oxide groups that are often found in alkaline solutions. However this does make it a good route for the production of graphene oxide. Parvez *et al*. have worked on the effect of pH on the electrochemical synthesis of graphite using 1 M H_2SO_4. They found that graphite fell from the electrode after 2 minutes of exfoliation at 10 V. However; the resultant product was more than 80 % ≤ 3 layers, with a C/O of 12.3 and sheet resistance 4.8 kΩ sq^{-1}. Additional sonication was required to achieve this high proportion of thin graphene. They also found that with reduced concentrations of H_2SO_4, the yield for exfoliated graphene was much lower, with 34 % and 2 % for 0.05 M and 0.01 M respectively.[54] Chang *et al*. employed ammonium hydroxide as the electrolyte with a pH of 13. The exfoliation took place at 10 V for 30 minutes and the product was primarily GO. After anodization the pH was 7.[55] Ionic liquids have been advocated as a green alternative to current electrolytes for the electrochemical synthesis of graphene, due to their low toxicity, vapour pressure, high chemical and thermal stability, and wide potential window. For example Luo *et al*. managed to synthesise ionic liquid functionalised graphene consisted of crumpled sheets 1 µm in size using 1:1 1-octyl-3-methyl-imidazolium hexafluorophosphate ([C8mim]þ[PF6]): water electrolyte.[56]

Anodic

The majority of the published work on the electrochemical exfoliation of graphene has been on anodic exfoliation. This is due to the ease of mono-layer (oxidised) graphene synthesis, by the oxidation of graphite, which increases the repulsive forces between the graphitic sheets, preventing re-stacking. In this synthesis the graphite anode is oxidised through oxidative potentials, and all the products are at least partially oxidised. This cannot be avoided as the potentials to facilitate ion intercalation are higher than the potentials to oxidise graphite. Anodic interaction usually involves the use of electron acceptor compounds like H_2SO_4,[54] HNO_3,[57] $FeCl_3$,[58] and H_3PO_4.[59] Nitrates have been shown to exfoliate graphite well due to their planar structure with NO_2^+ ions oxidising the graphite edges.[60] In general chlorides promote intercalation as a precursor, not as an intercalation agent itself.

Zeng *et al*. have used phosphate ions to successfully synthesise graphene. In their work, they use 0.025 M phosphate buffer solution at pH 6.9, and the exfoliation is performed using a potential window of 0 – 3 V in the form of 2 – 5 CV scans. The exfoliation was facilitated by the introduction of oxygen functionalities which weakened the bonds between the graphitic sheets, giving a highly oxidised product with a C/O of 3.45.[61] This highly oxidised product will then need to be reduced for supercapacitor applications. If GO is desired, the chemical oxidation of graphite is a more widely used route, as the mechanism is more understood due it being a widely researched area, and the oxidation is more controllable as large potentials are not used.

Colloidal solutions have been used to exfoliate graphite, shown in work by Li *et al*. Sodium dodecylbenzenesulfonate (SDBS) was used as an electrolyte and a potential of 30 V was applied for 48 hours. They suggested that SDBS can intercalate and also stabile the sheets. The resultant product was a stable colloidal solution of 1.2 nm thick graphene functionalised with SO_3^-.[62] Parvez *et al*. used sulphate ions to make a colloidal solution again. Neutral conditions gave the largest C/O (17.2) and lowest defect density, with a sheet resistance of 1.96 kΩ sq^{-1}. It was also high yield, with > 85 % of the graphene composed of ≤ 3 layers and up to 44 µm in size. **Figure 3.11** proposes a mechanism of this intercalation. During exfoliation, water is hydrolysed by reduction at the cathode. This creates OH^- anions which undergo nucleophilic attack at the edges and grain boundaries of the graphite. This oxidation at the edge depolarises the graphite and allows the SO_4^{2-} to intercalate, along with additional water molecules. Additionally the SO_4^{2-} anions and water undergo oxidation to form gaseous SO_2 and O_2 which further exfoliates the graphite.[63]

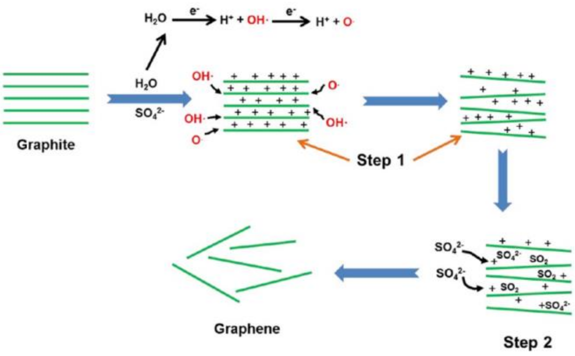

Figure 3.11: The mechanism of ion intercalation into graphite. First, water is broken down into OH^- and O^- anions. These attack the edges of the graphitic sheets, causing a positive potential in the sheets. This facilitates the intercalation of SO_4^{2-} anions, which, due to their large size, separate the graphitic sheets.[54]

Cathodic

The chemistry of anodic oxidation is complex due to the large potentials involved, multiple steps, and reactive chemicals. These can lead to various interpretations of the exfoliation mechanism. Anodic exfoliation produces mono-layer graphene by partially oxidising the surface, meaning reduction also needs to take place in order to obtain graphene-like material, which introduces more chemicals and processes which could contaminant and extend the process. Sonication is also often needed, which is very expensive on a large scale. These problems are why anodic oxidation has not led to the development of graphene on a large scale for industrial applications. Thus cathodic electrochemical exfoliation is being explored. Graphite has been used as the negative electrode in lithium ion batteries for decades, and this lithium intercalation also boosts electrical conductivity. The cathodic electrochemical exfoliation of graphite was initial inspired by lithium ion batteries, with the intercalation of lithium into negative graphite electrodes.

Cathodic exfoliation involves the use of donor intercalating species typically alkali metals and alkali earth metals, like potassium[64] and lithium. Rubidium and caesium can also be used, however potassium is usually preferred as it is cheaper and more readily available.[65] In a typical exfoliation, when the ions intercalate, they form graphite intercalation compounds. The compounds physically expand the electrode, unlike the anodic intercalation which results in functionalisation. The kinetics of intercalation is dependent on the size of the intercalating ions, however even without electrochemical facilitation, K, Ru, and Cs have been shown to intercalate at low temperatures (not using electrochemical exfoliation).[66] The distance between the graphitic sheets increases with the formation of graphene interaction compounds. For instance, the interlayer distance increases to 0.53 for K, 0.56 for Pb, and 0.59 for Cs. This is 1.5 times larger than the separation due to lithium.[64] Though Li^+ is mostly used due to its ease and speed of intercalation. Some notable research has looked into other ions such as Na^+, though addition reagents are required to stabilise the graphene-intercalation-compounds. For example Zhou *et al*. used Na^+/DMSO complexes to intercalate graphite, however additional thionin acetate salt was required to stabilise the graphene.[67]

Concerning lithium intercalation, Xu *et al*. have based their exfoliation on the lithium intercalation in batteries using lithium metal. Once intercalated these graphene-intercalation-compounds were dissolved in water to give lithium hydroxide and graphene. The process is slow, due to lithium being unable to penetrate the whole graphitic sheets. The method was repeated as a second step, and additional sonication was required for thinner (1 – 3 layer) graphene.[68] To overcome this slow intercalation, Huang *et al*. used molten lithium hydroxide, giving Li_xC_y. A constant current of 15 A for 30 mins at 600 °C was used, with fast intercalation shown by a high cell voltage. The fast intercalation facilitated mechanical stress on the graphite, leading to detachment of graphene stacks, which were added to water under sonication releasing hydrogen. The product was 80 % graphene, which also had a low density of defects. However this method is expensive due to high temperatures and sonication steps involved.[69]

As lithium is small, larger compounds are often required to facilitate the separation of the graphene sheets. Zhong and Swager intercalated graphite foil with Li^+, followed by tetra-alkyl-ammonium cations in two separate steps. In this potential controlled experiment they were able to control the degree of functionalization. TBA was used at -5 V for 24 hours, giving a low functionality product (removed via laser ablation) with a yield of 31 %. A high potential difference resulted in the electrolysis of the electrolyte, giving off propylene gas. This allowed lithium (lithium perchlorate) to readily intercalate into the graphite foil working electrode, with TBA eventually penetrating through cation exchange. Subsequent electro-decomposition of TBA, neutralised the graphite, and consequently increased the driving force of TBA cations into the graphite. The product required additional sonication; however, the graphite flakes were all < 5 layers thick.[70] This two-step exfoliation is slow and so was further refined by Cooper *et al*. In this work a graphite rod was intercalated with tetra-alkyl-ammonium cations producing FLG flakes with a 2 nm thickness and 100 nm diameter. The intercalation was done via voltammetry at 0.1 V s^{-1} using TBA^+ up to -2.5 V. Though large at a radius of 0.826 nm, the flexibility of the alkyl groups allows for intercalation. Conversely, due to the inflexibility of TMA (radius: 0.558 nm) 2-5 layer graphene was able to be produced.[71] They also found due to the high crystal orientation of HOPG, intercalation was difficult resulting in a reduced yield of exfoliated material.[72] Abdelkadar *et al*. further refined the work by Copper *et al*. They utilised a potential controlled single step exfoliation to produce FLG from graphite. The electrolyte of LiCl and TEA intercalated via solvated ions, and subsequently decomposed in the graphitic layers of the working electrode, forming gases that help separate the sheets. Large flakes (1 – 20 µm) can be synthesised in gram quantities. The detailed reduction mechanism is provided below. [53, 73]

$$nEt_3N + e^- + C = (Et_3N)_nC^-$$

$$mLi + e^- + C = Li_mC^-$$

$$nEt_3N + mLi + e^- + C = Li_m(Et_3N)_nC^-$$

$$Li_m(Et_3N)_nC^- + e^- + 2Et_3NH^+ = C + mLi + (n+2)Et_3N + H_2$$

$$Li_m(Et_3N)_nC^- = C + mLi + nEt_3N + e^-$$

This exfoliation technique was adapted for us in order to obtain graphene from graphite in this PhD project. What was brilliant about this exfoliation was that was one step, allowing for the quick synthesis of graphene, and that sonication was not used, which would prolong the synthesis of the graphene. Sonication is the slow-step in many electrochemically synthesised graphene papers. For example Wang *et al.* was only able to obtain a high yield of 70 % < 5 layer FLG flakes using lithium salts ($LiClO_4$) and organic solvents (PC and DMF)[74] after prolonged sonication in concentrated LiCl and thermal shock.[75] This is not feasible for commercial applications, where large amounts of good quality graphene are required to be made quickly.

3.2.3 Graphene Oxide

Graphene Oxide (GO) is an oxidised form of graphene, synthesised by the oxidation of graphite using oxidative chemicals. Due to the many functional oxide groups, GO it is an insulator; however it has found a niche in strength applications. GO is desirable for use as a precursor for graphene due to its relative ease of synthesis with a high product yield and low cost, its high hydrophilicity due to the oxide groups, and diverse reduction techniques which can tune the resultant product as desired.

Graphene Oxide Structure and Properties

Due to the difference in methods, reactive chemicals, degree of oxidation, and starting graphite that can be used to synthesise GO, coupled with the high degree of oxidation, the structure of GO cannot be resolved very accurately. The most recognised model was proposed by Leif and Klinowski. This rejects previous models which postulate a lattice of repeating units and instead puts forth a nonstoichiometric and amorphous one.[76, 77] GO is defined by a flat sheet of hexagonal carbon, on which there are a variety of oxygen-containing functional groups attached in a range of oxidations. These surface functional groups vary in concentration and abundance, as these depend on what method was used to synthesise the GO, the extent of oxidation and the initial, raw graphite material used. Acidic groups form on the edges of GO (though this is still up for debate), which stabilise the GO in aqueous solutions, while phenols and epoxides appear on the basal plane. This makes GO an amphiphile, as it consists of the hydrophobic basal plane (phenol rings) and hydrophilic edges (acidic group dipole and quadrupole vdW interactions). **Figure 3.12** shows the general proposed structure of GO.

Due to the hydrophilicity of GO, it can form stable colloids in solution. GO has desirable physical properties, with monolayer GO (thickness: 0.7 – 1.2 nm) having a Young's modulus of 207.6 GPa.[78] GO is an insulator due to the oxide groups on the surface, and generally has a high sheet resistance (10^{12} Ω sq^{-1}; FLG = ~400 Ω sq^{-1}). GO is brown which is due to the loss of electronic conjugation from the oxidation.[79]

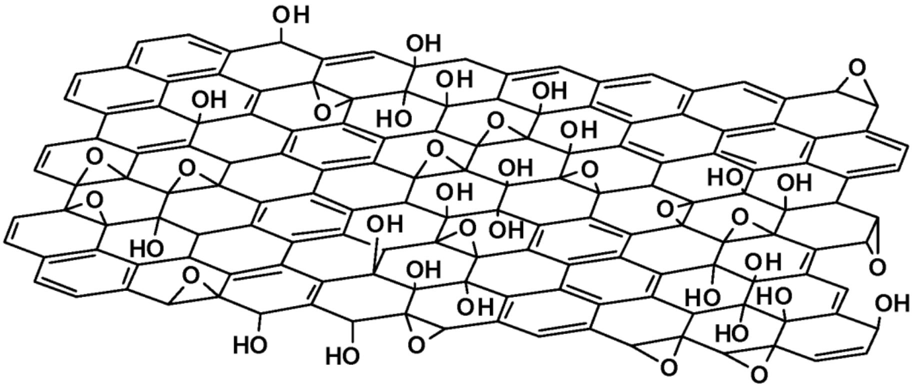

Figure 3.12: Leif and Klinowski proposed GO structure, without the carboxylic acid groups on the periphery of the basal plane.[80]

Synthesis

The first synthesis of GO was over 100 years ago; however it was only recently where the importance of this product was discovered. Thus the route to GO has not changed in over 50 years, with only a couple of prominent methods in use. The Hummers method, first created in 1957 still proves to be the most popular way to synthesis GO.[81] GO is synthesised via the chemical oxidation of graphite, though the direct mechanisms are debated due to the highly reactive chemicals and varying conditions of the reaction.

There are two other main methods, the Brodie[82] and Staudemaier[83] methods, which use $KClO_3$ and nitric acid, and the Hummers method which uses potassium permanganate and sulphuric acid. Staudemaier's method differs from Brodie in that he applied the chlorate over time and sulphuric acid. In both the Brodie and Staudemaier methods, nitric acid is used as it is a strong oxidising agent, and produces NO_2 and N_2O_4. Potassium Chlorate, which can use the source of dioxygen *in situ*, is also a strong oxidising agent. Flake graphite is used, as it is purified to remove hetero atomic contamination. Due to this purification, there are π-defects in its structure to facilitate oxidation.[84] Flake graphite is made via the intercalation of acidic anions and heating to 800 °C, which breaks to flakes up resulting in a crystal lattice with thickness of less than 100 nm. Due to their already thin state, flake graphite can be used directly for battery applications due to their size and conductivity.

In the Hummers method the graphite is treated with the strong oxidant potassium permanganate in acidic conditions. A detailed synthesis is featured in **Section 4.2**. It has been confirmed that the active species in this synthesis is diamanganese heptoxide, which forms *in-situ* from a reaction between potassium hydroxide and sulphuric acid:[85]

$$KMnO_4 + 3\ H_2SO_4 \rightarrow K^+ + MnO_3^+ + H_3O^+ + 3HSO_4^-$$
$$MnO_3^+ + MnO_4^- \rightarrow Mn_2O_7$$

This chemical synthesis can yield many grams of GO over the course of a week; however work up and purification can take much longer, though compared to other methods of graphene synthesis, GO synthesis and reduction is relatively quick. To compare, CVD can only synthesise a few milligrams of graphene per deposition, while the extreme temperatures used are costly. Electrochemical exfoliation methods can produce gram quantities of exfoliated graphite, but the product will be a mixture of FLG and thicker pieces of material, which can also be functionalised depending on which method is chosen.

3.2.4 Reduced Graphene Oxide

The reduction of graphene oxide is a popular way to synthesise graphene. It is fast, reliable, low cost, and high yield, but defects are prevalent. For electrical applications GO needs to be reduced to increase the conductivity, as the many oxygen containing groups make the material an insulator, compared to the conducting graphene. Thus to determine the extent of reduction a good measure is the C/O ratio. Oxygen functionality causes irreversible disruption to the π-electron system which, even with reduction, causes irreversible changes to the electronic structure of the graphene, causing a loss in the electronic capability.

Structure and properties

The extent of reduction, reduction mechanism, and the initial GO will all have an influence on the structure of the rGO, which means most rGO samples will be different to each other, but rGO can be described by broad terms. In general rGO will be graphene-like in that it is a 2D hexagonal complex of sp^2 carbons. Many reduction techniques involve harsh chemicals, which can damage the rGO sheets and cause imperfections. Commonly, there are gaps in the hexagonal carbon system, causing a loss of conductivity. Other defects are prevalent with sp^3 carbon atoms (causing a localisation of electrons) and residual oxygen containing groups from the incomplete reduction of GO. Colloidal rGO is more similar in colour than graphene (black) than the GO (brown). During reduction reactions the reduced sheets will aggregate and precipitate out of solution.[86] However rGO still exhibits a higher hydrophilicity than graphene.[79, 86]

rGO has relatively high sheet resistances of 1 – 70 kΩ sq^{-1} which is due to the oxidation and subsequent reduction causing flake damage. Some of the highest reported values are still ~ 100 – 1000 Ω sq^{-1}, using spin coated GO films reduced using thermal treatment.[87] (For CVD synthesised graphene the sheet resistance is around 280 Ω sq^{-1}.)[36] These are still about two orders higher than pristine graphene. The extent of reduction can be measured by the conductance of the resultant films as reduction restored the π-electron network. An elastic modulus of 0.25 TPa has been recorded for rGO, which is only a quarter of that of graphene. This is due to disruptions on the rigid 2D hexagonal system and its increased cross-sectional area.[88]

Synthesis of reduced Graphene Oxide

The main purpose of reduction is to remove the oxygen-containing functional groups from the surface of the GO, restoring the sp^2 hybridized carbon network, and ensuring good electrical properties, while reducing the number of defects that remain. There are many ways to reduce GO, and the main procedures will be highlighted below. Note all reduction mechanisms can still produce rGO with sp^3 defects and oxygen containing group impurities.

Chemical

Chemical reduction can employ a range of chemicals from strong reactants to 'green' acids. In general these reduction techniques require little to no additional heating, are relatively quick, and can be green depending on which chemicals are used.

Stankovich *et al*. have used hydrazine hydrate in water to reduce graphene, giving a high surface area material of 466 $m^2\ g^{-1}$, with a C/O atomic ratio of 10.3; 2.7 for the initial GO. The conductivity increased from 0.0206 to 2420 $S\ m^{-1}$ after reduction. Hydrazine also introduces nitrogen into the RGO with a recorded C/N ratio of 16.1[79] This happens via a reaction with the lactones, anhydrides and quinones which form hydrazides (via anhydrides and lactones) and hydrazones (via quinones).[89] Hydrazine is considered the chemical agent that produces the most reduced rGO of all other chemical reduction techniques; however it is very toxic and introduces nitrogen doping. Though hydrazine is highly used to reduce GO in the literature, its use in this project was not considered. This was mainly due to the added functionality the hydrazine provides the resultant rGO. Due to an efficient comparison with the electrochemically synthesised graphene, the rGO would have to not be functionalised, as functionalisation can change the conductivity and ability to create EDLs, among other concerns.

Metal hydrides (e.g. $NaBH_4$) are classic reducing agents and work fairly well with GO. However they are quick to react with water, which GO is routinely dispersed in. In addition $NaBH_4$ focusses on reducing C=O groups, while other groups (e.g. epoxy, alcohol, acid) prove harder to reduce. Shin *et al*. report on GO reduction using $NaBH_4$, in a simple

2 hour reaction with 150 mM $NaBH_4$, with no addition heating required. The product rGO had a C/O ratio of 8.6 (previously 2.2) with a conductivity of 45 S m^{-1} and a sheet resistance of 2600 Ω sq^{-1}. Short reaction times were used to prevent the self-oxidation of $NaBH_4$ in water. They also found that 10 mM $NaBH_4$ performs better than 50 mM N_2H_2 in lowing sheet resistance, due to hyradzine creating a donor rGO p-type hole due to nitrogen introduction.[90]

Iodic acid has grown in prominence to reduce GO, and is considered one of the best methods for reduction. Moon *et al*. report on using HI in a simple reduction mechanism utilising acetic acid and HI at 40 °C for 40 hours with stirring. The resultant flexible product had a C/O ratio of 15.27 (previously 0.96), conductivity of 30,400 S m^{-1} and a sheet resistance of 19.6 Ω sq^{-1}.[91] Many other groups have used hydriodic acid for GO reduction in fibres to preserve their flexibility, and HI has been used to reduce GO in colloidal, film and powder forms.[92]

The use of ascorbic acid as a chemical to reduce GO has grown in popularity as it is non-toxic, does not react with water, works relatively well, and can be a route to hydrogel formation. It has been reported that the C/O of the GO can nearly quadruple in respect to the unreduced GO.[93] Zhang *et al*. have reported on GO reduction using ascorbic acid, with the product having a relatively high conductivity of 800 S m^{-1}, with a C/O ratio of 12.5. Additionally aggregation is not present in the rGO, making it suitable for capacitor applications where a high surface area is required.[94] The mechanism of ascorbic acid reduction is not well known however it has been proposed that the mechanism proceeds via a reaction between the hydrogen atoms in the ascorbic acid 5 membered ring and the oxygen atoms on GO. Nucleophilic attack and thermal elimination will return conjugation.[95] Due to the ease of use, zero functionality, and good quality final rGO product, the use of ascorbic acid to reduce the GO was used in this PhD project.

Thermal

Thermal treatment of GO causes the formation and rapid expansion of CO and CO_2 gases, creating pressures of up to 130 MPa at 1000 °C. (Note to separate two GO platelets, only 2.5 MPa is required.[96]) However the resultant reduced graphene oxide sheets are small and wrinkled due to the loss of carbon atoms in the form of the CO and CO_2 gases, which split the sheets. This will cause deterioration in the full potential of both physical and electrical properties.

Wang *et al*. showed that increasing the annealing temperature increased the conductivity of the resultant rGO, with the conductivity increasing from 49, 93, 383 to 550 S cm^{-1} with an annealing temperature of 500 °C, 700 °C, 900 °C, and 1100 °C respectively.[97] Shortcomings of thermal reduction include the high costs involved in producing the high temperatures required and making sure the atmosphere is completely free of oxygen by utilising a high quality vacuum or an inert or reducing atmosphere, as reactions with residual oxygen in the atmosphere can occur re-oxidising the rGO. However, thermal reduction can produce high quantities of rGO, which is why it is still used often.

Photo irradiation can also be used to reduce GO, and has the advantage of being able to direct the reduction to produce a specific pattern of reduction. Kaner *et al.* laser scribed GO to produce rGO using an IR laser. The laser irradiates the functional groups, producing gases, which in turn create a porous carbon network. The resultant product has a conductivity of ~1650 S m^{-1} and a C/O ratio of 27.8. They also showed that tuning the laser intensity can alter the production of rGO (**Figure 3.13**:).[98, 99]

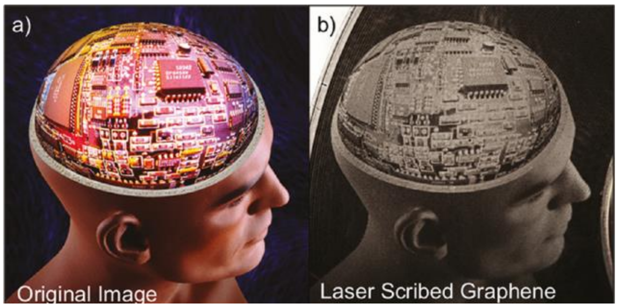

Figure 3.13: Patterns created using the LightScribe method on a DVD disk. This image is created using a pattern and applying different amounts of radiation to the graphene oxide. It also showed you can manipulate how much the graphene oxide gets reduced, as shown by the creation of different shades of the grey scale. [90]

Solvothermal

Solvothermal synthesis works on the basis of using both heat and chemical methods to reduce the GO. High temperatures create pressure which can aid in preventing the re-stacking of the GO sheets. Dubin *et al*. report on the solvothermal synthesis of rGO using NMP. Refluxing the mixture reduces the mixture and gives a stable colloidal solution. NMP has oxygen-scavenging properties at high temperatures, but also disperses the graphene well and thus stabilises it. The C/O ratio was 5.15 (6.03 after thermal annealing at 1000 °C). Electrical conductivity was 3.74×10^{2} S m^{-1}, which increased to 5.73×10^{4} S m^{-1} after thermal annealing at 1000 °C.[100]

Electrochemical Reduction

In electrochemical reduction the function groups are removed by simple electron exchange between the GO and electrodes. This ‘green’ synthesis can occur in neutral solution eliminating the need to harsh chemicals and high temperatures, while the reaction is also fast and controllable. However, the product is often a film, which cannot be used for applications that require dispersed graphene.[101]

Zhou *et al*. report on a low cost and environmentally friendly reduction method to produce electrochemically synthesised rGO. Linear sweep voltammetry in phosphate buffer solution (pH 4.12) over 80 hours was performed to produce a GO film with a C/O ratio of 23.64 (previously 1.45), and conductivity of 8500 S m^{-1} (previously 0.028 mS m^{-1}).[102] This highly reduced GO has a C/O well over what classic chemical reduction methods can achieve. It was considered for this research project, however due to the film formation it was abandoned due to the need discrete rGO particles for fibre synthesis.

rGO hydrogels

During the reduction of graphene oxide, hydrogels can form by the reaction between the graphene oxide sheets during reduction. Hydrogels are highly porous materials, with an interconnected pore structure, which affords them very large surface areas. Hydrogels form through interactions between the sheets. These interactions can include, hydrogen bonding, $\pi - \pi$ interactions, electrostatic interactions and coordination. Additional additives can help stimulate the hydrogel formation, including small organic molecules, polymers, and ions.[103]

Xu *et al*. prepared a hydrogel by a hydrothermal method. GO in water was heated at 180 °C in an autoclave. The resultant product was a porous graphene hydrogel. The sheets of graphene were crosslinked via hydrogen bonds, π-π stacking and van der Waals bonds. Overlapping of the graphene sheets promoted the π-π stacking making the product stronger. The pores ranged from sub-micron to multi-micron, and were made from thin layers of graphene.[104]

3.2.5 Wet Spinning

A growing interest in flexible electronics, that do not suffer a loss of efficiency after many bending cycles, has developed in recent years with the advent of the light-weight, highly conductive, and flexible graphene. Fibres are ideal for flexible devices as they can be integrated into wearable technology and are resistant to bending cycles and strain. While there are many different spinning techniques from the relatively new blow-spinning[105, 106], force spinning, electro-spinning and dry-jet spinning, this section of the report will focus on wet-spinning.

Wet-spinning was first used in the early 20th century and gained prominence in the 1970s as the main synthesis route for the commercially available, high-strength Kevlar® (also known as Twaron). Since then it has been a reproducible way to synthesise fibres, quickly and efficiently. Wet spinning encompasses three different methods, liquid-crystal, gel, and phase separation. The liquid crystal method relies on a liquid crystalline solution of a lyotropic polymer, where solidification occurs through a solid crystalline region in solution. In gel spinning, the polymer is solidified through intermolecular bonds in the solution, caused by a temperature or concentration change in solution. Phase separation, two different phases occur in the solution, one polymer-rich; the other polymer-lean.[107]

For GO spinning, the gel method is the most appropriate for fibre formation. In a general synthesis, one solution containing the dispersed spinning dope is extruded into a solution coagulation bath, in which the fibre precipitates. **Figure 3.14** shows a schematic representation of the wet-spinning technique. Rollers are employed to stretch the fibres, and they are often treated in oil baths before drying in order to increase the length of the fibres and reduce the effect of shrinkage due to the drying process.[108]

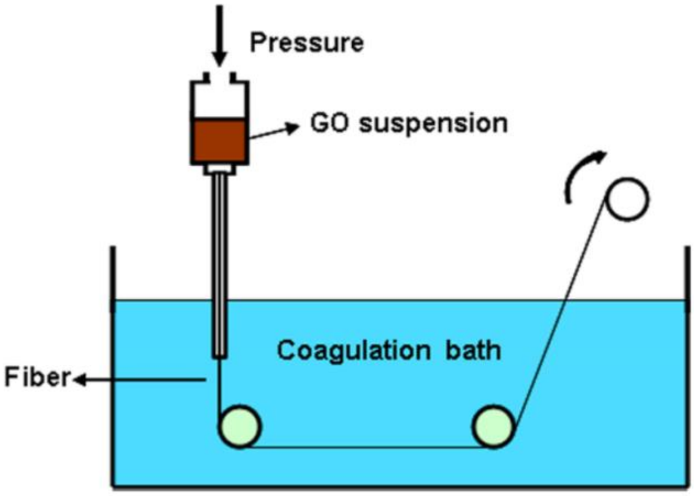

Figure 3.14: Schematic representation of the simple coagulation spinning technique. In this set-up the GO spinning dope is syringed into the coagulation bath where a fibre is formed by solvent exchange. This is then taken out of the bath using rollers for further treatment and drying. [109]

Extruding the solution into the coagulation bath slows down the extrusion, as the dope starts coagulating immediately. However it offers advantages of being able to use smaller amounts of mixture, as there is no constant need for solution. As GO is negatively charged, a positive cation is required for coagulation. Many divalent cations have been used (Ca^{2+}, Cu^{2+}, $Mg^{2+,}$) along with positively charged polymers.[110, 111]

This particular precipitation allows for fibres with controllable properties to be created, by varying the gauge of needle, flow rate, and concentration of the solution. Additionally it can be used to align fibres, as well form porous or dense wires of materials. Benefits include ease of synthesis and no requirement for binder, which makes this method suitable for electrode fabrication. In the academic landscape there are few examples of wet-spinning graphene directly, most concentrate on wet-spinning graphene oxide and subsequently reducing it to graphene.[112] In these studies, few concentrate on the subsequent energy storage capabilities of the fibres, but rather the potential applications in reinforcement industries.[110]

To date, only macroporous rGO fibres have been synthesised, as the pore size cannot be easily controlled.[113] Mesoporous materials (pore range: 2 – 50 nm) have pores open enough for a large surface area and facile ion transport, while not constricting the flow of ions that seems to be prevalent in some micro-porous materials (pore range: < 2nm), thus performing the best in electrochemical applications. Adding salts (ions (pH)) to the mixture can increase the surface area and the pore volume, shown in electro-spinning where adding salt increased the conductivity and diameter of the resulting fibres.[114] The density of wet spun graphene fibres is generally < 1 g cm^{-3}. This pales in comparison to conventional carbon fibres (1.7 g cm^{-3} – 1.9 g cm^{-3}) and graphite crystals (2.2 g cm^{-3}).[110]

Xu *et al*. have synthesised ultra-strong fibres from GO sheets. In this method GO was spun from a concentrated liquid crystal phase. They employed GO with high aspect ratios (18.5 µm) to reduce defect edges, and low concentration liquid crystal spinning (4 mg mL^{-1}) to reduce viscosity (and flowing friction) ensuring the fibres can be continuingly spun. The coagulation bath was $CaCl_2$, as Ca^{2+} ions can improve the strength of the fibres via crosslinking. The GO fibres had a tensile strength of 364.6 MPa, and a Young's modulus of 6.3 GPa. (When KOH was used as a coagulant the bath these values were 184.6 MPa and 3.2 GPa respectively). After chemical reduction using hydroiodic acid, the rGO fibres had a tensile strength 501.5 MPa and Young's modulus of 11.2 GPa.[110] This method was adapted for this research project in order to spin GO fibres for supercapacitor electrodes. This was due to the impressive mechanical properties of these fibres, which will ensure the fibres are able to go through many charge-discharge cycles without significant deformation.

Vigolo *et al*. have made an orientated CNT fibre from wet-spinning a CNT solution into a PVA coagulation bath. The CNTs were first dispersed in SDS, and then extruded into the PVA solution where they formed a nanotube mesh. These fibres could be bent without breaking, with high elastic (Young's) modulus of 9 – 15 GPa. Though this is several magnitudes lower than individual CNTs, it is much higher than high quality bucky paper.

Additionally they found they could make knots using the fibres without breaking.[115] However, again good quality CNTs are extremely expensive to synthesise, thus making any effort to create these fibres commercially moot.

Jalili *et al*. have explored the use of different coagulation routes. They demonstrated that wet-spinning could be scaled by using a 50-hole spinneret instead of a 1 hole spinneret. The best GO fibre strength was 442 MPa (coagulation by chitosan), which is better than other GO papers (120 MPa) and rGO/PVA fibres (120 MPa). $CaCl_2$ also performed very well with an ultimate stress of 412 MPa. These were both comparable to rGO made by a $CaCl_2$ coagulation bath (501 MPa).[111] rGO in general has better mechanical characteristics than GO. The removal of oxygen on the GO reduces the amount of hydrogen bonds between the GO sheets, weakening crosslinking. However as the sheets are closer together, there is greater alignment. Additionally the electrical properties are much better offering higher conductivities and lower resistances due to the reformation of a conjugated network.[116]

Zhang *et al*. have experimented with GO as a reinforcement material for wet spun PVA fibres. In this approach, PVA is the primary ingredient, while GO acts as a supplement to change the PVA fibre properties. With the addition of 0.1 wt% GO the fibre showed a 43 % improvement in breaking strength and an 81% improvement in initial modulus. They also observed that the orientation and crystallisation of the fibres increased. The fibres were spun into a Na_2SO_4 coagulation bath and hot drawn at 170 °C, then 200 °C, and finally 220 °C for 2 minutes under tension.[117] In this project, PVA is being used as a scaffold for the GO. This is due to GO (more aptly rGO) being the main source of capacitance in this mixture which makes it more desirable to be in higher concentrations.

To improve alignment of the fibres, which can increase the fibre strength, the material can be stretched or larger GO flakes can be used. Xiang *et al*. report on both of these in wet-spun GO fibres. They used large and small GO flakes (22 µm and 9 µm diameter respectively). The larger GO particles had a 178 % increase in specific stress, 188 % increase in specific modulus and 278 % increase of elongation at break relative to the smaller GO particles. They also found the dope had to be highly viscous for this. A higher draw ratio (stretching) can also increase the orientation of the flakes within the fibre, and it was found that fibres with best mechanical performance were from a draw ratio of 1.45, with a modulus of 47 GPa, which at the time was 10 times better than the best GO fibre. At a higher draw ratio (1.82) there was increased orientation of the flakes, while at a medium draw rate the fibre (1.27) remained flexible, easily woven into a piece of freestanding textile.[119] Li *et al* also using drawing techniques (wet-spinning at 60 °C into a 0 °C menthol bath followed by hot drawing) to produce a 244 % increase in tensile strength (356 MPa to 867 MPa) and a 294 % increase in Young's modulus (5.4 – 15.9 GPa) at 2 % rGO.[118] In this research project the fibres were stretched during the synthesis in order to increase the orientation of the flakes. This was done using a magnetic stirrer bar, which drew out the dope during the synthesis. An increase in alignment will grant a higher chance of a percolating network for electrical conductance, increasing the conductivity of the fibre.

Only recently has wet-spun GO been explored for capacitance applications, which will further be explored in **Section 3.4.2**.

3.2.6 Graphitization of Carbon Fibres

Carbon fibres first rose to prominence in the early 1970s, when high carbon content carbon fibres were able to be made commercially. Since then they have proved beneficial for reinforcement applications, due to their strength and flexibility.

Carbon fibres are classified as having a carbon composition of more than 92 %. The graphite content in a carbon fibre can range from 0 % – 100 %, with a highly graphitic fibre being described as graphite fibre. The graphite layer composition differs from the strict AB stacking in graphite, with the graphite c-axis both perpendicular and parallel to the fibre. While crystalline carbon is desired, amorphous carbon can also occur when the carbon layers are not parallel to each other. Other alternatives to carbon fibre are ceramic fibres such as SIO_2, Al_3O_3, which are denser than carbon fibre, more expensive, and cannot be made in a continuous fibre form.

The synthesis of carbon fibres occurs from the graphitization of precursor molecules including PAN or pitch. Pitch-based carbon fibres have carbon layers parallel to the fibre axis (3D graphite crystals), which increases the modulus of the fibres. However, PAN-based carbon fibres only have 2D graphite crystals, making sheer easier between the layers increasing strength. PAN-based carbon fibres are also smaller and less dense.[120] Additionally pitch-based carbon fibres have expensive purification and processing procedures, making the fibres more expensive overall.[121] For the purpose of this thesis only PAN-based carbon fibres are considered.

The mechanism for the conversion of PAN into carbon fibres is not well understood, due to the high temperatures involved. Though, in general, a cyclisation takes place due to the loss of the nitrile group on the monomer (**Figure 3.15**).

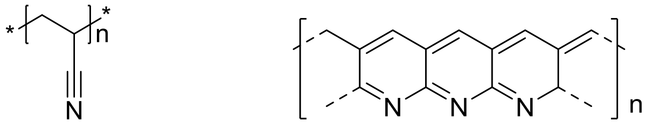

Figure 3.15: (Left) An acryolonitrile monomer; and (Right) the results of cyclisation due to the loss of the nitrile group.

A controlled heating gradient is needed to ensure full graphitization. The first step in graphitization involves heating the PAN in air at 200 °C – 300 °C. This increases the stiffness of the fibre, and avoids chain scissoring and relaxation during actual graphitization.[122] Cyclization, crosslinking, dehydrogenation, aromatization, and oxidation take place during this step to form a ladder-like structure. During stabilisation the colour of the PAN will go from white to yellow to black, where the colour is formed from the ladder ring structure which introduces a delocalised network of electrons. It also converts from a thermoplastic to a non-plastic compound.

Carbonisation follows at temperatures of 800 - 1500 °C in an inert atmosphere. During this, aromatic groups grow and the PAN polymerises, causing a carbon content of up to 95 %. Carbonisation at lower temperatures (< 1500 °C) will form fibres with low modulus. Carbonisation happens in two steps: thermal pyrolysis (600 °C) then ring formation (1500

°C). A high heating rate to 1500 °C is required to attain a stable high temperature, reducing damage to the structure of the PAN. Ring formation is caused by the loss of C=N during heating. **Figure 3.16** shows a brief outline of the conversion of PAN to carbon fibre by heat treatment.

Further heating the PAN to 1500 °C – 3000 °C causes graphitisation to occur, leading to orientation along the direction of the fibre axis and higher modulus fibres.[123]

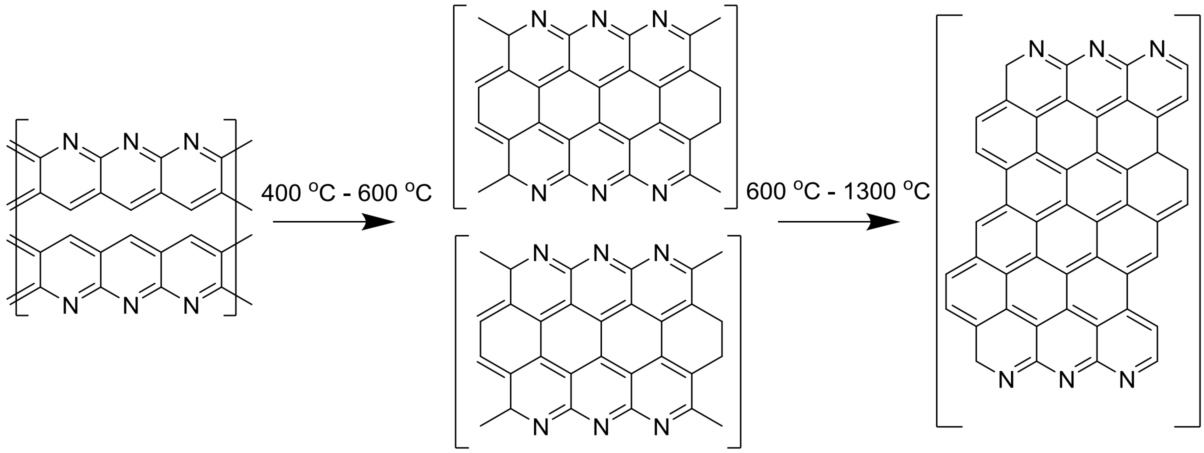

Figure 3.16: A schematic of the carbonisation process. First the ladder like structure is formed at 400 °C to 600 °C, then the structures react together, removing most of the nitrogen in the system from 600 °C to 1300 °C.

Xu *et al*. showed that a moderate carbonization temperature results in an increased surface area and pore volume. They found the optimum temperature to be 600 °C, which resulted in graphitized pan cloths with the highest capacitance with 208 F g^{-1} in their sample.[124] Though when reporting the capacitance they used a charging current of 50 mA g^{-1}, which is so low that the capacitor would never be operated on at this range. At higher charge currents (1 A g^{-1}), the capacitance reduced to ~ 100 – 150 F g^{-1}. In this PhD research the supercapacitor device was operated at currents that could be practically used in commercial applications.

Lee *et al*. have carried out conductivity measurements and strength measurements on PAN based carbon fibres. In this work they found that a conductivity of 500 S cm^{-1} was common, with a high 620 S cm^{-1} from carbonisation temperatures of 1500 °C. The structural properties are proportional to the stabilisation tension during carbonisation, with a higher tension generally giving better properties. A stabilisation tension of 11 MPa gave the highest tensile strength of 2.5 GPa and a tensile modulus of 400 GPa.[125] (Note that stabilisation stresses are used as standard in commercial production.)

To determine the extent of cyclisation a number of analytical techniques can be used. Due to the formation of a hexagonal sp^2 carbon lattice the carbon fibre will now be Raman active, and due to resonance these peaks will be very easy to see in the resultant Raman spectrum. They can also assess where the fibres are produced at low temperatures.[126] FTIR can also be used, as during stabilisation the C≡N bonds convert to C=N bonds, which appear in different regions of the IR spectrum.

3.3 Capacity

The conversion and storage of energy are key concerns in the current energy climate. There is currently a decline in the use fossil fuels and a movement towards greener energy, which requires the development of better energy storage technology. Energy and its storage device can come in many different forms, from the storage of potential energy in a wind-up clock, to gravitational potential energy in a hydroelectric dam, to chemical energy in a battery. In this thesis, only capacitors will be reviewed in-depth due to their importance in this study.

3.3.1 Capacitance

Capacitance is a physical mechanism of storing energy. Whereas batteries store energy through reactions with ions in solution, capacitors store energy through charge interactions at their electrodes' surfaces, called the electrical double layer. Once a material is charged, a layer of opposite charges (or adsorbed ions) will form on the surface, which is the double layer (**Figure 3.17**). As no reactions are directly happening to form the EDL, the materials have a high power density, meaning they are able to deliver this charge quickly when required; however comparatively, batteries hold much more charge, meaning they have a higher energy density, due to the physical reactions that take place.

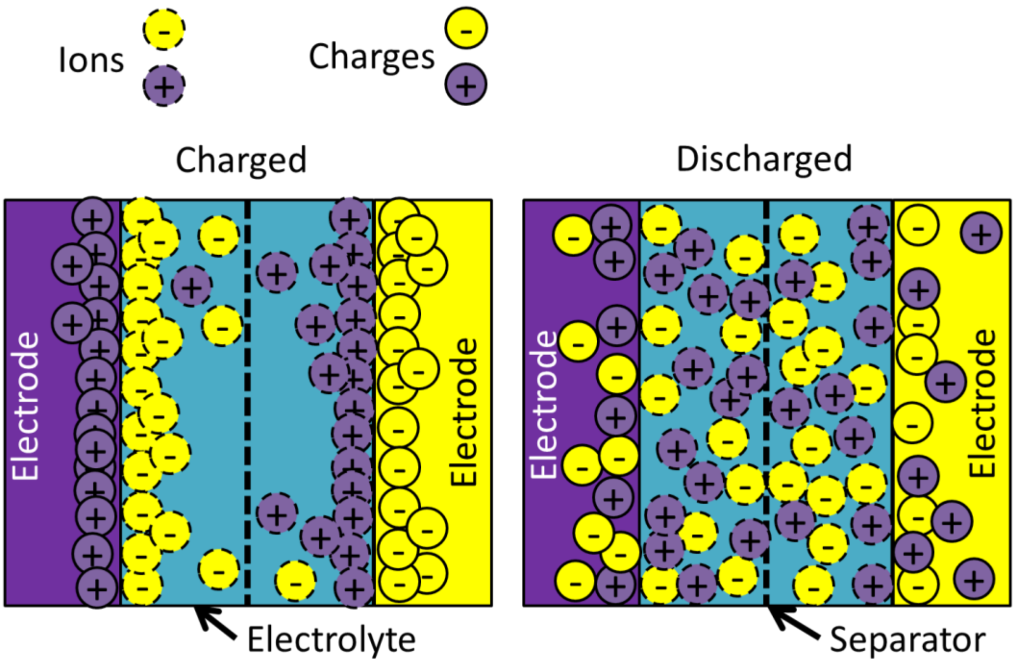

Figure 3.17: A representation of the Double Layer Effect in a capacitor with an electrolyte medium. A charged electrode causes an opposite layer of charges on the surface, as a store of energy, while a discharged electrode will have no such affect.

Capacitance is defined as 'the ratio of charge stored to voltage applied' (**Equation 3**). Capacitance is expressed by the unit Farad, and the relationship with charge and potential is: if a capacitor has a potential difference of 1 volt created by 1 coulomb, it is a 1 farad capacitor.[127] The capacitance of a material can also be expressed as a function of mass, area or volume (F g^{-1}, F cm^{-2}, or F cm^{-3} respectively), with researchers expressing the units which are most appropriate or sometimes highest.

$$C = \frac{q}{V}$$ **Equation 3**

Where the capacitance (C) is a function of the charges on the plates (q), and the voltage between the plates (V).[128]

Equation 4 shows the capacitance (*C*) of a two plate capacitor is proportional to the surface area (*A*) of the plates and the distance between the capacitor plates (*d*). Thus a good capacitor will have large surface area electrodes spaced closely together. Porous materials are widely used as capacitors, due to their high surface area, with activated carbon popular due to its high surface area of well over 2000 m^2 g^{-1}. Good electrical conductivity is also required if the capacitor is to function at high energy densities, which activated carbons do not possess.

$$C \propto = \frac{A}{d}$$ **Equation 4**

Where the capacitance (*C*) is a function of the area (*A*) and the distance between the double layers (*d*).

3.3.2 Capacitors

A typical capacitor consists of two plates in a circuit separated by a dielectric insulator. Opposite charges develop at the plates when a potential is applied. This in turn causes opposite charges to be stored at the surface of these plates. In classic capacitors the plate material was metal, as metals are highly conductive and can be easily introduced into an electrical circuit. The separator was typically ceramic or glass (or even air), as these are polarizable and easy to synthesise. Banerjee *et al.* reported on a capacitor made from tin nitride, with an insulator of Al_2O_3. This capacitor was synthesised by atomic layer deposition, with the structural thickness of 25 nm, giving the device a capacitance of 100 µF cm^{-2}, which exceeds classical electrostatic capacitors.[129]

Current research is focussing on electrochemical capacitors. They differ from classical capacitors as electrolyte is used as the medium between the plates. Electrolytes can store the charge through ions, giving them a higher capacity than classical capacitors. Electrolytes also have a higher potential window than ceramics or glass. This means, that a higher capacitance can be achieved. These capacitors are commonly referred to as super-capacitors because of their ability to store order of magnitudes more charge than conventional capacitors. There are three types of super-capacitors, double-layer, pseudo-capacitors, and a combination of the two. Electrical double-layer capacitors store charge through the Helmholtz double layer, while pseudo-capacitors store charge through Faradaic reactions on the surface. A combination will occur when an electrically double layer capacitor is also made out of a material that can be stable at different oxidation states.

Double Layer Super-Capacitors

Supercapacitors store electrical charge through surface interactions with ions in electrolyte solutions (**Figure 3.18**). While there are many models for the double layer formation between a charged surface and electrolyte, including the Helmholtz, Gouy-Chapman, and Stern double-layer, they all specifically concern the formation of a layer of oppositely charged ions on a potential charged surface. Double layer super-capacitors offer larger capacitances than classical capacitors but generally less than pseudo-capacitors. However they are very stable to deformation and can retain a high performance after over 10,000 charge cycles. The electrodes for the super-capacitor need to be stable, unreactive, have a high surface area, high mobility of charge carriers, and (for certain applications) flexibility. These desired features make graphene a highly likely candidate to improve capacitor development and charge storage.

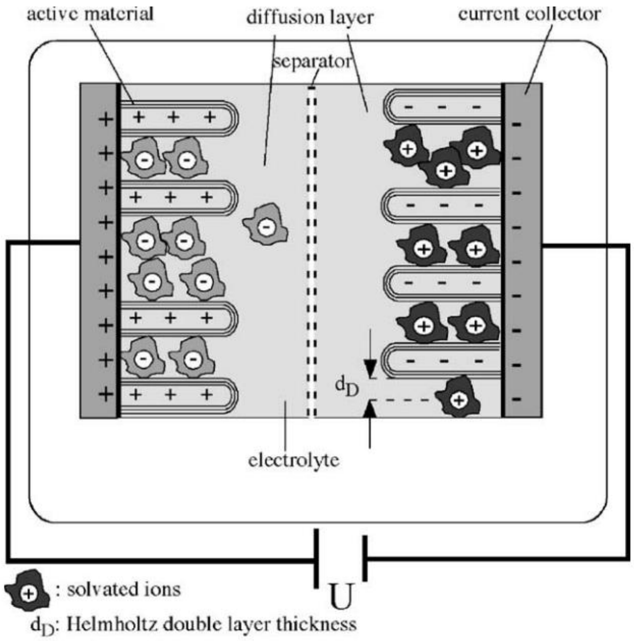

Figure 3.18: A capacitor with MWCNT as the active material. Charging the material causes a separation of ions in the solution, storing that charge.[130]

Pseudo-Capacitor

Pseudo-capacitors are primarily made out of polymers or metal oxides like MnO_2, and store charge through Faradic reactions with the electrolyte. Metals are used due to the ease of accessing different oxidation states which facilitates the redox reactions, and thus the storage of charge. These redox reactions allow the storage of more charge than the EDL capacitors, but they will also cause the deformation of the capacitor, making these capacitors less stable than carbonaceous super-capacitors. These materials should also be high surface area, highly conductive, stable, and also flexible. Although the electrical conductivity is often low, and the Faradic reactions can cause a loss of stability, they have a higher energy density than carbonaceous materials.

Hybrid-Capacitors

Both pseudo-capacitors and super-capacitors have advantages that the other does not possess (high energy density, and stability and high power density respectively), which is why it is becoming more common to see hybrid capacitors. The synergistic effect between the materials can outperform standard materials. This can be seen in MnO_2 – Graphene capacitors, as graphene can support the MnO_2, so that the redox reactions do not deform it, while also providing a scaffold that is also conductive and contributes to the capacitance too. Graphene can also disperse metal oxides, enhancing electrical conductivity.

Electrolyte

There are many different electrolytes that can be used with super-capacitors, namely aqueous, organic, and ionic liquid. All three of these have ions in solution that will can either form EDLs or perform redox reactions. Choosing the correct electrolyte is essential to ensuring a good capacitance.

For aqueous electrolytes commonly KOH is used. KOH consists of the very small ions K^+ and OH^- (152 pm and 133 pm respectively), which are small enough that they have good kinetic capabilities and can penetrate through nanopores. Concerning conductivity, K^+ has the highest conductivity after H_3O^+ among cations, while OH^- has the highest among anions. However all aqueous electrotypes feature water in solution, which undergoes electrolysis at 1 V. As a capacitor can only be cycled within the operating potential window of the electrolyte, this reduces the potential window for the material, which can reduce the energy density. Other common aqueous electrolytes include H_2SO_4, however it is not convenient for practical devices due to corrosion and high self-discharge rate.

Organic electrolytes use charged organic molecules for the electrolyte. These are often larger molecules, which can inhibit their mobility, reducing conductivity. However, the capacitor can be cycled through a larger operating window, increasing energy density. Example organic electrolytes include, TEA, which has an ionic radius of 0.385 nm.[131]

Ionic liquids are primarily made up of ionic species in liquid form. These tend to be very vicious liquids, which inhibits their mobility through the capacitor and thus conductivity. To combat this, the electrolytes are often heated when performing electrical tests. They feature ions which are larger than organic electrolytes, which could inhibit their penetration through a material, especially a porous one, reducing the maximum capacitance. However, they have the largest potential window of all electrolytes (up to 4.5 V), which can increase the energy density of the material. Example ionic liquids include ($[BMIM]PF_6$) which has been used to create high energy density super-capacitors.[132]

The pore size of materials has an effect on which electrolyte can be used. Electrolyte in activated carbons, which have a majority of very small micro-pores (< 2 nm)[133], cannot penetrate through the material sufficiently. This is due to the large ions / ion hydration shells, which is especially apparent when using organic electrolytes, due to the larger ionic radii.[134] Activated carbons only perform to about 10 % – 20 % of their theoretical capacitance. This is because of the micro-pores which are inaccessible to the solvent, the wetting deficiency of electrolytes, or the pores are too small to form EDL.[135] Activated carbon with a surface area of 1000 $m^2\ g^{-1}$ should have an ideal capacitance of 200 $F\ g^{-1}$ – 500 $F\ g^{-1}$, however due to the small pore sizes this cannot be achieved. Activated carbons also have many pores that are < 0.5 nm in diameter. These cannot form double layers and thus cannot contribute to capacitance.[136] The majority of capacitance for porous materials is derived from meso-pores, which are between 2 nm – 50 nm in diameter.[137]

The low conductivity of activated carbons also produces a high internal resistance and low power density.

Applications of Capacitors

Capacitors deliver energy very quickly, which gives them a edge for use in many applications. The main application is energy storage. To develop this application, current research is searching for ways to increase the energy density and capacitance of the devices. As seen in the Ragone plot (**Figure 3.1**), electrochemical capacitors could push into applications that currently use batteries. To increase the energy density and capacitance of a material, the material would need a higher mobility of charge carriers and a higher specific surface area, while reducing the amount of material needed to achieve these goals. Due to the high power density of capacitors, applications that require energy very quickly are suited to supercapacitors. Supercapacitors can be used as a back-up for electronic power supplies (uninterruptible power system). In these systems, mainly computer and telecommunications, the power needs to be supplied instantaneously, thus supercapacitors are favoured.[138] Hybrid electrical vehicles use supercapacitors to extend their batter life.[139]

Although already used in a number of applications, targeting the transportation market is one of the main draws of electrochemical capacitors, as breaking and accelerating requires a high power delivery.[140] The use of electrochemical capacitors in commercial applications, such as the F1 racing event, has been examined. When a high speed car breaks it releases energy that can be quickly stored in a super-capacitor. This energy would then be used for subsequent accelerating in an energy recovery system. However in 2009 a report found that due to the low energy density of capacitors at the time, they could not be used to advance the energy recovery technology in racing vehicles.[141] A far larger (heavier) capacitor would need to be used for this application, due to the low energy density, which would be disadvantageous for this application.

One of the key areas of the energy storage market is mobile devices, as these need to be charged quickly and hold their charge for a long time, while the devices get thinner and smaller. It is hoped that in the future capacitors can be used within portable devices to provide a quick dose of power when needed.[142]

3.4 Graphene Materials in Super-capacitors

Graphene has been shown to have great conductivity, surface area, mechanical flexibility and chemical stability making it apt for use within electrochemical capacitors. Incorporating graphene into useable electrodes and ensuring it retains its unique features is a crucial aspect of graphene-capacitor manufacture. To make pristine graphene, only to reduce the surface area significantly when using it as an electrode, is a waste. Electrodes can be made by incorporating graphene in a number of different ways, and moving graphene up the usable hierarchy is one on the main concerns when developing graphene capacitors. This goes from graphene nanoparticles, to 1D fibres, 2D films, and 3D foams.

These electrochemical super-capacitors could in the future complement or replace batteries on a large scale, thus consideration needs to be taken in order for the manufacture to be low cost, high yield, and high capacitance. For example, Kaempgen *et al*. looked at printable electrodes which have high throughput, making them ideal for commercial manufacture.[143]

To maximise the capacity of any capacitor, ELDC and pseudo-capacitor, the specific surface area, pore size and electrical conductivity need to be controlled. All these have an effect on the capacitance of the material. The material also needs to be carefully considered as the charges / redox reactions are formed at the electrode-electrolyte interface.

The theoretical maximum specific capacitance of graphene is 21 $\mu F\ cm^{-2}$, or 550 $F\ g^{-1}$. This is the maximum with no loss due to agglomeration of the sheets or defects.[144] This capacitance for pure graphene is only obtainable on very small pieces of pristine graphene. As more graphene is added to a system, there is a higher likelihood of defected graphene or re-staking of the graphene sheets. This can happen at any stage during synthesis, processing and application, so care needs to be taken in all stages of capacitor manufacture and usage.

Composite materials have also grown in prominence as mixing graphene with other materials can improve the attributes of both materials and studies have shown that come composites can have higher stability and retention of capacitance than just pure graphene. Of particular note is a graphene-polyaniline composite which has given specific capacitances of over 750 F g^{-1}. The pseudocapacitive (redox) process which polyaniline goes through puts stress on the fibres, reducing capacitance after a number of cycles. Adding graphene can increase the stability of the polyaniline without significantly reducing the capacitance. Graphene is a good candidate for this as it is not only strong, robust and inert, but it is also conductive and can contribute to the capacitance through EDLC.[145]

3.4.1 Graphene-Based Powder Capacitors

These capacitors utilise manufactured graphene directly as the active material in the capacitor without first converting into another structure. This can be as a powder, dot, or other form.

Previous research by Mitra and Sampath has shown that exfoliated graphite is a reasonable capacitor even without full exfoliation. The graphite material was exfoliated by first intercalation of a bisulphate anion from H_2SO_4:HNO_3 for 24 hours followed by thermal shock treatment at 800°C for 2 minutes. The electrodes were prepared through pressing at 5 tons cm^{-2}. Solid electrolyte was used (Poly(ethylene oxide))$_9$$LiClO_4$:ethylene carbonate (2:3), in propylene carbonate, giving a capacitance of 0.98 mF cm^2 with low surface area of only 33 m^2 g^{-1} at 200 mV s^{-1}.[146] From this long exfoliation time and costly conditions used (such as high temperatures) it would be hoped that the graphite would be fully exfoliated, down to at least FLG, and give a higher capacitance that it currently does. Though the method is promising, it requires further refinement in order to become usable for the commercial production of graphene capacitors.

Kai *et al*. used interlayered rGO as a capacitor. They found the best surfactant to use was TBA OH which gave a capacitance of 194 F g^{-1} at 1 A g^{-1} in 2 M H_2SO_4 electrolyte.[147] The electrode was prepared by using the intercalated powder and casting it onto a glassy carbon electrode. They also found that surfactants enhanced wettability of the graphene, which ensured the electrolyte had better contact with the graphene, increasing the amount of area EDLs could form. Block co-polymers have also been used to intercalate graphene giving good results.[148] rGO is desirable for use within capacitors due to the low manufacture cost and high yield. However the introduction of surfactants adds dead weight to the capacitor, as these will be unlikely to perform as well as graphene in terms of increasing the capacitance of the capacitor. Thus in this PhD surfactants were not used during the electrochemical or GO / rGO synthesis of the graphene.

Wang *et al*. used $Ni(OH)_2$ nanocrystals grown on lightly oxidised graphene as a capacitor with an extremely high specific capacitance of 1335 F g^{-1} at 2.8 A g^{-1} in 1M KOH.[149] Due to $Ni(OH)_2$ being a primary electrode in alkaline batteries, it made sense to use it in capacitors to increase the energy density. In the electrode, although the graphene sheets overlap with each other they are not physically connected. Similarly Lonkar *et al*. synthesised graphene composites with layered double hydroxides (metals that are stable at 2+ oxidation states like zinc). In this method GO was reduced *in-situ* with urea, while $Zn(OH)_2$ was grown on it by urea hydrolysis under microwave conditions. The product had a C/O ratio of 5, while the initial GO had a ratio of 1. The resultant capacitance of the product was 428 F g^{-1} at 2 A g^{-1} in 1 M KOH which was 20 % more than synthesised rGO (361.5 F g^{-1}).[150] The use of metal hydroxides is common in order to increase the capacitance with pseudo-capacitive processes. In this project, however, just EDL capacitance was desired, in order to accurately analyse the capacitance produced, and for an efficient comparison between the capacitors created by electrochemical exfoliation and GO / rGO synthesis.

Murugan *et al*. have synthesised graphene nanosheet-PANI composites for energy storage applications. In this method which used GO as a precursor, both microwave and solvothermal synthesises were employed. The microwave-solvothermal process occurred at 300 °C, over a short reaction time of 5 – 15 minutes. Scale up could be possible to reduce production costs due to the small amount of time required. While the pristine graphene nanosheets have a capacitance of 100 F g^{-1} the composite also utilises the pseudo-capacitive PANI for a capacitance of 408 F g^{-1} at 5 mV s^{-1} in 1 M H_2SO_4. The oxygen content goes from a C/O of 2 to a C/O of 11. The GO rapidly absorbs the microwave radiation, increasing the temperature and pressure which reduces the GO, while the solvent the GO is in further reduces it under solvothermal conditions.[151] Using two reduction techniques in tandem allowed for further reduction, however similar results have been shown to be obtained from using just chemical reduction with reactants like ascorbic acid and hydrazine.[80,91] This research will only use one reduction technique, as this allows for a better analysis of the effect of the reduction. Changing two variables (using two reduction techniques) will result in each reduction technique being unable to be characterised separately. Again the pseudo-capacitive PANI allowed for a dramatic increase in capacitance, however in this project the capacitor shall remain an EDL capacitor.

3.4.2 Graphene-Based Fibre Capacitors

Graphene based fibres are a sought after for their mechanical flexibility, which gives them uses in wearable devices and electric vehicles. They are mainly made from spinning, however they can be converted from films or built from the ground up.

Meng *et. al*. demonstrated the use of a graphene fibre super-capacitor that could be woven intro textiles due to its highly compressible and stretchable properties. The capacitance was 40 F g^{-1} at 20 mV s^{-1} in H_2SO_4-PVA solid electrolyte. This is comparable to activated carbon fibres which have a capacitance of 70.2 F g^{-1}. The graphene fibres were prepared by baking GO in an oven at 230 °C in a glass mould.[152] Further research indicated the graphene fibre was covered in a porous graphene structure, which was made from electrolyzing graphene oxide in $LiClO_4$ on graphene fibres.[153] Similarly Seyed *et al*. have made very porous fibres via wet spinning of GO. The surface area for graphene oxide fibres is 2605 m^2 g^{-1}, while for reduced graphene oxide fibres is 2210 m^2 g^{-1}, which is close to graphene and activated carbon. The capacitance was reported as a very high 409 F g^{-1} at 1 Ag^{-1} in 1 M H_2SO_4.[154] $CaCl_2$ promotes ionic crosslinking. Again, in this work they measured too little substance that would not accurately represent the entire fibre. The capacitance was measured using just 50 µg of active substance. The electrochemical test for these fibres created by Meng *et al*. used only 1 cm of the fibre, while Seyed *et al*. utilised just 50 µg of fibre. This will not give a good representation of the whole fibre, as only a small section of the fibre was used. 1 cm of fibre could even be just 1 mg of fibre in weight. In this PhD project, the weight of the fibres analysed was 20 mg, with the length ranging from ~ 20 cm for the carbon fibres to ~ 5 cm for the PVA-rGO fibres. Using a larger amount of fibre will mean that there is less chance of efficient electrolyte and electrode contact, while being a better representation of the overall fibre, at a cost of the capacitance.

Bao and Li have made activated carbon textiles, by treating cotton with NaF, and heating it to 120 °C and 1000 °C. This gave a textile with a capacitance of 70.2 F g^{-1} at 2 mV s^{-1} in 1 M Na_2SO_4. Due to the porous nature of the fibre they added MnO_2 via electrochemical deposition, giving a capacitance of 269.5 F g^{-1} at 2 mV s^{-1} in 1 M Na_2SO_4.[155] Again the use of metal hydroxides dramatically increased the capacitance of the fibre, and in this PhD project only EDL capacitors are being considered.

Fibres can also be used to create electrodes as a composite material. These can be flexible, which is useful for a variety of industries, such as medical, portable and compact energy devices.[156] Ways to create these fibres include coagulation spinning (wet-spinning) and electro-spinning. Tai *et al*. have created flexible carbon nanofiber / graphene composites using electrospinning. Polyacrylonitrile was used as the carbon fibre base to which graphene nanosheets could attach to. The polyacrylonitrile was converted to carbon fibre by heat treatment. The BET surface area of the composite was 447 m^2 g^{-1}, which was significantly more than the pure carbon fibre paper (270 m^2 g^{-1}) and graphene nanosheets (98 m^2 g^{-1}). The composite had a capacitance of 197 F g^{-1} at 1.25 A g^{-1} in 6 M KOH. This was a 24% improvement over carbon fibre paper (159 F g^{-1}), without additional graphene nanosheets, showing graphene can improve the capacitance of electrospun carbon fibres.[157] Ra *et al*. also report on the synthesis of a supercapacitor paper using carbon nanofibers from a PAN nanofiber paper base. Electro-spinning was used for 30 hours to form the 200 µm thick paper. The paper did not have any additional binder, and after activation at 1000 °C had a surface area of 705 m^2 g^{-1} and a capacitance of 240 F g^{-1} in 6 M KOH at 50 mA g^{-1}.[158] Electro-spinning was used as a route towards graphene-carbon fibres, however in this project the carbonisation was not optimised and resulted in the fibres mats decomposing into small particles, which could not be used to create a supercapacitor.

Conversely Kou *et al*. have spun GO for use within supercapacitors and wearable electronics. These fibres differ from others by being coated in PVA to make sure they cannot short circuit. In this method wet-spinning was used to synthesise the fibres, in a solution of ethanol/water (5:1 v/v) with 5% $CaCl_2$. The fibres were then reduced in hydriodic acid for 1 hour at 95 °C. The resultant fibre has a capacitance of 269 mF cm^{-2} at 0.1 mA cm^{-2} in 1 M H_2SO_4. The fibre was then interwoven to form 40 cm long coaxial fibres, which showed they could be used in wearable technology.[92] This method was the basis for the fibre spinning used in this PhD project as this *Nature Communications* paper proved that wet-spinning is a viable route towards high capacity graphene fibre supercapacitors.

Fibres can also be converted from films. In this way the films are twisted or shrunk to get the fibres. Films can be made by evaporation which are then cut into strips and twisted into fibre, or from unzipping of CNTs with the same chemicals to oxidise graphite, creating a graphene oxide nano-ribbon.[159] Carretero-Gonzalez *et al*. synthesised a graphene nano-ribbon from CNTs. In this process the CNTs were chemically unzipped using H_2SO_4 and $KMnO_4$[160] and the reduced via hydrazine vapour and annealing in argon at 300 °C for 2 hours. A capacitance of 99 F g^{-1} was obtained at 10 mV s^{-1} in 0.1 M tetrabutylammonium tetrafluoroborate in acetonitrile. This is nearly 5 times more than the starting MWNT yarns at 20 F g^{-1}.[161] Using CNTs as the base ingredient for the capacitor already affords the capacitor a high price, due to the costly nature of CNTs. This is unfeasible for the constant creation of graphene super-capacitors. Additionally the fibres cannot be continuously spun in order to synthesise mass amounts of fibre, meaning this method was not considered for this PhD research.

3.4.3 Graphene-Based Film Capacitors

Graphene papers and films are hard to produce due to agglomeration causing restacking between the sheets, reducing conductivity surface area and electrolyte diffusion rates. In order to counteract these problems spacers can be used, or the graphene sheets can be crumpled, making restacking far more difficult.

In terms of intercalated papers Wang *et al*. have reported on graphene papers which have been intercalated with carbon black via vacuum filtration. This simple method gave a capacitance of 138 F g^{-1} at 10 mV s^{-1} in 6M KOH, which was a 700% improvement over the electrode without carbon black (although this is at a faster rate).[162] While Choi *et al*. intercalated MnO_2 as a spacer between CMG for use as a capacitor. First polystyrene particles were used as a sacrificial template for CMG. Then a thin layer of MnO_2 was deposited on the surface. The porous structure of the product lead to fast ionic transport and decent electronic conductivity, with a capacitance of 389 F g^{-1} in 1M $NaSO_4$ at 1 A g^{-1}. This was about double the capacitance of pure embossed CMG (202 F g^{-1} at 1 A g^{-1}), which is double the capacitance of CMG film (93 F g^{-1} at 1 A g^{-1}).[163] These process of making these films means that they cannot be made continuously, limiting their use for commercial supercapacitors.

Kaner *et al.* report on the direct synthesis of electrodes by laser reduction of GO films. The specific capacitance of the electrodes was 276 F g^{-1} at 10 A g^{-1} in $EMIMBF_4$ ionic liquid electrolyte. The porous structures have a high surface area of 1520 m^2 g^{-1}.[99] These flexible micro-supercapacitors can be written reproducibly and quickly at a low cost. **Figure 3.19** shows an example in-plane supercapacitor.[164, 165] The programs used to write these electrodes is a simple program used to write CDs, showing that advanced methods for capacitor creation do not need to be highly costly or time consuming. Kang *et al*. showed that these novel capacitors, can take many different arrangements, and can be moulded in any desired ways. Although, large amounts of high quality GO is required in order to first create the film, and it needs to be highly controlled in order to have a similar thickness (and this reduction) across the entire film. Furthermore, large amounts of dead weight (in the form of GO) is present, and if this ever were to reduce, through charge cycling, the capacitor would short circuit.

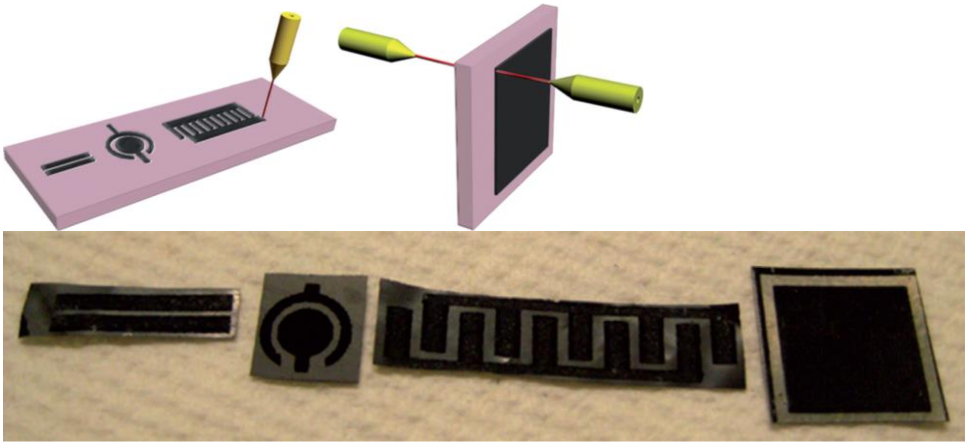

Figure 3.19: rGO capacitors made from light irradiation reduction of GO films. (Top Left) An in-plane device set-up; (Top Right) a sandwich device set-up; (Bottom) the synthesised capacitors from GO film irradiation. [154]

Liu *et al*. synthesised curved graphene sheets that would not re-stack and performed well in capacitance. This meso-porous curved graphene stops restacking even after compression, with pores in the range of 2 nm to 25 nm. The electrodes were made from graphene mixed with 5 wt.% Super-P (carbon black) and 10 % polytetrafluoroethylene. The capacitance was 154.1 F g^{-1} at 1 A g^{-1} using an ionic liquid electrolyte 1-ethyl-3-methylimidazolium tetrafluoroborate ($EMIMBF_4$). This is significant as the capacitance is still high with a large and viscous ionic liquid, which would not be able to penetrate into activated carbons.[135] This gives the capacitor a lot of dead weight, areas that are unable to form EDLs and contribute towards capacitance.

Wang *et al*. synthesised thin film electrodes from graphene oxide. These were reduced with hydrazine vapour over 72 hours in a desiccator. The product had a C/O ratio of 7.3 and C/N of 15.1. The rGO was mixed with PTFE binder and electrodes were created giving a capacitance of 205 F g^{-1} at 0.1 A g^{-1} in aqueous 30% KOH electrolyte. The heteroatoms were thought to increase the wettability of the electrode, increase the capacitor performance.[166] However, heteroatoms change the electrochemical characteristics of the capacitor, which is why hydrazine is not in use during this PhD project.

Kaempgen *et al*. investigated the use of SWCNTs by printing a thin film of SWCNT for supercapacitor use. The SWCNT works as both the electrode and charge collector, improving the efficiency of the electrode by eliminating the charge collector – active material interface. The capacitance of the material was 120 F g^{-1} at 1 A g^{-1} in 1 M H_3PO_4.[143] Liu *et al*. have previously synthesised SWCNT/PAN film supercapacitors. The film was synthesised by simply mixing SWCNTs and PAN in DMF, followed by evaporation and then film casting. Physical activation to create high specific surface area and porous materials was used by heating the composite films at 700 °C in argon for 30 minutes. The capacitance was 380 F g^{-1} with a discharge voltage of 0.2 V at a 0.001 A discharging current in 6 M KOH.[167] Again, both these methods utilise CNTs, which are extremely costly and cannot be used in order continuously form graphene-based capacitors at low costs.

Wang and Kaskel have explored the used of KOH as an activator for carbon materials. Activation can increase the surface area of a carbon material dramatically by developing a pore network in the material, with over 3000 m^2 g^{-1} achievable. KOH can lower the temperature barrier of activation to 400 °C – 900 °C from the standard carbonization activation temperatures of up to 600 °C – 1200 °C. As KOH involves low temperature activation, it is a desirable route for activation. Though the mechanism of activation is not well understood it has be proposed that it proceeds via oxidation of the carbon, and reduction of potassium, creating a defined micro-pore distribution.[168] Examples of KOH activation can be seen in a paper by Wang *et al*. on the activation of carbon aerogels. Capacitance increased from 107 to 244 F g^{-1} with KOH activation (surface area from 520 m^2 g^{-1} to 3247 m^2 g^{-1}) at 10 mV s^{-1} in 30% KOH electrolyte.[169] Similarily Zhu *et al*. have synthesised activated graphene for production of a supercapacitor. Chemical activation of GO produced a material with a surface area of 3100 m^2 g^{-1}. The material was a 3D network of highly curved graphene, with 0.6 – 5 nm diameter pores. The GO powders were irradiated in a microwave, and then placed in KOH, followed by filtration and drying. These were then heated at 800 °C for 1 hour under argon. The capacitance of microwave exfoliated graphene oxide with a specific surface area of 2400 m^2 g^{-1} was 165 F g^{-1} at 1.4 A

g^{-1} in 1-butyl-3-methyl-imidazolium tetrafluoroborate (BMIM BF_4/AN) electrolyte. For reference the specific capacitance of a specific surface area of 3100 m^2 g^{-1} was 150 F g^{-1} at 0.8 A g^{-1}.[170] Both of these methods utilise KOH to partially activate the graphene. This is why KOH is used during the electrochemical tests in this PhD project as KOH activation may be able to boost the capacitance of the manufactured supercapacitors.

3.4.4 Graphene-Based 3D Porous Capacitors

For supercapacitors, one of the main ways to increase the capacitance is to increase the surface area. Highly porous materials have a very large surface area, making them ideal for super-capacitors. Porous materials include aero- and hydro-gels. Hydrogels can easily integrate the electrolyte into the pores through solvent exchange.

Cao *et al*. have used porous nickel foam to make CVD graphene. The porosity allows the electrolyte deep access into the NiO surface and fast electron transport between the EDLC material and the current collector. The specific capacitance was 816 F g^{-1} at 5 mV s^{-1} in 3 M KOH. Other reactions happening in solution include the Faradic exchange with NiO and hydroxide. Additionally they found depositing NiO onto the foam gave a capacitance of 305 F g^{-1} at 5 mV s^{-1}.[171] Wang *et al*. also report on CVD experiments on nickel foam. They report on a FLG/MWCNT 3D porous structure created from CVD at ambient pressures. The 3D foams were grown on nickel foam using acetylene and hydrogen, and then MWCNTs were grown on the graphene foam. The structure is very porous with a large surface area of 743 m^2 g^{-1}. The product shows a high specific capacitance of 286 F g^{-1} at 50 mV s^{-1} in 6 M KOH.[172] In both these studies the porous nature of the nickel foam helped facilitate the porous nature of the CVD graphene. This is why nickel foam was used in the creation of electrochemically exfoliated graphene capacitors in this PhD project. However, the nickel did not contribute to the overall capacitance as much as in this work by Cao *et al*. This high capacitance is only due to the support from the pseudo-capacitive NiO, and it is unknown what the capacitance could be without the NiO. CVD was pursued briefly during the PhD, however it was noted that CVD is a costly procedure and in order to make gram quantities of graphene for capacitor manufacture, it is unfeasible to use.

A large number of groups report on the synthesis of 3D structures that use GO as the base[174]. Xu *et al*. have made a number of hydrogel capacitors[104] but one in particular report in *Nano Letters* details the synthesis of a compound they call 'holey graphene oxide'. This was created by mixing GO and H_2O_2, and freeze drying the product to give a material with a surface area of 1330 m^2 g^{-1}. This material had numerous in-plane nano-pores (2-70 nm), which allowed for greater electrolyte penetration. It was used directly as super-capacitor with no additional binder needed. The recorded capacitance was 283 F g^{-1} at 1 A g^{-1} in 1M H_2SO_4. They also synthesised a graphene hydrogel from rGO with a surface area of 430 m^2 g^{-1} (GO: 180 m^2 g^{-1}) to compare the capacitance which was 205 F g^{-1} in 1M H_2SO_4.[173] Though a high capacitance was reported, only a very small amount of capacitor (~ 1 mg) was electrochemically characterised, which would not be fully representative of the capacitor at a larger scale, thus inflating the capacitance of the synthesised compound. Currently there is no standard for the electrochemical characterisation of compounds, so using very little material or a very low charge-discharge rate is acceptable, even if the report claims that the device could be used on a large scale as Xu *et al*. do.

Yang *et al*. discovered that CCG (Chemically Converted Graphene) can form stable colloids in solution without additional surfactants. The sheets of CCG were prevented from re-stacking giving a high surface area product. This was achieved by utilising water acting as a spacer, the corrugated structure of the sheets, and the colloidal interaction between the sheets. The specific capacitance was 215.0 F g^{-1} at 1 A g^{-1} in 1 M H_2SO_4 electrolyte, with a high capacitance of 156.5 F g^{-1} at an ultrafast charge/ discharge rate of 1080 A g^{-1} also, indicating the material is less affected by charger/discharge rates.[175] They performed similar experiments using CCG's micro-corrugated configuration and self-assembly to create materials formed by capillary compression with liquid electrolyte. These hydrogels were porous and did not re-stack due to the repulsive inter-sheet electrostatic forces and the corrugated formation. This material also had a continuous ion transport network, which allowed for deep integration of the electrolyte and led to a material with a capacitance of 203.2 F g^{-1} at 0.1 A g^{-1} in 1 M H_2SO_4. This capacitance was less than previous results however the packing density of the material was much improved giving a volumetric capacitance of 255.5 F cm^{-1} at 0.1 A g^{-1} in 1 M H_2SO_4.[176] Even though both these materials obtained good capacitances, the meta-stable material is unrecoverable if dried. Due to this highly likely failure and the fact the capacitors created in this PhD will have to be used many times, this route towards graphene capacitors was not pursued.

3.5 Conclusions

In a review by Wang and Ke they conclude that the best possible way to improve graphene energy storage technology, is to make the capacitor electrodes flexible, composite, and porous.[177] The literature landscape has shown that while graphene has suitable supercapacitor properties, it is difficult to include into a capacitor, with no pure graphene capacitor getting near to the theoretical maximum graphene capacitance of 550 F g^{-1}, while composite materials regularly pass this theoretical maximum.

The route to graphene synthesis can be selected based on what applications the graphene will be used in. If pristine graphene is required, CVD offers the fastest and cheapest way to synthesise high quality graphene. However this is still expensive due to the high temperatures involved and low yield. This graphene is better for use in transparent conductive electrode applications, due to its pristine nature. Mechanical exfoliation can also produce pure graphene; however this is very low throughput, with only very small amounts of graphene produced.

If the application does not require pristine graphene electrochemical exfoliation and the reduction of graphene oxide both offer a quick way to synthesise FLG with few defects, and monolayer graphene with a small amount of defects respectively. Routes to synthesise graphene show rGO and the electrochemical exfoliation of graphite are advantageous due to their relative low cost, ease of synthesis, high yield, and moderately pure products. Though electrochemical cathodic reduction often produces FLG, the product can be refined through repeat cycles of exfoliation, and is relatively defect free. rGO can be synthesised in bulk, and is often of good quality an easily stored. However adequate reduction of the GO is needed to reduce defects (sp^3 carbons and oxygen containing groups), which could interfere with the electrical properties of the rGO. Additionally the most common reduction techniques use hazardous chemicals, and can only be performed on a small scale.[79] Due to these reasons, both graphene produced by the electrochemical exfoliation of graphite and reduced graphene oxide will be as the synthesis methods for the production of graphene in this PhD. Both these routes to graphene offer graphene which is suitable for electrical applications, as the conductivity is retained with few defects.

For applications that do not concern electrical devices, GO can be synthesised in a bulk synthesis. It retains some of the excellent physical properties graphene has including strength and strain, making it suitable for reinforcement applications to strengthen a composite material. There is a drive to improve the mechanical properties of nanocomposites by the addition of nano-fillers. It is hoped these fillers will exceed the performance of conventional fillers, though used at a far lower concentrations in order to give better results. Previously CNTs were used for these reinforcement applications, however their high cost means the effort for making them does not exceed the benefit of having them. In a paper by Liang *et al*. GO has been used to reinforce PVA. In these nanocomposites, a 0.7% addition of GO was able to improve the mechanical properties of the PVA significantly with a 76% increase in tensile strength and a 62% increase in Young's modulus. These composites were simply made in a 'green' synthesis.[178]

Regardless of ultimate capacitance, the hierarchical structure of graphene that is required will depend on the end use of the material. For instance, if the graphene is best suited for a coin cell, a film is often advantageous; whereas for applications where flexibility is required, a fibre would be best suited.

Fibres have been used in capacitors and due to their flexibility and strength have been shown to weave easily into textiles for wearable electronic applications. Other applications for fibres include use as a rotational motor and in solar cells.[179] Work has recently focussed on making fibres into cables. These fibres need to have little reduction in capacitance after many bending cycles and charge / discharge cycles, making graphene a viable contender for all these applications. Graphene fibres are also usable as wires when they require a heavy current.

Cheng *et al*. have looked into the use of graphene fibre for smart actuators, and motors. They first synthesised a fibre via spinning, and reduced just one side of the fibre by laser ablation. Bending of the graphene side of the fibre occurred in a reversible process when the fibre was subject to moisture (humidity 80).[180]

Xu and Gao review the applications of graphene fibre, specifically as a replacement of traditional carbon fibres. As carbon fibres are derived from organic molecules hey are poly-crystalline that can weaken their potential mechanical and electrical properties. They deduce the best way to synthesise graphene fibres which are scalable and continuous is wet-spinning. Composite fibres can also be synthesised using this process. [179]

Table 3.1 is a table showing papers concerning graphene super-capacitors at differing hierarchies. As discussed in **Figure 3.3**, there are thousands of journals published in scientific literature regarding graphene super-capacitors. The following papers are discussed due to their inclusion in high impact journals and their influence on future research (including citations). From this it can be seen that for each hierarchy there is a wide range of different capacitances which are likely to be achieved. The best capacitances have been achieved using composite materials. For pure graphene materials, all sections of hierarchy are available for use, as the maximum capacitances are comparable. **Figure 3.20** is a Ragone plot with additional points corresponding to the energy and power density of some graphene related super-capacitors. It can be seen that graphene related super-capacitors are surpassing the conventional limits of electrochemical supercapacitors.

Material	Capacitance	Electrolyte	Reference
Graphene Theoretical Maximum	550 F g^{-1}	N/A	[135]
Powder			
Exfoliated Graphite	0.98 mF cm^2 at 200 mV s^{-1}	Solid	[146]
rGO (with TBAOH surfactant)	194 F g^{-1} at 1 A g^{-1}	2 M H_2SO_4	[147]
$Ni(OH)_2$ on graphene	1335 F g^{-1} at 2.8 g^{-1}	1 M KOH	[149]

Graphene-Metal Hydroxides	428 F g^{-1} at 2 A g^{-1}	1 M KOH	150
Graphene-PANI composite	408 F g^{-1} at 5 mV s^{-1}	1 M H_2SO_4	151
Fibre			
Graphene Fibre w/ 3D Graphene	40 F g^{-1} at 20 mV s^{-1}	H_2SO_4-PVA	153
MnO_2 Activated Carbon Fibre	269.5 F g-1 at 2 mV s-1	1 M Na_2SO_4	155
Highly porous Graphene Fibre	409 F g^{-1} at 1 Ag^{-1}	1 M H_2SO_4	154
Electro-spun (PAN) Carbon Fibre	197 F g^{-1} at 1.25 A g^{-1}	6 M KOH	157
Wet-Spun GO with PVA sheath	269 mF cm^{-2} at 0.1 mA cm^{-2}	1 M H_2SO_4	92
Graphene Nano-ribbon	99 F g^{-1} at 10 mV s^{-1}	0.1 M TBA/AN BF_4	161
Film			
Graphene- Carbon Black Papers	138 F g^{-1} at 10 mV s^{-1}	6 M KOH	162
CMG Film with MnO_2	389 F g^{-1} at 1 A g^{-1}	1 M $NaSO_4$	163
Laser reduced GO films	276 F g^{-1} at 10 A g^{-1}	$EMIMBF_4$	99
Curved graphene	154.1 F g^{-1} at 1 A g^{-1}	$EMIMBF_4$	135
rGO Films	205 F g^{-1} at 0.1 A g^{-1}	20% KOH	166
Activated graphene	165 F g^{-1} at 1.4 A g^{-1}	BMIM BF_4/AN	170
SWCNT/PAN film	380 F g^{-1} at 0.001 A g^{-1}	6 M KOH	167
KOH activated carbon aerogel	244 F g^{-1} at 10 mV s^{-1}	30 % KOH	169
Printed SWCNT film	120 F g^{-1} at 1 A g^{-1}	1 M H_3PO_4	143
3D Porous			
CVD Nickel Foam	816 F g^{-1} at 5 mV s^{-1}	3 M KOH	171
Holey GO	283 F g^{-1} at 1 A g^{-1}	1 M H_2SO_4	173
rGO Hydrogel	175 F g^{-1} at 10 mV s^{-1}	5 M KOH	104
Graphene / NF Hydrogel	161.1 F g^{-1} at 1 A g^{-1}	6 M KOH	174
CCG Hydrogel	215.0 F g^{-1} at 1 A g^{-1}	1 M H_2SO_4	175
CCG 3D structure (Same	203.2 F g^{-1} at 0.1 A g^{-1}	1 M H_2SO_4	176

Person)			
FLG / MWCNT 3D Structure	286 F g^{-1} at 50 mV s^{-1}	6 M KOH	172

Table 3.1: Table of hierarchal graphene super-capacitors, with their capacitance and electrolyte displayed.

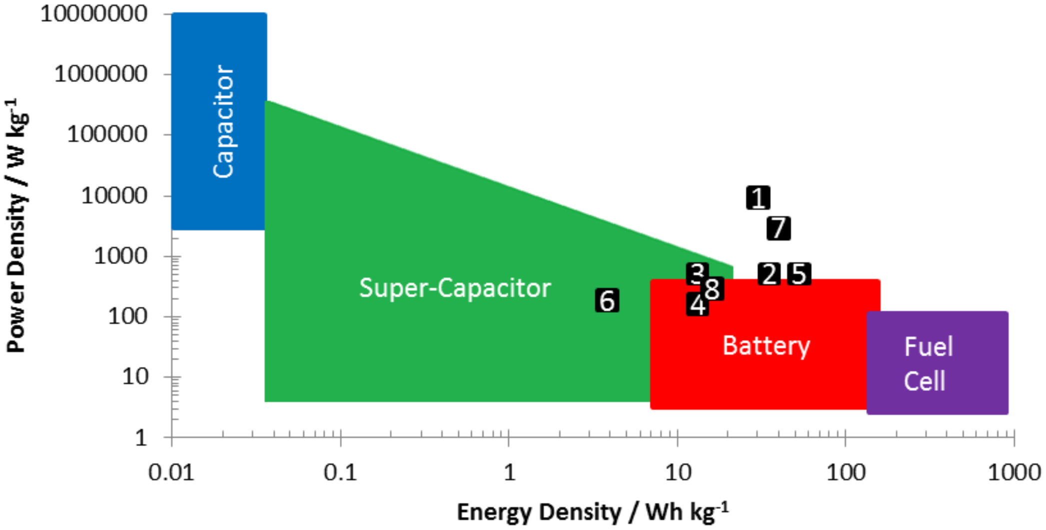

Figure 3.20: Modified Ragone plot with additional points relating to graphene-related super-capacitor materials. The numbers in brackets are the formatter '(energy density, power density). 1: Ni(OH)2 on graphene (37, 10000)[149]; 2: rGO (with TBAOH surfactant) (24, 437)[147]; 3: Highly porous Graphene Fibre (14, 720)[154]; 4: Electrospun (PAN) carbon fibre (16, 436)[157]; 5: Curved Graphene (50, 1000)[135]; 6: Graphene- Carbon Black Papers (4, 200)[137]; 7: FLG / MWCNT 3D Structure (40, 3700)[172]; and 8: rGO Hydrogel (18, 420)[104].

4 Experimental Methodology

This chapter focuses on the analytical techniques and experimental procedures used. Firstly, the theory and applications of the instruments used to characterise the materials synthesised will be detailed. There is a particularly focus on Raman spectroscopy due to its extensive use within the project. Secondly, the experimental procedures carried out during the project, including the reagents and materials used, will be outlined.

4.1 Analytical Techniques

4.1.1 Scanning Electron Microscopy

Electron microscopy is one of the most powerful imaging techniques available with resolutions as high as 50 pm and quantitative applications for elemental analysis.[181] It was invented in the early 1930s by Knoll and Ruska, for which Ruska was awarded the Nobel Prize in physics.[182, 183] The resolution (r) for imaging techniques is affected by the wavelength (λ) of the incident beam, angles used (α), and the numerical aperture of the lenses. **Equation 5** shows how this can be applied to electron microscopy, where the lenses have an insignificant influence on the refractive index and only very small angles used. An electron microscope using electron wavelengths of 0.0037 nm and angles of 0.1 radians will give a maximum resolution of 0.02 nm,[184] though other factors often limit the maximum resolution with a typical maximum resolution in the nanometre range for SEM.

$$r = \frac{0.61\lambda}{\alpha}$$ **Equation 5**

During imaging an electron beam is rastered over a sample and a CCD camera then captures the scattered electrons to produce an image on the computer. A vacuum is used to stop radical formation and scattering of the electrons by gaseous molecules. The sample thickness is must be larger than the mean free path of electrons, so that the electrons are scattered within the sample. Two basic contrasts are available, secondary electron (SE) and back scattered electron (BSE). SE contrast records the inelastic scattering of electrons knocked out of the atomic shells. They have low energy, but are more abundant than BSE, giving a better resolution. BSE contrast records elastic scattering, where electrons are recorded after being scattered inside the material. These BSE are higher in energy, with the ‘brightness’ of the signal proportional to the atomic number, thus they can be used to characterise the elements present in the sample.

Instrument

A Philips ‘XL-30’ SEM with a Field-Emission-Gun source was used in this research project. The FEG source produces an electron beam when a high electric field is applied to tungsten tip, which results in electrons being released from the surface. This source is 100 times brighter than traditional tungsten filaments, due to the focused beam, leading to higher quality images. The electron energy was selected at ~ 6 – 8 kV due to the soft materials used, with a working distance of 10 mm. The sample was created by applying a carbon based electrically conductive adhesive disc onto an aluminium stub, to which the sample was deposited on. To reduce charging in some samples, which can distort the images, a thin layer of gold was deposited onto the sample using a precision coating physical vapour deposition system. For rough samples, the gold was coated at three different angles to ensure full coverage.

To quantify the size of the particles in the SEM images ‘Image J’ was used, with 100 measurements taken on each image. First, the length of the scale bar was measured, and a value was calculated as a function of the scale bar distance. Then the length of identifiable whole particles was measured with the long axis recorded. This was multiplied by the calculated scale bar value to calculate the size of the particles. So for instance if using ‘Image J’ a scale bar of 20 µm has a length of 2, then a particle with a length of 1 would be estimated as 10 µm in size.

4.1.2 Raman Spectroscopy

Raman spectroscopy is an analysis technique that utilises the inelastic scattering of light in order to obtain information about the bonds within a sample. The technique is fast, non-destructive, and repeatable, which makes it ideal for the quick characterisation of graphene samples. Raman scattering was first observed in the 1920s, by Sir C. V. Raman. The effect contributed to a Nobel Prize in Physics in 1930 “for his work on the scattering of light and for the discovery of the effect named after him”[185], with instruments to measure this affect made available in the 1930s.[186]

When light interacts with a sample, the electrons in the bonds vibrate. The electrons then scatter this energy back into another photon. This inelastic scattering, with a shift in frequency, is the basis of Raman spectroscopy. The scattered photon can increase or decrease in energy by destroying or creating a phonon, referred to as Stokes and anti-Stokes processes respectively (**Figure 4.1**). The energy difference between the incident and scattered photons is characteristic of the bonds, thus enabling the bonds to be characterised. The resultant spectra are displayed with intensity on the y-axis vs Raman shift from the laser (cm^{-1}) on the x-axis, with the wavenumbers derived from 1 cm^{-1} = 10^{-7} nm^{-1}. Typically only the Stokes scattering is recorded as it has a higher intensity than the anti-Stokes scattering. Raman is a primarily surface technique, with a 633 nm laser being able to probe to a depth of up to 3 μm.[187]

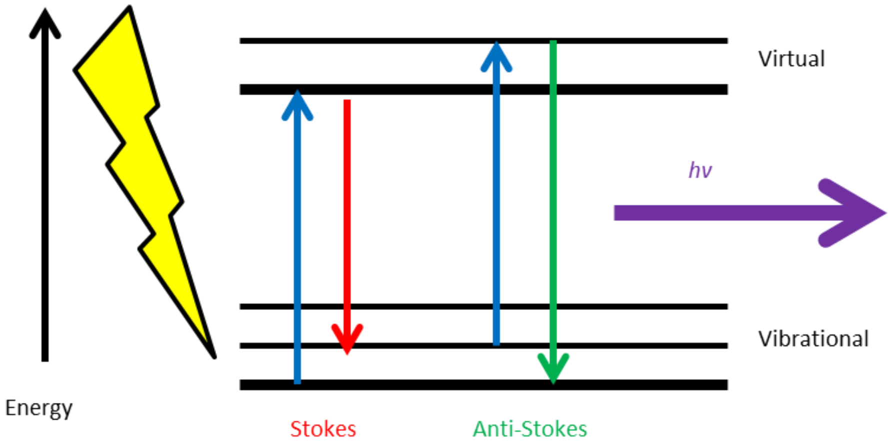

Figure 4.1: When light interacts with a material the electrons are promoted from the vibrational state to a virtual state. Energy is released when the phonon drops to the vibrational states. Two forms of radiation, Stokes and anti-Stokes differ due to the material gaining and losing energy, which causes the scattered photon to lose and gain energy respectively.

Raman spectroscopy is commonly used to characterise graphitic samples, due to the rich band structure of sp^2 carbon materials, and the dispersive nature of the photons which can assess the thickness of the graphite at low numbers of layers. Herein, Raman spectroscopy was specifically used to analyse the degree of exfoliation for the electrochemically produced exfoliated graphite, to determine the formation of carbon fibres, perform polarization experiments and to quantify the extent of GO reduction.

Instrument

In this project, an 'In-Via' Renishaw Raman spectrometer with a HeNe laser (λ = 633nm = 1.96 eV) was used. The system was calibrated using silicon dioxide and analysis was performed using a 50x objective. This gives a laser spot size of ~ 1.4 µm (according to Laser Spot size = 1.22 x λ / NA (50 x objective = 0.55)). A standard experiment comprised a 20 second extended scan from 100 cm^{-1} – 3100 cm^{-1} with three accumulations. For graphene oxide the laser power was lowered to reduce heating of the sample. Peaks were fitted with the 'Wire 4.2' software, giving the peak position, height, width, and shape.

Analysis of Raman Spectra

Raman spectra of sp^2 carbons are primarily composed of first and higher order Raman modes and disorder induced features, which are all related to phonons in graphene at the ***Γ*** point within the interior of the Brillouin Zone and near the boundary of the Brillouin Zone (**Figure 4.2**). The modes, associated with the K points, are only activated as high order modes or by defects. These modes are also dispersive, and can be used to measure the electron and phonon dispersion of nanocarbons using double resonance. These are high precision, although the Raman features are only averages of the phonons around the Γ and K point, as double resonance only selects the $|k|$ and $|q|$ wave vectors for electrons and phonons respectively.

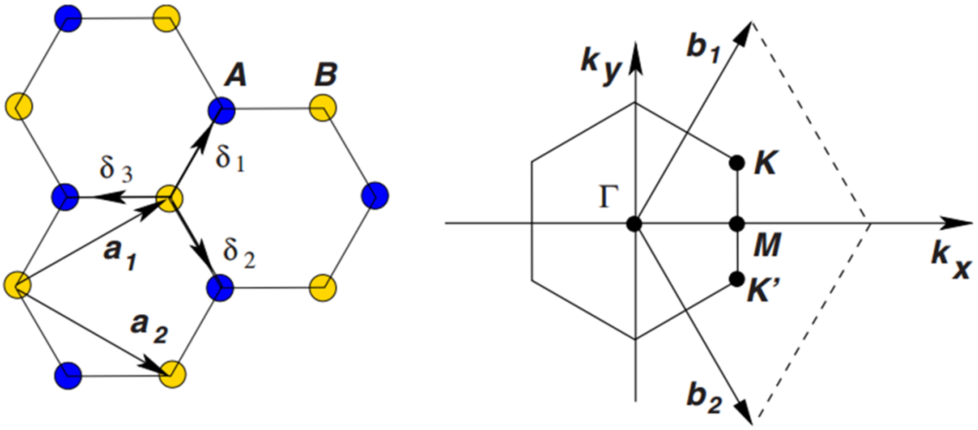

Figure 4.2: Left: Lattice structure of graphene; Right: Brillouin zone of graphene. Dirac cones are located at the K and K' points, while the Raman features are related to the Γ and K points. [18]

Raman spectroscopy is particularly powerful for the analysis of graphitic samples, due to visible wavelength photons being in resonance of the π-bonds. Resonance occurs when the laser energy (E_{Laser}) is equal to the actual energy gap between the valence and conductance bands, enabling the excited electron to enter a real state and thus making the probability for a scattering 1000 times more probable. This increase in scattering cross section and hence signal is especially crucial for nanomaterials as otherwise the peaks would not be able to be easily studied. The D, G, and 2D (G') bands all feature prominently in the Raman spectrum due to resonance in the sp^2 electronic structure.[188]

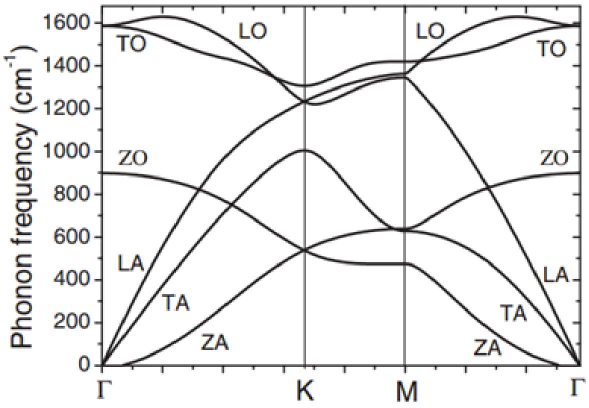

Figure 4.3: Phonon dispersion in graphene at the Γ, K, and M points. The 6 phonon polarization branches occur due to transverse (T), longitudinal, (L), or out-of-plane with

displacement on the z-axis (Z) vibrations, which can be optic (O) or acoustic (A). eg. a transverse optical phonon (TO).[189]

G Band

The **G** band is a signature of all sp^2 carbons and appears ~ 1580 cm^{-1}. It is a first order Raman in-plane stretching of the C-C bond (E_{2g}).[190, 191] This is a stretching between sp^2 carbon bonded atoms, in rings and chains.[188] The band is actually made of two different modes, since adjacent planes can vibrate in and out of phase, the optical in-plane transverse optic phonon (iTO) and the longitudinal optical phonon (LO), which are symmetric, so degenerate at the Γ point, due to the need to preserve the conservation of momentum (**Figure 4.3**). However due to the weak interlayer forces it appears as one band.[190] In general the linewidth is 10 cm^{-1} – 15 cm^{-1}. The **G** band is sensitive to strain in all sp^2 carbon systems,[192] and as it is made of two different modes, stretching the sample will split the G peak into G^- and G^+, parallel and perpendicular stretching respectively. Bending can also split the peak. In graphene the **G** peak can move into a higher position with fewer graphitic layers.[188] However this is not a good metric to measure the number of graphitic layers in a sample, as the peak can also be shifted by hydrostatic pressure, and doping, with p-doping and n-doping causing blue and red shifts respectively.

G' Band

The **G'** band also occurs in all sp^2 carbons and appears ~ 2650 cm^{-1}. It is also referred to as the **2D** peak, as it is caused by an overtone of the **D** peak, and is a two phonon process with $q \neq 0$. [193, 194] This band is frequency dependant on E_{laser}. It occurs from a second order phonon (A'_1) at the **K** point. This second order process is a double resonance process, which is responsible for the dispersive nature of it, so it is an intervalley double resonance two phonon process. The phonon in the vibrational structure of graphene has a wave vector q and phonon energy Eq. This means it can connect two conduction electric states, in turn making the phonon resonant.

The position of the peak has a strong dependence on the perturbation of the electron / phonon structure, meaning it can be used as a sensitive probe to find out the number of layers within a sample, due to the dispersive behaviour of the **G'** band.[195, 196] In graphite the 2D peak has two components, $2D_1$ and $2D_2$, with the $2D_1$ peak being classically smaller, commonly referred to as the shoulder. The peak comes from two phonons with opposite momentum near the **K** point (A_1' symmetry).[197] The two phonon emission connects the energy bands at the **K** and **K'** points. In graphene this peak has 4 components $2D_{1B}$, $2D_{1A}$, $2D_{2A}$, $2D_{2B}$, which appear at < 5 layers.[188] This monolayer peak can be fitted with a single lorentzian curve, and is 2 – 4 times the magnitude of the G peak.[198] For bilayer graphene, the peak is fitted with four lorentzian curves, and it is the same magnitude as the G peak. Bilayer graphene has two valence and conductance bands, with additional layers having increasingly more chances of scattering process, with three layers having 15 curves to be fitted, which becomes impossible at any more graphitic layers.[199] Turbostratic graphene has a single peak, which is slightly blue shifted 20 cm^{-1} from the peak in graphene.[200] So to distinguish between graphene and graphite, the FWHM can be analysed as the graphite has a much larger FWHM of 50 cm^{-1}.[188,201]

The G' peak can also be used to assign p- and n-type doping, with blue and red shifts indicating p- and n-doping respectively.

D band

The peak, found at ~ 1330 cm^{-1}, is due the A_{10} mode of small crystallite (< 0.5 µm; smaller than the wavelength of light) and is thus due to disorder. This is why this peak is referred to as the **D** peak.[190] More specifically it occurs from the breathing of carbon hexagons and the boarders of this crystallite, which causes a loss of translational symmetry. [190, 191] The D band is activated via double resonance which is a four order process (**Figure 4.4**).

Only phonons at centre of the Brillouin Zone are 1st order Raman allowed ($q = 0$) by symmetry, momentum conservation, and translational symmetry. Breaking the translational symmetry causes a breakdown of momentum conservation by activation of phonons at interior *k* points in the Brillouin zone. D peaks occur from zone-boundary phonons. The momentum is conserved due to a lattice defect, most commonly an edge defect but it can also be a vacancy, impurity, or dislocation, though it requires hexagonal carbon rings to appear.[188, 202] It is only active due to double resonance phonons, and it is frequency dependant on E_{Laser}. In graphene the D peak will have one peak on the edge. In bulk material there will be two peaks D_1 and D_2.[193]

The intensity of the D peak can be used to qualify the amount of disorder in the sample, and the nanocrystallite size. Commonly the I_D/I_G ratio (ratio of the intensity of the D and G peaks) is used to measure the amount of disorder. This is equal to A / L_a (lattice spacing and crystallite size) which can be used to work out a constant for the fixed Raman excitation frequency / crystallite size.[202] The width of the D peak can vary from 7 cm^{-1} to 100 cm^{-1} for very defective carbon materials. The D peak can also be used to analyse what type of graphene edge is in the system, with the peak being forbidden at edges with a zigzag structure. Additionally the average distance between the defects can be estimated for monolayer graphene by using I_D/I_G.[203]

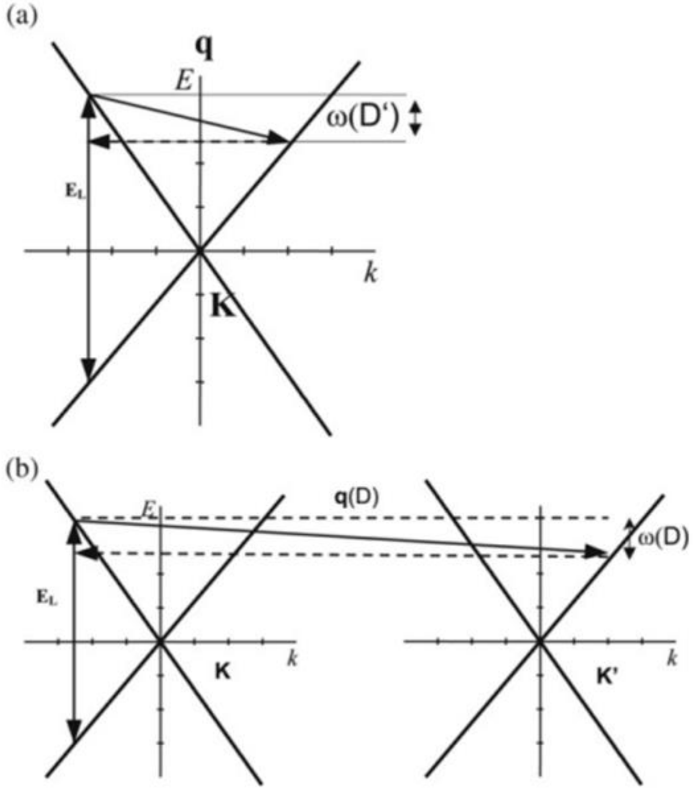

Figure 4.4: The double resonance of the 2D peak and D peak. In (a) an intra-valley process is shown, which causes the small q D' peak at ~1620 cm^{-1}. In (b) the activation of the D peak is shown. First the laser (E_L) excites an electron-hole pair; then the electron-phonon is scattered with an exchanged momentum q~K; then defect

scattering; finally the electron-hole recombines. Double resonance occurs when the energy of all the transitions is conserved throughout. [188] **Adapted from** [204]**.**

Other notable bands

Another disorder band appears at 1620 cm^{-1}.[205] The peaks at ~2930 cm^{-1} and 2970 cm^{-1} are due to a G + D and a D' + D transition respectively. A second speak appears at 3170 cm^{-1} which is an overtone of the G mode, often referred to as 2G.There is a peak at 3240 cm^{-1}, which comes from the intravelley second order process where q ≠ 0 at the Γ point. These peaks are often not mentioned in literature papers for the characterisation of graphene as they are not required.[206]

Overview and example Raman spectra

Table 4.1 shows a summary for the assignment of key Raman modes from sp^2 carbon materials (D, G, 2D) and additional peaks that may appear in sp^2 carbon Raman spectroscopy.

Name	ω /cm^{-1}	Resonance	dw/dE / cm^{-1}	Notes
D (iTO)	1350	DRd1	53	interV (q ~ 2k near K)
G (iTO, LO)	1585	SR	0	q = 0 (i.e. at Γ)
D' (LO)	1620	DRd1	10	intraV (q~ 2k near Γ)
G' (2iTO)	2700	DR2	100	interV + interV (q ~ 2k near K)
G+ D	2935	DRd2	50	intraV + interV
D' + D	2970	DRd2	60	intraV + interV
2G	3170	SR	0	overtone of G mode

Table 4.1: Table of the key Raman modes in sp^2 carbons. Single Resonance (SR); Double Resonance (DR); Double Resonance disorder active 1 phonon (DRd1); Double Resonance disorder active 2 phonons (DRd2); Change in phonon frequency by change of 1 eV laser energy (dw/dE).[207]

Example Raman Spectra

In this project to identify the presence of graphene, Raman spectroscopy will be the most useful tool, with a focus on the 2D band. The position, width, and shape of this band will give an indication of the amount of exfoliation. A shift to a lower wavenumber, a reduction in peak width, and a single peak will in general indicate a higher amount of exfoliation. **Figure 4.5** and **Figure 4.6** show example Raman spectra of graphene, with a specific focus on the 2D band. Additionally the effect of laser wavelength and stacking of the graphitic sheets is also shown.

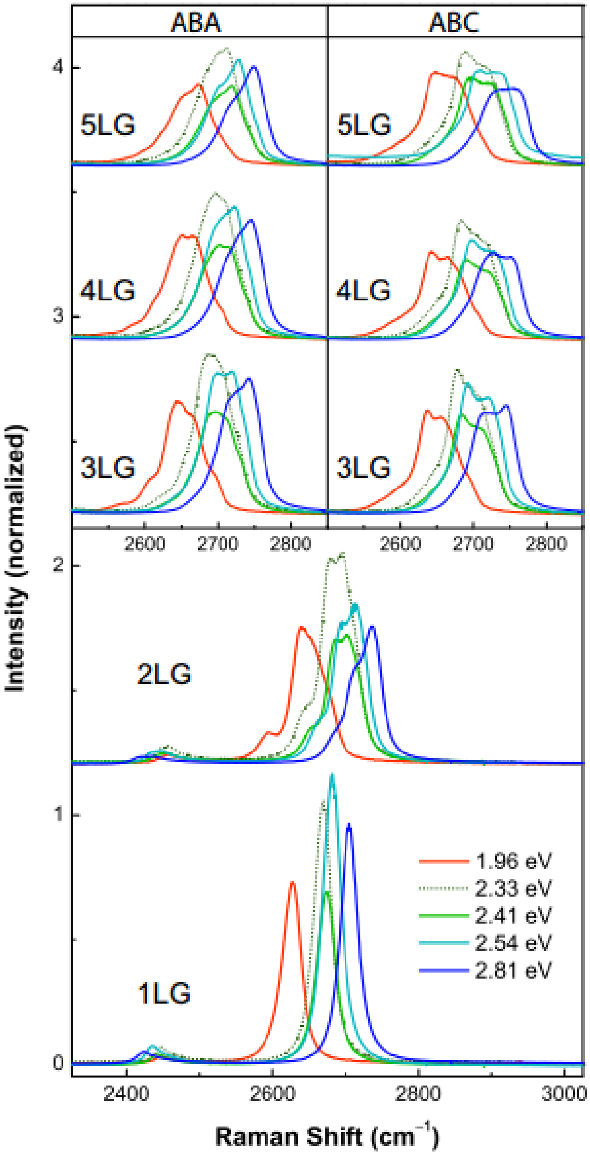

Figure 4.5: The Raman spectrum of the 2D band in graphene (and additional graphitic layers) at different laser excitations and stacking. [208]

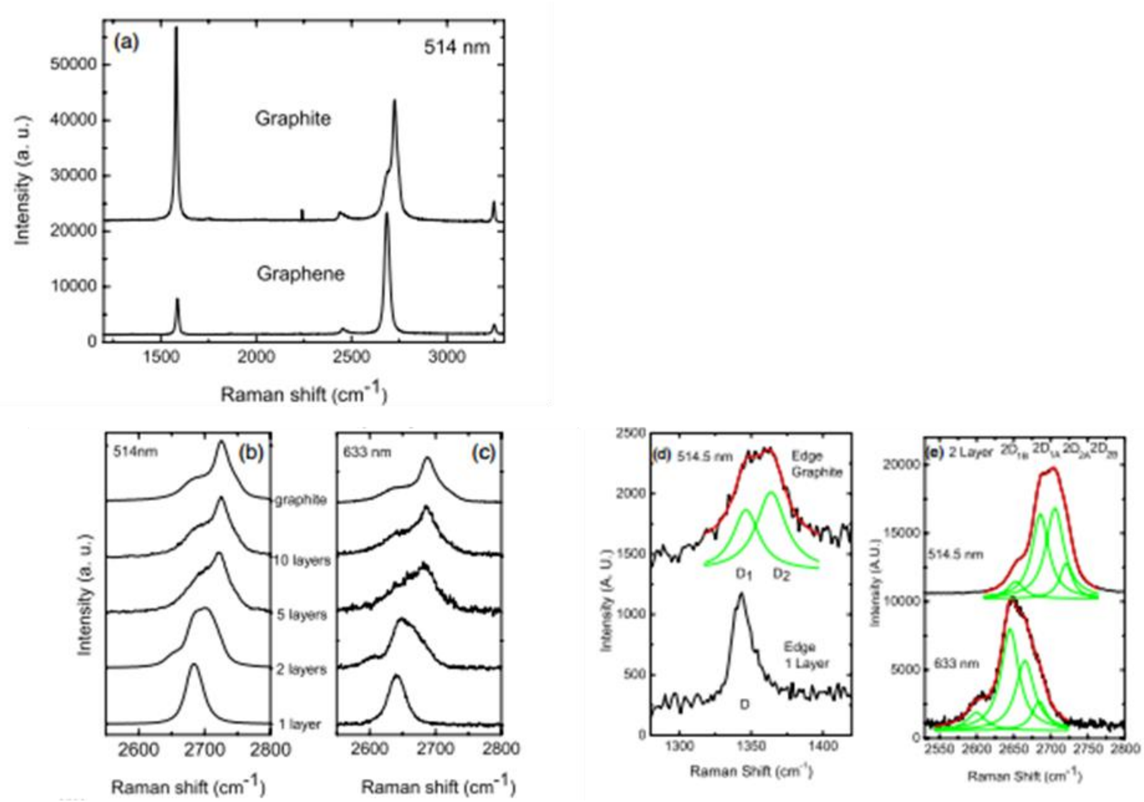

Figure 4.6: The selection of Raman spectra of graphene and graphitic layers. (a) The Raman spectrum of graphite and graphene; (b-c) the Raman spectrum of the 2D band in graphene and additional graphitic edges at different laser energies; (d-e) the Raman spectrum of graphene and bilayer graphene showing peak fitting of the 2D and D peaks at different laser energies. [198]

4.1.3 X-Ray Diffraction

When an X-ray hits a material, the X-ray is scattered in a specific direction, according to the elemental composition and arrangement of atoms within the material. The orientation and spacing of the planes will also have an effect on the scattering of electrons. The relationship between these is called Bragg's law, proposed by William Henry and William Lawrence Bragg in 1912, both of whom won the Nobel Prize in Physics for their work in 1915[209] (**Equation 6**). This means the elements present in a material, the distance between the planes, and the orientation of atoms can be resolved. The integer of multiple λ (*n*) and the wavelength of the incident x-ray (λ) are equal to the distance between the lattice planes (*d*) and the angle of the incident x-ray (ϑ). **Figure 4.7** is a representation of Bragg's law.

$$n\lambda = 2d\sin\theta$$ **Equation 6**

In a typical experiment, X-rays are focussed onto a material, while a detector records the intensity of the scattered x-rays at different angles. The spectra feature the angle of the X-ray (2θ) vs the number of counts recorded. Using a database of standards the peaks can be fitted to specific materials, giving a rough elemental composition, and spacing between the lattice planes. The shape of the peaks also gives information on the crystallinity of the materials, with more single crystalline materials giving sharp peaks due to the aligned nature of the planes, while amorphous materials give broad peaks. XRD was used to ascertain the spacing between the graphite planes and the presence of impurities in the electrochemically exfoliated materials.

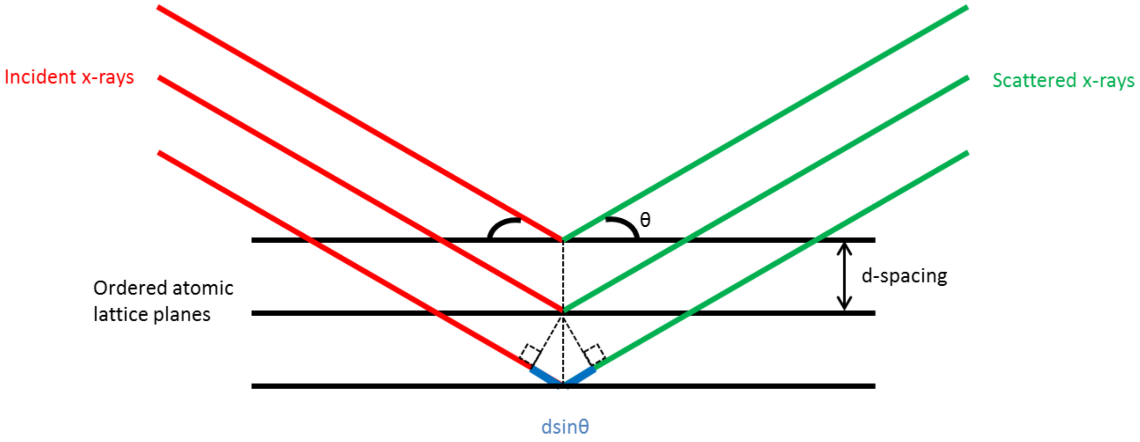

Figure 4.7: A representation on how the X-rays are scattered in a material which would give information on the lattice spacing / Bragg planes and elemental composition. The incident ray (red) is scattered by the atoms in the planes, which produces a scattered beam (green).

Instrument

A Philips 'X'Pert' diffractometer with a copper source (λ = 1.54 Å, ~ 8 keV) was used, with a scan rate of 0.03 ° s^{-1} from 4 ° to 100 °. Analysis was performed using 'High Score' software with peaks fitted using standards from the 'International Centre for Diffraction Data' (ICDD) database. Powder samples were loaded into pans and pressed carefully to ensure near identical packing, while non-powder samples were supported on a zero-background silicon (51.1) substrate with Vaseline. **Figure 4.8** is an example XRD pattern of the zero-background holder with Vaseline. This holder did not give a zero-background, with high intensity regions at 2θ = 18, 21 and 23 °.

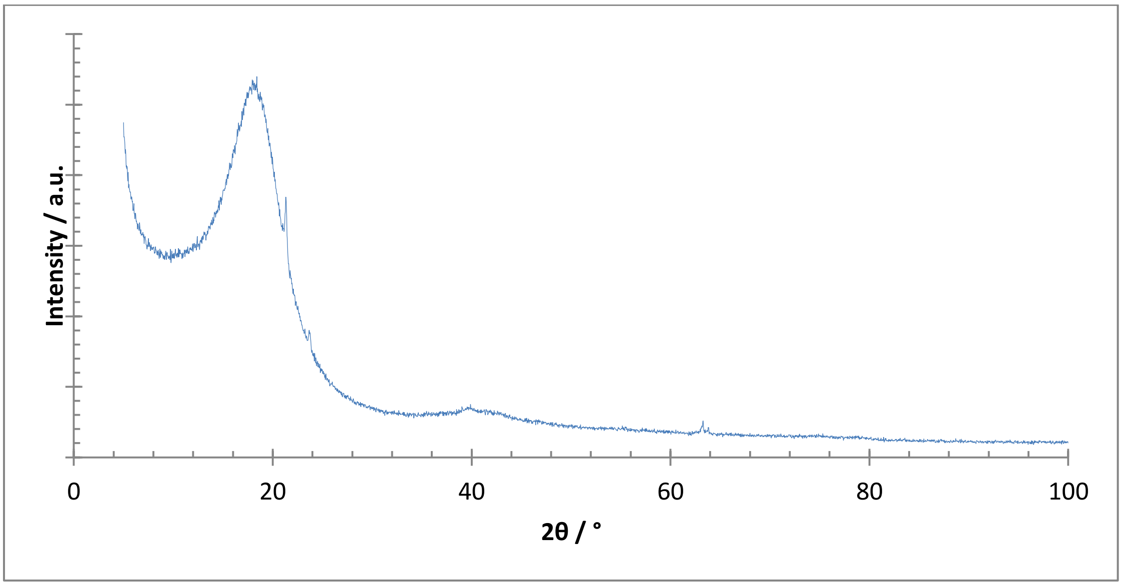

Figure 4.8: The XRD pattern of a silicon wafer with Vaseline. This was used to affix fibre samples and shows the impurities that will appear in all other spectra.

4.1.4 Thermal Gravimetric Analysis

Thermal gravitational analysis (TGA) is an instrumental technique which analyses the mass loss of a sample during heating. This thermal analysis can reveal information like composition, thermal stability, oxidative reactions, and adsorbed materials. The instrument consists of a precision balance and a programmable furnace, where the sample is heated while the mass is recorded. The resultant spectra feature a plot of temperature vs mass loss. Exfoliated graphite samples were analysed to ascertain the composition and impurities, while graphene oxide and carbon fibre composites analysed for composition and extent of reduction.

Instrument

A TA instruments TGA ‘Q_{500}’ machine was used, attached to an ‘Evolved Gas Analysis’ (EGA) furnace. 10 mg of sample was loaded into platinum pans and these were heated in an air atmosphere to 1000 °C. An air atmosphere was used to assess the oxidation of the graphite, as well as the inorganic impurity of the samples. Sample loading and set-up was performed by Mrs Polly Greensmith and Miss Jasmine Fernley. A high resolution mode was used in which a baseline heating rate of 10 °C min^{-1} is used but this heating rate is slowed as soon as mass loss is recorded, ensuring the reaction is complete before the heating is accelerated again. Resultant data were analysed using 'TA Universal Analysis' software. Quantitative data for the spectra were established using the weight and derivative weight (**Figure 4.9**).

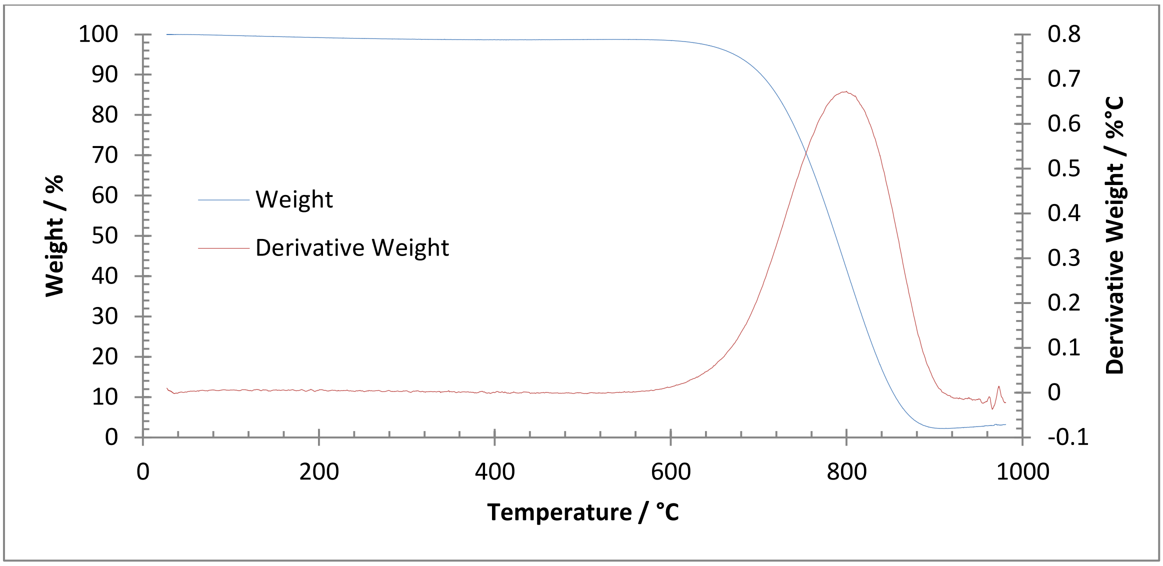

Figure 4.9: TGA profile of naturally sourced Graphexel 197, showing the weight (%) and derivative weight (% °C), both used to analyse the important events that occur during thermal decomposition, including the onset point, end point, and the point of quickest decomposition.

4.1.5 Infra-Red Spectroscopy

FTIR spectroscopy is used to identify the chemical bonds in a molecule. Like Raman, a laser is used to induce vibration in molecular bonds. These bonds can rotate, bend and stretch, giving off different frequencies, due to the change in the dipole moment of the bond. FTIR is a useful tool for analysis; however, it will only give qualitative information about a sample. Thus it is useful for determining the groups present in GO, or how functionalised graphene is. It can also test the extent of carbonisation in carbon fibres, due to the loss of the nitrile group.

Instrument

Infra-red measurements were taken on a Thermo Electron Corporation 'Nicolet 5700' FTIR spectrometer. Due to the high absorbance of IR by graphite, transmission mode was used for analysis, requiring the use of KBr discs. KBr (200.5 mg) and sample (0.5 mg) were grinded together and pressed at 10 tonnes of pressure for 3 minutes, producing a 13 mm disc. This was then analysed immediately on the IR spectrometer. The resultant spectrum was a combination of 32 scans, with a data spacing of 1.928 cm^{-1}. 'OMNIC' software was used to record the spectra. As KBr is very hydroscopic all resultant spectra contained an O-H band, even if it was not present in the material.

4.1.6 Absorption Spectroscopy

UV-Vis is an absorption spectroscopy technique that utilises a white beam source that can be used to probe the composition, absorption coefficient, and concentration of a sample. The source scans from the UV to the visible range (from λ = ~ 200 – 800 nm), and the degree of absorption of the transmitted light is measured. Absorption measures the atomic transition when visible light hits a molecule, as the electrons are promoted from the ground state to the excited state. Beer's law, **Equation 7**, shows the relationship between the absorption (A), coefficient (ε), concentration (c) and path length (l, a constant and generally 1). UV-vis spectroscopy can be used to analyse the extent of GO reduction and concentration of solutions. The resultant spectra are a plot of wavelength vs absorption.

$$A = \varepsilon c l \qquad \textbf{Equation 7}$$

Instrument

A Thermo Scientific "Evolution 201" UV-Visible Spectrometer was used for absorbance measurements. Sample concentrations of ~ 0.001 mg mL^{-1} were analysed between 200 nm and 800 nm in quartz cuvettes. Before analysis a background was taken using the appropriate solvent.

4.1.7 Atomic Force Microscopy

AFM is an imaging technique that can be used to assess the thickness, force constant, and roughness of a material. AFM can image materials at very high resolutions, with the best instruments reaching atomic scales. In AFM a cantilever, with a small tip, is rastered over a surface. The cantilever will deflect as it passes over structures of different heights. This deflection is recorded as an electrical signal, with voltage proportional to the displacement of the cantilever. Higher points in a sample will displace the cantilever more than thinner areas, thus the height can be recorded. Other measurements that can be taken include stiffness and force constant, via adhesion strength and stickiness respectively. There are three operational modes for AFMs, which changes the way the cantilever interacts with the sample: tapping mode, contact mode, and non-contact mode. In contact mode, the cantilever stays in constant contact with the sample's surface, while in tapping mode, the cantilever is oscillated above the sample with contact occurring during oscillations of the tip, but it does not interact with the surface enough to pick up debris. Tapping mode is one of the most used modes for AFM measurements. In non-contact mode the tip does not touch the sample, meaning less debris is picked up or damage can occur, but surface of the material needs to be pristine. The type of tip can also influence the measurement. A sharper tip will give a more accurate better resolution image.

Failings of AFM include, imaging errors that can be misattributed to the samples. For instance, large differences in height can cause the tip to incorrectly record the height, which is especially prevalent at higher scan speeds. Additionally tip contamination and tip blunting will record the images incorrectly, as the tip height profile will be less accurate. **Figure 4.10** shows typical AMF images, with the corresponding height profile.

Instrument

A Bruker 'Multimode' AFM was used to record the AFM spectra of the materials, with image analysis using 'Image J'. Samples were deposited on a silicon dioxide wafer (Thermo Scientific 300 nm) via dip coating and washing. The machine was operated in tapping mode with Bruker 'TESPA-V2' tips. Analysis was performed using 'NanoScope Analysis' software, where the images were flattened and sections were taken to assess the height. Additional height profiles were performed by white light interferometry. A Veeco 'Contour GT' with a 50x objective was used with measurement and analysis was performed using 'Vision 64'.

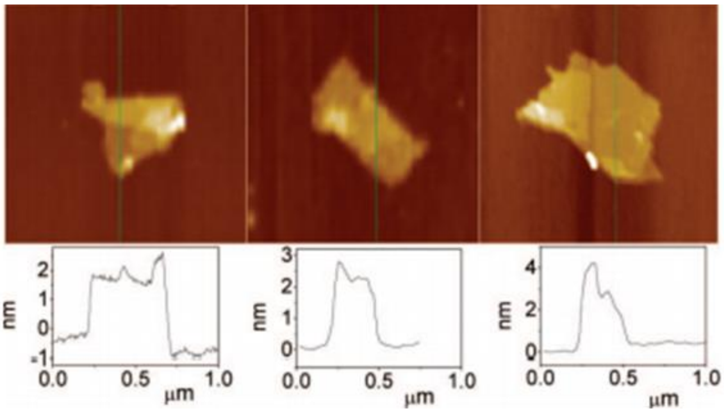

Figure 4.10: AFM height image and height profile of liquid exfoliated graphene.[210]

4.1.8 Capacitance Analysis

Capacitance is a physical mechanism where charge is stored on the surface of a supercapacitor via the adsorption of ions or redox reactions. To determine the capacitance of a material a potentiostat is used, which can measure the charge of a material at different potentials. There a two broad methods for calculating capacitance, cyclic voltammetry (I/V curves) and galvanostatic discharge (chronopotentiometry). I/V measurement involve cycling the material across a range of potentials and measuring the charge, which produces a CV curve, while charging and discharging the material at a constant current will give the galvanostatic discharge curve. Using the galvanostatic discharge curve is the most common way to calculate the capacitance (**Equation 8**).[211]

$$C_m = \frac{I\Delta t}{\Delta V m}$$ **Equation 8**

The gravimetric capacitance (C_m) is calculated by multiplying the constant charge (I) applied by the time it takes to discharge the material (Δt), divided by the potential difference (ΔV) multiplied by the mass of the material (m). To work out the specific capacitance, this can be streamlined by dividing the slope of the discharge curve ($\Delta V/\Delta t$) by the scan rate (I) (**Equation 9**). Galvanostatic charge and discharge cycles can also give an indication of the stability of a material by measuring the deterioration in capacitance after many (1000 – 10,000) charge cycles. The shape of the curve can also give an indication of the electrochemical performance of the material with a large IR drop, curved lines, and larger windows between curves (proportional to charge density) indicating that there is large resistance in the material, a non-ideal capacitor, and a high capacitance respectively.

$$Csp = \frac{I}{{\Delta V}/{\Delta t}} \qquad \textbf{Equation 9}$$

Cyclic Voltammetry can also be used to calculate capacitance by recording the current over a potential range, with **Equation 10** showing how to calculate the capacitance of the material in a two electrode system.[212] The shape of the curve also gives information on the type of capacitance with rectangular curves, curved edges, and peaks demonstrating an ideal EDL capacitor, large amounts of resistance, and redox reactions (pseudo-capacitance) present in the system respectively.

$$Cs = \frac{\int_{E1}^{E2} i\,(E)dE}{2(E_2 - E_1)mv} \qquad \textbf{Equation 10}$$

The specific capacitance (*Cs*) is calculated by dividing the total potential charge of the positive and negative CV sweep ($\int_{E1}^{E2} i\,(E)dE$) by two times the potential window ($E_2 - E_1$), mass of the sample (*m*), and the scan rate (*v*). This method is seen as less accurate than the galvanostatic measurement. In general CV is used as a qualitative method, while galvanostatic discharge is used more widely for calculations.

Energy and power density can be derived from capacitance and indicate the amount of energy a capacitor can hold and the rate of delivery respectively. The energy density of a material is a function of the operating voltage and specific capacitance, **Equation 11**, where C_{cell} is the specific capacitance of the cell and *V* is the voltage. At higher operating voltages the energy density of the cell will be higher, thus ionic liquid electrolytes are preferred for measurement. For a symmetrical cell configuration, where the potential window is 1 V, the energy density can be calculated by dividing the capacitance by 8.

$$E = \frac{1}{2}C_{cell}V^2 \qquad \textbf{Equation 11}$$

Power density is a function of the energy density and discharge time, **Equation 12**, where *E* is the energy density and *Δt* is the discharge time. Delivering a higher amount of energy over a short discharge time will increase the power density of the material.

$$P = \frac{E}{\Delta t} \qquad \textbf{Equation 12}$$

Instrument

An Ivium 'Stat' potentiostat was used for electrochemical testing. A symmetrical two electrode cell set-up was created, with the same material at both electrodes; counter and working. The electrolyte was 6 M KOH and the potential was cycled from 0 V to 1 V. Titanium foil was used as a connector and silver paint as an adhesive, while butterfly clips were used to compress the electrodes together. **Figure 4.18** shows an example of this set-up. For CV measurements the scan rate was selected as 20 mV, 40 mV, 100 mV, 200 mV, 300 mV, and 400 mV, with a step size of 4 mV. For galvanopstatic measurements, the material was charged and discharged at 10 mA, 20 mA, and 40 mA, with an interval time of 0.01 s. For cycle life measurements, the capacitor was subject to 2000 charge-discharge cycles at 100 mA.

Example CV and discharge curves:

Figure 4.11 and **Figure 4.12** are example CV and discharge curves, sourced from literature for the calculation of capacitance. In general a lower scan rate or charge current will give a larger area CV curve and a larger window for galvanostatic discharge. These both correlate to a larger capacitance, and thus measurements are usually taken at low scan rates and charge current. **Figure 4.13** is a CV and discharge curve of a pseudo-capacitor. Here the peaks are noticeable on both graphs, which translates to redox reactions happening between the material and electrolyte.

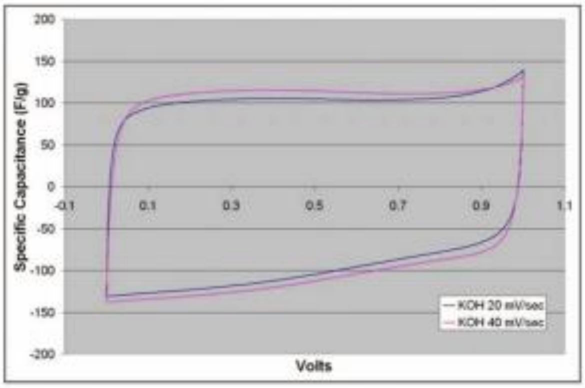

Figure 4.11: The CV curve of chemically modified graphene (CMG) recorded using a KOH electrolyte.[22]

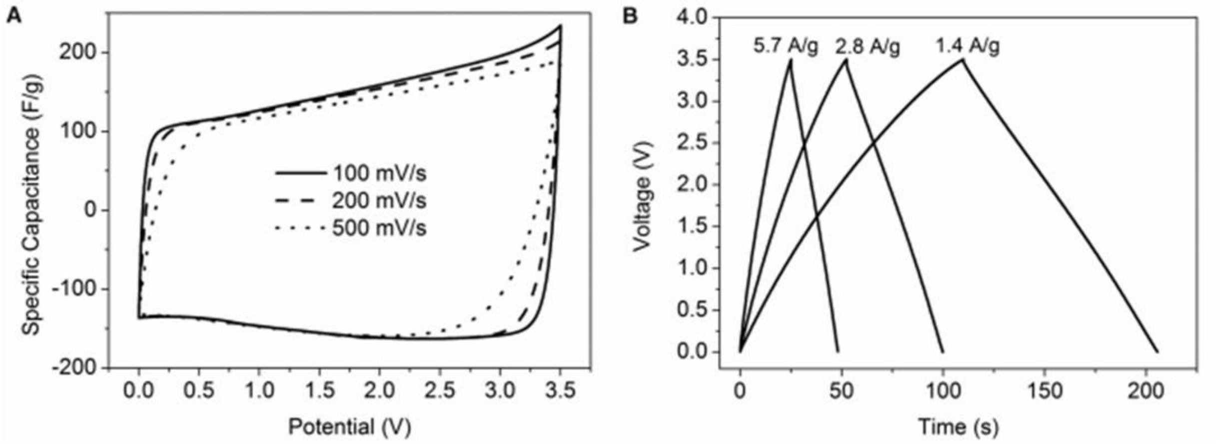

Figure 4.12: (a) A potential vs specific capacitance scan of a-MEGO in BMIM BF_4/AN. Notice the larger electrochemical window for ionic liquid electrolytes; (b) the galavanostatic charge and discharge curves of a-MEGO at different constant currents.[170]

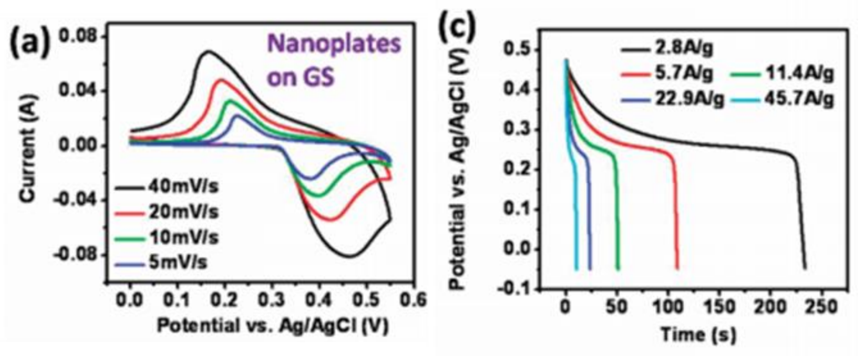

Figure 4.13: (a) The CV and (c) galvanostatic discharge curves for pseudo-capacitive graphene-Ni(OH)$_2$ hexagonal nanoplates. Peaks indicate faradic reactions taking place in the system.[149]

4.1.9 Impedance Spectroscopy

Impedance is a complex measure of resistance that is not limited by the concept of an ideal resistor. Like CV, during measurement a potential is applied and the current is measured. However the AC potential applied causes an AC current signal that can be considered a Fourier series. These are then processed into frequency Z_0 and phase shift ϕ, where impedance is expressed as the complex number (**Equation 13**).

$$Z(\omega) = \frac{E}{I} = Z_0 \exp(j\varphi) = Z_0(cos\varphi + jsin\varphi)$$

Equation 13

$Z(\omega)$ has a real and imaginary parts, which are plotted on the impedance spectrum with the real response on the x-axis and imaginary on the Y-axis. These are called Nyquist plots and are the most common way to display impedance results. This plot must be made in terms of an electrical circuit to justify the frequency used, with components added to satisfy the data. A Nyquist plot gives qualitative and quantitative data about the material. For instance, the x-axis intercept gives the resistance, while the shape of the curve can give an idea of the capacitive performance of the material, with a more vertical the line indicating a better EDL capacitor.

Bode plots can also be used to present the data, with the *x*-axis log frequency, and the *y* axis absolute impedance values and phase shift. In these plots the capacitance can be more easily visualised.

Instrument

In this work an Autolab ‘Metrohm’ was used to measure impedance. The electrode set up was similar to the capacitance measurements (**Figure 4.18**). The material was analysed from using a sinusoidal signal at 0 V and amplitude of 5 mV from 0.1 Hz to 100000 Hz.

Example Spectra

Figure 4.14 and **Figure 4.15** are example Nyquist plots for graphene materials, as these are the most common representation of the impedance. Using these graphs the resistance can be estimated using the x-axis intercept.

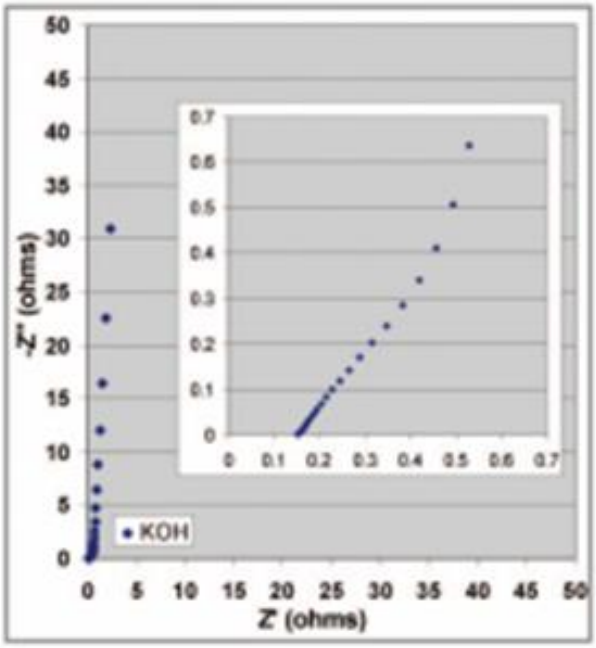

Figure 4.14: Nyquist plot of CMG with KOH electrolyte.[22] Often an inset of the curve at a higher resolution is present to more accurately analyse the curve shape.

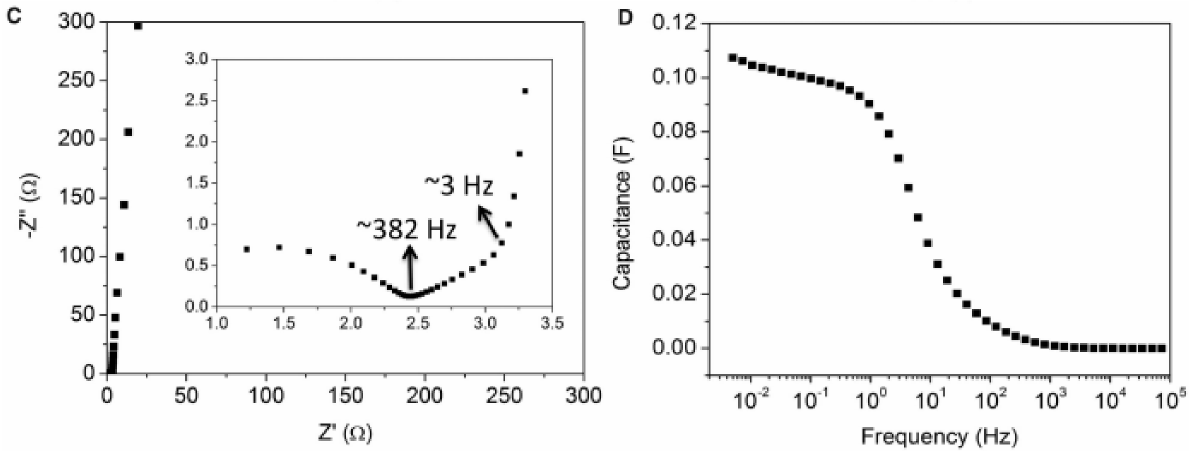

Figure 4.15: (c) The Nyquist plot; and (d) frequency response of the gravimetric capacitance of an a-MEGO super-capacitor.[170]

4.2 Experimental Procedure

4.2.1 Electrochemical exfoliation of graphite

Materials

Graphite (Four grades from two sources): 197, 399, (Graphexel, natural graphite), 15 µm, 25 µm (xGnP® Grade M, XG Sciences, synthetic graphite nano-platelets); DMSO (99%, VWR Chemicals); TEA-Cl (99%, Acros Organics); LiCl (Anhydrous, 99%, Alfa Aesar); Gum Arabic (from Acacia Tree, Sigma).

Pellet Electrode

Graphite powder (0.95 g) was stirred under heat with gum arabic (0.05 g) in ethanol (10 mL) until the ethanol had evaporated. The resultant powder was pressed at 1 tonne of pressure into a 13 mm pellet and attached directly to the power supply via a clip as the cathode. This cathode was then wrapped in a muslin cloth. This was immersed into an electrolyte of LiCl (1 M) and TEA-Cl (0.5 M) in DMSO. This electrolyte solution was chosen because the synthesised graphene should remain un-functionalised to increase the capacitance. Cathodic reduction is the best way to achieve this, and the mentioned electrolyte solution has been routinely shown to synthesise FLG (Cooper *et al.*). A graphite rod counter electrode was also placed into the electrolyte. The material was exfoliated at 150 mA and a variable voltage at maximum of 10 V for 16 hours. The mixture was then washed with excess water for 2 hours and vacuum filtered using a 1 µm filter paper with three further washing cycles. This was then placed in an oven at 80 °C overnight. To ensure a good exfoliation, the process was repeated up to 4 times. The material was collected via forced settling using a centrifuge at 3000 rpm and stored in an air-tight container.

Aluminium Cage Electrode

Graphite was placed into an aluminium cage attached to a power supply via a clip. Electrolyte (1M LiCl, 0.5 M TEA-HCl in DMSO) was placed into the cage with a graphite rod counter electrode. The material was exfoliated at 150 mA with a variable voltage at a maximum of 10 V for 16 hours. The material was then washed with excess water for 2 hours and vacuum filtered using a 1 µm filter paper with three further washing cycles. The material was then washed with dilute acid to remove metal impurities and DMSO in 3 cycles. Again, the material was collected via forced settling using a centrifuge at 3000 rpm and stored in an air-tight container. **Figure 4.16** shows a schematic representation of the exfoliation set-up.

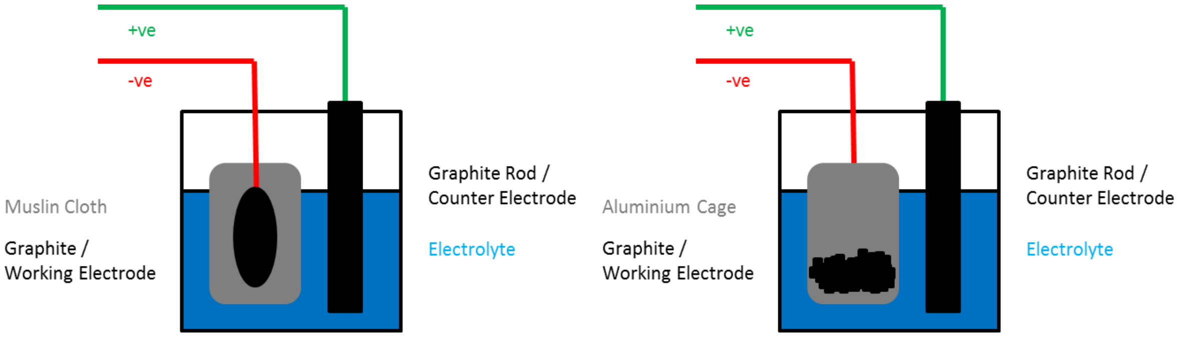

Figure 4.16: (Left) Pellet electrode; (Right) Aluminium cage electrodes. Both methods were used for the electrochemical exfoliation of graphite in a 1M LiCl, 0.5 M TEA-HCl in DMSO electrolyte.

4.2.2 Graphene Infiltration into a porous electrode

Materials

Electrochemically exfoliated graphite: 197, 399 (Graphexel); 15µm, 25µm (xGnP® Grade M, xG Sciences); DMF (99%, Sigma-Aldrich); Nickel Foam (Porosity: 95%, 99.5%, GoodFellow).

Method

Electrochemically exfoliated graphite (0.1 g) was dispersed into DMF (100 mL) under stirring for 1 hour. This was added to nickel foam, and was consequentially evaporated at 120 °C under pressure. Subsequent additions of graphene in DMF were added once dried to ensure total coverage of the nickel foam.

4.2.3 GO Synthesis

Materials

Flake Graphite 2369 (Graphexel); $NaNO_2$ (98%, Alfa Aesar); H_2SO_4 (95%, Fisher); $KMnO_4$ (99%, Sigma-Aldrich); H_2O_2 (30 w/v, Fisher); Dialysis Tubing (Snakeskin, Thermo Scientific); NaOH (97%, Fisher).

Method

Graphite (5 g) and $NaNO_3$ (4.5 g, 0.05 M) were added to H_2SO_4 (169 mL, 3.17 M). This mixture was stirred and cooled to 0°C and $KMnO_4$ (22.5 g, 0.14 M) was added over 70 minutes. (It should be noted that care needs to be taken at this step to prevent a thermal runaway reaction.) After adjusting to room temperature, the mixture was stirred for 7 days. The solution was then dispersed into 5 wt% H_2SO_4 in water (550 mL) over 1 hour, and stirred for an additional 3 hours. H_2O_2 (15 g, 30 vol) was added over 5 minutes, and was stirred for an additional two hours. 3 wt% H_2SO_4/0.5 wt% H_2O_2 (500 mL) was added and the solution was left to stir overnight. After centrifugation at 8,000 rpm for 20 minutes, the resulting viscous liquid was dispersed into 3 wt% H_2SO_4/0.5 wt% H_2O_2 (500 mL). This was repeated 12 times, and finally diluted to 3 mg mL^{-1}. The mixture was neutralised by dialysis. Adapted from the Languir method in Angewandte Chemie.[213]

Base washing of GO

As prepared GO (50 mL, 150 mg dry GO) was stirred for 24 hours with water (250 mL). NaOH (1g, 0.025 mol) was added, after which the mixture darkened. The mixture was then refluxed, followed by centrifuging at 11,000 rpm for 30 minutes. After layers separated, a clear, colourless mixture was decanted. The black product was acidified with HCL (250 mL, 1 M) and refluxed for 1 hour, followed again by centrifugation at 11,000 rpm for 30 mins. After removal of the clear liquid, the black pellet was washed with water (250 mL) and finally centrifuged at 11,000 rpm for 2 hours.

4.2.4 rGO synthesis

Materials

Graphene Oxide (Synthesised); Ascorbic Acid (99%, Sigma-Aldrich);

Method

GO was first sonicated in water at a concentration of 3 mg mL^{-1} for 20 minutes. The GO solution was stirred at 95 °C with ascorbic acid (10 mM) for 24 hours. To increase the pH sodium hydroxide was added to achieve pH 11 where necessary. In the case of PVA-GO composite fibres, the fibres were not sonicated, and the pH was not adjusted.

4.2.5 PAN Fibre Spinning

Materials

PAN (M_W: 150,000, Aldrich); Electrochemically exfoliated graphite: 399 (Graphexel); 15µm xGnP® Grade M (xG Sciences); DMF (99%, Aldrich); Diethyl ether (99%, Aldrich)

Method

Solutions of graphene with PAN polymer in DMF at different concentrations were prepared. Fibres were spun into a rotating coagulation bath (diethyl ether; water) at a rate of 0.05 ml min^{-1} to 0.5 ml min^{-1}. The needle gauge used varied from 18G to 23G. The collected fibres were washed with water and dried. **Figure 4.17** is a schematic representation of the wet-spinning process. This applies to both the wet-spinning of PAN and graphene oxide.

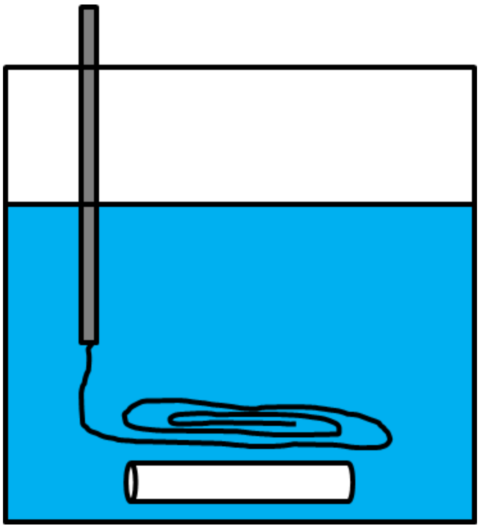

Figure 4.17: A schematic representation of the wet-spinning procedure. A stirrer bar coupled with a syringe pump is used to draw out the spin dope into the bath at a consistent rate.

4.2.6 Wet-Spinning of Graphene Oxide

Materials

GO (Synthesised); Ethanol (95%, Sigma-Aldrich); PVA (M_W: 61000, 10-98, Aldrich); $CaCl_2$ (Anhydrous, 93%, Alfa Aesar)

Method

Previously synthesised graphene oxide was concentrated to 20 mg mL^{-1} via centrifugation at 11,000 rpm for 2 hours. PVA was heated at 90 °C under stirring until it had dissolved into water. The GO and PVA were then stirred together at a range of concentrations. This mixture was then extruded into a solvent bath of 5:1 ethanol / water (v/v) with 5 wt% $CaCl_2$. After 30 minutes the fibres were washed with ethanol and water. These were left to air dry overnight. After creation the fibres were placed in methanol for 12 hours to increase crystallinity. Adapted from Gao *et al.*[214]

4.2.7 Carbonisation

Materials

Electrochemically exfoliated graphite: 399 (Graphexel); 15µm (xGnP® Grade M, xG Sciences)-PAN composite fibre; graphite foil (Sigma, 99.8 %, thickness 0.5 mm)

Method

PAN-graphene fibres were placed in graphite foil and heated to 240 °C in air at a rate of 10 °C min^{-1}. The sample was then heated to 1500 °C at a rate of 40 °C min^{-1} in an argon atmosphere. The sample was held at 1500 °C for 2 hours, and then left to cool to room temperature.

4.2.8 Electrochemical Analysis

Materials

KOH (Merck, powder); Titanium foil (Alfa Aesar, 99.7 %, thickness 0.89 mm); Silver conductive ink (Alfa Aesar)

Method

Figure 4.18 is a schematic of an example of the electrode set-up. The material was immersed in the electrolyte and placed onto titanium foil with silver paint. Filter paper separator was soaked into electrolyte and added to the electrode. The electrode was sealed with insulating tape and pressed with clips. The electrolyte was 6 M KOH.

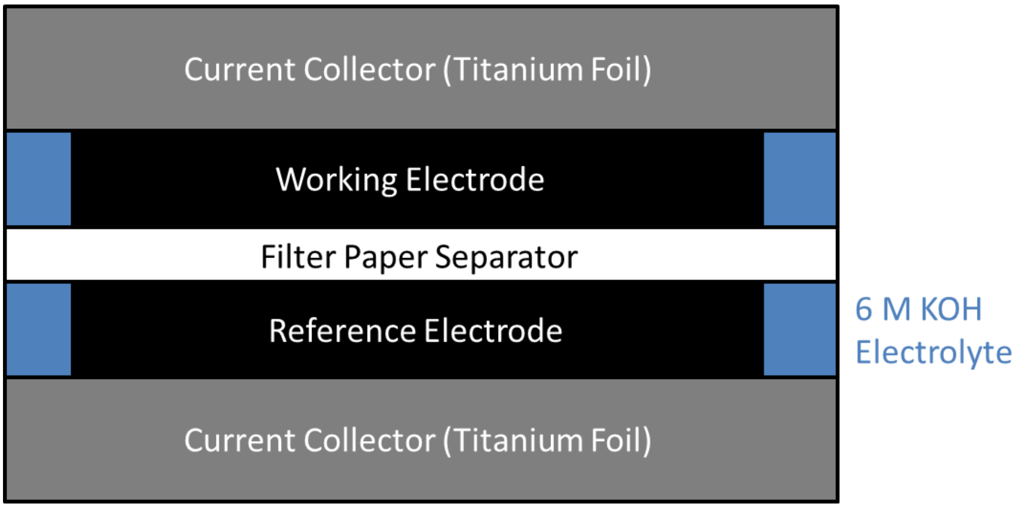

Figure 4.18: Electrode set-up for capacitance measurement. The device is held together and packed tightly using insulating tape and binder clips.

4.3 Presentation of Results

Results will be presented in each chapter first by characterisation using instrumental techniques, then by the characterisation of the electrochemical properties. Typical results will be shown for each material, as showing all the data collected would be impractical. Data in comparison graphs has been manipulated, to show each graph in a stack. Due to the large background in some Raman measurements, this was subtracted for easier viewing of the typical peaks.

5 Graphene Infiltration into a Porous Matrix

This chapter studies the electrochemical exfoliation of graphite to graphene and the capacitance performance of the resultant products. The degree of exfoliation is investigated as a function of starting graphite, with four different grades of graphite sourced from two different companies. The form of the graphite from the two sources differed. One was from natural graphite, while the other was graphite nano-platelets, which have been previously exfoliated. Both of these sources had two grades of graphite, large and small. These were chosen to test whether the degree of exfoliation was affected by previous exfoliation, and also if the size of the material made an impact on the potential for exfoliation. The cathode for the exfoliation process was formed by either pressing the graphite into a pellet or holding the powder in an aluminium cage. The electrochemically exfoliated graphene was then deposited onto nickel foam to make a capacitor and the electrochemical performance of the graphene was analysed.

5.1 Electrochemical Exfoliation

5.1.1 Characterisation of the Starting Graphite Grades

Graphite can vary widely in elemental content (e.g. oxygen), degree of crystallinity, and particle size, all of which can affect the extent that it can be exfoliated into graphene. Four different grades of graphite were examined in this project:

- Graphexel 197 (abv. 197)
- Graphexel 399 (abv. 399)
- xGnP® Grade M 15 µm (abv. 15 µm)
- xGnP® Grade M 25 µm (abv. 25 µm)

The Graphexel materials were mined and processed from naturally occurring graphite deposits. This material was selected since previous preliminary results from our laboratory suggested the graphite could be exfoliated. The xGnP grades, however, were graphite nano-platelets which the commercial producer has exfoliated from graphite using thermal shock. These were selected to study if a thinner material could be more easily exfoliated than a large crystal and if the role of the particle size had an effect on exfoliation. For example, Cooper *et al.* showed that HOPG could not be exfoliated.[72]

These different starting graphite grades were all characterised by SEM, Raman, XRD, TGA, and FTIR.

Scanning Electron Microscopy (SEM)

SEM was used to measure the dimensions of the graphite flakes and examine their morphology. In order to separate the graphitic sheets fully during electrochemical exfoliation, the ions need to penetrate through the whole sheet, thus it can argued that the smaller flakes have a higher probability to be fully exfoliated. **Figure 5.1** shows typical SEM images, from which the size distribution of the graphite in each of the samples was calculated (**Table 5.1**) and then plotted (**Figure 5.2**).

The naturally occurring graphite (197 and 399) comprised two distributions; large flakes (60 µm and 30 µm respectively) with smaller flakes (< 1 µm) on the surface. The xGNP materials had a smaller diameter distribution and did not have these smaller flakes on the surface. The Graphexel 399 and xGnP 25 µm had similar size larger particles, enabling a comparison later in the thesis. The topography of the flakes differs depending on whether the material was previously exfoliated. The natural graphite is mostly rectangular in shape, with strict flat surfaces. The previously processed material is wrinkled and crumpled, seen especially in the 15 µm graphite. The exfoliated graphite also has torn edges, unlike the flat edges of the naturally occurring graphite, possibly due to the effects of exfoliation.

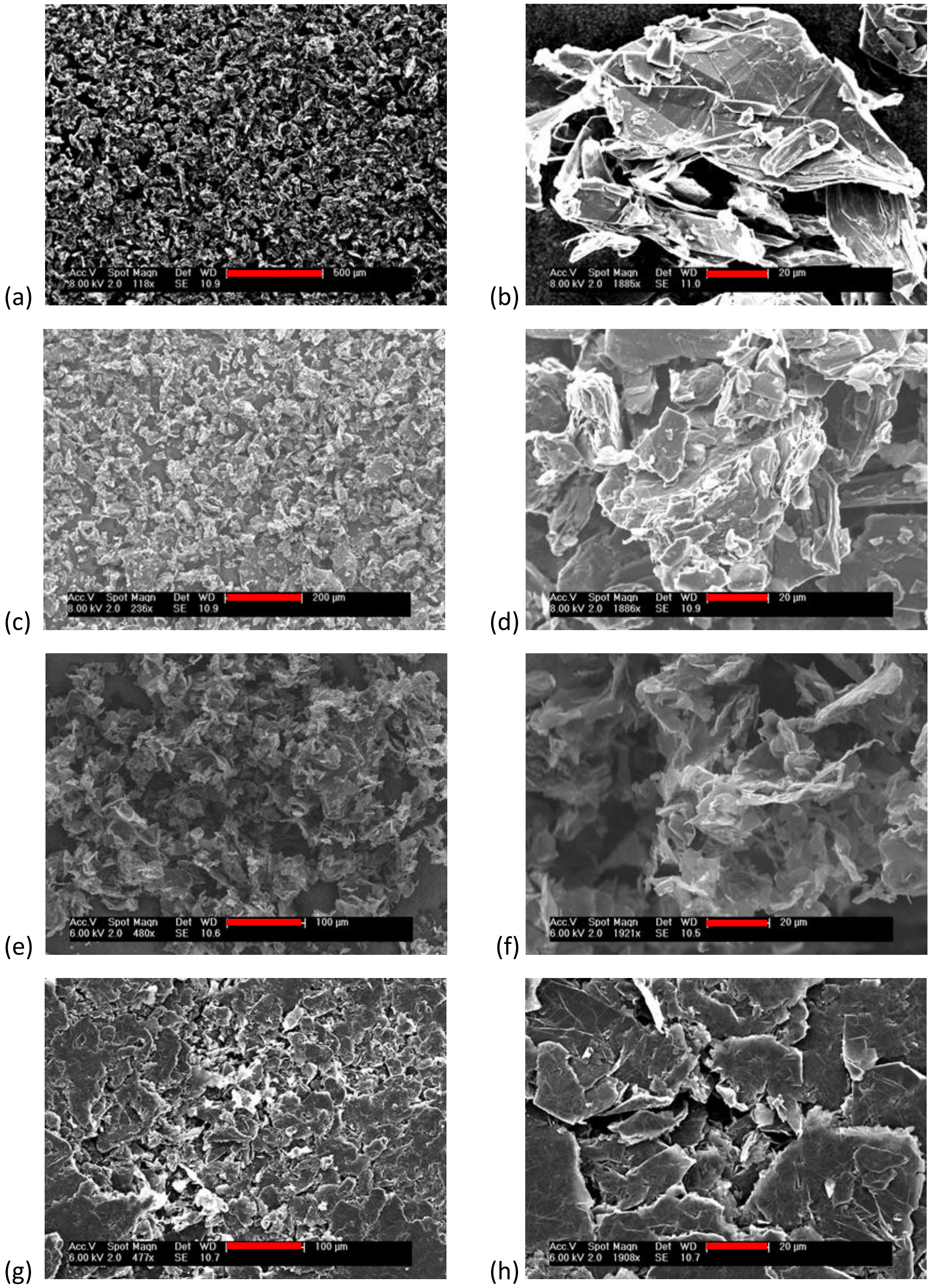

Figure 5.1: Typical SEM images of initial graphite grades. (a-b) 197; (c-d) 399; (e-f) 15 µm; and (g-h) 25 µm graphite. Error bars: (a) 500 µm; (c) 200 µm; (e & g) 100 µm; (b, d, f, h) 20 µm.

Sample	Average size of the graphite flakes / µm
197	63.0 ± 33.5
399	35.0 ± 25.6
15 µm	14.5 ± 11.1
25 µm	30.4 ± 23.6

Table 5.1: The average size of a hundred graphite flakes measured using 'Image J' from captured SEM images.

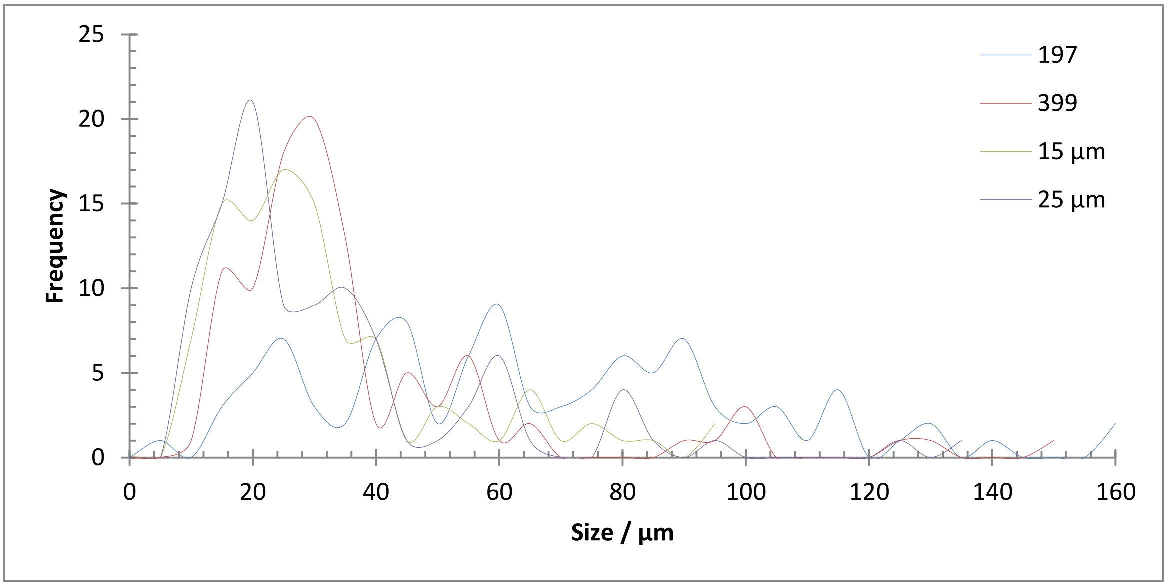

Figure 5.2: Distribution curves of the flake sizes created from the measurement of a hundred different flakes in each of the starting graphite grades. BIN size: 5 µm.

Raman Spectroscopy

Figure 5.3 shows typical Raman spectra for the materials**,** with the key data, including 2D peak position, in **Table 5.2**. The composition of all four samples is graphite, as shown by the characteristic D, G, and 2D Raman bands. These occur in all sp^2 materials, although for graphite these appear at ~ 1330 cm^{-1}, ~ 1580 cm^{-1}, and ~ 2680 cm^{-1}, for the D, G, and 2D bands respectively. Additional peaks, including the D' peak which appears at 1620 cm^{-1} in all spectra, are not considered for the characterisation.

The previously exfoliated (xGnP) graphite has a higher I_D/I_G ratio, likely due to defects induced during their exfoliation. The 2D band of the natural graphite grades 197 and 399 contain a small shoulder, commonly associated with multi-layer graphite. However the previously exfoliated materials show a broadening of the 2D peak, which is common for turbostratic graphite. The I_{2D}/I_G ratio can also give an indication of the extent of exfoliation. As expected, for the initial graphite before exfoliation, the I_{2D}/I_G ratio is small. Finally the 2D peak position can indicate if graphene is present in the material. All the 2D peaks appear at ~ 2685 cm^{-1}, which again indicates only graphite is present in the material.

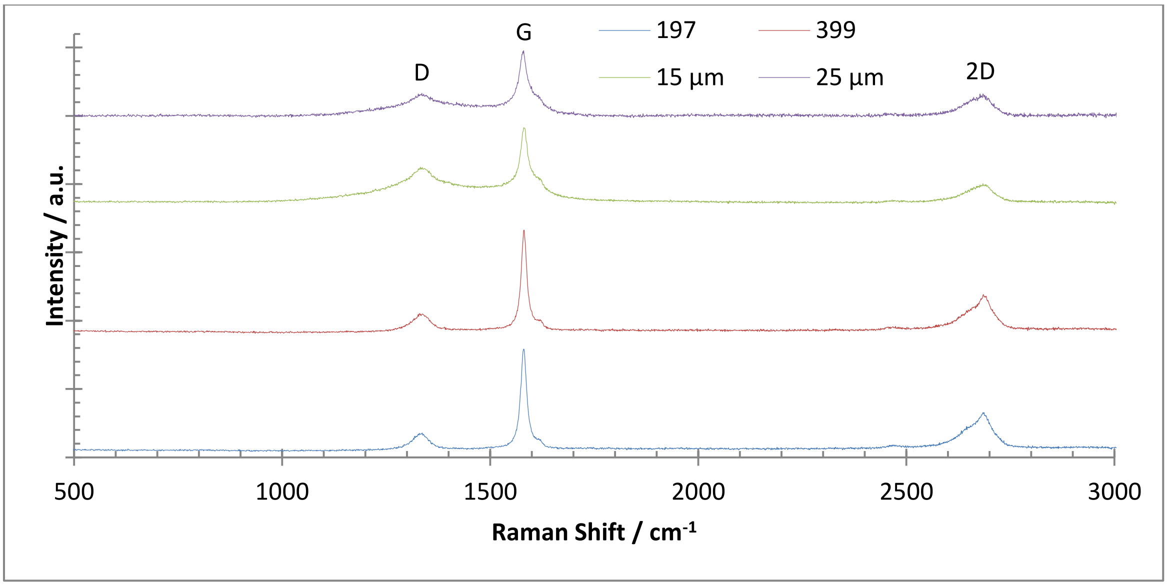

Figure 5.3: Example Raman spectra of starting graphite grades, 197, 399, 15 µm, and 25 µm. They all show the three graphite peaks which appear at ~ 1330 cm^{-1}, ~ 1580 cm^{-1}, and ~ 2680 cm^{-1}.

Sample	I_D/I_G	I_{2D}/I_G	2D Peak Position / cm^{-1}	2D Peak Width / cm^{-1}
197	0.12	0.36	2687.2 ± 2.8	51.6 ± 11.7
399	0.13	0.37	2685.0 ± 2.6	60.6 ± 15.0
15 µm	0.62	0.18	2689.6 ± 1.5	97.7 ± 45.9
25 µm	0.25	0.23	2689.9 ± 0.9	65.6 ± 29.5

Table 5.2: Key Raman spectral data of starting graphite, which could be used to identify the presence of graphene.

X-Ray Diffraction

Figure 5.4 shows XRD patterns for all four graphite grades with the resultant peak data in **Table 5.3**. All four graphite powder exhibit the characteristic peak of the 00.2 plane in hexagonal graphite at ~ 2θ = 26 °. This d-spacing of ~ 3.35 Å for all of the samples is comparable to the literature value for the interlayer distance of graphite.[215] (Care was taken to ensure that sample depth was the same in the tests, as graphite is a soft X-ray scattered and hence depth could affect data such as this.)

Both of the previously exfoliated graphite samples have a smaller d-spacing than the natural graphite. The FWHM of the exfoliated graphite is also larger than the natural graphite, indicating the presence of smaller particles, confirmed by SEM.

Using the Scherrer (**Equation 14**) equation the crystallite size can be calculated.

$$L = \frac{k\lambda}{\beta cos\theta}$$ **Equation 14**

where L is the crystallite size in nm, k is the orientation factor taken as 0.89, λ is the copper X-ray wavelength (0.1541 nm), β is the FWHM of the peak ~ 2θ = 26 °, and ϑ is the Bragg angle in °.[216] For these initial graphite samples, the crystallite size was calculated as 2.0 nm, 2.2 nm, 1.4 nm, and 1.9 nm for the 197, 399, 15 µm, and 25µm graphite respectively. The natural graphite has larger sizes, as they have not been previously exfoliated.

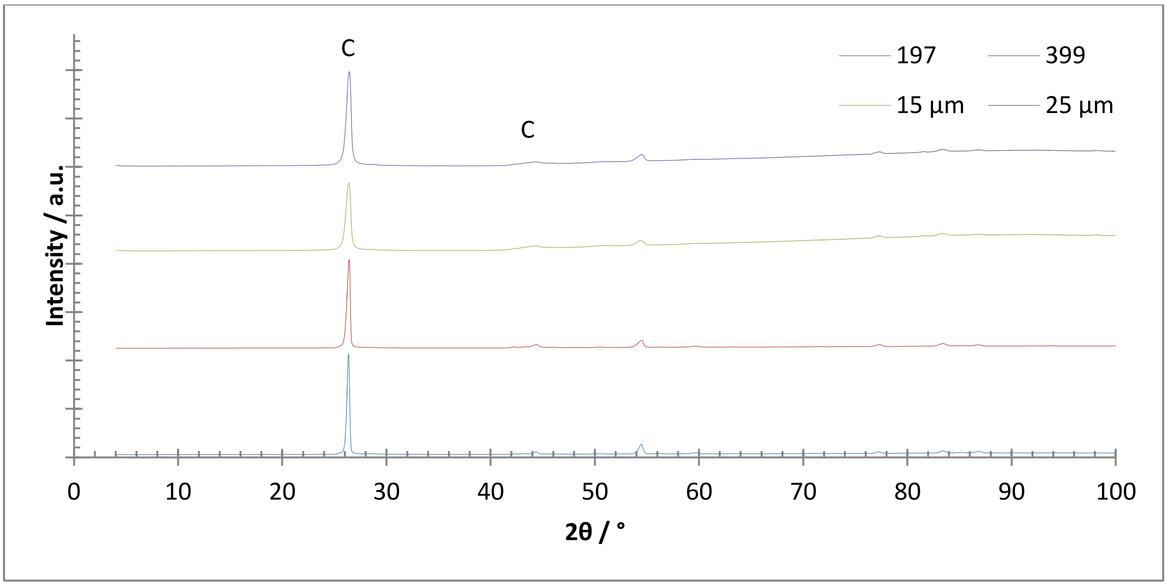

Figure 5.4: XRD patterns of staring graphite grades, all showing the characteristic graphite peaks, particularly the 00.2 peak at 2θ = 26° and 00.4 peak at 2θ = 44°. The xGnP spectra had to be manipulated due to the small intensity of the peaks, by multiplying the values by a factor of two.

Sample	2θ / °	d-spacing / Å	FWHM / °
197	26.46 ± 0.10	3.37 ± 0.03	0.28 ± 0.02
399	26.50 ± 0.06	3.36 ± 0.01	0.31 ± 0.02
15 µm	26.53 ± 0.05	3.36 ± 0.00	0.58 ± 0.07
25 µm	26.55 ± 0.03	3.36 ± 0.02	0.47 ± 0.02

Table 5.3: A table showing the 00.2 peak position and FWHM in the XRD pattern of the four starting graphite grades, with the corresponding d-spacing.

Thermal Gravimetric Analysis

TGA was used to probe the functionalities and impurities of graphite. **Figure 5.5** shows the TGA spectra of the starting graphite grades conducted in an air atmosphere, with key data given in **Table 5.4.** During heating an initial mass loss can happen due to adsorbed water species on the surface of the graphite but this was not observed for these samples.

The GNP graphite had two oxidation processes, one at ~ 350 °C and another at ~ 520 °C, while the natural flakes had just one at a higher temperature of ~ 590 °C. The first mass loss in the previously exfoliated material is likely due to the retention of intercalation compounds from the exfoliation process or the removal of oxidative species on the surface. The oxidation process at ~ 550 °C, which occurs in all graphite grades, is due to the burning of the graphitic regions in the graphite. The lower oxidation temperature for this process in the previously exfoliated graphite is due to the higher surface area of the material causing a quicker decomposition.

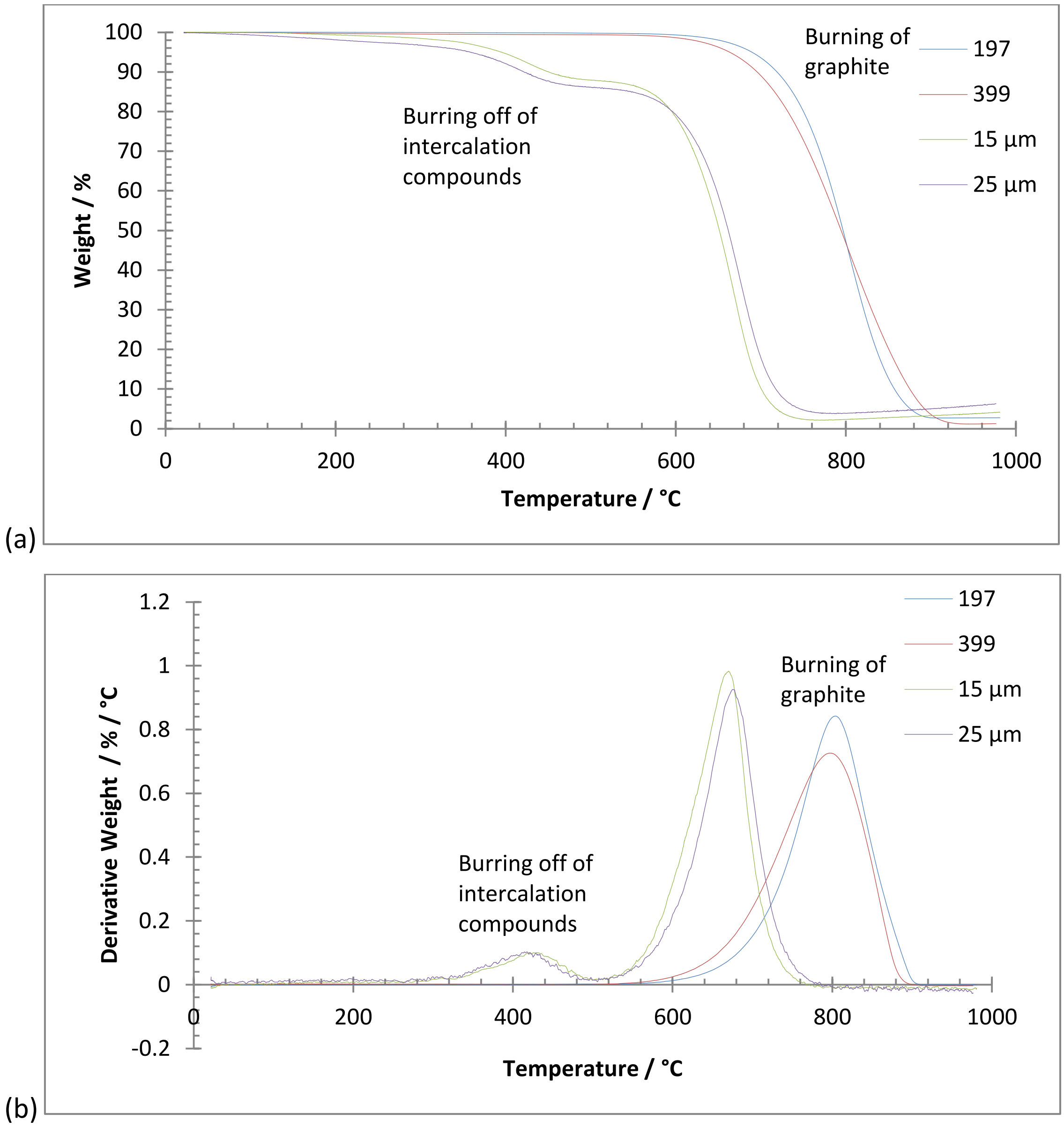

Figure 5.5: Thermal decomposition profiles for the starting graphite grades in air from room temperature to 1000 °C. (a) the weight-loss curve; and (b) the derivative (temperature) weight-loss curve.

Sample	Onset Temp. / °C	Peak Temp. / °C	Final Temp. / °C	End Weight / %
197	588.6 ± 18.7	806.7 ± 3.2	904.0 ± 1.0	3.4 ± 1.0
399	589.2 ± 22.5	810.7 ± 9.3	930.2 ± 23.9	1.1 ± 0.2
15 µm	516.4 ± 6.9	666.3 ± 7.9	768.8 ± 10.0	4.0 ± 0.2
25 µm	524.9 ± 3.8	679.0 ± 3.6	790.0 ± 11.4	5.9 ± 0.8

Table 5.4: Data obtained from the TGA spectra for the larger mass loss that occurs at ~ 550 °C in all graphite grades.

Infra-Red Spectroscopy

Figure 5.6 shows the infra-red spectra for the initial graphite grades. The graphite has very little to no oxygen content and consist of totally C=C double bonds in the hexagonal lattice. Residual oxygen from the atmosphere can partially oxidise graphite, which appears weakly at 1600 cm^{-1}, however this is overshadowed by the presence of the aromatic C=C bond at 1650 cm^{-1} (stretch). The band which appears at 2900 cm^{-1} is due to =C-H (stretch). It is partially overshadowed by the broad peak at 3300 cm^{-1}, which is due to the KBr, which is unavoidable as it readily acquires oxygen from the air. The =C-H bond can be seen again weakly at 800 cm^{-1}.

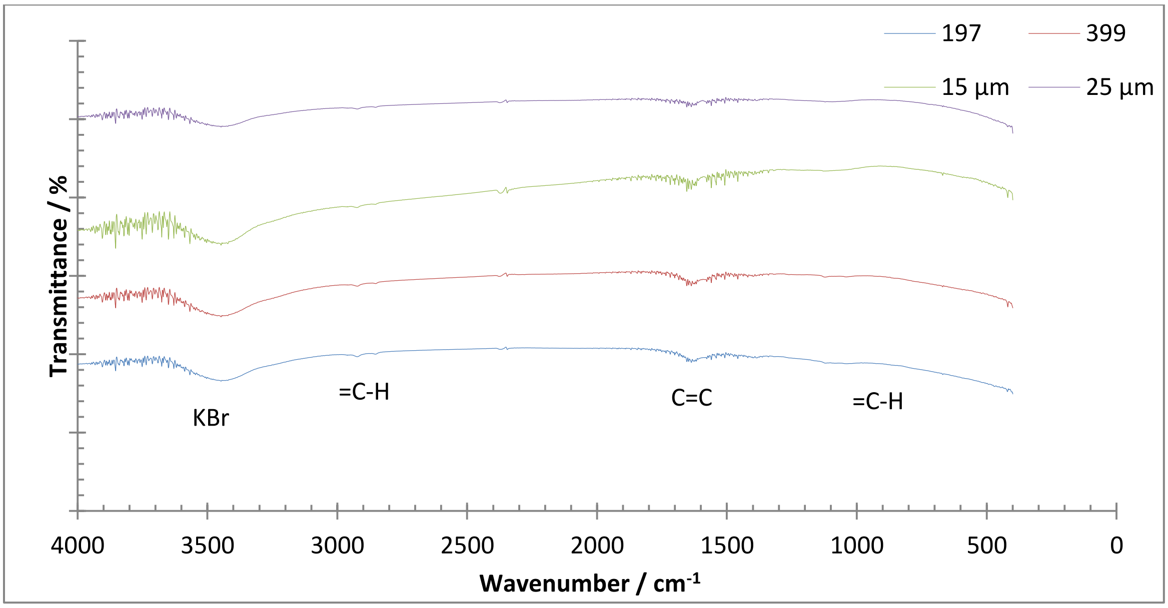

Figure 5.6: FTIR spectra of the initial graphite grades showing peaks which conform to the aromatic nature of graphite.

Summary

All of the initial materials have been characterised as graphite. The natural graphite is ordered and pristine shown by all the characterisation techniques. SEM, Raman, and XRD reveal the previously exfoliated graphite is crumpled, turbostratic, and has amorphous content. The TGA and FTIR reveal no significant functionality, though the TGA shows intercalated material is still present in the graphite. These starting materials, which have been fully characterised as graphite, will form a good base for future comparisons after they have been completely electrochemically exfoliated.

5.1.2 Electrochemical Exfoliation of the Pellet Electrode

The same conditions were used for all the pellet electrode experiments. In this method the graphite was first pressed into a pellet and directly attached to a power supply. The pellet was then electrochemically exfoliated in electrolyte, washed, and oven dried.

It was observed that as the exfoliation process was repeated, filtering took much longer. This is due to smaller particulates in the material, which can inhibit the pores of the filter paper, slowing down the filtering process. The pore size of the grade 1 filter papers was 11 µm, which is indicative of the exfoliated material. During exfoliation the pellet would fall into the electrolyte within the first 20 minutes of exfoliation, suggesting rapid intercalation. During exfoliation the electrolyte would occasionally degrade, shown by a change in colour. This was likely due to the deterioration of the pellet, with the high potentials applied degrading the solvent. The voltages applied (10 V) were far outside the potential window of DMSO (+1 to -4 V).[217]

Scanning Electron Microscopy

Figure 5.8 shows representative SEM images of the 5x pellet exfoliated product from all four graphite sources. These flakes had been through a cycle of five exfoliation steps including washing and cleaning. The lateral dimensions of the particles were calculated (**Table 5.5**) with distribution curves plotted (**Figure 5.7**).

After exfoliation the Graphexel 197 graphite has reduced in size compared to the starting material, while all other exfoliated samples have remained a similar size. The Graphexel 197 graphite starting material was the largest of the samples at ~ 60 µm in size and has reduced to ~ 30 µm. As the others graphite samples have remained at a similar size as their starting material, this suggests that the upper limit for flakes size in this exfoliation process is approximately 30 µm. The size distribution curves show that all exfoliated graphite samples have a diverse range of differently sized particles present, with the 15 µm graphite having the smallest range. This shows that the exfoliation has not fully exfoliated larger flakes. All graphite material is beam stable; however the graphite is no longer conductive, with a gold coating needed to reduce charging during imaging. This may be due to the presence of electrolyte, which inhibits the conductive exfoliated graphite.

The strict rectangular shape of the natural graphite is no longer present, with now a more diverse range of shapes. These are formed from aggregation of the smaller sized graphite sheets caused by the presence of retained electrolyte which binds the graphite particles together. Small pieces of graphitic material, similar to the ones found on the un-exfoliated natural graphite appear in all samples now. These are the products of exfoliation, where the electrolyte has successfully broken apart the graphitic sheets. The exfoliated 15 µm graphite retains its thin crumpled nature.

Sample	Average size of the starting graphite / µm	Average size of the 5x exfoliated graphite / µm
197 x5 (P)	63.0 ± 33.5	32.6 ± 18.8
399 x5 (P)	35.0 ± 25.6	33.8 ± 29.5
15 µm x5 (P)	14.5 ± 11.1	15.1 ± 10.4
25 µm x5 (P)	30.4 ± 23.6	32.2 ± 25.9

Table 5.5: Average size of the initial and 5x exfoliated graphite samples synthesised form the electrochemical exfoliation of graphite using the pellet method.

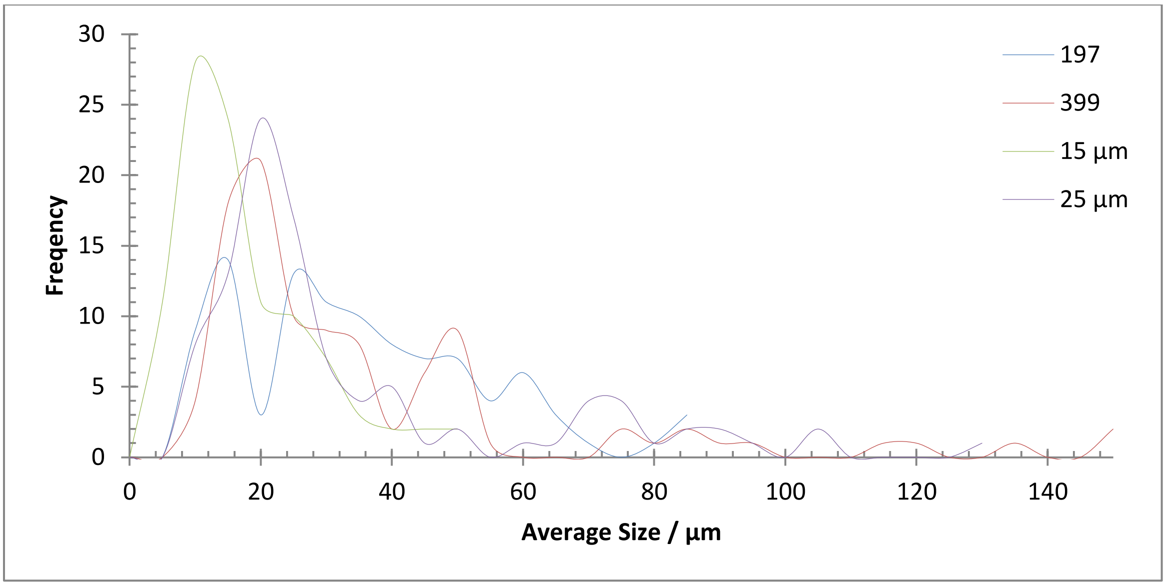

Figure 5.7: Distribution curves for the 5x electrochemically exfoliated graphite by the pellet method. BIN size: 5 µm.

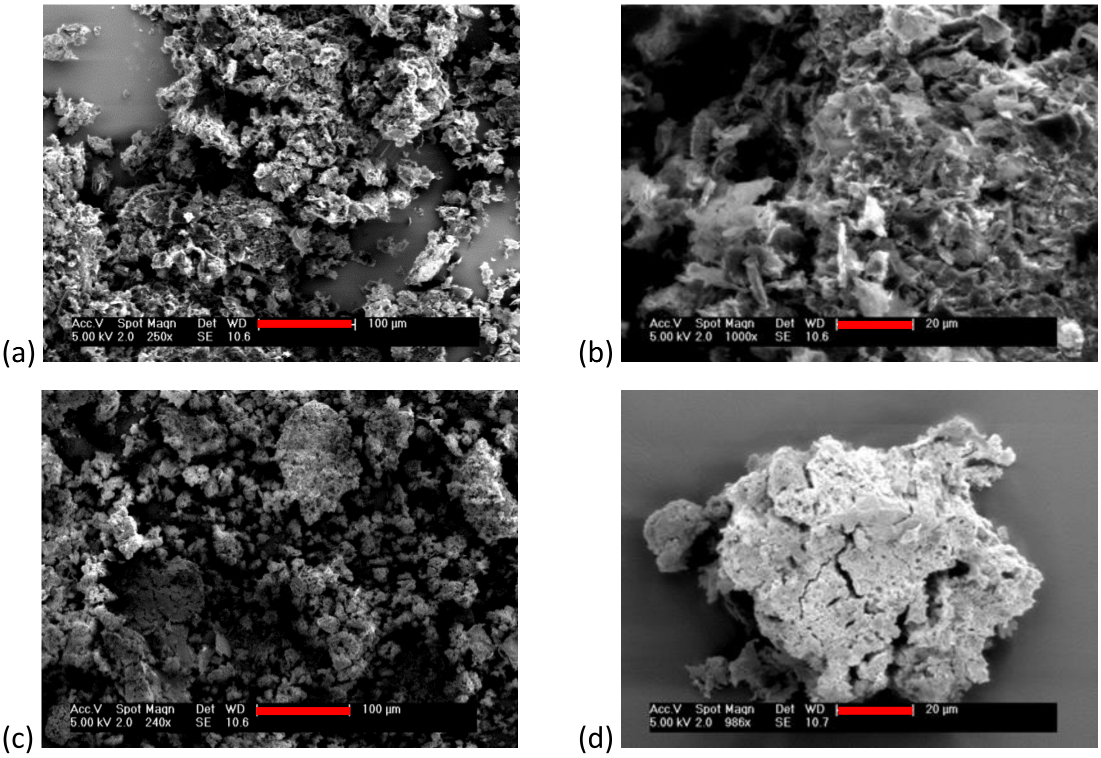

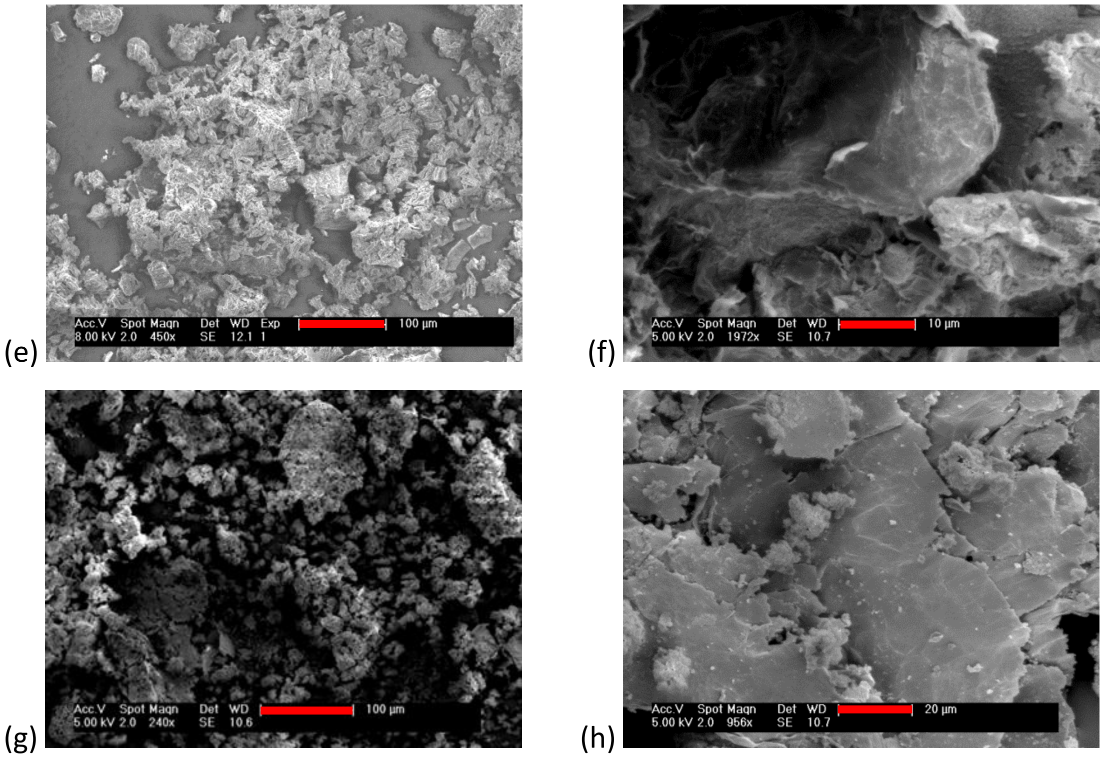

Figure 5.8: Typical SEM images of the 5x electrochemically exfoliated graphite by the pellet method. (a-b) 197; (c-d) 399; (e-f) 15 µm; and (g-h) 25 µm 5x pellet exfoliated graphite. Error bars: (a, c, e, g) 100 µm; (b, d, h) 20 µm; (f) 10 µm.

Raman Spectroscopy

Figure 5.9 shows the Raman spectra of the 5x electrochemically exfoliated graphite, with **Figure 5.10** showing the change in the position of the 2D band. A shift towards a lower wavenumber can be interpreted as better exfoliation, due to the reduction in the thickness of the graphite. The I_{2D}/I_G ratio can also be examined as can also determine the extent of exfoliation. A larger 2D peak will indicate graphene-like material.[188]

The Raman data (**Table 5.6** and **Figure 5.11**) shows a shift in the 2D band to a lower wavenumber for all graphite samples over the progression of exfoliation. However the extent to what these could be considered monolayer to FLG differ. The 2D band of the 197 material shows the smallest difference from the starting material. This is likely due to incomplete exfoliation of the large graphite flakes. The 2D band of the 15 µm graphite is the only one to undergo a large Raman shift and increase in I_{2D}/I_G. This indicated the 15 µm material underwent the most exfoliation. Both the 399 and 25 µm graphite have a

2D band shifted to a significantly lower wavelength. However the presence of graphene cannot be ascertained due to the low I_{2D}/I_G. Each material has a large variation in the 2D peak position. This suggests not all the material was exfoliated. This is expected of the pellet electrode as the graphite falls into the electrolyte quickly giving uneven exfoliation. The exfoliated Graphexel 197 graphite shows a significant increase in the I_D/I_G, while the others remain similar. This is likely due to the drastic reduction in size, which increases the number of defect edges. A large fluorescence from electrolyte impurities also increases the height of the D peak, contributing to the increase in the I_D/I_G.

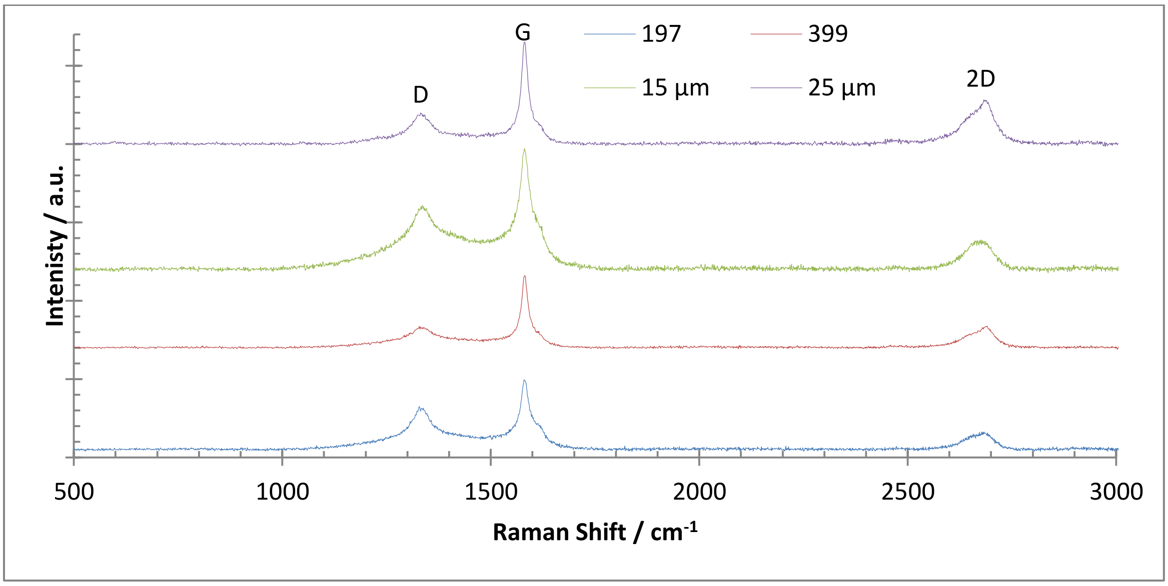

Figure 5.9: Example Raman spectra for the 5x exfoliated graphite using the pellet method.

Sample	I_D/I_G	I_{2D}/I_G	2D Peak Position / cm^{-1}	2D Peak Width / cm^{-1}
197 x5 (P)	0.44	0.36	2683.51 ± 7.06	51.43 ± 30.00
399 x5 (P)	0.14	0.33	2674.87 ± 13.76	56.29 ± 22.88
15 µm x5 (P)	0.47	0.28	2676.47 ± 6.92	81.27 ± 16.59
25 µm x5 (P)	0.23	0.35	2676.38 ± 4.38	76.78 ± 9.87

Table 5.6: The important Raman data for the 5x electrochemically exfoliated graphite from the pellet method, which could be used to identify the presence of graphene.

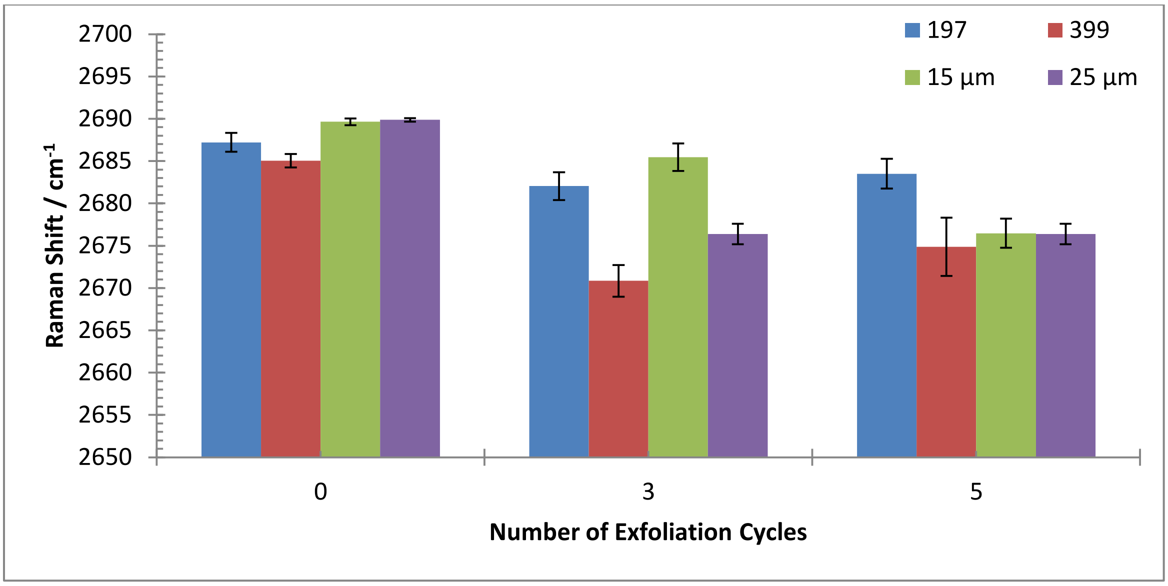

Figure 5.10: The progression of the 2D peak position after subsequent exfoliation cycles by the pellet method. Error bars are calculated using the deviation from the mean, which is calculated from the standard deviation divided by the square root of the sample size (20).

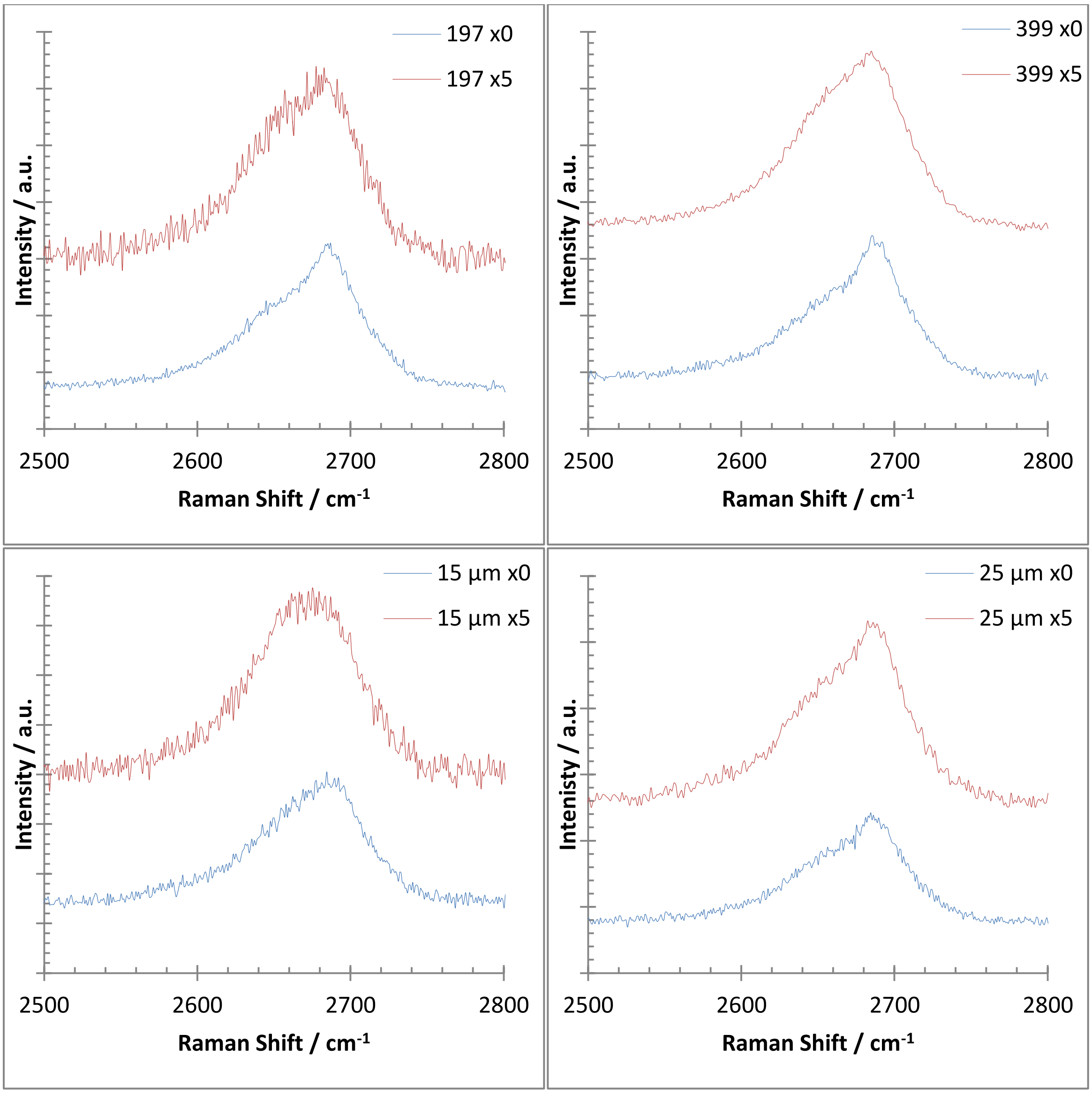

Figure 5.11: A selection of Raman spectra (with a special focus on the 2D band) for the initial and 5x electrochemically exfoliated graphite by the pellet method.

X-Ray Diffraction

Figure 5.12 show the XRD patterns of the pellet exfoliated graphite, with the values in **Table 5.7**. The peaks were checked against standards, with anomalous peaks verified.

The d-spacing is what you would expect from the graphite; however the d-spacing has reduced in size from initial graphite used. The likely cause is a step in the cycle of electrochemical exfoliation using the pellet method requires the compression of the material at 1 tonne of pressure. This could cause the material to re-stack and the d-spacing to shrink. The 197 and 15 µm graphite had little to no other functionalities (peaks) as shown in the XRD pattern, while the 399 and 25 µm graphite contained some impurities. These were confirmed against standards as the electrolyte solution, particularly Li, and LiOH. The peaks even appear even after extensive washing, suggesting they are intercalated into the graphitic sheets in the graphite. The standard deviation for previously exfoliated graphite increases after the pellet exfoliation, suggesting there is a high amount of different thickness graphite in the exfoliated material.

The crystallite size was calculated using the Scherrer equation, which gave values of 2.6 nm, 3.7 nm, 1.7 nm, and 2.2 nm for the pellet exfoliated 197, 399, 15 µm, and 25µm graphite respectively. The crystallite size for all samples has increased from the initial graphite. This is likely due to aggregation and the loss of very small graphite particulates which were present in the initial graphite.

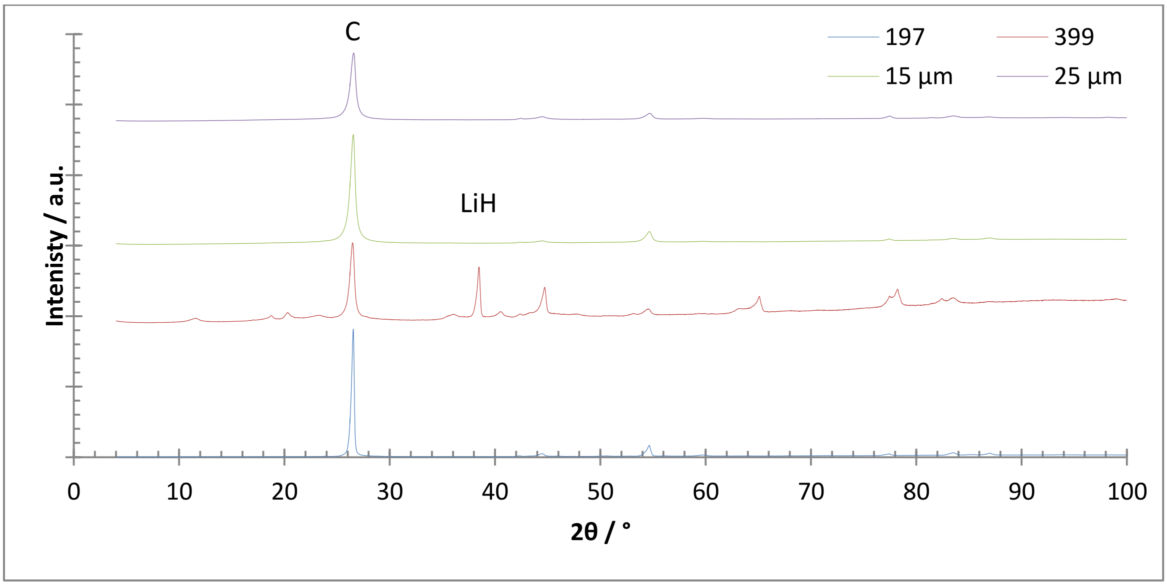

Figure 5.12: XRD patterns for the 5x electrochemically exfoliated graphite by the pellet method. Note: to make the size of the peaks comparable, the 197 spectra values were divided by 4, while the 399 values were multiplied by 5.

Sample	2θ / °	d-spacing / Å	FWHM / °
197 x5 (P)	26.52 ± 0.01	3.36 ± 0.00	0.29 ± 0.09
399 x5 (P)	26.58 ± 0.08	3.35 ± 0.01	0.30 ± 0.05
15 µm x5 (P)	26.50 ± 0.17	3.35 ± 0.00	0.40 ± 0.05
25 µm x5 (P)	26.47 ± 0.19	3.34 ± 0.02	0.26 ± 0.05

Table 5.7: The analytical data derived from the XRD patterns for the 5x electrochemically pellet exfoliated.

Thermal Gravimetric Analysis

Figure 5.13 shows the TGA spectra of the pellet exfoliated graphite, with the thermal decomposition data in **Table 5.8**. The TGA spectra for the pellet electrochemically exfoliated graphite reveal that for three of the four graphite samples electrolyte residue remains even after extensive washing. This is shown by the multiple points of increased thermal decomposition, which occur at ~ 150 °C, ~ 250 °C, and ~ 320 °C. The 399 graphite appears to be mostly clean, with only one full decomposition profile, which is contrary to the XRD pattern, where it was seen the 197 and 15 µm graphite did not contain anomalous peaks. The major weight loss found in the initial graphite samples starts ~ 550 °C for all samples due to the burring of the graphitic regions in the graphite. For the 15 µm graphite this occurs earlier, suggesting the graphite is thinner and thus more exfoliated than the other exfoliated graphite materials. This is due to the reduced vdW interactions compared to the initial powder, which lowers the thermal stability. The final weight of the exfoliated graphite varies wildly, from ~ 5 % for the 399 and 15 µm graphite, to ~ 40 % for the 197 and 25 µm graphite. In air the carbon will combust, with very little remaining. This left weight is from electrolyte impurities. For instance, the boiling points of Lithium, Lithium Oxide, and Lithium Hydride are all over 1000 °C, meaning they will all remain after the thermal analysis, contributing to the final weight.

(a)

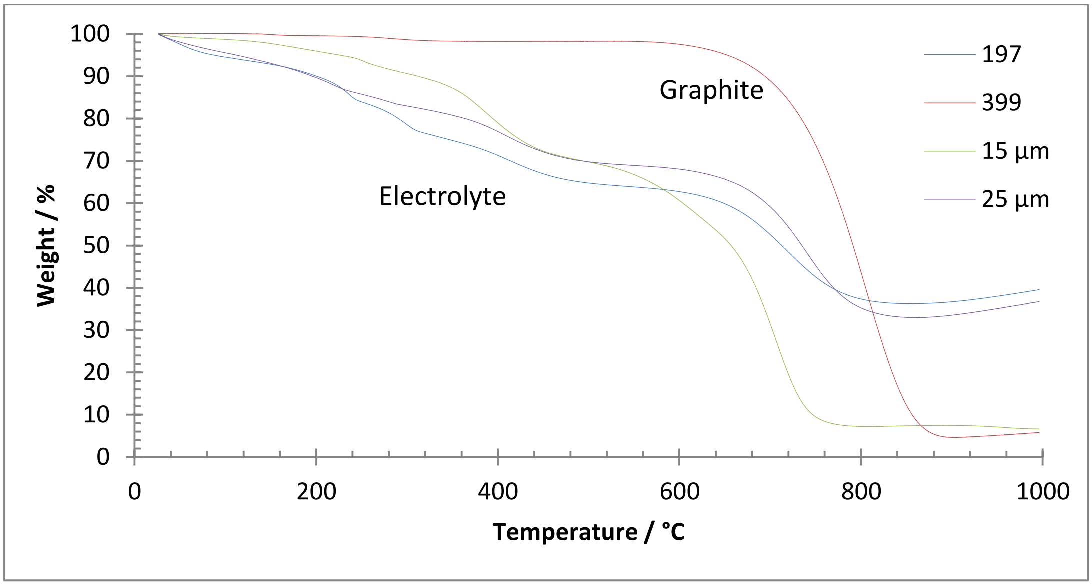

(b)

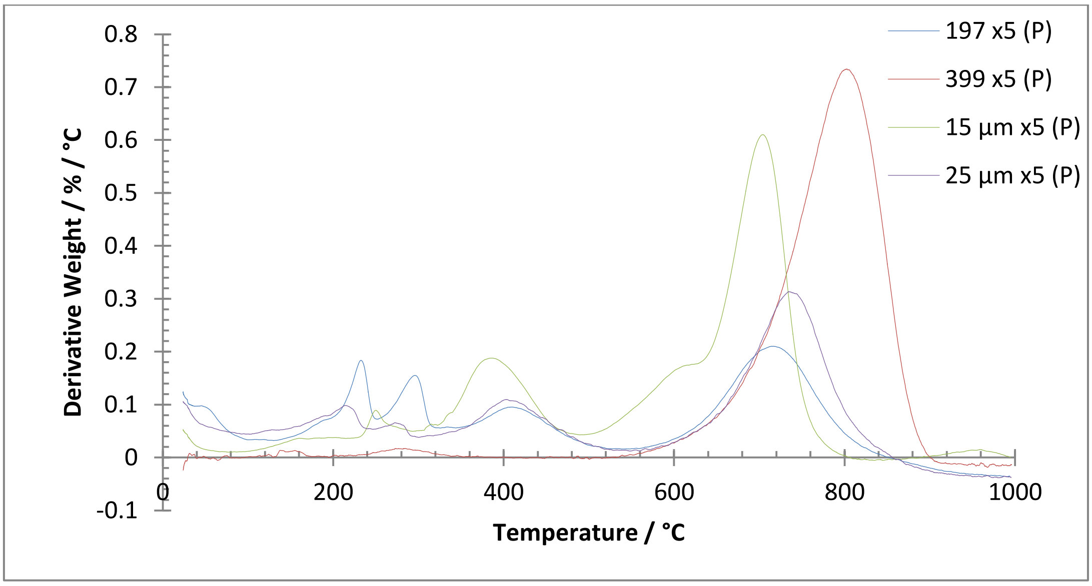

Figure 5.13: TGA spectra of the 5x electrochemically exfoliated graphite by the pellet methods up to 1000 °C in an air atmosphere. (a) the weight-loss curve; and (b) the derivative (temperature) weight-loss curve.

Sample	Onset Temperature / °C	Peak Temperature / °C	Final Temperature / °C	Final Weight / %
197 x5 (P)	561.6 ± 1.3	720.9 ± 5.2	909.2 ± 0.8	40.0 ± 0.8
399 x5 (P)	547.1 ± 6.4	806.4 ± 7.8	903.8 ± 3.9	6.1 ± 0.4
15 µm x5 (P)	507.9 ± 2.6	706.3 ± 2.6	810.0 ± 7.7	5.8 ± 1.3
25 µm x5 (P)	573.4 ± 2.6	739.1 ± 5.2	890.1 ± 10.3	35.2 ± 2.9

Table 5.8: Thermal decomposition data for the 5x electrochemical exfoliated graphite via the pellet method.

FTIR

Figure 5.14 is the FTIR spectra of the 5x exfoliated graphite by the pellet method. The FTIR spectrum shows marginal additional functionality with new peaks appearing at ~ 1100 cm^{-1} due to amine C-N (stretch). This appears due to the addition of electrolyte, which was also observed in the XRD and TGA spectra. Again the 25 µm graphite appears to have retained the highest amount of electrolyte due to the stronger transmission peaks. In all of the electrochemically exfoliated material by the pellet method, peaks were observed at 1635 cm^{-1} which is an aromatic C=C bond (stretch), 2900 cm^{-1} due to =C-H (stretch), and 800 cm^{-1} due to =C-H bond (stretch).

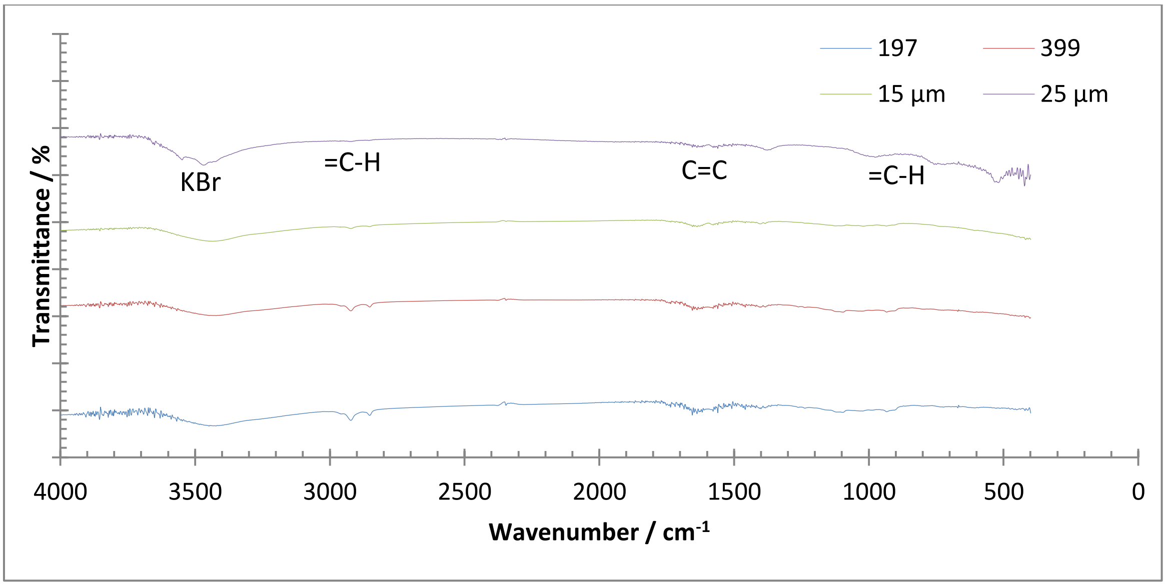

Figure 5.14: FTIR spectra for the 5x electrochemically exfoliated graphite via the pellet method.

Yield

The yield of the graphene formation was estimated using all the analysis techniques, with a particular emphasis on Raman spectroscopy. The presence of graphene material < 10 layers thick was chosen as graphite that has been successfully exfoliated, due to the properties of the material being graphene-like. Twenty Raman spectra were analysed on various areas of different graphitic particles. The 2D peak width, position, and shape all contribute towards graphene identification. For instance, if 10 out of the 20 Raman spectra are determined to include < 10 layer graphene, then the yield would be 50 %. **Table 5.9** shows the estimation of the yield for graphene synthesis by the electrochemical methods.

From this sample it can be estimated that the 399 and 15 µm performed best. These have the largest shift in the 2D band. Most of the material after 5 exfoliations was graphite, while 20 % of the material had a 2D which had significantly shifted to a lower wavelength.

Sample	< 10 layer graphene for the starting material / %	< 10 layer graphene after 3 exfoliations / %	< 10 layer graphene after 5 exfoliations / %
197 x5 (P)	0 ± 0	0 ± 0	0 ± 0
399 x5 (P)	0 ± 0	20 ± 5	20 ± 10
15 µm x5 (P)	0 ± 0	0 ± 0	20 ± 5
25 µm x5 (P)	0 ± 0	20 ± 5	20 ± 5

Table 5.9: Estimation of the % formation of graphene-like material from the pellet exfoliation of 4 different graphite grades.

Summary

The pellet method successfully exfoliates graphite, though the yield of graphene still remains low. SEM shows that continuous exfoliation cycles have not reduced the size of the graphene flakes for all starting graphite samples bar the Graphexel 197. This is not indicative of exfoliation, as the intercalation and exfoliation of graphite should result in the reduction of graphite flake size. The Raman analysis shows that the 2D peak of the graphite has shifted for all graphite samples bar the Graphexel 197 (from 2685 cm^{-1} to 2675 cm^{-1}). However a large amount of the analysed exfoliated graphite remains as pure graphite. This is compounded by the large deviation of error for the samples, which shows much was not exfoliated. XRD shows the 399 graphite has multiple impurities from the lithium in the electrolyte, while all FTIR and TGA spectra show impurities from the electrolyte. It was noticed that the pellet quickly fell into the electrolyte. This poor exfoliation means less electrolyte will intercalate into the pellet, resulting in less exfoliation.

5.1.3 Electrochemical Exfoliation of the Aluminium Cage Electrode

A second electrochemical exfoliation method was employed to compare the two methods. The electrolyte and initial graphite grades used were kept the same; however the graphite was placed in an aluminium cage which was connected to the power supply. The material was not pressed, nor heated.

Again it was observed that after each exfoliation process the vacuum filtering became slower than the previous cycle due to the formation of nanomaterials. Long exfoliation times resulted in the aluminium breaking apart into solution, with a slight amount of aluminium in the product, even with acid washing. However, the electrolyte did not degrade. White solids often formed on the aluminium, indicating products other than graphene.

Scanning Electron Microscopy

SEM showed that the material has reduced in size, which is indicative of exfoliation, as the sheets are broken and forced apart (**Figure 5.15**)**.** Fewer particulates from the electrolyte are present, and there is no charging on the surface, showing the material is a good electrical conductor. **Table 5.10** shows the sizes of the 5x exfoliated graphite measured using ‘Image J’, with distribution graphs shown in **Figure 5.16**.

All graphite grades have reduced dramatically in size, which is indicative of exfoliation, with the 15 µm graphite reducing the furthest to the smallest particle sizes. The 197 graphite reduced the least compared to the other graphite samples, and this may be due to its larger starting size, which inhibits the exfoliation of the graphite. This is different to the pellet electrode where only the 197 graphite reduced in size while the other graphite grades remained the same size. The size distribution of all the aluminium exfoliated graphite grades is smaller than the pellet exfoliated graphite suggesting a better exfoliation also.

The morphology of the aluminium exfoliated natural graphite retains the rectangular shapes, with additional torn edges, suggesting exfoliation. There is an increased presence of graphitic debris, which was present in the starting material. This also suggests exfoliation. The previously exfoliated 15 and 25 µm graphite have fewer crumpled areas, however there is graphitic debris in the powders as a result of exfoliation. The 15 µm graphite previously had very thin transparent edges; however the exfoliated graphite does not. This could suggest some form of re-stacking. Additionally there is some contamination due to retained electrolyte present.

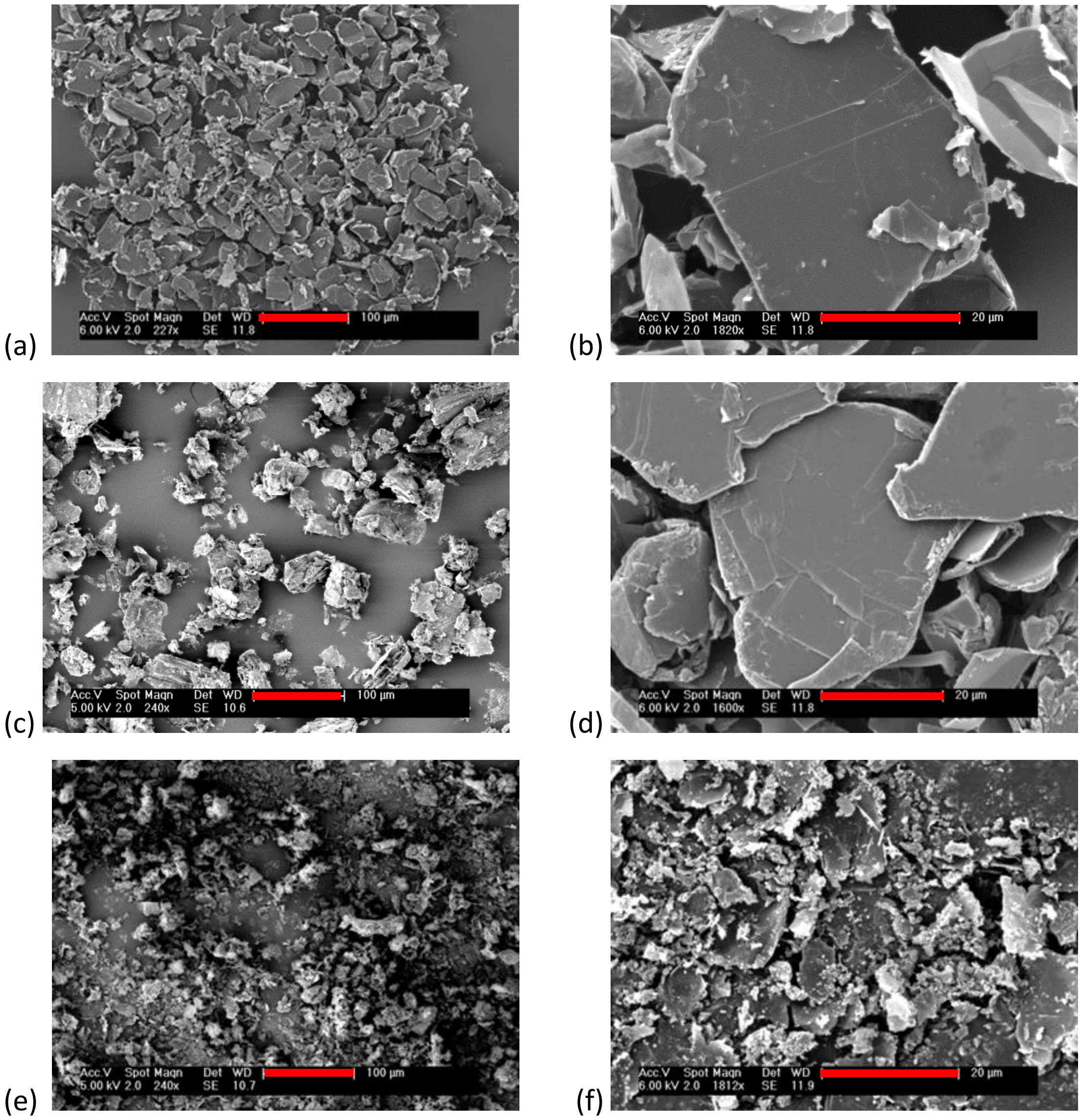

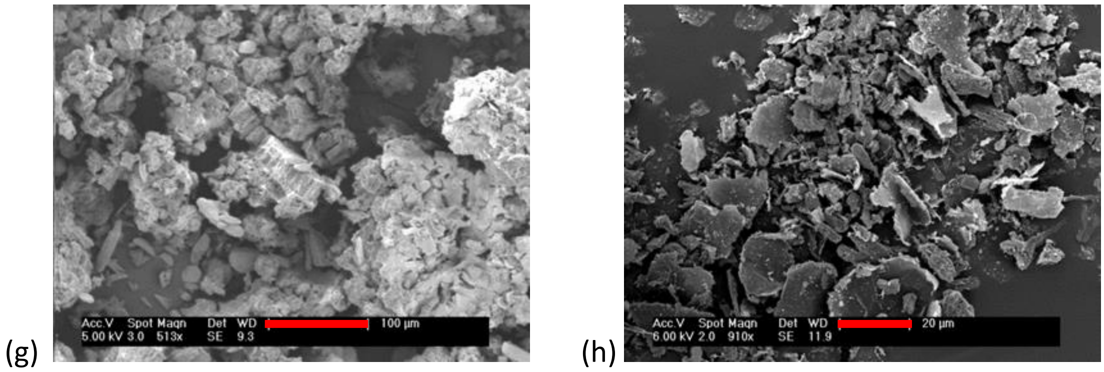

Figure 5.15: Typical SEM images of the 5x electrochemically exfoliated graphite by the aluminium cage. (a-b) 197; (c-d) 399; (e-f) 15 µm; and (g-h) 25 µm 5x aluminium cage exfoliated graphite. Error bars: (a, c, e, g) 100 µm; (b, d, f, h) 20 µm.

Sample	Average size of the starting graphite / µm	Average size of the 5 x exfoliated graphite / µm
197 x5 (A)	63.0 ± 33.5	46.4 ± 36.6
399 x5 (A)	35.0 ± 25.6	16.8 ± 9.9
15 µm x5 (A)	14.5 ± 11.1	8.7 ± 5.7
25 µm x5 (A)	30.4 ± 23.6	11.4 ± 6.8

Table 5.10: Average size across 100 particles for the 5x electrochemically exfoliated graphite by the aluminium cage method.

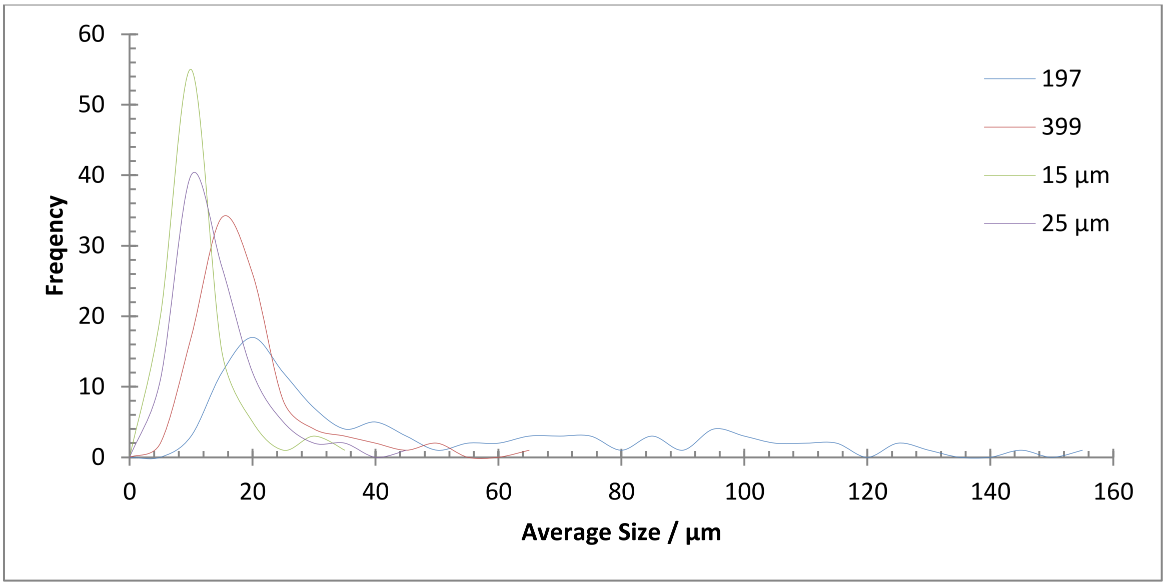

Figure 5.16: Distribution Curves for x5 electrochemically exfoliated graphite material by the aluminium cage method. These were measured using 'Image J' on captured SEM images. Bin size: 5 µm.

Raman Spectroscopy

The exfoliated materials were analysed after each exfoliation by Raman spectroscopy. **Figure 5.17** shows the Raman spectra of the 5x electrochemically exfoliated material, (data in **Table 5.11**), with **Figure 5.19** and **Figure 5.18** showing the evolution of the Raman 2D peak over the course of multiple aluminium cage exfoliation cycles.

These graphs indicate that there are a range of graphite flake thicknesses in each exfoliation cycle by the large error bars. However, in general the peak shifted to a lower wavenumber, with graphite 399 and 15 µm having the largest shift. This exfoliation down to < 10 graphitic layers suggests the formation of FLG and not monolayer graphene, as the 2D peak did not shift to below 2660 cm^{-1}. An increase in the I_D/I_G ratio also indicates smaller flakes in the graphite material upon exfoliation, which is confirmed with SEM. The width and height of the 2D peak is also a measure of exfoliation. The I_{2D}/I_G increased for most of the exfoliated graphite grades, while the width of the 2D peak increases for the 197, 399, and 25 µm exfoliated graphite, while reduces for the 15 µm graphite. As more graphitic layers are stacked the 2D band gains more components, due to electron band effects (the interaction of the π and π* bands) on successive graphitic sheets.[198] Raman peaks also broaden due to disorder. During exfoliation the flakes reduce in size, which also introduces more disorder (as when analysis is performed there will be more defect edges in the laser spot size than with larger flakes), which in turn increases the Raman peak width.

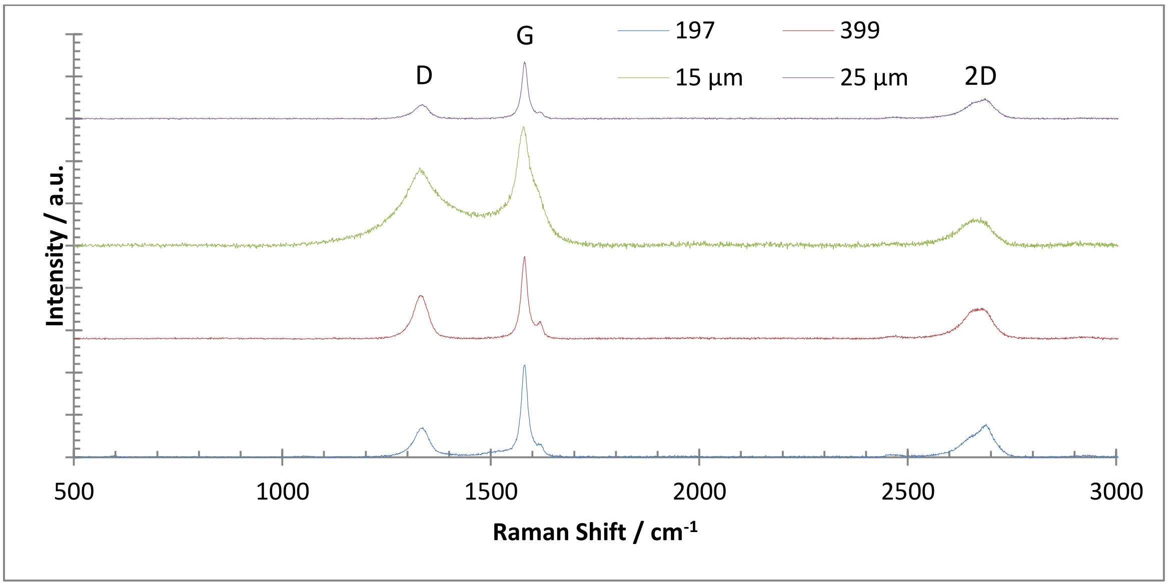

Figure 5.17: Raman spectra for the 5x electrochemically exfoliated graphite by the aluminium cage method.

Sample	I_D/I_G	I_{2D}/I_G	2D Peak Position / cm^{-1}	2D Peak Width / cm^{-1}
197 x5 (A)	0.25	0.25	2671.5 ± 9.4	74.9 ± 9.3
399 x5 (A)	0.60	0.39	2668.2 ± 4.9	75.9 ± 14.8
15 µm x5 (A)	0.90	0.24	2670.6 ± 9.3	87.5 ± 11.4
25 µm x5 (A)	0.31	0.30	2675.3 ± 8.1	73.0 ± 13.6

Table 5.11: Table of quantitative data for the electrochemical exfoliation of graphite using the aluminium cage electrode method.

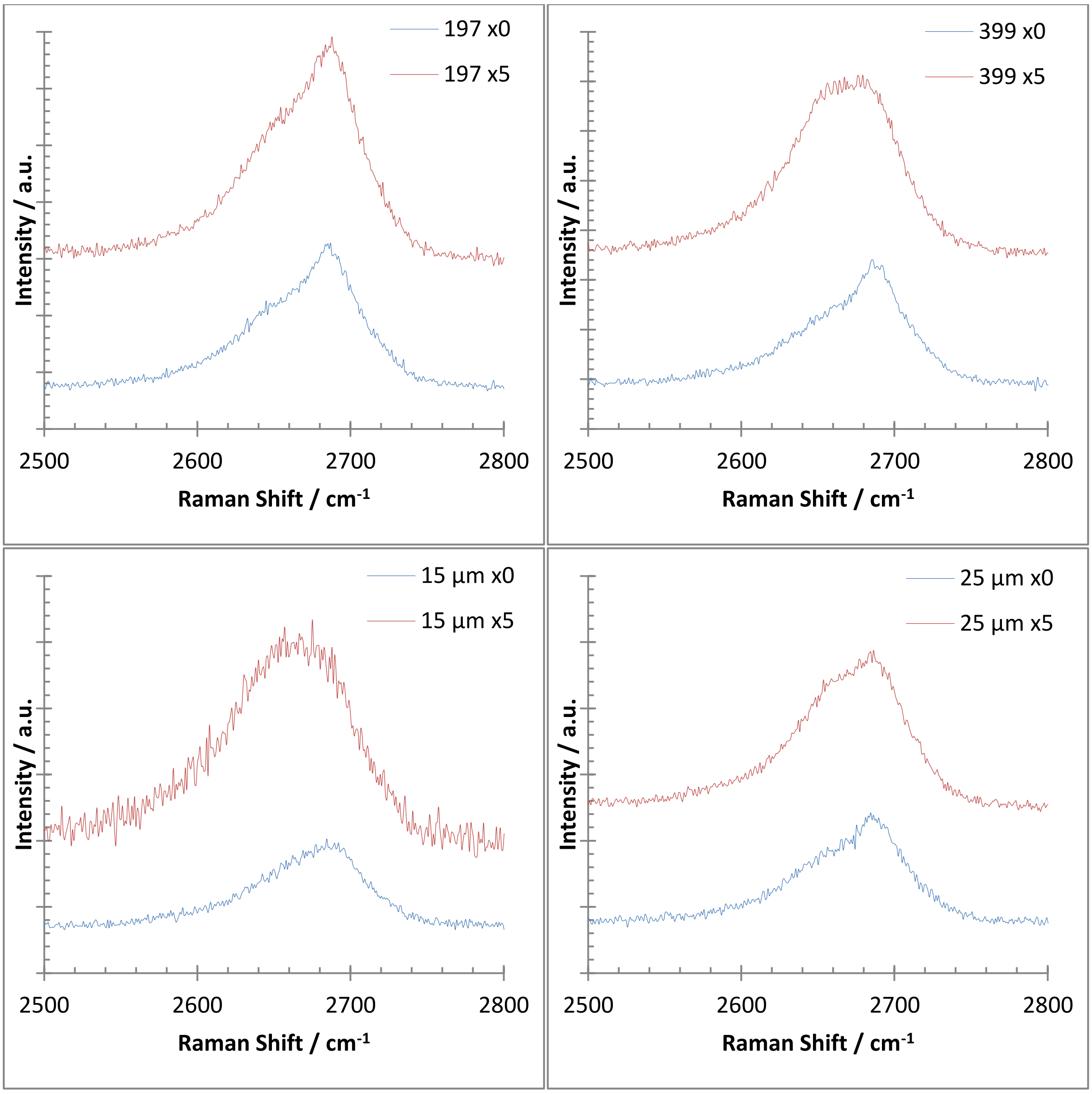

Figure 5.18: A selection of Raman spectra (with a special focus on the 2D band) for the initial and 5x electrochemically exfoliated graphite by the aluminium cage method.

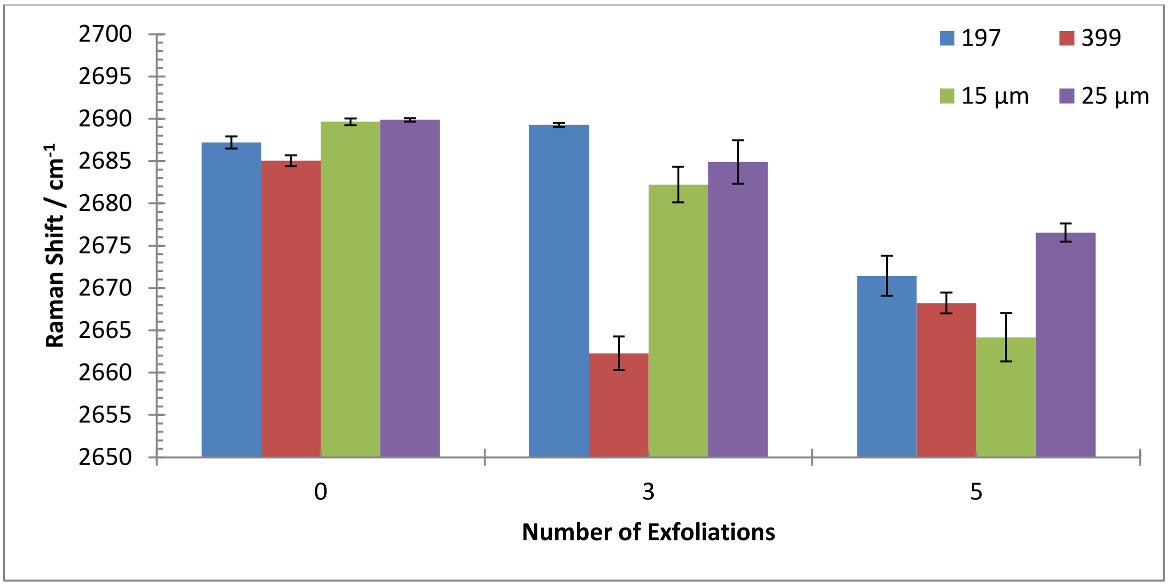

Figure 5.19: Position of the 2D peak in the Raman spectrum for progressively exfoliated graphite by the aluminium cage method.

X-Ray Diffraction

XRD pattern (**Figure 5.20**) and data (**Table 5.12**) show the d-spacing of each material was comparable to the starting materials.

The 197 and 399 material showed the least impurities compared to the previously exfoliated material. This is shown by the relatively pure graphite peaks in the XRD pattern. The 15 µm and 25 µm exfoliated graphite have retained the intercalation compounds after exfoliation, even after extensive washing. An increase in the number of peaks within the material can be attributed to aluminium (Al, 2θ = 38 °, 45 °, 65 °, 78 °), aluminium hydroxide ($Al(OH)_3$, 2θ = 18 °, 20 °), aluminium oxide (Al_2O_3, 2θ = 43 °, 25 °), lithium hydride (LiH, 2θ = 38 °, 45 °), among others, verified against standards. Aluminium appears due to the aluminium cage the graphite is exfoliated in. LiH impurities could be synthesised in-situ from the breakdown of lithium aluminium hydride ($LiAlH_4$, 2θ = 22 °, 38 °). White powder on the aluminium confirms the presence of $LiAlH_4$, as when it is exposed to air it breaks down into lithium hydroxide (LiOH) and aluminium hydroxide ($Al(OH)_3$). $LiAlH_4$ was most likely formed from a reaction between LiH and aluminium chloride ($AlCl_3$, 2θ = 12 °, 38 °) in solution. These are all likely to occur due to the relatively high voltages used in the electrochemical exfoliation. The crystallite size was calculated as 3.3 nm, 3.4 nm, 9.8 nm, and 6.9 nm for the 197, 399, 15 µm, and 25µm graphite respectively. The size has increased dramatically when compared to the initial graphite and pellet exfoliated graphite. This could be due to aggregation or the removal of the smaller crystallites during the exfoliation process.

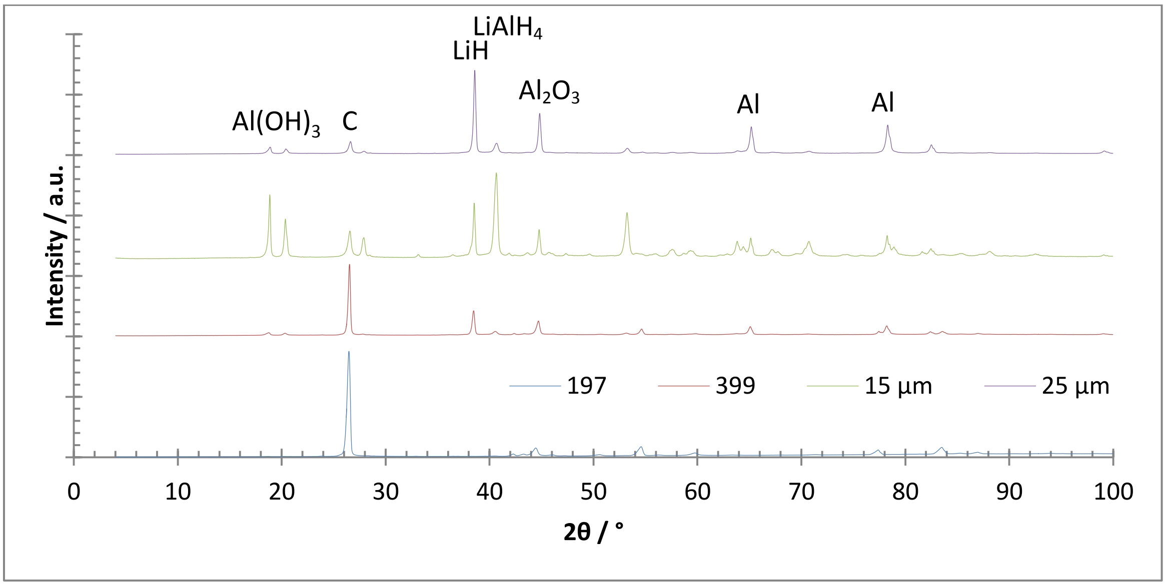

Figure 5.20: XRD pattern of the 5x electrochemically exfoliated graphite by the aluminium cage method.

Sample	2θ / °	d-spacing / Å	FWHM / °
197 x5 (A)	26.53 ± 0.02	3.36 ± 0.00	0.24 ± 0.11
399 x5 (A)	26.48 ± 0.20	3.35 ± 0.01	0.18 ± 0.07
15 µm x5 (A)	26.63 ± 0.06	3.35 ± 0.01	0.19 ± 0.09
25 µm x5 (A)	26.62 ± 0.03	3.35 ± 0.01	0.24 ± 0.02

Table 5.12: Data from the XRD results for the electrochemically exfoliated graphite by the aluminium cage method.

Thermal Gravimetric Analysis

Figure 5.21 shows the TGA curves of the materials, with the results in **Table 5.13**. TGA was performed in air to ascertain the oxidative decomposition profile of the materials.

The exfoliated 197 graphite was mostly pure with little functionality shown by the single decomposition and lower weight left after full thermal decomposition. The decomposition profile closely matches that of the original stating graphite. The 399, 15 µm, and 25 µm graphite all have a significant amounts of residue left, while also sporting multiple mass loss events. The first mass loss event is likely due to the loss of adsorbed electrolyte impurities in the graphite from the electrochemical exfoliation. In all three materials, this occurs at ~ 200 °C. The higher final weight of the material is likely due to aluminium left over which has oxidised. This would also explain the increase in weight from ~ 800 °C. Aluminium typically has an onset temperature of oxidation at ~ 600 – 800 °C, which coincides with the increase in temperature in the TGA spectra.[218] These aluminium impurities will likely make the graphene less conductive as the propagation of charge through the graphene can only truly be achieved by a percolating network. The main mass loss event which occurs ~ 600 °C is due to the burning of the graphite. The 197 graphite had the lowest starting temperature, while the 25 µm graphite had the highest. The exfoliated natural graphite products had the highest peak and final temperatures, while the exfoliated processed graphite and the lowest. This indicates a better exfoliation for the natural graphite. Graphene has a lower starting temperature for mass loss. This is in part due to the high surface area of the material. All of these are lower than the starting graphite materials, indicating some form of exfoliation. The final weight of all the exfoliated graphite materials bar the 197 graphite is very high and all curves increase in weight during heating. This may be due to left over lithium from the electrolyte and aluminium. Both of these can form oxides at high temperatures, which will add weight, and are stable under 1000 °C.

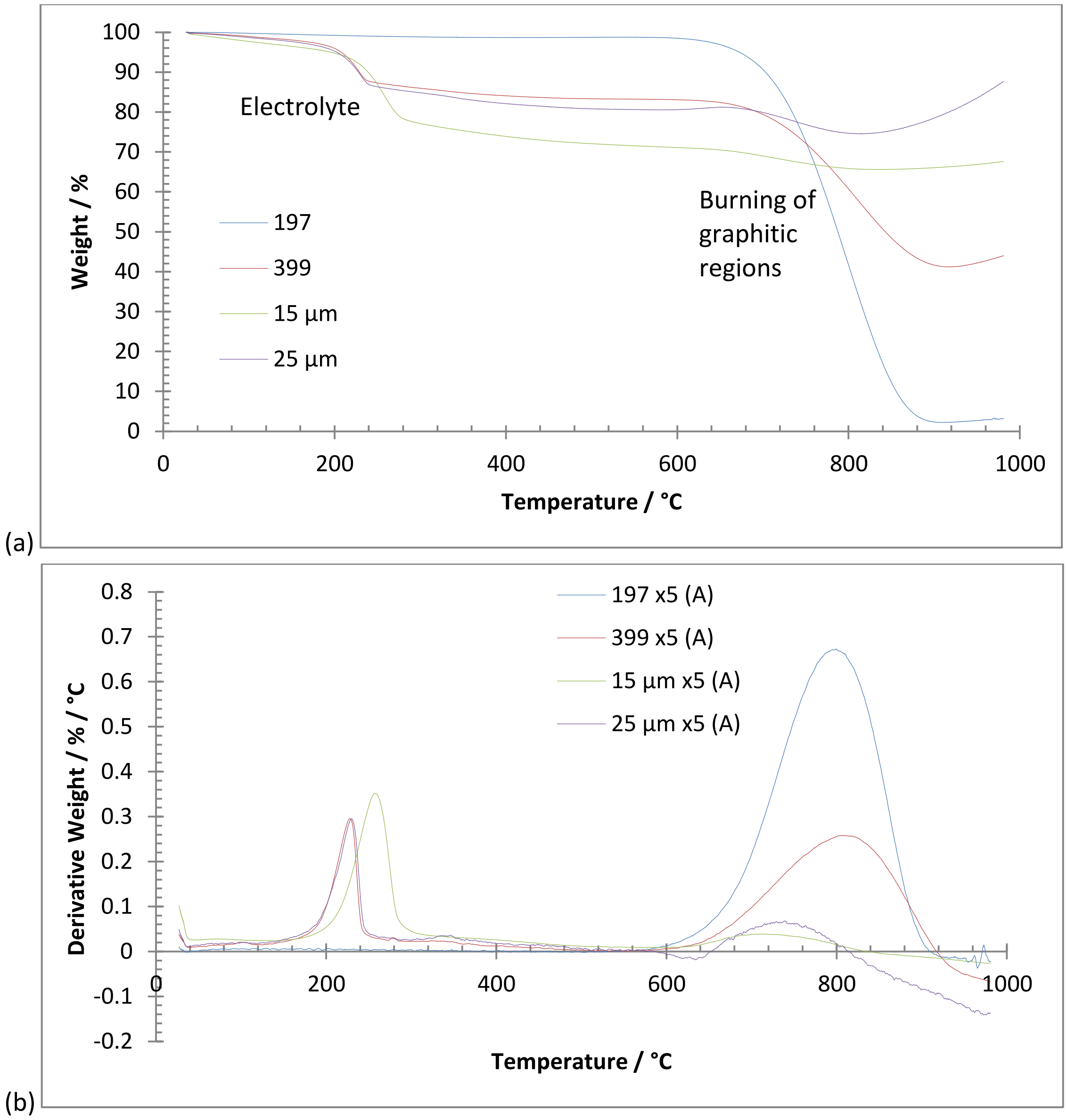

Figure 5.21: The TGA profiles in air for the 4 graphite sources which have been electrochemically exfoliated 5x by the aluminium cage method. (a) the weight-loss curve; and (b) the derivative (temperature) weight-loss curve.

Sample	Onset Temperature / °C	Peak Temperature / °C	Final Temperature / °C	Final Weight / %
197 x5 (A)	586.8 ± 16.4	798.5 ± 2.8	912.0 ± 4.8	3.7 ± 1.6
399 x5 (A)	596.2 ± 6.4	809.1 ± 1.3	947.5 ± 1.3	40.9 ± 0.6
15 µm x5 (A)	599.5 ± 21.7	716.6 ± 3.8	839.8 ± 4.6	62.7 ± 2.6
25 µm x5 (A)	638.1 ± 1.3	732.7 ± 6.4	834.6 ± 1.3	75.9 ± 1.9

Table 5.13: Table displaying TGA values for the 5x electrochemically exfoliated graphite by the aluminium cage method. Three temperatures are displayed: when the sample starts to decompose (onset); when the sample decomposes the quickest (peak); and when the sample stops decomposing (final).

Infra-Red Spectroscopy

Figure 5.22 shows the FTIR spectra for the 5x electrochemically exfoliated material. The spectra show all the classic graphitic peaks.

Peaks appear at 1635 cm^{-1} due to an aromatic C=C bond (stretch), 2900 cm^{-1} due to =C-H (stretch), and 800 cm^{-1} due to =C-H bond (stretch). Unlike the initial graphite and the pellet exfoliated graphite, many additional peaks appear in the FTIR spectrum of the aluminium cage electrochemically exfoliated graphite due to partial functionalisation of the material. The functionalisation occurs during exfoliation due to the high voltages involved and the deterioration of the aluminium cage electrode. These new peaks appear ~ 1340 cm^{-1}, ~ 944 cm^{-1}, and ~ 536 cm^{-1} and are likely due to C-N (stretch), =C-H (bend), and C-Cl (stretch) respectively.

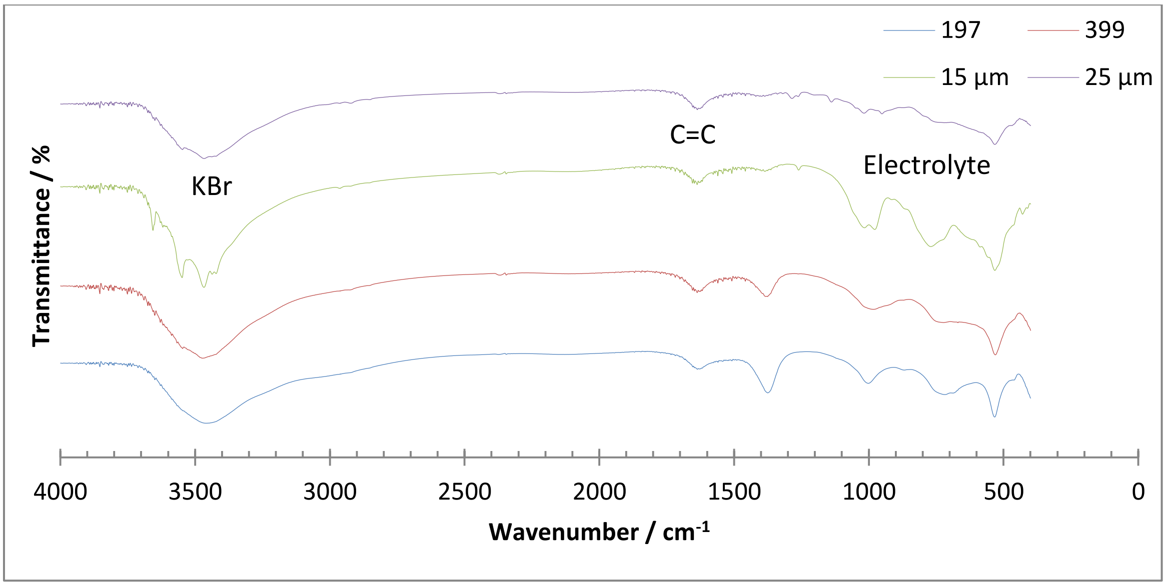

Figure 5.22: FTIR transmittance spectra of the 5x electrochemically exfoliated starting graphite by the aluminium cage method.

Yield

Raman spectroscopy, among other analysis techniques, was used to estimate the yield of the graphene formation. The definition of graphene in this case, is anything < 10 graphene layers. This is where the unique properties of graphene are available (though at a diminished rate compared to graphene) and obtainable. To do this, 20 Raman spectra were analysed with a focus on the 2D band of the graphite. The position, shape, and width of the 2D band all give an indication as to the thickness of the graphite particles. **Table 5.14** shows the results of these estimations. From the aluminium cage results, it can be estimated that the in order to obtain graphene from the starting material should be either 399 or 15 µm graphite. These 2 materials have the largest shift in the 2D band, had 2D bands with no shoulder, and had 2D bands which were thin.

Sample	< 10 layer graphene after 0 exfoliations / %	< 10 layer graphene after 3 exfoliations / %	< 10 layer graphene after 5 exfoliations / %
197 x5 (A)	0 ± 0	5 ± 0	20 ± 5
399 x5 (A)	0 ± 0	30 ± 5	25 ± 5
15 µm x5 (A)	0 ± 0	5 ± 0	30 ± 10
25 µm x5 (A)	0 ± 0	0 ± 0	20 ± 5

Table 5.14: Estimation of the % formation of graphene-like material from the aluminium cage exfoliation of 4 different graphite grades.

Summary

The aluminium cage exfoliation of the graphite gives a more pronounced exfoliation, while the material appears to be slightly functionalised, which are both due to the exfoliation method. The aluminium cage offers more points of exfoliation than the pellet method. The stability of the aluminium cage can push the exfoliation to completion, while the pellet dissolves quickly during exfoliation. Perhaps the exfoliation of the pellet electrode would have a more pronounced if it was able to be exfoliated for longer. This may also results in the same amount of functionalisation as the aluminium cage method.

All measurements and estimations of yield are of the bulk material. It is likely that dispersing the exfoliated graphite in NMP and separating the size of the particles via centrifugation, would produce a more pronounced yield of graphene. The yields obtained are higher than what can be obtained from the ultra-sonication of graphite, which has yields of ~ 1 %, after many hours of sonication. This material would also be much smaller than the material obtained from electrochemical exfoliation and contain far more defects.[45]

5.1.4 Comparison of Exfoliation Techniques in terms of Graphene Yield

Figure 5.23 shows the change in the position of the 2D band in the graphite grades after both exfoliation methods. This shows that exfoliation reduced the wavenumber position of all the graphite samples. In general the 2D peak position of the aluminium cage exfoliated graphite was reduced further than the pellet, suggesting that the aluminium cage performed better. The largest change in 2D peak is from the 15 µm and 399 aluminium cage exfoliated graphite. The 25 µm graphite performed similarly for both the pellet and aluminium cage, while the 399 graphite performed better for both exfoliation methods. These two graphite grades were originally the same size, but the 399 was more easily exfoliated. It could be due to the rigid structure of the graphite that more readily exfoliated, or the smaller graphitic particles on the surface that are more easily exfoliated.

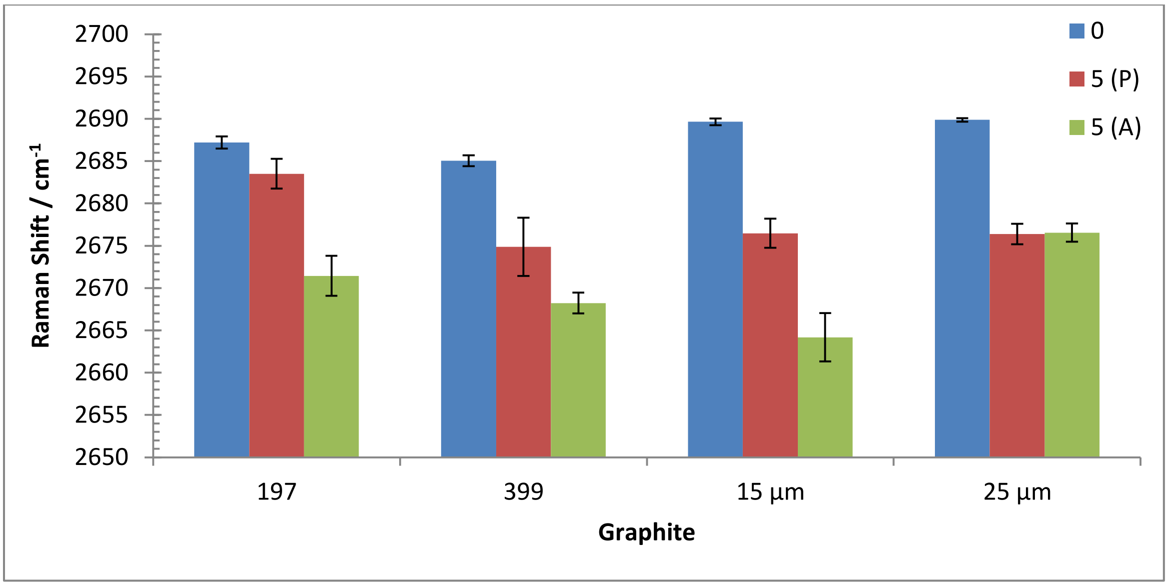

Figure 5.23: Evolution of the 2D band from the initial graphite (0) and the 5 x electrochemically exfoliated graphite by two methods, pellet (P) and aluminium cage (A).

5.2 Super-Capacitor Electrode Manufacture and Testing

In order to assess the electrochemical performance of the graphite material, the electrochemically exfoliated graphite by both electrochemical methods was deposited onto nickel foam. Given the estimated yield of < 10 layer graphite reached 30 % at best in the bulk samples produced, the larger, un-exfoliated flakes were removed prior to deposition by sedimentation. The initial graphite powders were also infiltrated as a control. This was then used directly as an electrode for electrochemical tests in KOH electrolyte. The characterisation of the graphite deposited onto nickel foam, as well as the electrochemical performance of these materials is shown below.

The nickel foam used was to create a porous structure to which the exfoliated graphite can bind to. The un-exfoliated graphite did not bind closely to the nickel foam and would often separate from the nickel foam upon gentle movement. The extent to which this happened in the exfoliated material was greatly reduced.

A number of solvents were used to disperse the exfoliated graphite, with the best results coming from NMP and DMF. DMF was eventually chosen as the solvent, due to the lower boiling point, making it easier to remove. Chloroform was also used due to its very low boiling point, however the surface tension compatibility between the solvent and solute was not ideal, and thus the exfoliated graphite was not dispersed well and would not adhere to the nickel foam.

Scanning Electron Microscopy

Figure 5.24 shows SEM images of the pure nickel foam, nickel foam infiltrated with un-exfoliated graphite, and nickel foam infiltrated with aluminium exfoliated graphite. While the nickel foam was found to be mostly pure, particulates do appear on the surface, likely dust from the environment. Thus prior to using the nickel foam, it was thoroughly cleaned using ethanol**.**

The incorporation of the initial graphite shows that the graphite does not bind well to the nickel foam. Even at higher concentrations while there is a lot of graphite present, very little is adhered to the surface of the nickel foam. This is likely due to the large size of the graphite flakes, which inhibits adhesion to the nickel foam. The addition of the exfoliated graphite shows it adheres well to the surface of the nickel foam, due to its smaller size.

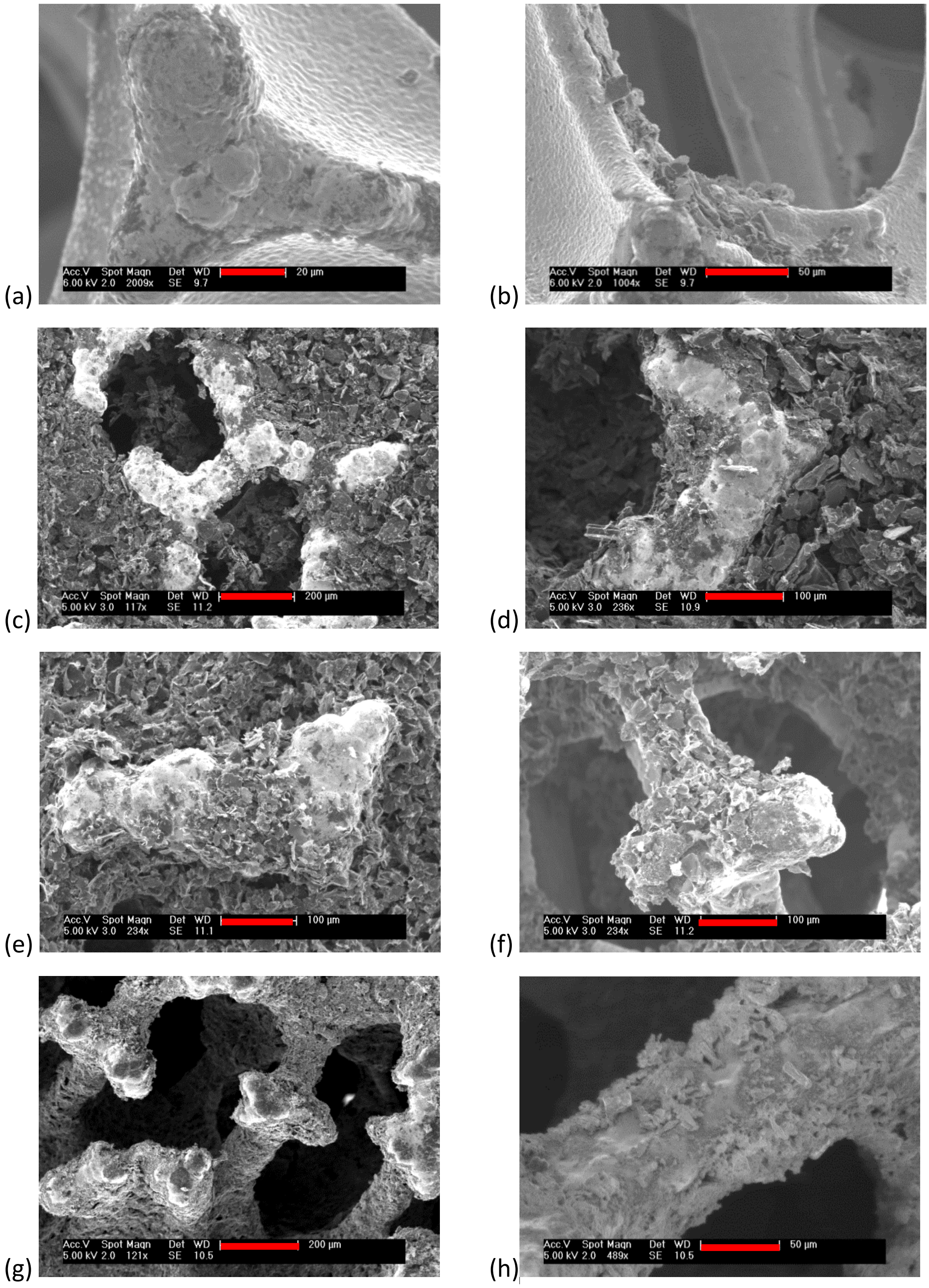
(a)
Acc.V Spot Magn Det WD 20 µm
6.00 kV 2.0 2009x SE 9.7
(b)
Acc.V Spot Magn Det WD 50 µm
6.00 kV 2.0 1004x SE 9.7
(c)
Acc.V Spot Magn Det WD 200 µm
5.00 kV 3.0 117x SE 11.2
(d)
Acc.V Spot Magn Det WD 100 µm
5.00 kV 3.0 236x SE 10.9
(e)
Acc.V Spot Magn Det WD 100 µm
5.00 kV 3.0 234x SE 11.1
(f)
Acc.V Spot Magn Det WD 100 µm
5.00 kV 3.0 234x SE 11.2
(g)
Acc.V Spot Magn Det WD 200 µm
5.00 kV 2.0 121x SE 10.5
(h)
Acc.V Spot Magn Det WD 50 µm
5.00 kV 2.0 489x SE 10.5

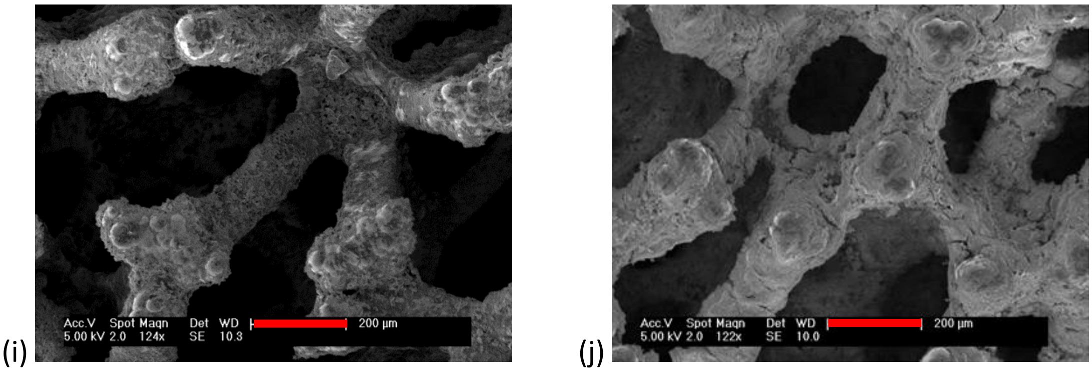
(i) (j)

Figure 5.24: SEM images of nickel foam and graphene infiltrated nickel foam. (a-b) pure nickel foam; (c-f) 197, 399, 15 µm, and 25 µm initial graphite infiltration; and (g-j) 197, 399, 15 µm, and 25 µm aluminium cage exfoliated graphite infiltration.

Raman Spectroscopy

Raman spectroscopy was performed to characterise the graphite infiltrated into the nickel foam (**Figure 5.25**). This can give an indication of the thickness of the film on the nickel electrode, by the observation of nickel peaks in the Raman spectrum. Here, no peaks can be seen suggesting a film thickness of over 3 µm (the penetration depth of the 633 nm Raman laser light). The example Raman spectrum of the exfoliated graphite shows the characteristic graphite peaks at 1333.70 ± 3.11 cm^{-1}, 1581.83 ± 0.18 cm^{-1}, and 2673.73 ± 12.51 cm^{-1}. Adding un-exfoliated graphite gave the Raman peak positions at 1335.35 ± 5.02 cm^{-1}, 1580.88 ± 2.29 cm^{-1}, and 2683.85 ± 2.80 cm^{-1}. From this we can see that the graphite retains its degree of exfoliation when added to the nickel foam.

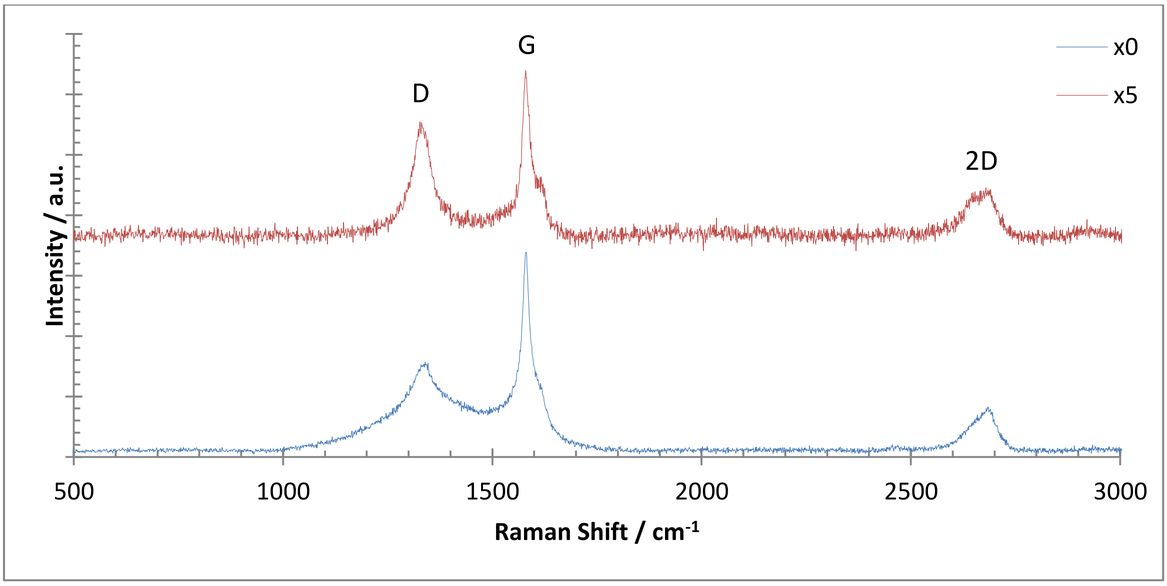

Figure 5.25: Example Raman spectra for the graphene infiltration of un-exfoliated and 5x exfoliated 25 µm graphite, showing the graphite retains its exfoliation after addition to the nickel foam.

Cyclic Voltammetry and Galvanostatic Discharge

To assess the capacitance of the materials, two methods were used, CV and galvanostatic discharge. The shapes of the curves can give an indication of the type of electrochemical behaviour the electrodes are performing.

First the electrochemical behaviour of the nickel foam electrode (**Figure 5.26a**) and the silver paint (**Figure 5.26b**) were analysed by CV. The curve shows a Redox peak ~ 0.6 V in the charging scan. This is the electrochemical formation of Ni^+ from the Ni metal. The peak at ~ 0.45 V on the discharge scan is the reverse of this reaction (Ni^+ to Ni). These redox reactions happen as the electrolyte facilitate the formation of nickel oxide. The capacitance of the nickel foam was calculated as 0.01 F g^{-1}.

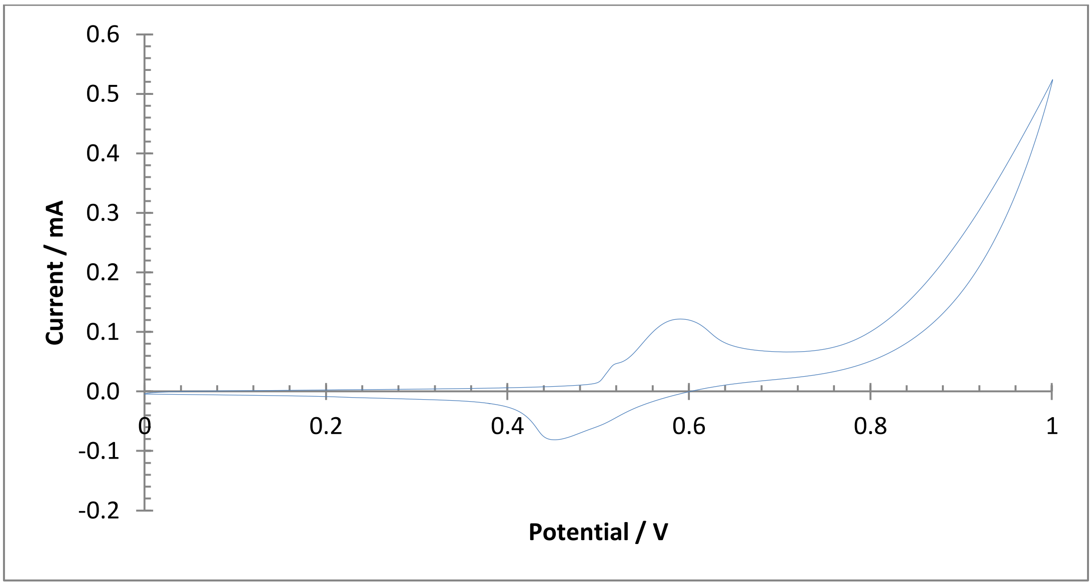

(a)

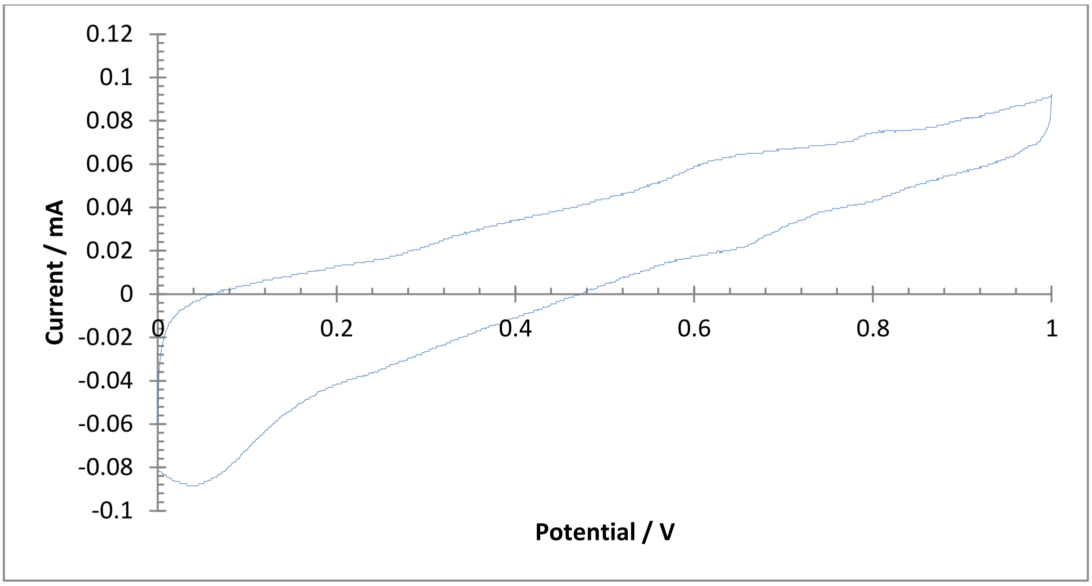

(b)

Figure 5.26: A CV curve of (a) pure nickel foam electrode; and (b) silver paint taken at 100 mV s^{-1}. No carbonaceous material has been added. The peaks confirm redox reactions are happening in the nickel foam and the silver paint.

When the (exfoliated) graphite is added to the nickel foam, the shape of the CV curve changes dramatically (**Figure 5.27** and **Figure 5.28**). The CV curve shows multiple peaks in the charge and discharge curve which are commonly due to metals changing redox states. In the CVs shown, these peaks are not due to the nickel foam, but rather the silver paint used to adhere the nickel foam to the glass slide where the connectors were placed. In the anodic (charging) sweep the first peak ~ 0.7 V can be attributed to the oxidation of Ag to Ag^+, while the second peak at ~ 0.9 V is due to the oxidation of Ag^+ to Ag^{2+}. In the cathodic (discharging) sweep, the first peak at ~ 0.85 V is due to the reduction of Ag^{2+} to Ag^+, while the second peak at ~ 0.7 V is due to Ag^+ to Ag. The peaks from nickel foam gradually diminished after successive graphite loading and are not present in the spectra below. In other curves, where the current out-performs the silver paint these peaks do not appear. However the negligible change in the curve shapes across four charge-discharge sweeps suggests stability as it is common for redox reactions to change the shape of the curve across successive scans, reducing the stability of the material. This also suggests silver paint is stable in KOH electrolyte, as typically in acidic and basic electrolytes deterioration can occur.

Other peaks present in the CV curves could possibly be due to lithium ion (Li^+) intercalation. Lithium is present in the electrolyte, and is difficult to completely remove from the graphene through washing, as seen in the seen in the XRD patterns. Li^+ can show strong CV peaks which all correspond to the formation of different intercalation stages. The CV can show cathodic CV peaks at 0.3 and 0.65 V, relating to the intercalation of the Li^+. This corresponds to the formation of stage 2 and 1 intercalation compounds (stage 1 where the graphite and intercalated layers alternate, stage 2 where two graphite layers alternate with the intercalated layer). Additionally there can be strong anodic CV peats at 0.1, 0.75, and 0.9 V, which relate to the de-interaction of Li^+. These relate to stage 1, 2 and 4 intercalation compounds (stage 4 where four graphite layers alternate with the intercalated layer).[72, 219]

The curves show a general lack of "squareness", especially when the redox peaks of the silver paint are involved. This suggests the capacitors are not perfect EDLC, but rather have some form of pseudo-capacitance too. These redox peaks are mostly prevalent in the 197 graphite and its exfoliated products, and the initial 399 graphite. The aluminium exfoliated 399 and 15 µm (especially) graphite show the most ideal EDLC shape, with a nicely shaped rectangular curve. The edges are still slightly curved though indicating moderate amounts of resistance in the material. There are no significant peaks which would be attributed to the aluminium in the CV curves of the aluminium exfoliated graphite, indicating the aluminium did not adhere to the nickel foam.

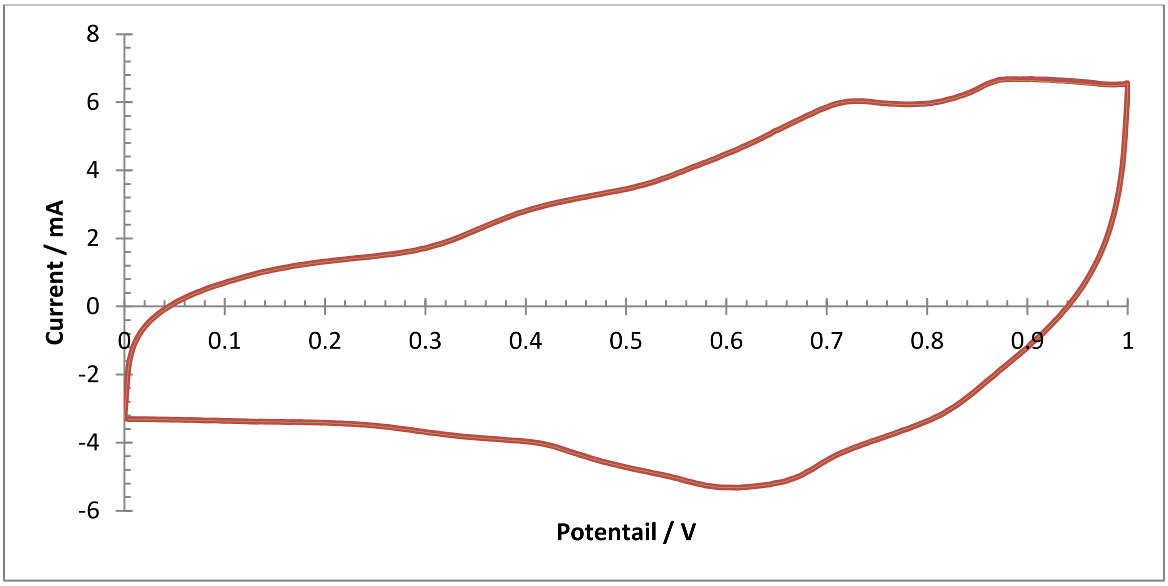

Figure 5.27: Three successive CV scans at 100 mV s^{-1} for the 5x electrochemically exfoliated graphite 197 by the aluminium cage method.

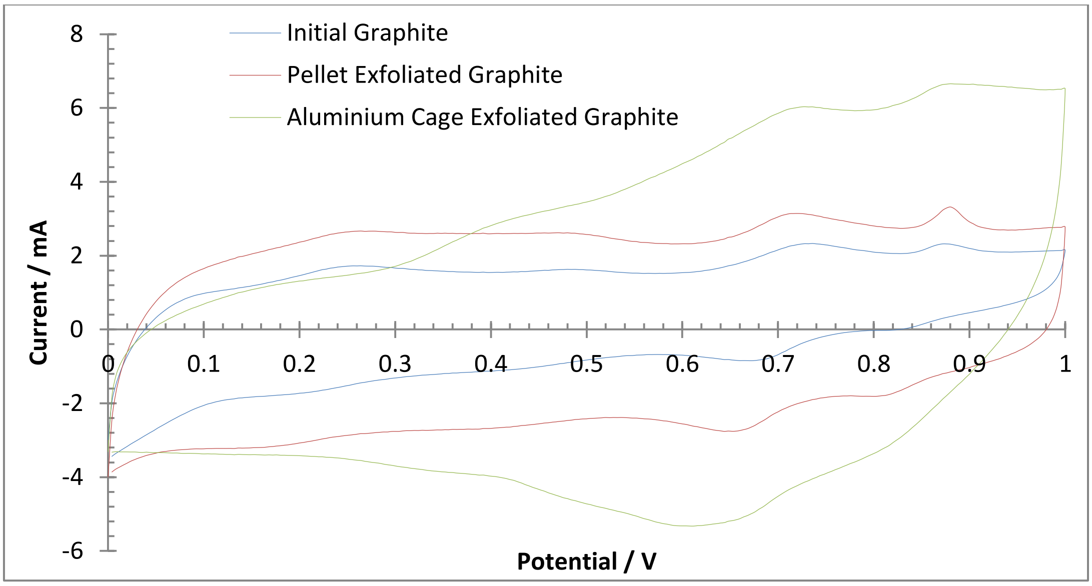

(a)

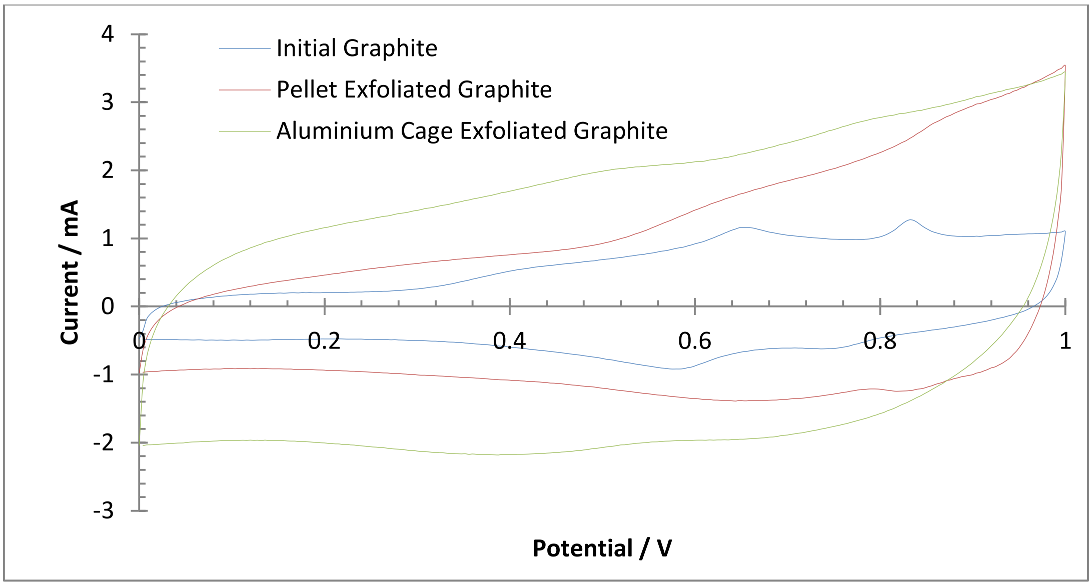
Initial Graphite
Pellet Exfoliated Graphite
Aluminium Cage Exfoliated Graphite
Current / mA
4
3
2
1
0
-1
-2
-3
0
0.2
0.4
0.6
0.8
1
Potential / V

(b)

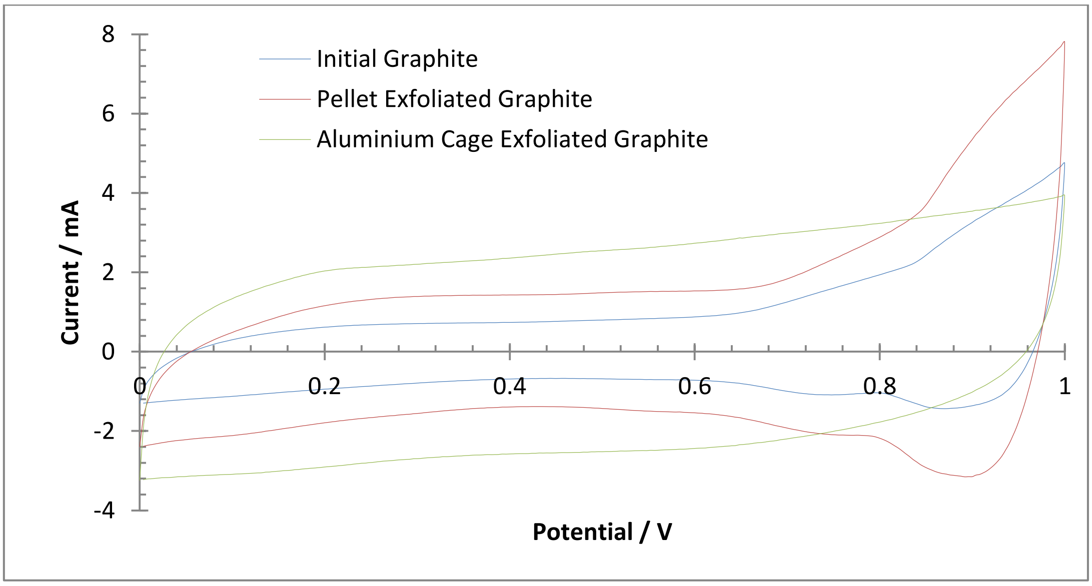
Initial Graphite
Pellet Exfoliated Graphite
Aluminium Cage Exfoliated Graphite
Current / mA
8
6
4
2
0
-2
-4
0
0.2
0.4
0.6
0.8
1
Potential / V

(c)

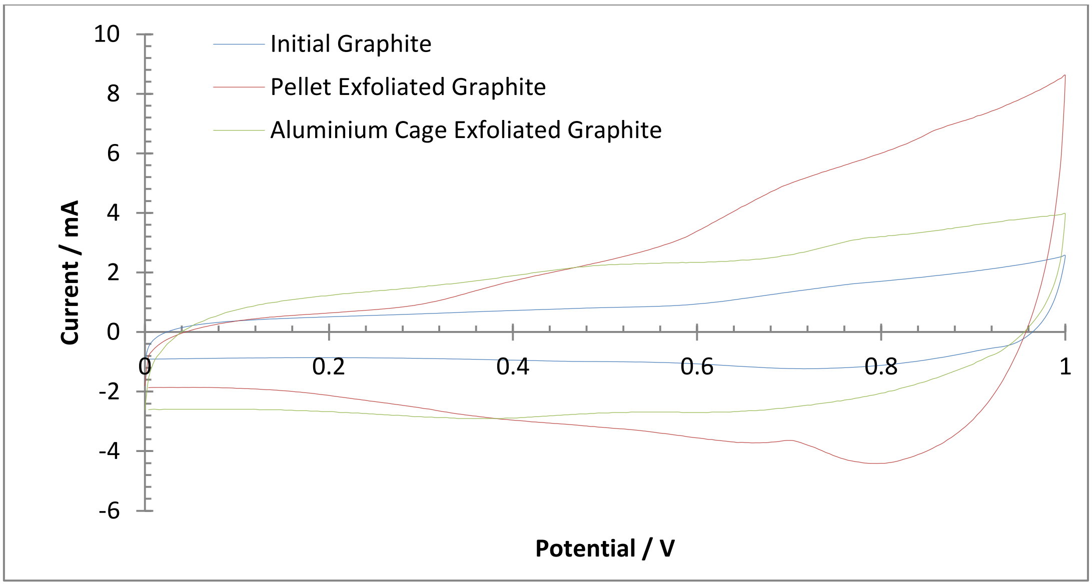
Initial Graphite
Pellet Exfoliated Graphite
Aluminium Cage Exfoliated Graphite
Current / mA
10
8
6
4
2
0
-2
-4
-6
0
0.2
0.4
0.6
0.8
1
Potential / V

(d)

Figure 5.28: CV curves for the initial, pellet exfoliated, and aluminium cage exfoliated infiltrated nickel foam electrodes. (a) 197; (b) 399; (c) 15 µm; and (d) 25 µm graphite.

Figure 5.29a shows the galvanostatic charge-discharge curves for the 5x electrochemically exfoliated graphite 197 by the aluminium cage method. The galvanostatic charge-discharge curves show a symmetrical triangle, which is typical for carbonaceous supercapacitors. The curve is nearly linear, which indicates that the capacitor is not a perfect EDL capacitor. A sharp drop when the material first undergoes discharge (sometimes called the IR drop) represents the limited mobility of the electrolyte in the electrode, called the equivalent series resistance (ESR). All cells will have this voltage drop, due to a change in the electrolyte potential and contact resistance.

Figure 5.29b is a comparison of the initial, pellet-exfoliated, and aluminium exfoliated 15 µm graphite. The aluminium cage exfoliated graphite gave the best performance giving almost double the current retention time of the other graphite samples. The initial graphite even did better than the pellet exfoliated graphite. All curves show the typical triangular shape, however the aluminium exfoliated graphite shows a non-ideal EDLC curve. This is due to the retention of electrolyte, which will contribute to pseudo-capacitive reactions, changing the shape of the curve.

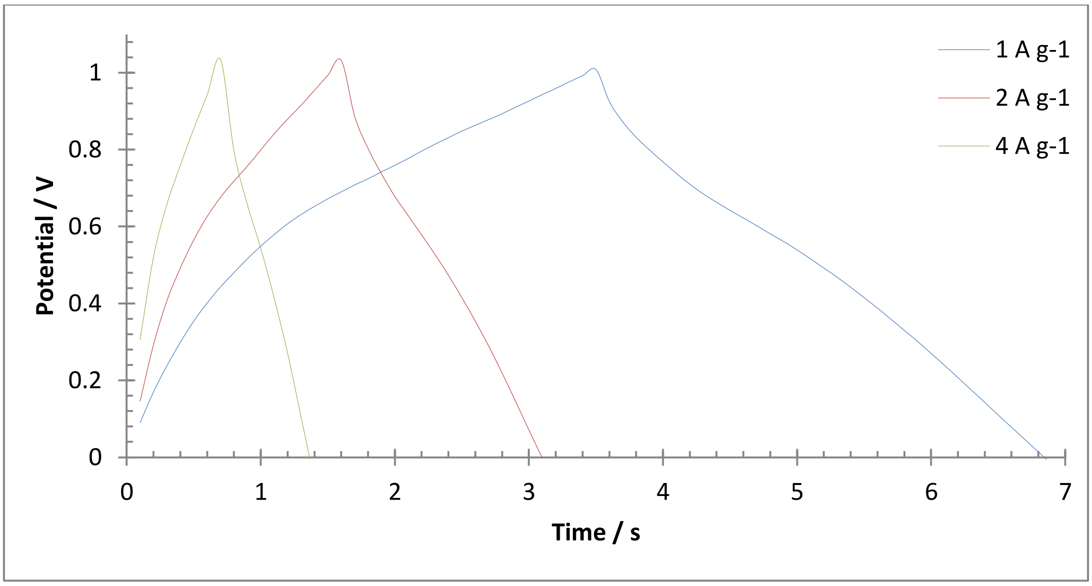

(a)

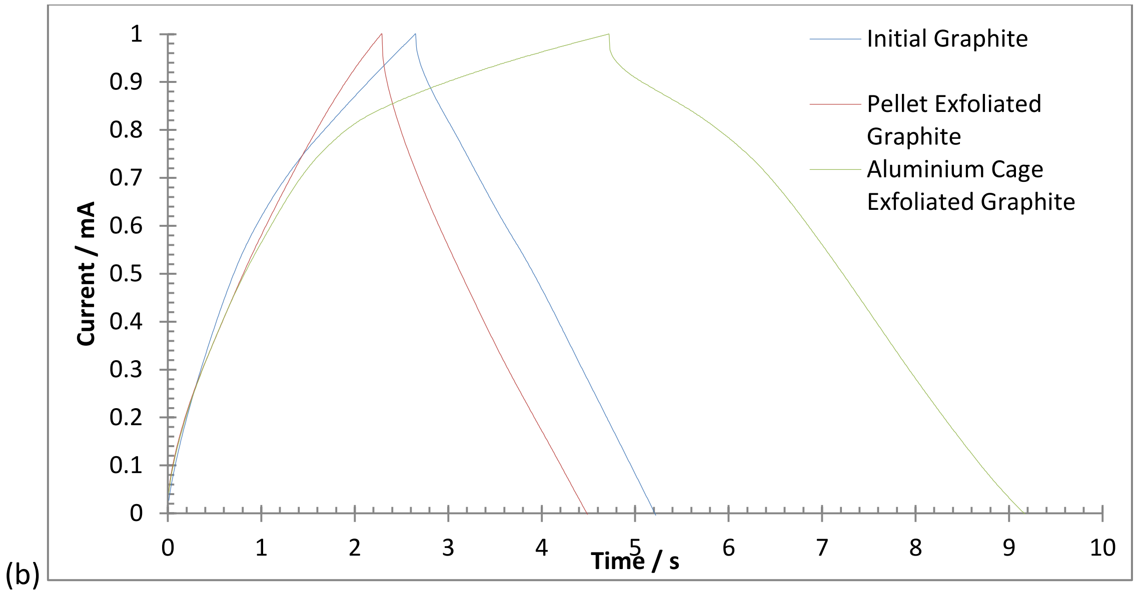

Figure 5.29: Galvanostatic charge-discharge curve of the exfoliated graphite infiltrated nickel foam electrodes. (a) 5x electrochemically exfoliated graphite 197 by the aluminium cage method at different charge-discharge rates and (b) the 15 µm initial graphite, pellet exfoliated, and aluminium exfoliated graphite.

Capacitance of the Exfoliated Nickel Foam

Figure 5.30 and **Table 5.15** show the calculated capacitance of all the nickel foam graphite infiltrated electrodes**.** The capacitance increases upon exfoliation for all the materials, and in general the capacitance for the graphite exfoliated by the aluminium cage method was higher than the pellet method. Interestingly the highest capacitance was achieved by the 5x exfoliation of the 25 µm graphite by the pellet method while this graphite showed the least exfoliation using the other characterisation techniques. Overall the highest capacitances were achieved by the previously exfoliated materials. This is due to the fact these have undergone more exfoliation cycles than the natural graphite.

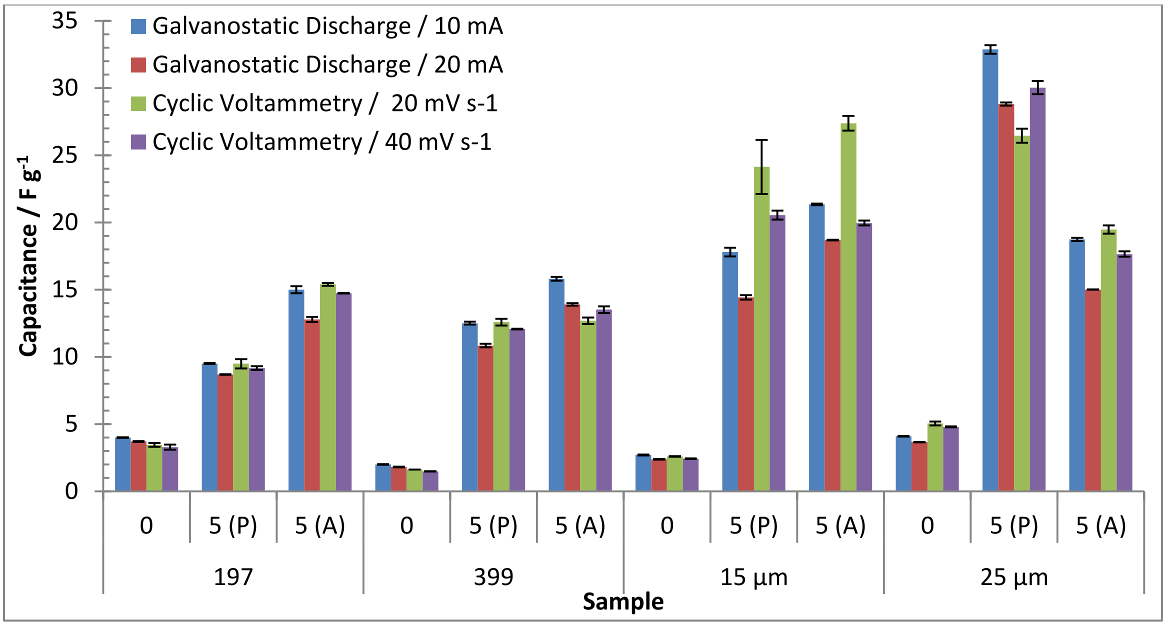

Figure 5.30: The calculated capacitances in F g-1 for the materials used in this part of the project using four different analysis parameters,.

Sample	Exfoliation	Galvanostatic Discharge / mA		Cyclic Voltammetry / mV s^{-1}	
		10	20	20	40
197	0	4.0 ± 0.0	3.7 ± 0.0	3.4 ± 0.1	3.3 ± 0.2
	5 (P)	9.5 ± 0.0	8.7 ± 0.0	9.5 ± 0.6	9.2 ± 0.1
	5 (A)	15.0 ± 0.3	12.8 ± 0.2	15.4 ± 0.1	14.7 ± 0.0
399	0	2.0 ± 0.0	1.8 ± 0.0	1.6 ± 0.0	1.5 ± 0.0
	5 (P)	12.5 ± 0.1	10.8 ± 0.1	12.6 ± 0.3	12.1 ± 0.0
	5 (A)	15.8 ± 0.1	13.9 ± 0.1	12.7 ± 0.2	13.5 ± 0.3
15 µm	0	2.7 ± 0.0	2.4 ± 0.0	2.6 ± 0.0	2.4 ± 0.0
	5 (P)	17.8 ± 0.3	14.4 ± 0.7	24.1 ± 2.0	20.5 ± 0.3
	5 (A)	21.4 ± 0.1	18.7 ± 0.0	27.4 ± 0.5	20.0 ± 0.2
25 µm	0	4.1 ± 0.0	3.7 ± 0.0	5.1 ± 0.1	4.8 ± 0.0
	5 (P)	32.8 ± 0.3	28.8 ± 0.1	26.5 ± 0.5	30.0 ± 0.5
	5 (A)	18.7 ± 0.1	15.0 ± 0.0	19.5 ± 0.3	17.7 ± 0.2

Table 5.15: Specific capacitance (F g^{-1}) of electrochemically exfoliated graphite infiltrated into nickel foam. (P) stands for the pellet method; while (A) stands for the aluminium cage method.

Further to calculating the capacitance, the capacitance of the infiltrated nickel foam was calculated at different scan rates, with the 5x electrochemically exfoliated 25 µm graphite used as an example (**Figure 5.31** and **Table 5.16**). When the scan rate increases, the CV curve window also increases. The evolution of the capacitance at increasing scan rates shows that the as the scan rate increases the capacitance decreases marginally. When the scan rate is increased by a factor of twenty, the capacitance is at 76 % of what it was.

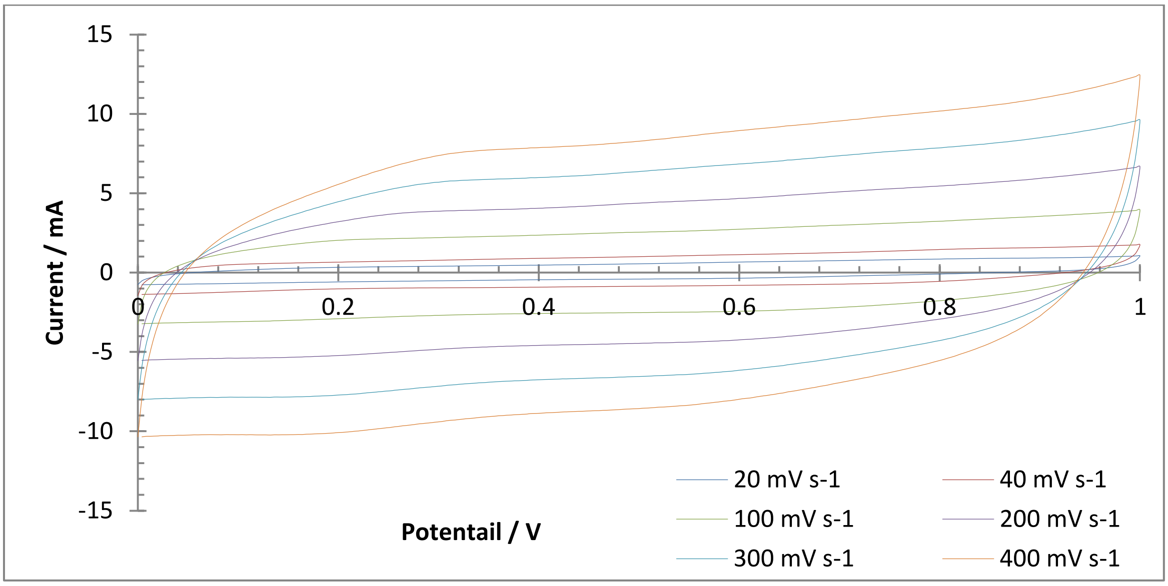

Figure 5.31: How the shape of the CV curve evolves when the scan rate is increased for the 5x electrochemically exfoliated 25 µm graphite by the pellet electrode.

Scan Rate / mV s^{-1}	Specific Capacitance / F g^{-1}
20	26.5 ± 0.5
40	30.0 ± 0.5
100	27.7 ± 0.1
200	23.2 ± 0.1
300	21.6 ± 0.1
400	20.3 ± 0.1

Table 5.16: A table showing the progression of capacitance at different scan rates for the 5x exfoliated 25 µm graphite by the pellet method.

Charge Cycling Stability

Table 5.17 and **Figure 5.32** show the cycle life of the graphitic materials, by assessing the change in capacitance after many charge-discharge cycles. Some graphite samples increase in capacitance after the 2000 charge-discharge cycles, notably the 399 and 15 µm graphite. This could be due to exfoliation *in- situ* or movement of the flakes during charging. This has previously been observed in MoS_2 capacitors where successive cycles of charging and discharge exfoliate the product.[220] The general trend sees the larger graphite materials (197 and 25 µm graphite) have a lower capacitance retention upon exfoliation after multiple charge-discharge cycles, while the smaller graphite samples (399 and 15 µm graphite) have a higher capacitance retention. This is likely due to in-situ exfoliation, which is far more effective on smaller initial graphite grades, as found earlier on the electrochemical exfoliation of the initial graphite. The exfoliated 197 graphite has the lowest capacitance retention of all the materials, while the 15 µm graphite has the highest.

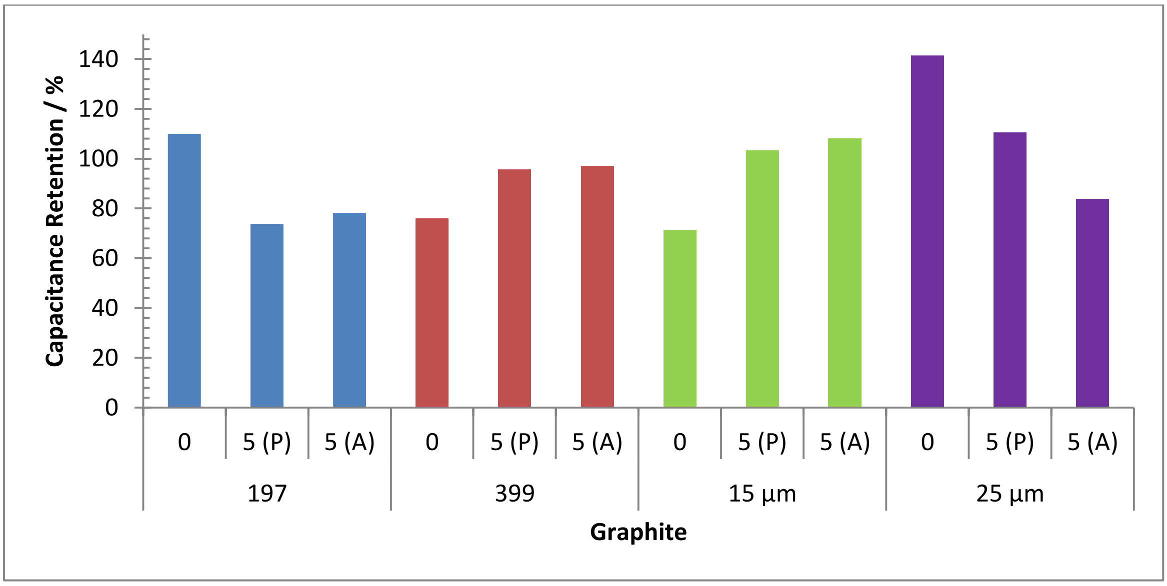

Figure 5.32: Capacitance retention of the graphite samples after 2000 charge-discharge cycles at 10 A g^{-1}. (P) stands for the pellet method; while (A) stands for the aluminium cage method.

Sample	Exfoliation	Capacitance Retention / %
197	0	110.0
	5 (P)	73.7
	5 (A)	78.3
399	0	75.9
	5 (P)	95.6
	5 (A)	97.0
15 µm	0	71.3
	5 (P)	103.3
	5 (A)	108.2
25 µm	0	141.3
	5 (P)	110.5
	5 (A)	83.8

Table 5.17: Capacitance retention of the graphite samples after 2000 charge-discharge cycles at 10 A g^{-1}. (P) stands for the pellet method; while (A) stands for the aluminium cage method.

Impedance

Impedance spectroscopy was used to characterise the electrochemical behaviour of the materials. **Figure 5.33** shows the Nyquist and Bode plots for the exfoliated graphite samples. All the materials exhibited capacitive behaviour, shown by the sharp vertical line in the Nyquist plot. The more vertical the curve, the better the cell can be considered an ideal capacitor. The x-axis intercept can be used to get the equivalent series resistance (ESR). The ESR for the materials is in the range of 0.1 Ω - 1 Ω for all the graphite samples, suggesting the electrodes have a very low internal resistance.

Overall the pellet exfoliated electrodes performed better than the aluminium exfoliated electrodes. The best example of an ideal super-capacitor in both the Nyquist and Bode plots is the 5x pellet exfoliated 25 µm graphite, which is comparable to the high capacitance this material achieved. The aluminium exfoliated 25 µm graphite also gave the best capacitive behaviour for the aluminium exfoliated graphite.

Bode plots can also be used to assess the capacitive behaviour of the materials. Materials which appear close to – 90 °C have ideal EDLC. Resistive and capacitive behaviour is presented with a phase angle of 0 ° and -90 ° respectively.[221] In this work the pellet exfoliated graphite is much closer to -90 ° than the aluminium exfoliated graphite. The frequency at which the phase angle become 45 ° can be used to assess when the capacitive behaviour becomes resistive.[222] The time constant for this is 47 ms, 21 ms, 36 ms, 0.11 s, 3.2 s, 2.4 s, 5.7 s, and 5.7 s for the pellet exfoliated 197, 399, 15 µm, and 25 µm graphite, and the aluminium exfoliated 197, 399, 15 µm, and 25 µm respectively. The fast times for the pellet electrode suggests better contact with the current collector. This may be due to the lack of aluminium electrode impurities in the sample.

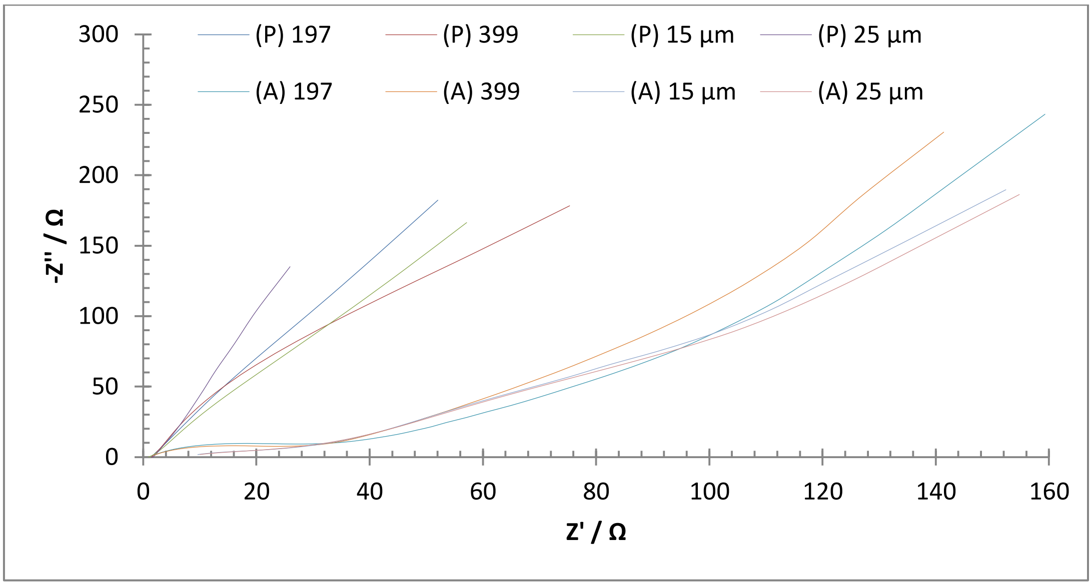

(a)

(b)

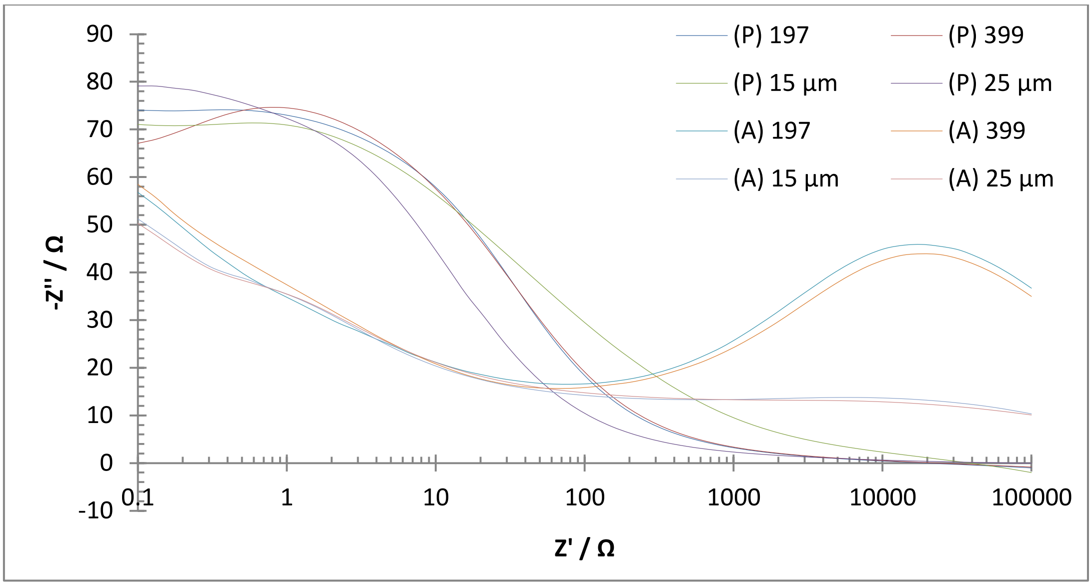

Figure 5.33: Impedance Nyquist and Bode plots of the exfoliated graphite material. (a) the Nyquist plot for the exfoliated graphite; and (b) the Bode plot for the exfoliated graphite.

Specific Energy and Power

The energy and power density of the graphene-infiltrated nickel foam electrodes was calculated using the capacitance and discharge time of the electrodes (**Table 5.18**, **Figure 5.34**). The electrodes have a low energy density due to the potential window used (1 V). Using organic and ionic liquid electrolytes will boost the energy density, as the energy density is proportional to the potential window squared.

All grades of graphite both natural and processed display an increase in energy and power density upon exfoliation. In general the aluminium cage exfoliated graphite exhibited the largest energy density, apart from the pellet exfoliated 25 µm graphite which produced the highest energy density of all the electrodes. The power density of the aluminium exfoliated graphite was decidedly higher than all the other graphite electrodes, although the aluminium exfoliated 197 graphite did not sport this marked increase. This suggests that the aluminium exfoliated material is the best exfoliation method overall, with the 399 and 15 µm graphite giving the best amounts of exfoliation.

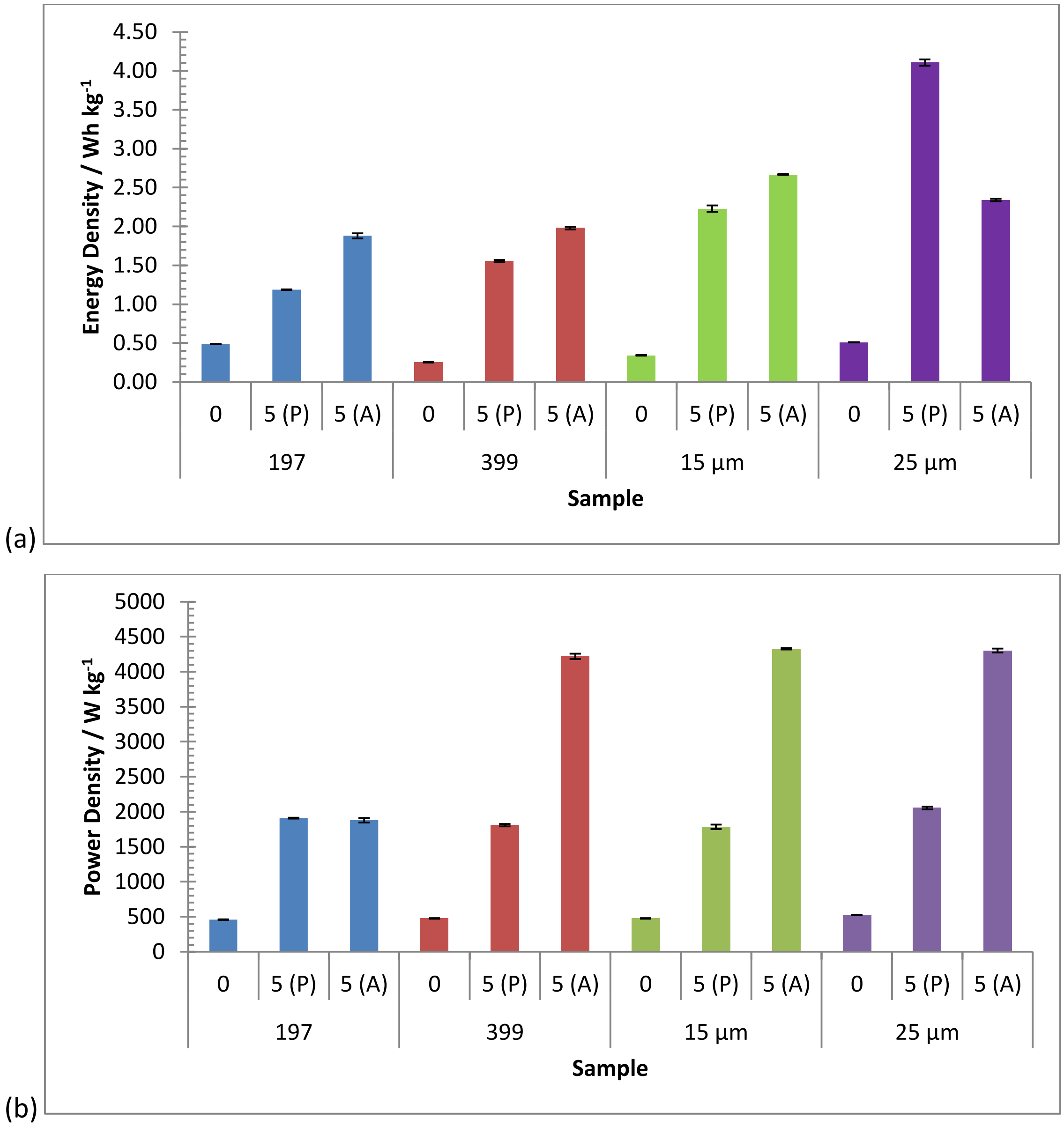

Figure 5.34: (a) Energy; and (b) Power Density of the graphene-infiltrated nickel foam electrodes. The exfoliation of the graphite is 0, 5 (P), and 5 (A), which represents no exfoliation, 5 exfoliation cycles by the pellet method, and 5 exfoliation cycles by the aluminium cage method respectively.

Sample	Exfoliation	Specific Energy / Wh kg^{-1}	Specific Power / W kg^{-1}
197	0	0.49 ± 0.00	458 ± 2
	5 (P)	1.12 ± 0.00	1908 ± 7
	5 (A)	1.88 ± 0.03	1879 ± 32
399	0	0.25 ± 0.00	475 ± 6
	5 (P)	1.56 ± 0.01	1807 ± 16
	5 (A)	1.98 ± 0.02	4218 ± 38
15 µm	0	0.34 ± 0.00	474 ± 5
	5 (P)	2.23 ± 0.04	1784 ± 32
	5 (A)	2.67 ± 0.01	4328 ± 12
25 µm	0	0.51 ± 0.00	525 ± 3
	5 (P)	4.12 ± 0.04	2054 ± 20
	5 (A)	2.34 ± 0.02	4300 ± 28

Table 5.18: Specific energy and power of the graphite, and electrochemically exfoliated graphite materials, calculated from the galvanostatic discharge curve at 10 mA. The exfoliation of the graphite is 0, 5 (P), and 5 (A), which represents no exfoliation, 5 exfoliation cycles by the pellet method, and 5 exfoliation cycles by the aluminium cage method respectively.

5.3 Conclusions

The two methods of electrochemical exfoliation of graphite both exfoliated the graphite, as seen by the characterisation, particularly the Raman spectroscopy. The shift to a lower wavenumber means the material has undergone some form of exfoliation. However the aluminium cage gave a greater degree of exfoliation than the pellet method. This is likely due to the pellet falling off from the power supply in the first 20 minutes of exfoliation. The pellet method would also not reduce the size of the graphite, which is characteristic of exfoliation.

Certain grades of graphite have the potential to be exfoliated further than others. The 399 and 15 µm material seem to have undergone the most exfoliation. Both of these materials have graphite flakes that are smaller than their counterparts, the 197 and

25 µm graphite. Characterisation indicated that's the only difference between the 197 and 399 materials, and the 15 µm and 25 µm initial graphite was the grain size.

In these studies the material was size selected for capacitor manufacture using sedimentation. Further sedimentation via forced sedimentation (centrifuge) could further improve the capacitance of the electrode. Size selection between exfoliation cycles could also improve the yield of graphene in the bulk product

In this study the nickel foam was excluded from capacitance calculations as it was deemed to not contribute much to capacitance in relation to the exfoliated graphite. This was conferred by CV and galvanostatic discharge. For commercial capacitor applications, the weight of nickel foam would limit its use within super-capacitors. The current work is currently a proof of concept, where the exfoliated graphite could be used in a capacitor.

The extent of exfoliation has an effect on the capacitance. When comparing the Raman results, the aluminium exfoliated material had the lowest average Raman 2D peak, and also highest capacitance. However considering the error, there is not much variation in the Raman exfoliation. This can be seen in the resultant capacitance, where they are all fairly similar.

Re-stacking is a problem for the transferability of the exfoliated graphite to a useable electrode. This is even a problem in perfect graphene, where the surface area collapses from 2360 m^2 g^{-1} to 15 m^2 g^{-1} upon drying.[223] This is caused by the smoothness of the material, which allows for efficient re-stacking lowering the capacitance. To counteract this decrease in capacitance the material can be crumpled.[224] Zang *et al.* created a supercapacitor using crumpled graphene papers, which prevented extensive re-stacking but were also stretchable and boasted a high capacitance of 196 F g^{-1}.[225] The 25 µm pellet exfoliated graphite which has the highest capacitance is also one of the more crumpled graphite materials. The aluminium exfoliated material has fewer defects on the surface, which causes the exfoliated graphite to be more pristine. This could facilitate the re-stacking of the graphitic sheets which would reduce the capacitance of the graphite.

In the literature most routes exploring the capacitance of electrochemically exfoliated graphite create graphene-pseudo-capacitive materials (like MnO_2, PANI, *etc.*) composites. The theoretical maximum capacitance of graphene is 550 F g^{-1}. The results in this chapter are not close to this value. This is because the graphene obtained is not pristine single-layer graphene, rather few-layer-graphene with significant defects and impurities.

In work by Wu *et al*. they assess the capacitance of pure electrochemically exfoliated graphite. They also created 3D foams on nickel, however they achieved a respectable capacitance of 113 F g^{-1} in 6 M KOH. This is far larger than the capacitances calculated in this chapter. This could be due to a more robust electrode design, where the nickel foams pressed and assembled into coin shaped supercapacitors of industrial grades. This would allow no electrolyte leakage and sufficient contact between the working electrode and the current collector. They also reported to have synthesised < 75 % FLG compared to the starting graphite using H_2SO_4 intercalation, where the best reported in this chapter is 30 %.[226]

6 Graphene-PAN based Carbon Nano-fibres

In the previous chapter the capacitance of exfoliated graphite was assessed by infiltration into metal foam. Whilst this approach provides a facile route for comparing materials, it is not scalable or commercially viable. There is growing interest in developing fibre-based supercapacitors, due to their mechanical flexibility and ease of synthesis, allowing incorporation in textiles and composites. However un-functionalised graphene cannot be spun on its own, due to the poor interactive forces between the graphitic sheets, causing the fibre to break apart easily. Electro-spinning is a common way to create carbon nano-fibres. Many research groups have used polyaniline as a template polymer to create graphene-supercapacitors due to its conducting nature. However the polymer contributes to the overall capacitance through pseudo-capacitive processes. It was decided that the desired polymer should be entirely carbon in an effort to keep the energy storage process electrical double layer (preserving lifetime) to make it so the fibre could be easily integrated into a circuit. Thus polyacrylonitrile (PAN) was chosen as the template polymer as while it can be easily spun, it can also be converted into carbon fibre, therefore contributing to the formation of electrical double layers, while also increasing the electrical conductivity and mechanical strength of the fibre. A graphene-carbon fibre composite will also be easily transferrable for use as a supercapacitor electrode. During research it was found that the electro-spun fibre mats were easily synthesised, however the conversion to carbon fibre proved difficult, with an extremely low yield after carbonisation. Another route was tested was continuous fibre wet-spinning, which was a success. In this research project, the previously electrochemically exfoliated graphite was spun with PAN to give composite fibres which were subsequently carbonised to yield fibres for use in supercapacitors. It was hoped that this approach would maintain the capacitance of the graphene whilst providing a suitable carbon matrix to hold the flakes in the desired microstructure and maintain electrical conductivity. Research groups, like Gao *et. al*. have previously synthesised graphene carbon fibres for mechanical applications. These were synthesised using graphene oxide (GO), which requires further reduction. These fibres have been shown to have a respectable tensile strength of 150 – 450 MPa.[227] The addition of graphene (non-functionalised graphene) directly to the composite for spinning is a relatively niche field, as most research groups use graphene oxide. These are also mechanically analysed instead of electrochemically analysed. This chapter discusses the electrochemical properties of graphene-based carbon fibres.

6.1 Characterisation of the pure PAN Fibres

PAN fibres were wet-spun from a DMF based dope into a range of different solvent coagulation baths including water, heptane, acetone, hexane, and toluene. Diethyl ether was found to be only solvent in which fibres were successfully spun, with the fibres typically breaking apart and dispersing in the other solvents. These successful fibres were then collected and characterised using scanning electron microscopy (SEM), Raman spectroscopy, x-ray diffraction (XRD), thermal gravimetric analysis (TGA), and infra-red spectroscopy (FTIR).

The fibres wet-spun into the diethyl ether coagulation bath formed very quickly. The quick coagulation meant the dope did not disperse into the solvent bath. The outside of the fibres were seen to coagulate first. It is likely that the PAN from the middle of the fibre was drawn to the outside edges, which resulted in a fibre with a porous structure inside. The quick coagulation also allowed for fast synthesis speeds, as the dope could be drawn into the bath quickly.

Scanning Electron Microscopy

Figure 6.1 shows typical SEM images of the wet-spun PAN fibres. The structure of the PAN fibres was highly folded with a smooth surface at high resolutions. Concerning the inside of the fibres, the structure closest to the surface of the PAN fibres appears to be more ordered than the middle, confirming that coagulation starts from the surface. This porous inside structure increases the surface area (and thus capacitance) of the fibre. The average diameter of the fibres was 85.69 ± 17.97 µm when spun from a 21 gauge needle, and 208.52 ± 81.36 µm when spun from an 18 gauge needle. These diameters are smaller than the inner diameters for the 21 and 18 gauge needles, 514 µm and 838 µm respectively, showing a factor of ~2 shrinkage. Preliminary experiments with the graphene-PAN dope found that spinning with needle gauges smaller than 23 caused blockages due to the graphene dope and thus a 21 gauge needle was used for the rest of the experiments. It has been shown by Razal *et al.*[228] that the needle aperture has an effect on whether the fibres can be continuously spun. At lower needle gauges (larger inner needle diameters), the graphene oxide will not spun into a continuous fibre. This does not occur at higher needle apertures (smaller inner needle diameters) where at high concentrations of GO, a continuous jet formation is observed, allowing for continuous fibre formation.

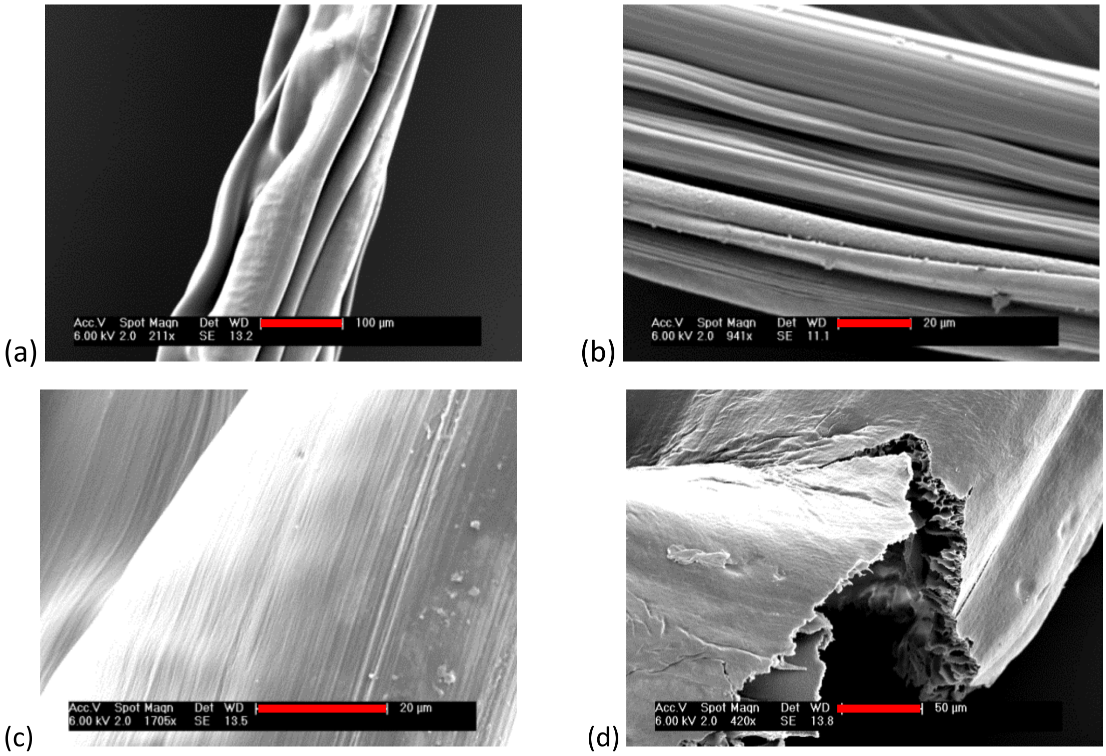

Figure 6.1: SEM images of the wet-spun synthesised PAN fibres using a diethyl ether coagulation bath.

Raman Spectroscopy

Figure 6.2 shows typical Raman spectrum of the PAN fibres. The Raman spectrum of PAN consists of two prominent bands, over a large background. Due to the low intensity peaks, an extended scan of 10 minutes with 3 accumulations had to be performed to more clearly distinguish the Raman bands. This scan was conducted at a reduced power to ensure as little change to the fibre structure as possible. The most intense peak appears at 2244.9 ± 0.2 cm^{-1} due to the nitrile (C≡N) group. A broader, less intense peak appears at 2931.3 ± 2.2 cm^{-1} in the Raman spectrum. This is due to the vibrational stretching of $–CH_2$. Both these peaks appear in all PAN Raman spectra.

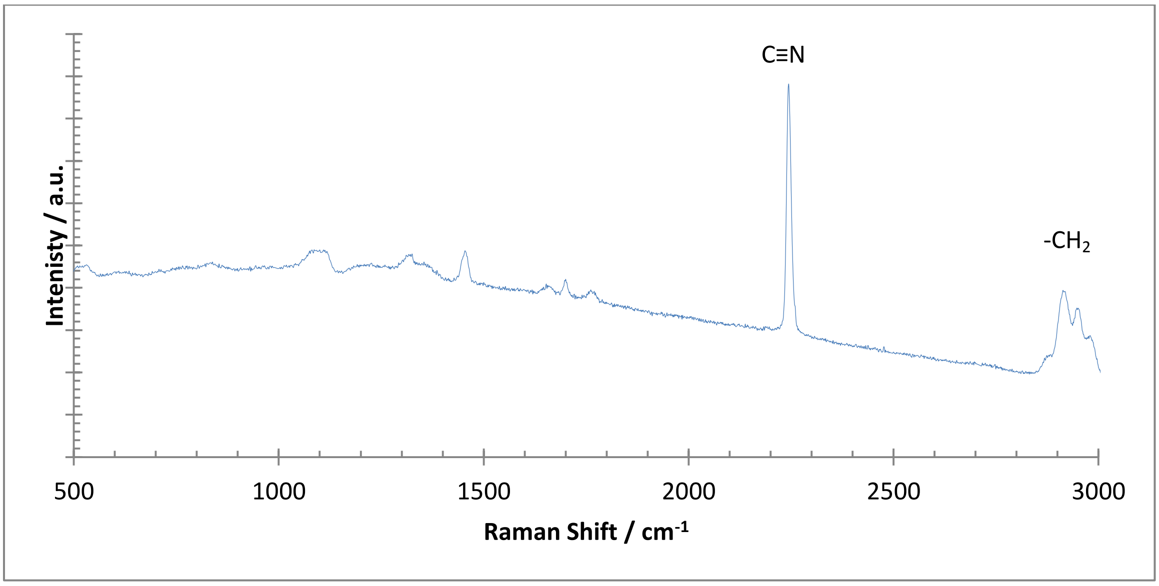

Figure 6.2: An example Raman spectrum of wet-spun PAN fibres, showing the two prominent peaks at ~ 2244 cm^{-1} (C≡N) and ~ 2900 cm^{-1} (-CH$_2$).

X-Ray Diffraction

Figure 6.3 shows the XRD pattern of the PAN fibre. The zero-background holder produces a broad and intense peak at ~ 2θ = 18 ° and 25 °, which causes a problem for PAN characterisation as these peaks overlap with active PAN peaks. Two peaks can be identified in the XRD pattern. A sharp peak at 2θ = 17.49 ± 0.27 ° and a smaller intensity peak at 2θ = 27.79 ± 0.31 °. These pertain to the 10.0 and 1.01 planes of the PAN, and a d-spacing of 5.06 Å and 3.21 Å respectively. For PAN fibres, this crystal size was calculated as 11.3 nm, which is significantly smaller than the wall thickness of the fibres. The ratio of d-spacing is 1.58, which is close to √3:1 (1.73), indicating that the PAN was hexagonally packed.[229]

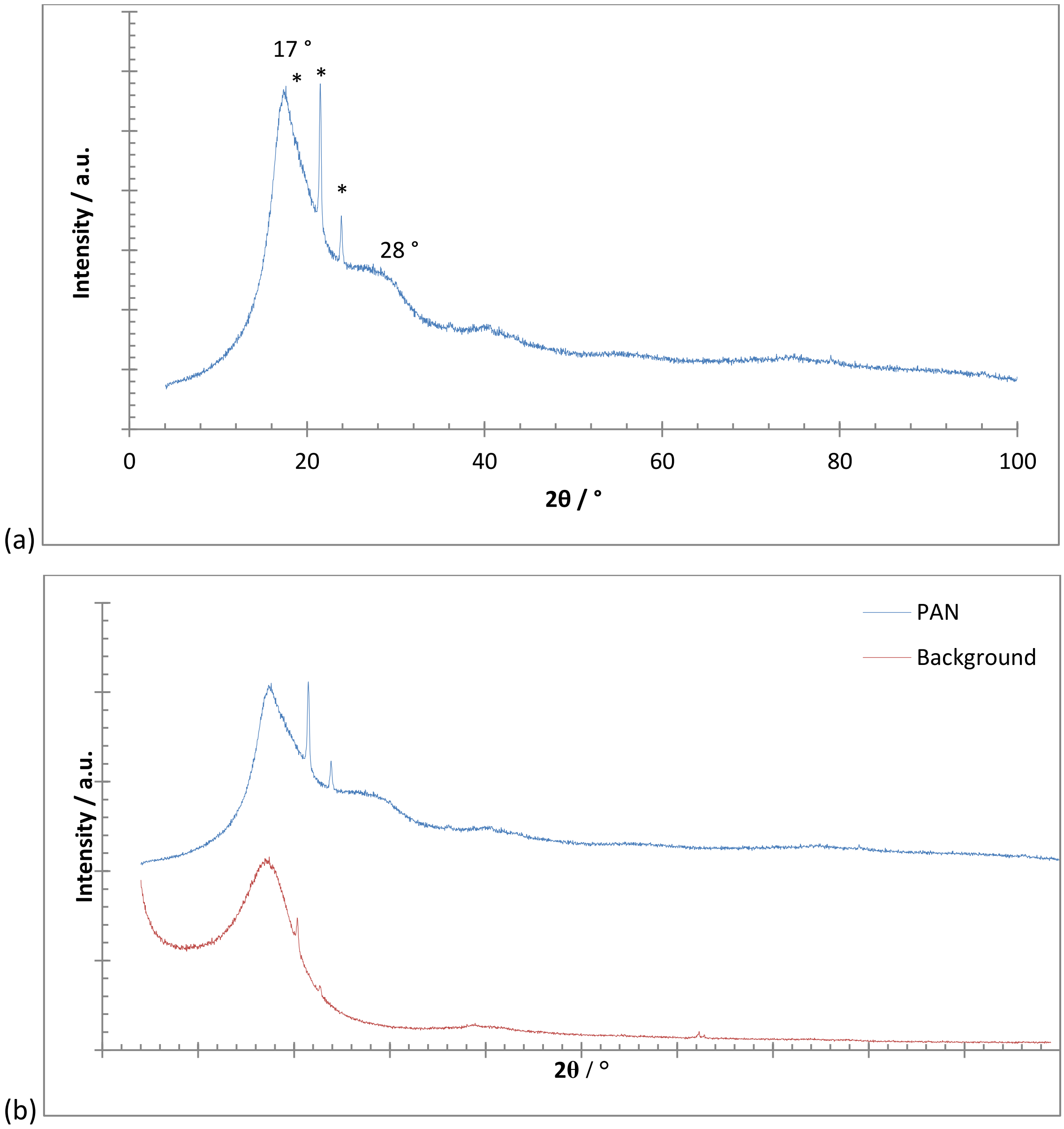

Figure 6.3: An example XRD pattern of the wet-spun PAN fibre. The numbers pertain to identifiable PAN peaks, while the '*' peaks are due to the zero-background holder. (a) the PAN fibre; and (b) the PAN fibre and background to show the peaks more clearly.

Thermal Gravimetric Analysis

Figure 6.4 shows the thermal decomposition profile of the PAN fibre in an air atmosphere. A small initial (up to 100 °C) weight loss of ~ 5 % occurs due to water loss. Next there are two major mass loss events during heating; the first appears at 285.3 ± 4.3 °C, which is slightly higher than the stabilisation step used for carbonisation, and corresponds to a mass loss of ~ 10 %. At this stage some nitrile groups are lost, while cyclisation starts. As this step generally is typically conducted in air in commercial fibre production, oxidation can occur.[230] The second and larger event (70 % weight loss) starts at 425.0 ± 14.0 °C, which is due to the carbonisation step, including ladder formation, where all the hetero atoms are removed from the PAN, including N_2 and HCN groups, and H_2 is lost in ladder formation. After 700 °C there is an increase in weight, which is not due to the fibre as the PVA and carbon should be burnt off in an air atmosphere. This small (10 %) increase in weight could be attributed to contaminants from the platinum pans used in analysis.

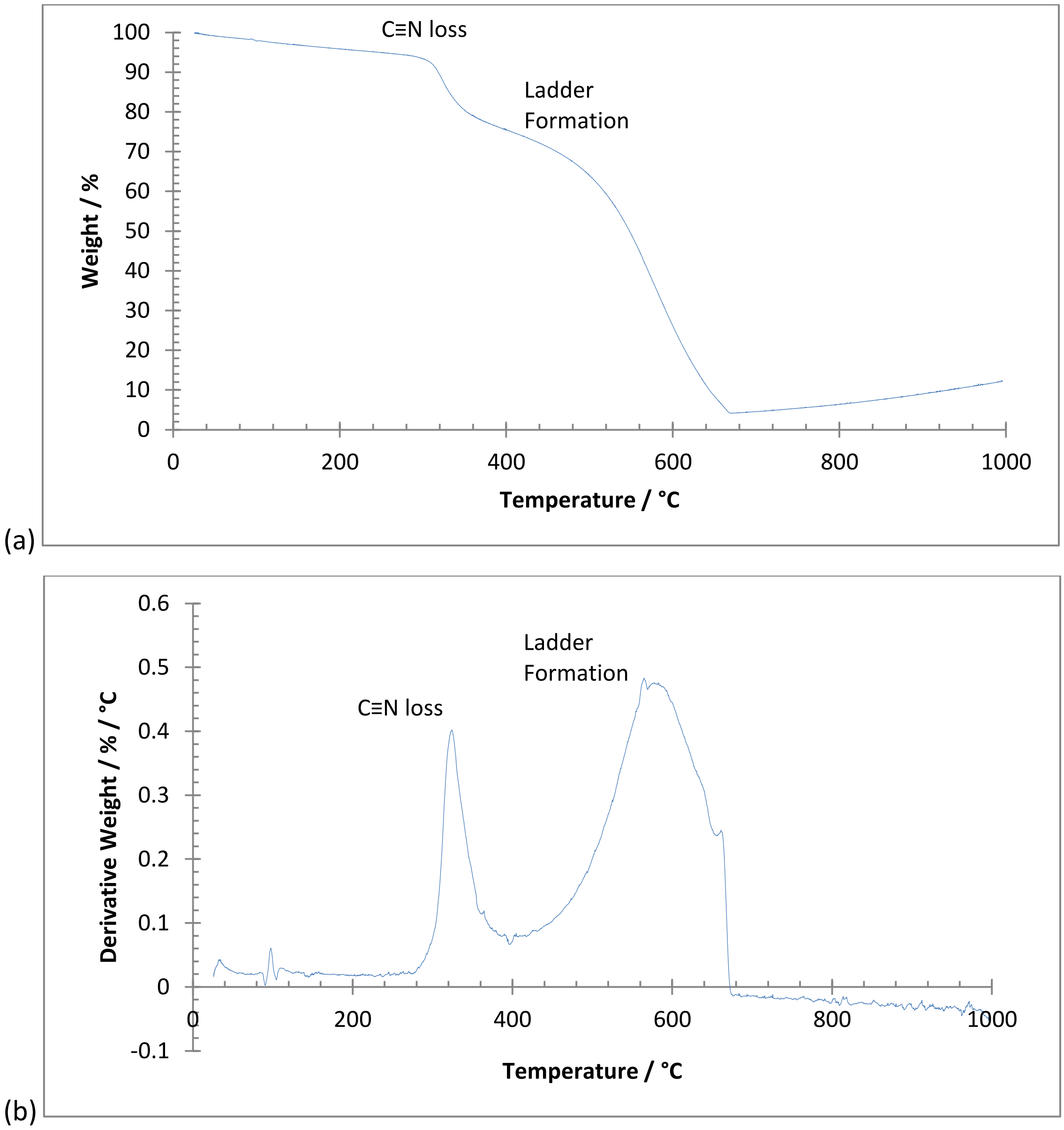

Figure 6.4: TGA spectrum of the PAN fibre, showing the thermal decomposition profile of the material in an air atmosphere (heating rate of10 °C min^{-1}). (a) the weight-loss curve; and (b) the derivative (temperature) weight-loss curve.

Infra-Red Spectroscopy

Figure 6.6 shows the FTIR spectrum of the wet-spun PAN fibre taken with a salt disk (**Figure 6.5**). The sharp peak at 2240 cm^{-1} is due to the presence of a C≡N nitrile group (stretch), which is part of the acrylonitrile monomer. Additional groups in the monomer are the –CH group which appears at 2940 cm^{-1} (stretch) and –CH_2 group which appears at 1452 cm^{-1} (bend). The broad peak from 3100 cm^{-1} to 3700 cm^{-1} is due to the hygroscopic KBr absorbing water from the atmosphere, as is the sharp peak at 1620 cm^{-1}.

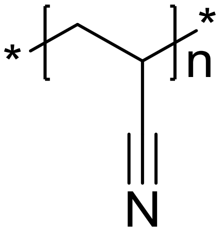

Figure 6.5: Skeletal diagram of the PAN polymer unit, showing the groups that appear in infra-red spectrum: C≡N, -CH, and CH_2.

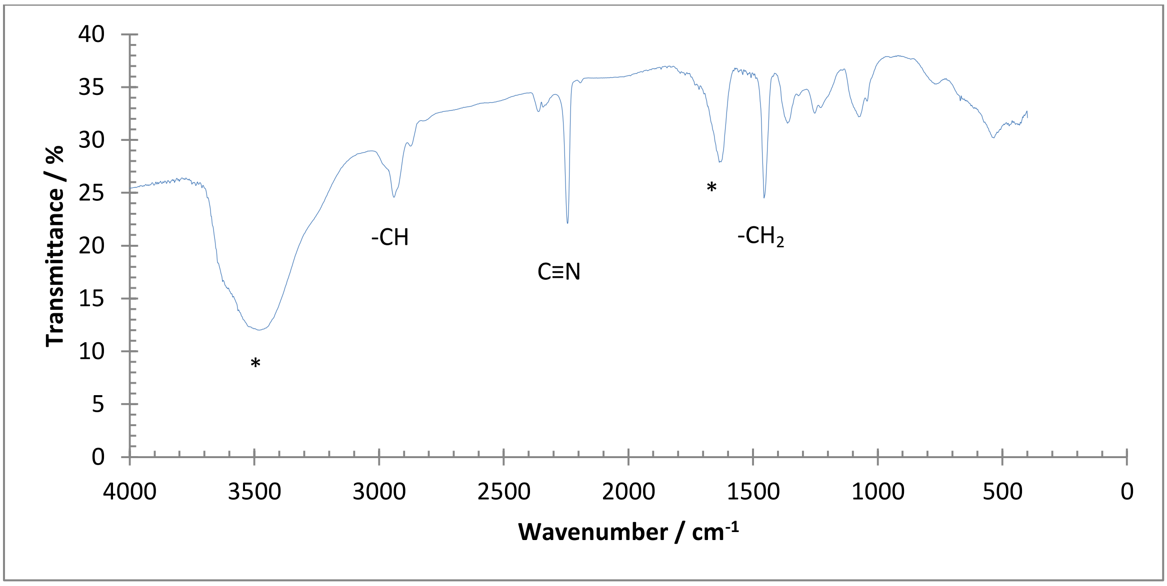

Figure 6.6: A typical FTIR spectrum of the PAN fibres. The '*' represents peaks from the hydroscopic KBr.

Summary

After much trial and error, the synthesis of wet-spun PAN fibres proved to be a success. Raman spectroscopy, XRD, FTIR, and TGA show the fibres are composed entirely of PAN.

This is shown by the presence of a nitrile group, and typical sp^3 hydrocarbon groups. The nitrile group acts as a leaving group facilitating the formation of carbon fibre, which is the desired product. The change in fibre structure upon the addition of the electrochemically exfoliated graphite will be analysed in the next section using SEM, while the presence of graphene will be confirmed through Raman spectroscopy and XRD in particular.

6.2 Characterisation of the PAN-Graphene Fibres

PAN-graphene fibres were synthesised from the wet-spinning of a PAN and electrochemically-exfoliated graphite in DMF dope. Two exfoliated graphite materials were used: the natural 5x exfoliated Graphexel 399 and the processed 5x exfoliated xG Sciences 15 µm, both electrochemically exfoliated using the aluminium cage method. These materials were chosen due to the successful electrochemical exfoliation of these materials, characterised in the previous chapter, and strong electrochemical performance. The electrochemically exfoliated xGnP 25 µm graphite by the pellet method was not used due to the instability of the created fibre and stalling during the wet-spinning procedure. This was possibly due to the size of the exfoliated graphite flakes destabilising the fibre material and aggregates of the material blocking the spinneret.

It was found that the PAN-graphene dope was easily spun into the diethyl ether bath to produce fibres. At high concentrations of exfoliated graphite (10 - 15 wt.%) the fibres could not be spun due to stalling in the syringe, as the higher viscosity caused blockages. At medium concentrations of exfoliated graphite (6 - 8 wt.%) the fibres would break easily, beading would occur in throughout spinning, and the exfoliated graphite would not be dispersed sufficiently throughout the fibre. Decreasing the speed of the extrusion of the dope into the coagulation bath (from 0.05 mL h^{-1} to 0.01 mL h^{-1}) reduced the dimensions of the fibre. Two coagulation baths were initially used, diethyl ether and water. The PAN-exfoliated graphite dope extruded into the water coagulation bath produced smooth fibres, however these were very brittle and could not be handled without breakage, thus are not considered in this discussion.

Electron Microscopy

Figure 6.7 shows SEM images of the PAN-exfoliated graphite fibres. After the addition of the electrochemically exfoliated graphite, the topology of the fibres changed. The exfoliated graphite is interspersed throughout the fibre, both inside and on the surface. The surface has become rough, while the inside retains its porosity. The exfoliated graphite flakes look to be dispersed aligned to the fibre axis, with few flakes perpendicular to the axis. The microstructure inside the 15 µm-PAN fibres shows tightly bound, randomly-orientated flakes, while the 399-PAN fibres have longer flakes more in-line to the fibre axis. This is a result of the size of the flakes, which affects the inner porosity. The average diameter of the fibres was calculated as 216.86 ± 16.30 µm for the 15 µm-PAN fibres and 244.74 ± 29.63 µm for the 399-PAN fibres. The wall thickness of these fibres is ~ 5 µm for the 15 µm-PAN fibres, and ~ 10 µm for the 399-PAN fibres, which are comparable to the aluminium cage exfoliated graphite sizes which were 8 µm and 15 µm respectively.

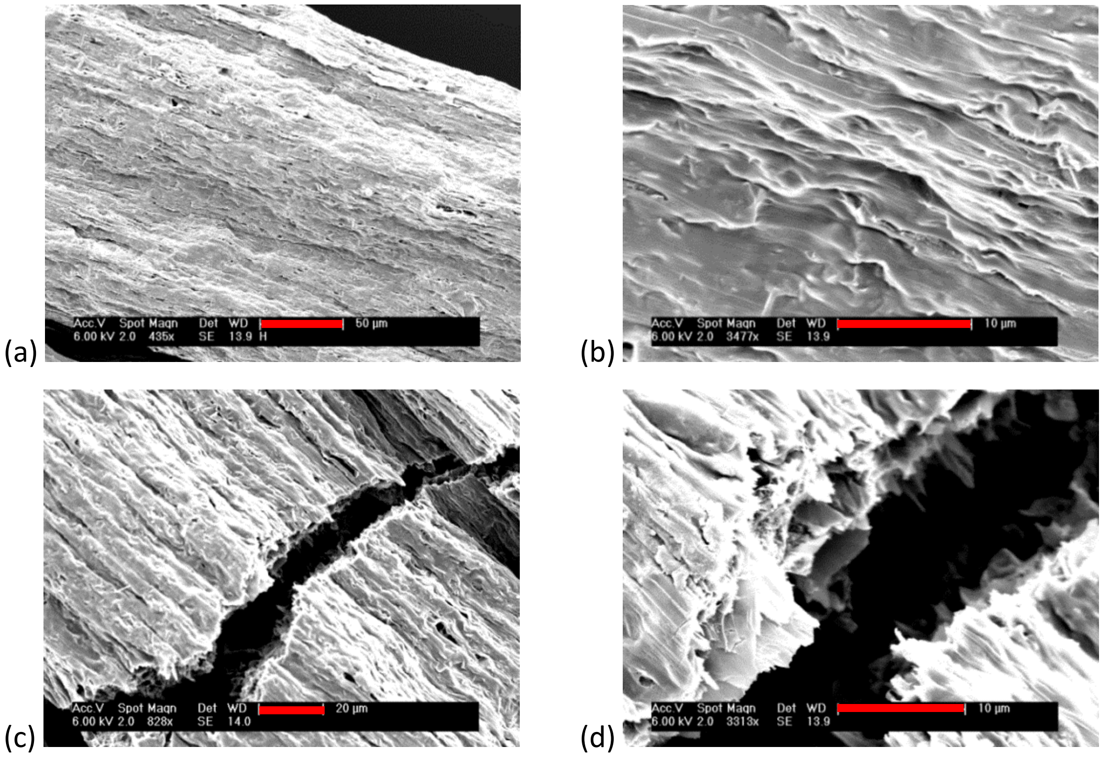

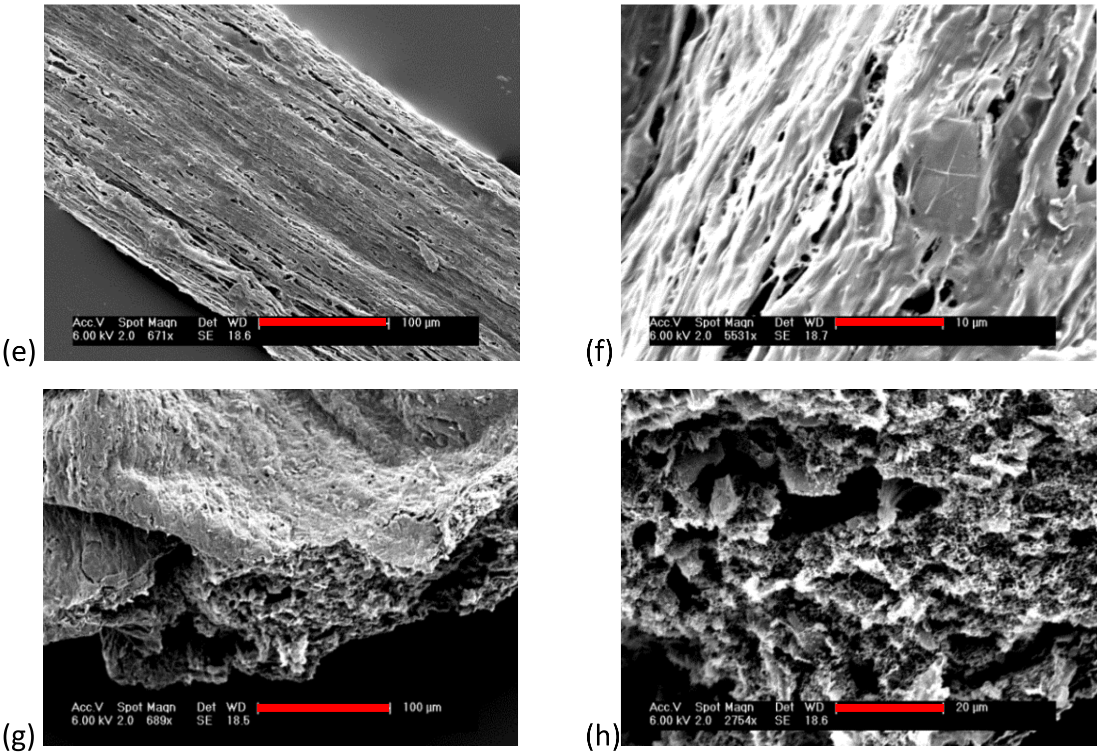

Figure 6.7: SEM images of the exfoliated graphite doped PAN fibre wet spun into a diethyl ether bath. (a-d) 399-PAN fibre; and (e-h) 15 µm-PAN fibre.

Raman Spectroscopy

Figure 6.8 shows an example Raman spectrum of the PAN-exfoliated graphite fibres, with a table of the key peaks in **Table 6.1**.

The fibre composite spectra feature 5 prominent peaks, 2 appearing due to the PAN and 3 belonging to the exfoliated graphite. The PAN peaks appear ~ 2244 cm^{-1} and ~ 2935 cm^{-1}, which correspond to the C≡N group and -CH_2 group respectively. The exfoliated graphite bands appear at ~ 1330 cm^{-1}, ~ 1580 cm^{-1}, and ~ 2675 cm^{-1}, which correspond to the D, G, and 2D bands respectively. The position and shape of the 2D peak shows some form exfoliation has been retained, however the coagulation did not further exfoliated the graphene in the fibre. The peak shift is likely due to strain, caused by the formation of the fibre. In the original exfoliated graphite the position 2D peak was 2668.2 ± 4.9 cm^{-1} and 2670.6 ± 9.3 cm^{-1} for the 5x aluminium cage electrochemically exfoliated 399 and 15 µm graphite respectively. This peak shift means some form of re-stacking has taken place during coagulation. This is again likely due to the poor dispersion of graphene in the DMF solvent due to electrolyte impurities.

Sample	D Peak / cm^{-1}	G Peak / cm^{-1}	C≡N Peak / cm^{-1}	2D Peak / cm^{-1}	CH_2 peak / cm^{-1}	I_D/I_G	I_{2D}/I_G
PAN	N/A	N/A	2444.9 ± 0.2	N/A	2931.3 ± 2.2	N/A	N/A
15 µm - PAN	1331.1 ± 6.2	1583.4 ± 1.0	2244.0 ± 0.8	2676.2 ± 3.1	2936.4 ± 23.9	0.56	0.36
399 - PAN	1333.0 ± 0.9	1582.0 ± 0.7	2242.2 ± 1.3	2674.6 ± 3.8	2938.8 ± N/A	0.46	0.34

Table 6.1: Table of Raman spectrum data, showing the key peaks belonging to PAN and graphite.

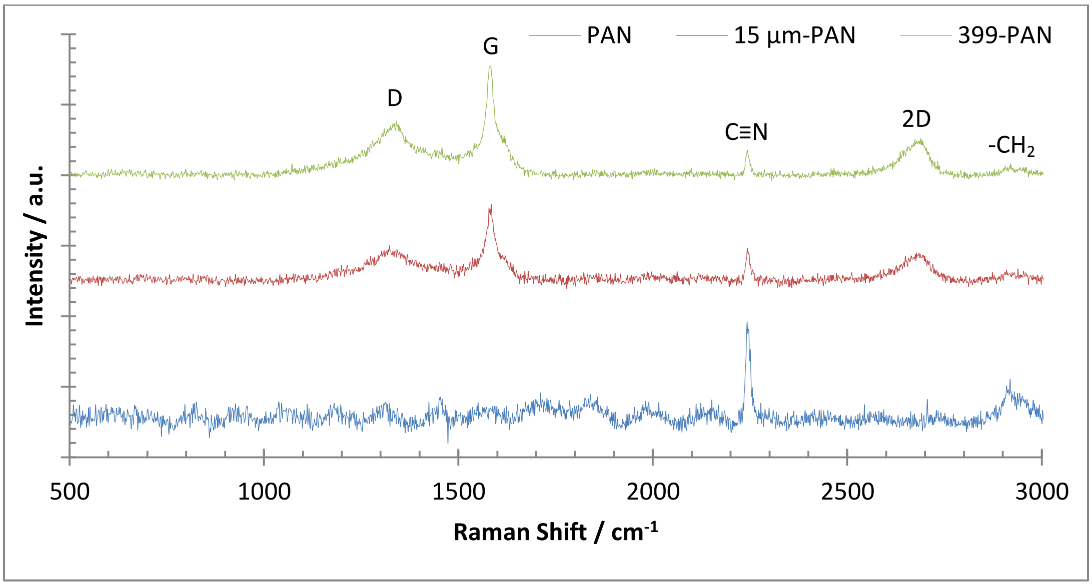

(a)

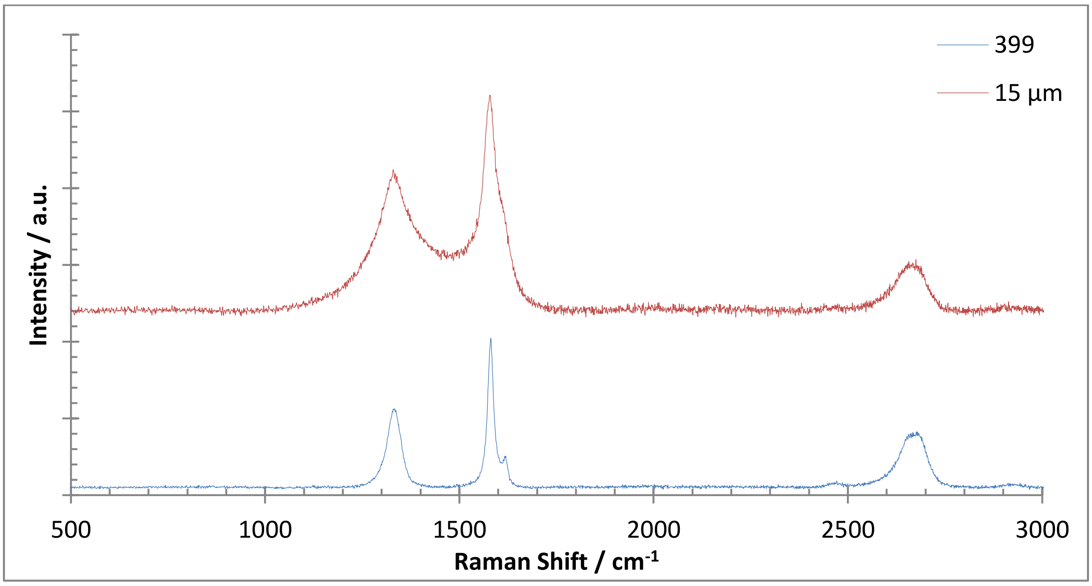

(b)

Figure 6.8: Raman spectra PAN composite fibre: (a) a comparison of the Raman spectrum for PAN, PAN-399, and PAN-15 µm electrochemically exfoliated graphite; and (b) example Raman spectra of the aluminium cage 5x electrochemically exfoliated 15 µm and 399 graphite.

X-Ray Diffraction

Figure 6.9 shows an XRD pattern of the fibres taken from a random orientated non-woven sample. Both PAN peaks are present, which appear ~ 2θ = 17.5 ° and 28 ° in all fibres, due to the 10.0 and 1.01 planes respectively. There is an additional peak at 2θ = 26 ° which is due to the 00.2 plane of the aluminium-cage exfoliated graphite. This peak appears at 2θ = 26.38 ± 0.31 ° and 26.40 ± 0.14 ° which pertains to a d-spacing of 3.37 Å and 3.47 Å for the 399 and 15 µm fibres respectively. This d-spacing is in line with graphitic species. Also of note is the lack of any impurities from the electrolyte, which was previously seen in the exfoliated graphite XRD patterns. **Figure 6.3b** shows the XRD patterns at 2θ = 26 °, where the peak at 26 ° is not present in the PAN fibre.

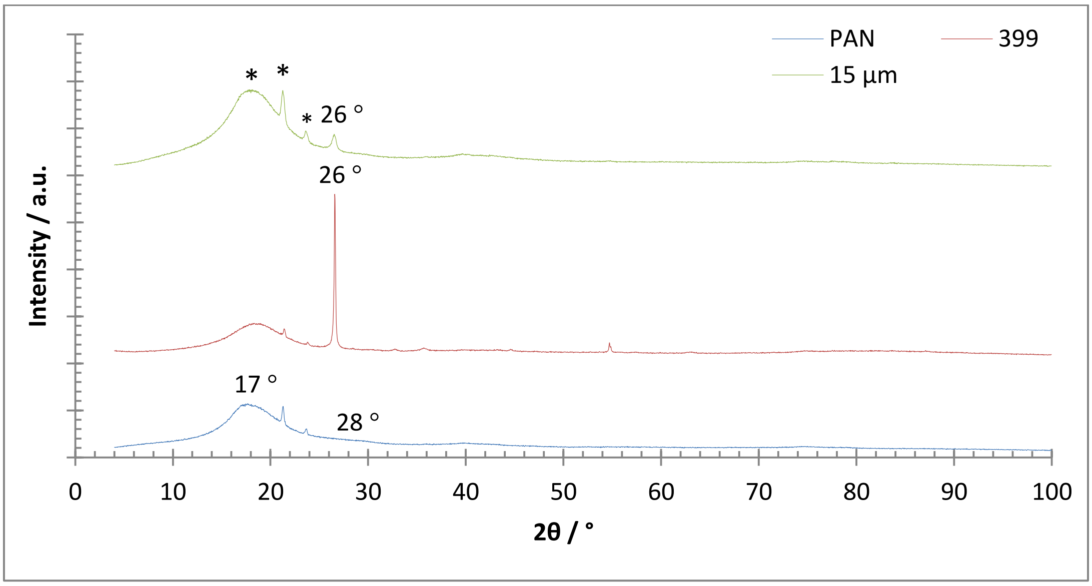

(a)

(b) 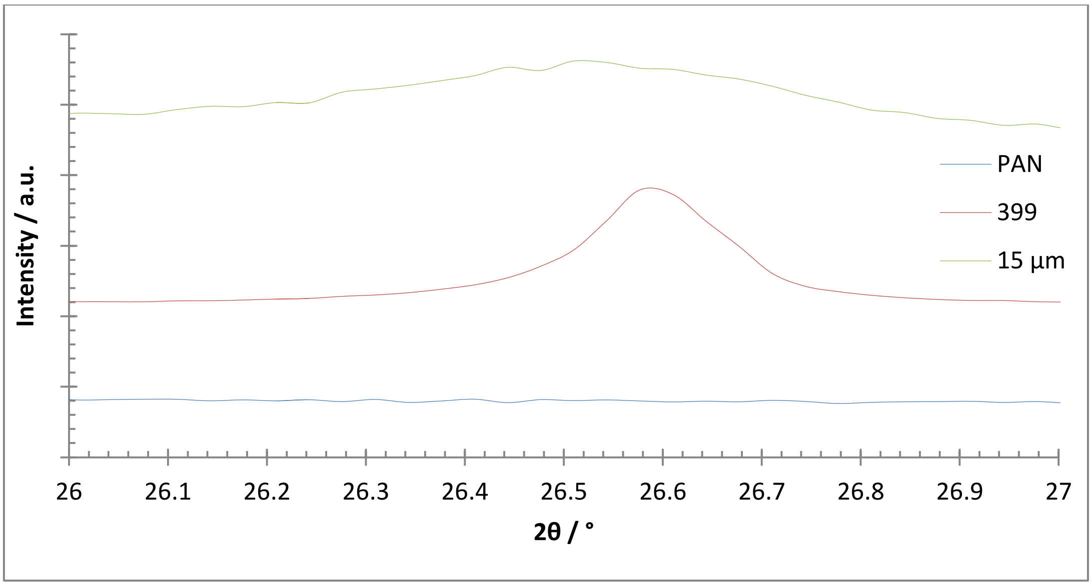

Figure 6.9: XRD patterns for the PAN, PAN spun with 5x exfoliated 399, and PAN spun with 5x exfoliated 15 µm graphite. The peaks are identified for clarity, with the impurities from the zero-background holder denoted by '*'. (a) the full spectrum; and (b) a focus on the exfoliated graphite peak at 2θ = ~ 26 °.

Thermal Gravimetric Analysis (TGA)

TGA was performed on the fibres in air to ascertain the thermal decomposition of the fibre material. **Figure 6.10** is an example spectrum, with the extracted key data given in **Table 6.2**. The thermal decomposition profile of the PAN-exfoliated graphite fibres closely resembles the PAN fibre, however there are additional mass loss events due to the graphene.

The first significant mass loss which occurs ~ 270 °C is due to the loss of some of the nitrile groups during the stabilisation phase, accounting for a small (~ 10 – 20 %) mass loss. The next event (~ 30 % weight loss) happens at ~ 400 °C and is due to the carbonisation of the PAN fibres, where the ladder is formed and N_2, HCN, and H_2 are lost. The next two steps at ~ 700 °C and ~ 800 °C, which do not appear with the pure PAN are sure to the burning of the graphitic exfoliated graphite. This is in line with the TGA from the pure exfoliated graphite. The composite fibres are slightly more stable to thermal decomposition as shown by the higher point of initial degradation. This stability is conferred through the higher burring point of graphene compared to PAN. The two fibres show similar behaviour until 600 °C, where the PAN-399 goes through an additional reaction through to 800 °C. This could be due to the impurities from the electrolyte in the electrochemically exfoliated 399, which decompose at higher temperatures, due to the stability of the electrochemically synthesised composites.

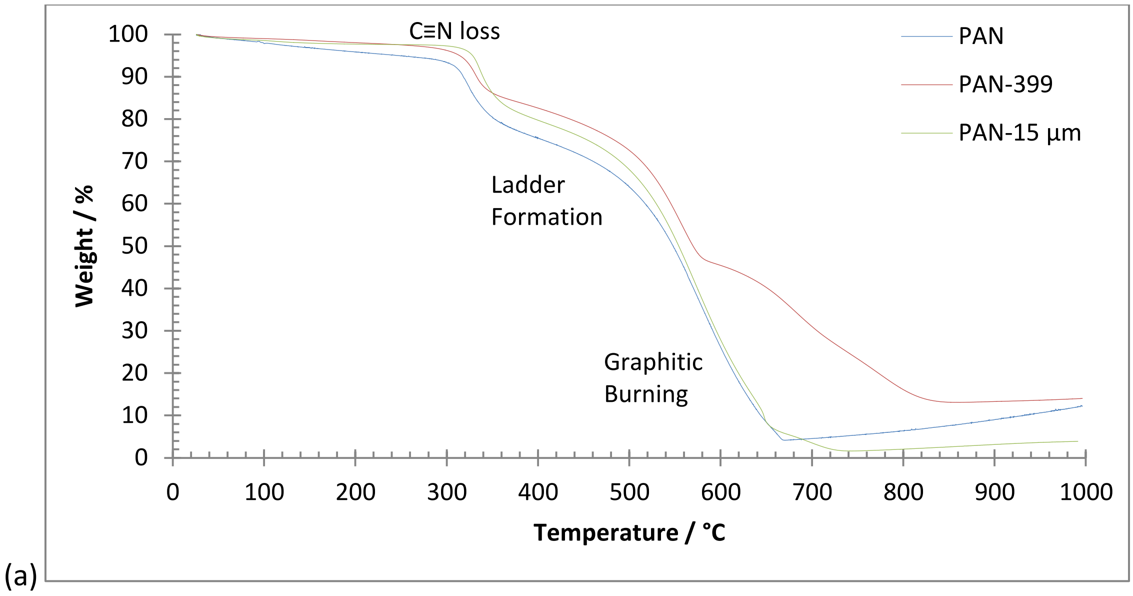

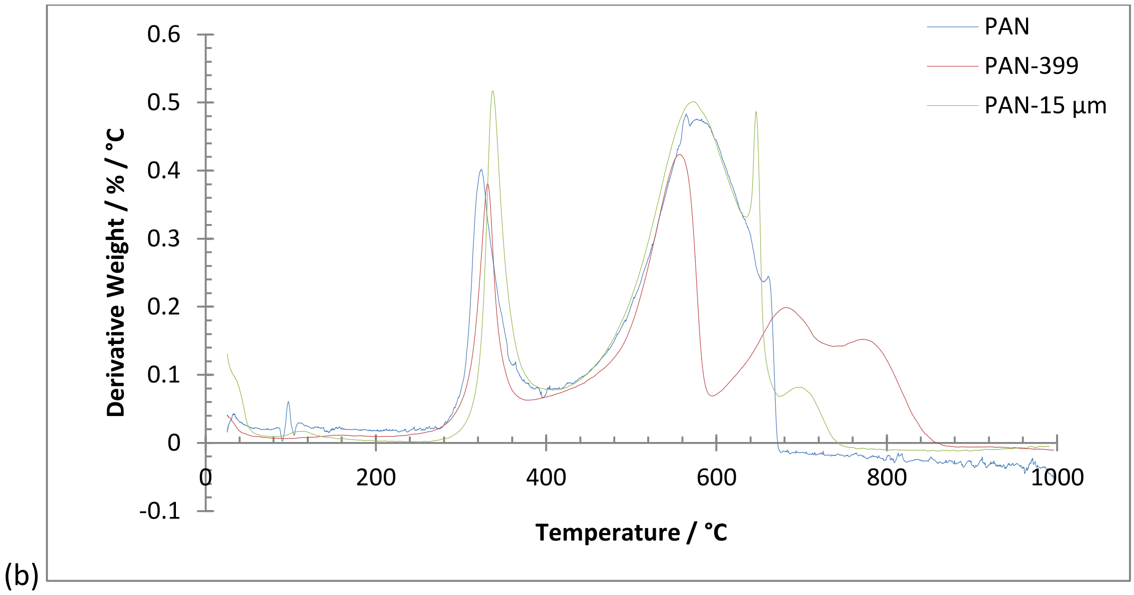

Figure 6.10: TGA spectra of the 5x electrochemically exfoliated graphite-PAN composite fibres. (a) the weight-loss curve; and (b) the derivative (temperature) weight-loss curve.

Sample	First Event / °C	Second Event / °C	Third Event / °C	Fourth Event / %	Final Event End / %	End Mass / %
PAN	285.3 ± 4.3	425.0 ± 14.0	N/A	N/A	677.2 ± 0.0	16.1 ± 6.1
15 µm - PAN	275.4 ± 0.0	419.5 ± 10.9	619.0 ± 9.1	658.8 ± 10.9	745.1 ± 12.7	2.7 ± 1.7
399 - PAN	272.2 ± 1.3	400.5 ± 15.4	595.3 ± 0.0	739.1 ± 2.6	863.7 ± 1.3	14.6 ± 0.8

Table 6.2: Data obtained from the TGA spectra of the 5x electrochemically exfoliated graphite-PAN composite fibres.

Infra-Red Spectroscopy

FTIR was used to confirm the presence of graphene within the PAN polymer (**Figure 6.11**). The peaks at 2240 cm^{-1}, 2940 cm^{-1}, and 1452 cm^{-1} are due to the presence of a nitrile C≡N group (stretch), -CH group (stretch) and -CH$_2$ group (bend) respectively, as seen in the pure PAN fibres. Similarly, the peaks at 3100 cm^{-1} – 3700 cm^{-1}, 1620 cm^{-1} are due to the hygroscopic KBr absorbing water from the atmosphere. New peaks appear at 2917 cm^{-1}, and 1575 cm^{-1}, which are due to the aromatic C-H group (stretch), aromatic C=C group (bend), which are due to the additional exfoliated graphite.

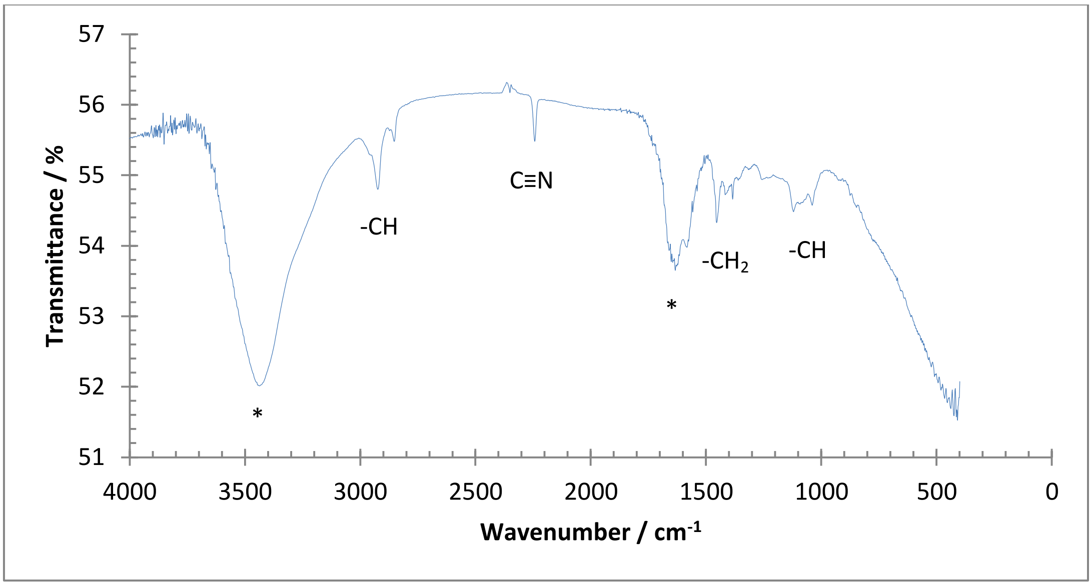

(a)

(b)

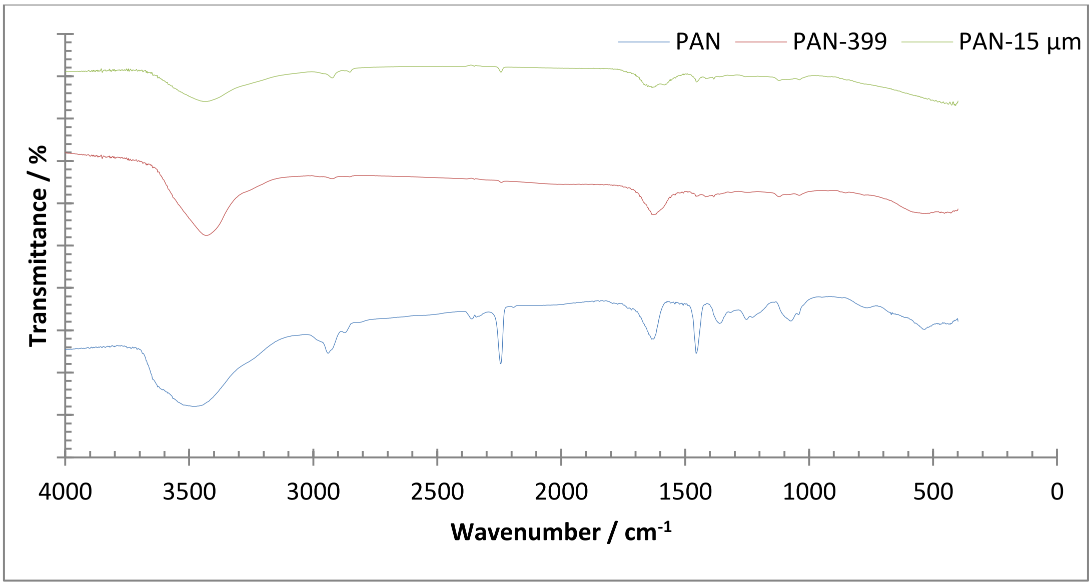

Figure 6.11: FTIR spectra for the PAN composite fibres. (a) PAN-15 µm graphite fibre; and (b) a comparison of all the exfoliated graphite-PAN fibres.

Summary

PAN-exfoliated graphite composite fibres were successfully spun from the composite dope. The SEM images show the presence of graphene through the graphene flakes that are on the surface of the fibre and incorporated throughout the inside of the fibre. Additionally Raman spectroscopy shows the characteristic graphene peaks (D, G, and 2D), XRD gives a large band at $2\theta = 26$ °, TGA shows graphitic burning, and FTIR has additional sp^2 carbon peaks.

The most important feature concerning the addition of graphene is whether the concentration of graphene in the fibre has changed, upon coagulation. The initial graphite had a graphene yield (< 10 layers) of 0 %. Upon exfoliation, the 399 and 15 µm graphite gave the best yield of graphene at ~ 20 – 30 % for both samples. In addition to using the above characterisation techniques, the graphene content was estimated using the shape, size, and position of the 2D band in 20 different Raman spectra. Each spectrum was assessed to see if it was < 10 layers of graphene on a pass / fail basis. The PAN-graphene fibres have an estimated graphene content of ~ 10 % ± 5 % for both fibres, when only assessing the sp^2 carbon material in the fibre. This suggests that the act of coagulation has re-stacked some of the graphene sheets. Coagulation requires tight bonds between the graphitic sheets in order to form a continuous fibre. The flat, planar structure of the initial exfoliated graphite would promote this re-stacking. These fibres will be carbonised in order, to develop carbon fibre-graphene composites. Carbonisation will improve the mechanical performance of the fibres, making them more robust, while also reducing the weight of the fibres, via the loss of the nitrile group. This will in turn increase the capacitance (in terms of F g^{-1}). Additionally, the carbon fibre composite will have a higher graphitic content, with a large sp^2 carbon network. This will allow for a higher number of EDL sites, and increase the charge propagation through the fibre.

6.3 Characterisation of Carbonised Fibres

Carbon fibres were synthesised from the PAN fibre precursors via a heat treatment. This treatment was to strengthen the fibres and improve their electrical conductivity.

After carbonisation, it was noticed that the fibres became more brittle and graphitic material was commonly found in-between the fibres. This is likely from the graphite foil, which the fibres are placed in during heat treatment. The PAN based fibres underwent a colour change from white to black after carbonisation, due to the formation of a conjugated network, which grants colour absorbance.

Electron Microscopy

SEM was used to probe the change in topography of the fibres upon carbonisation (**Figure 6.12**). The average diameter of the carbonised fibres was found to be 115.35 ± 11.97 µm, which is 55% of the size of the original PAN fibres. This reduction in size is due to the loss of a significant part of the molecule, along with the cyclisation of the fibre. The topology of the fibre is still smooth with some rippling. There are additional features in the form of the porous centre, which now shows on the surface of the material. This may be due to the cyclisation reactions deforming the fibre due to the loss of the nitrile group. This centre has an open pore structure, similar to foam, which increases the surface area of the fibre dramatically. This is good for supercapacitor applications as the increase in accessible surface area will correspond to an increase in sites which electrolyte can penetrate and form electrical double layers (EDLs) when charged. The pores are large(µm scale), which is ideal in terms of macro-pores. Studies report that mesoporous and macroporous materials (any pore above 50 nm) can facilitate electrolyte diffusion which improves the EDLC performance. This is especially prevalent at higher charge rates. This diffusion can also carry the electrolyte to micro-pore adsorption sites, which will form EDLs. Smaller pores (< 0.5 nm) will inhibit EDL formation due to their size.[136]

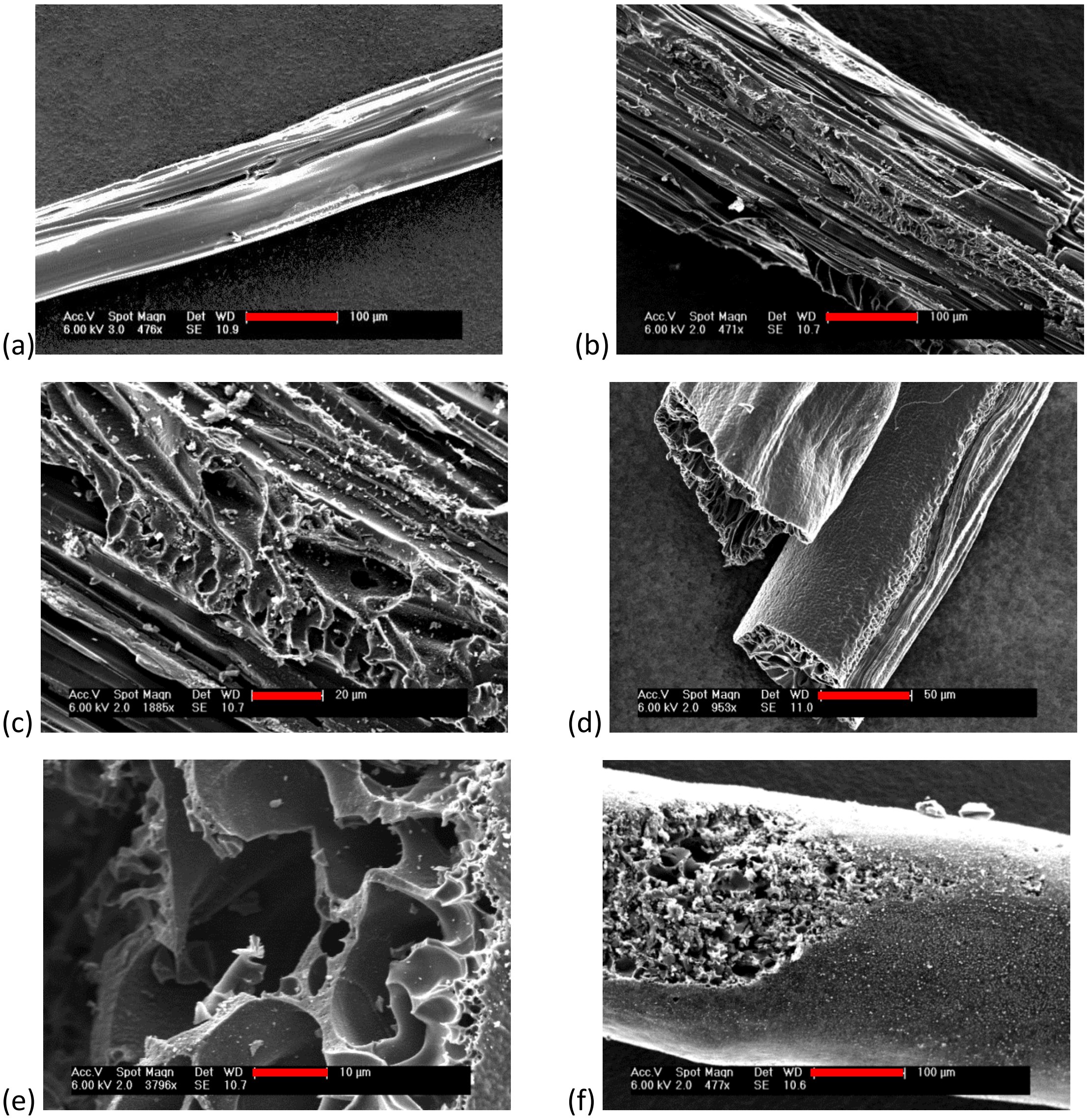

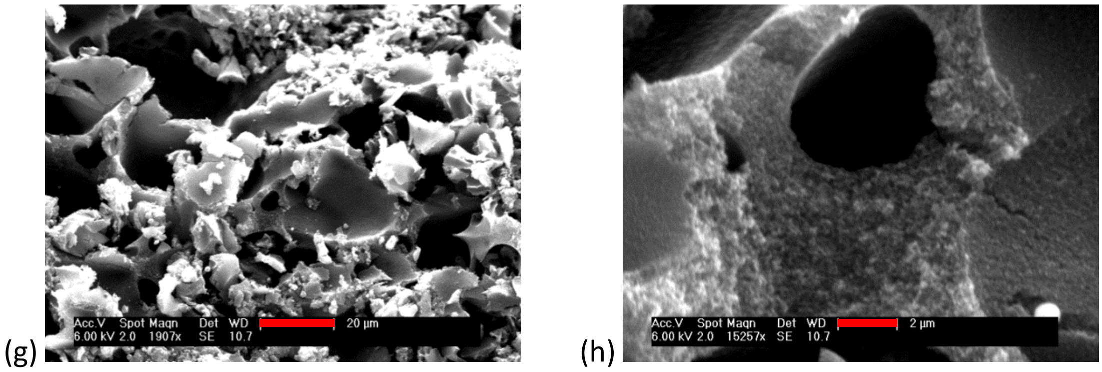

Figure 6.12: A selection of SEM images of the carbonised PAN fibres. (a-c) the topography of carbonised PAN fibres; (d-e) the surface and internal topography of the same fibre; and (f-h) images showing successive magnification on the same spot of a fibre to view the inside.

Raman Spectroscopy

Figure 6.13 shows the Raman spectrum obtained from the carbon fibres**.** The Raman spectrum of the carbon fibres shows that the prominent peak at around 2440 cm^{-1} for the nitrile group in the PAN fibres is now completely gone. Note: as carbon sp^2 bands are resonant with the laser in Raman spectroscopy, which could drown out or obscure the nitrile band if it is present. However this band is seen in the graphene-PAN composite fibres before heat treatment and it is absent in the IR of the carbon fibres, thus confirming the absence of the nitrile group. This is evidence of the successful carbonisation of the PAN fibres. The peak at 1323.7 ± 0.7 cm^{-1} can be attributed to the D mode of sp^2 carbons. This appears in non-graphitized fibres that have been synthesised at lower temperatures, i.e. fibres such as these. This mode is assigned to the A_{1g} vibrational mode.[190]

The peak at 1583.9 ± 1.2 cm^{-1} can be attributed to the G band of sp^2 carbon which is found in all carbon materials. This is assigned the vibrational mode E_{2g}.[190] The peak at 2617.7 ± 1.6 cm^{-1} is the 2D peak and, as in graphite, it appears from an overtone of the D peak. This disorder peak is common in non-graphitized carbon fibres. This disorder can also be in the form of small crystallite sizes.[231] The crystallite size can be calculated using a variation of the Knight formula[232] for lasers of different wavelengths. This new Cancado formula[233] (**Equation 15**) is:

$$La\ (nm) = \frac{560}{E_1^4}\left(\frac{I'_D}{I'_G}\right)^{-1}$$ **Equation 15**

where the integrated intensity of the two Raman peaks, D and G (I_D’ and I_G’) are inversely proportional to the laser excitation energy (E_1). For a 633 nm laser, this excitation energy is 1.94 eV. Thus the crystallite size can be calculated as 17.9 nm for the carbon fibre.

A peak would appear from highly crystalline graphitized fibres from 2690 cm^{-1} – 2730 cm^{-1}. This is from the G’ band, an overtone of the D band, and only occurs by very high temperature graphitization, and not carbonisation. At temperatures over 3000 °C this peak will split in two.[231] The very minor peak at 2903.3 ± 1.560.7 cm^{-1} can be attributed G’’ band.

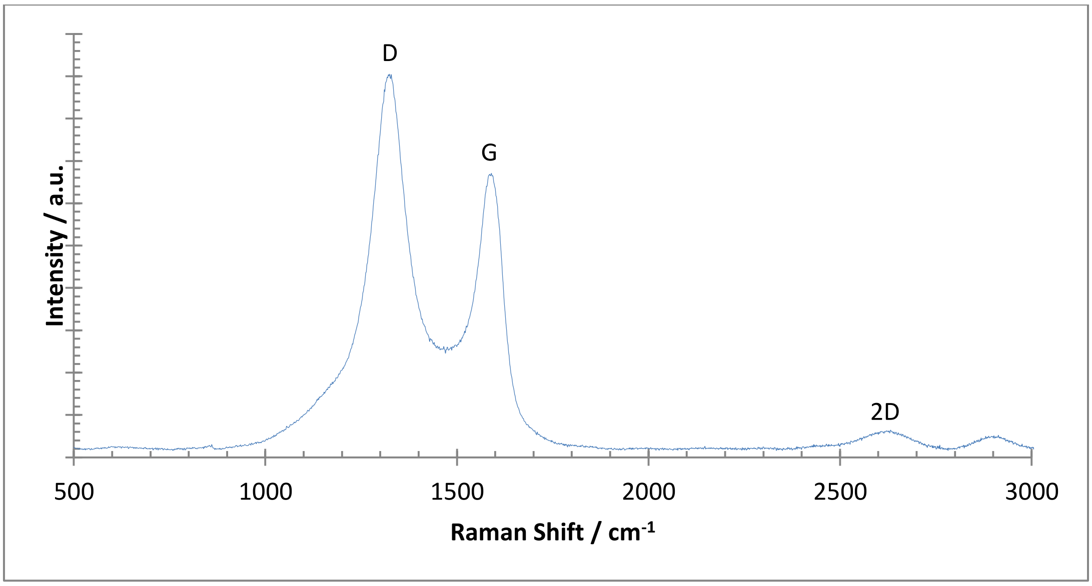

(a)

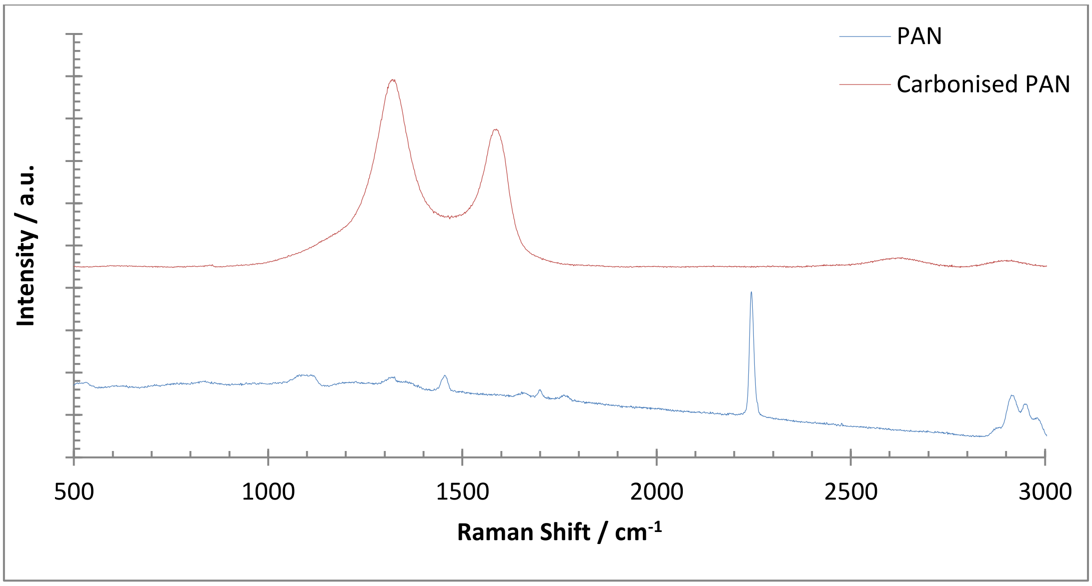

(b)

Figure 6.13: The Raman spectrum of: (a) carbonised PAN; and (b); PAN and carbonised PAN, with the background removed. The two peaks at ~2250 cm^{-1} and 2900 cm^{-1} disappear and three peaks at ~1350 cm^{-1}, ~1600 cm^{-1}, and ~ 2600 cm^{-1} appear.

X-Ray Diffraction

Figure 6.14 shows the XRD pattern of the carbonised PAN fibres. Analysis again proved was difficult due to large backgrounds provided from the zero background holders at positions where PAN peaks occur.

The carbonised PAN has prominent peaks at 2θ = 24.91 ± 0.48 ° and 42.33 ± 0.30 °,[4] which appear due to the 00.2 and 10. (10.0 and 10.1 overlapped) planes respectively.[234, 235] The new peak at 2θ = 25 ° appears due to the formation of the graphitic carbon from the cyclisation reactions, with a corresponding d-spacing of 3.65 Å. The peaks at ~ 2θ = 17 ° and 28 ° from the PAN precursor, which pertain to the 10.0 and 10.1 plane are no longer present after heating. The increase in the intensity of the 00.2 peak, and decrease in intensity of the 10. peak shows carbonisation has taken place.

The stabilisation index of carbon fibres can usually be calculated using the 10.0 peak, as a disruption to the orientation of the planes and crystalline structure will increase the full width half maximum (FWHM) of the peak. However due to the large background from the silicon wafer, which obscures the peak at ~ 2θ = 16 °, this cannot be calculated.

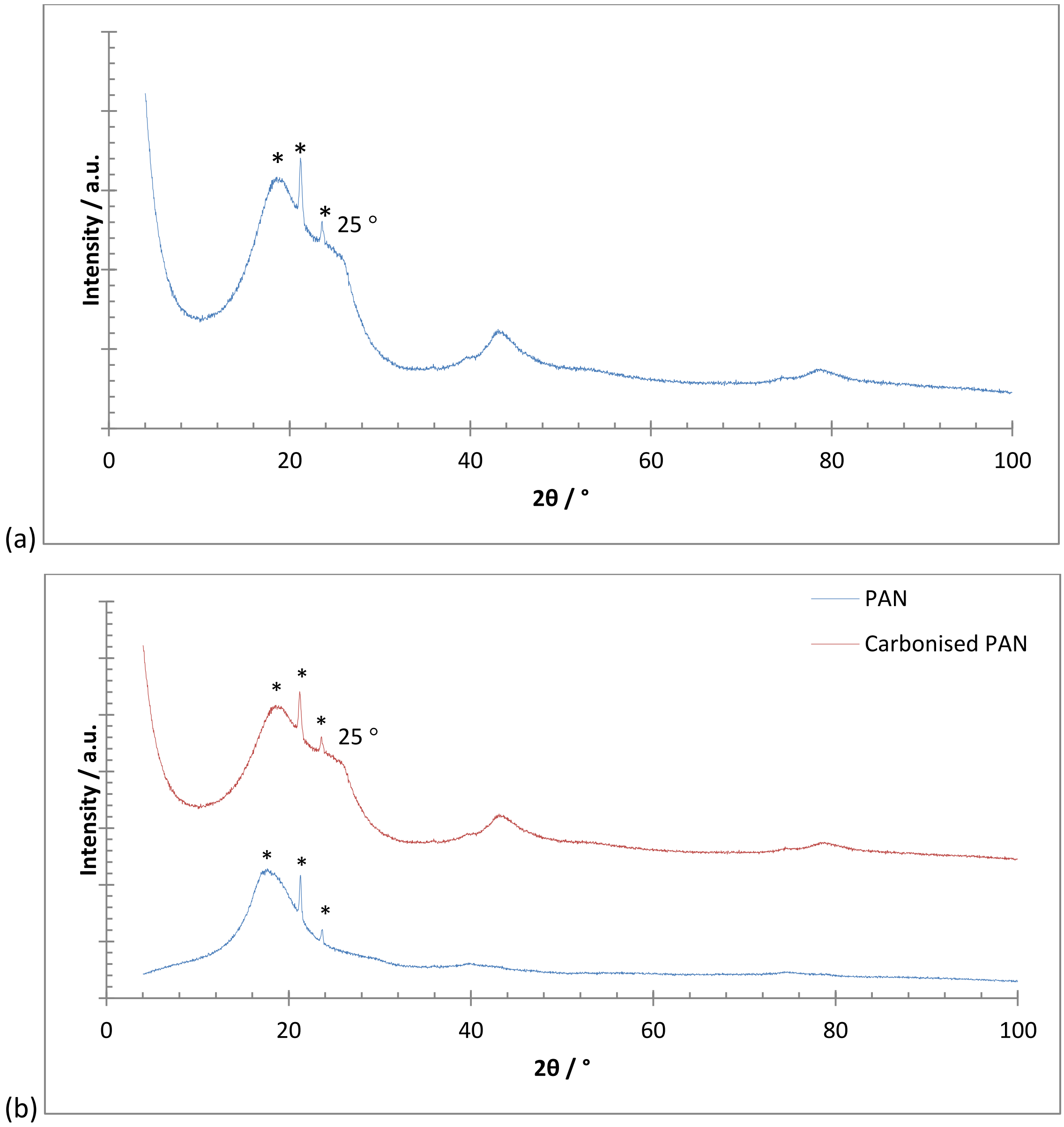

Figure 6.14: The XRD pattern of: (a) the carbonised PAN fibre; and (b) the PAN and carbonised PAN fibres.

Thermal Gravimetric Analysis

Figure 6.15 is the TGA spectrum of the carbonised and original PAN fibres. The carbonised fibre undergoes two mass loss events. A small mass loss (~ 5 %) occurs at 464.6 ± 5.5 °C with a larger mass loss event (~ 90 %) at 533.6 ± 5.5 °C. Both of these events are due to the oxidation of the graphitic network. The increased mass loss in the PAN at ~ 300 °C due to the loss of the nitrile group is no longer present, indicating efficient carbonisation. The end weight is less than the PAN fibre at 5.35 ± 3.80 %, rather than 16.61 ± 6.13 %.

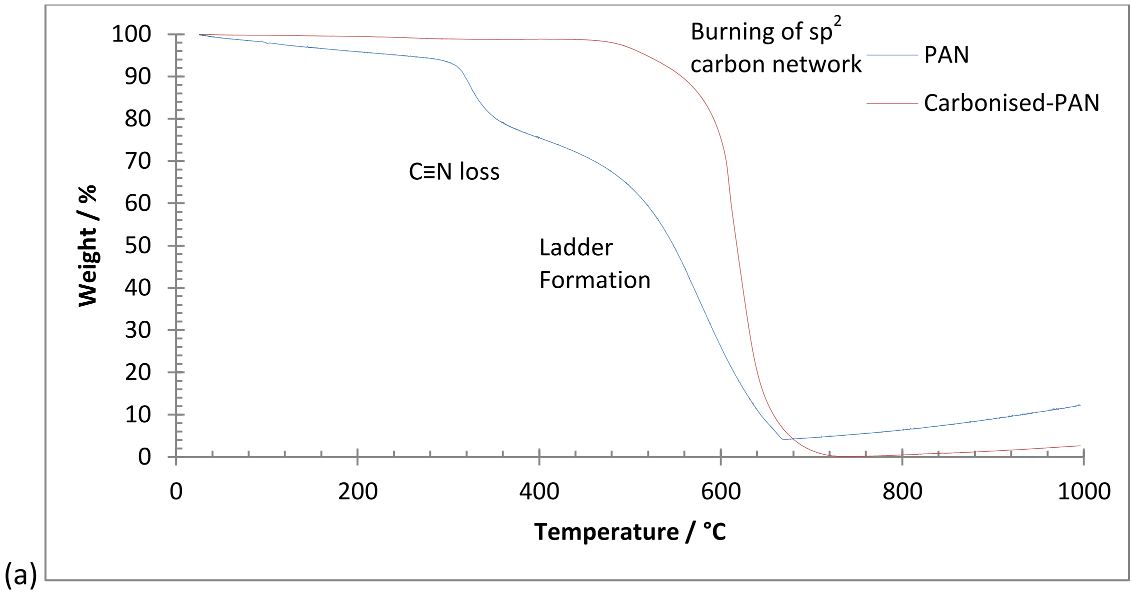

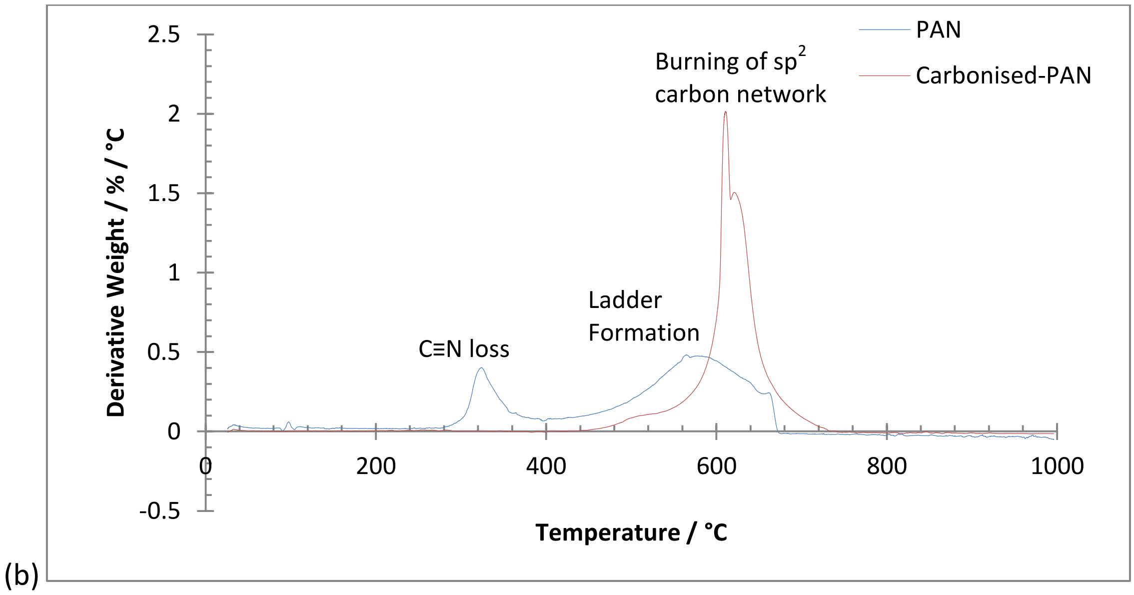

Figure 6.15: TGA spectra of the carbonised PAN fibres conducted in an air atmosphere. (a) the weight-loss curve; and (b) the derivative (temperature) weight-loss curve.

Infra-Red Spectroscopy

Figure 6.16 shows the IR spectrum of carbonised fibres. The two peaks which were very prominent in the PAN IR spectrum at 2940 cm^{-1} and 2240 cm^{-1} (corresponding to the –CH and C≡N stretch respectively) have almost completely disappeared. This is due to the cyclisation of the acrylonitrile. The new peak at 1600 cm^{-1} is due to C=N formation, which occurs after cyclisation. New peaks have formed around 800 cm^{-1} and 1600 cm^{-1}, which is due to the formation of C=C, =C-H bonds.[236]

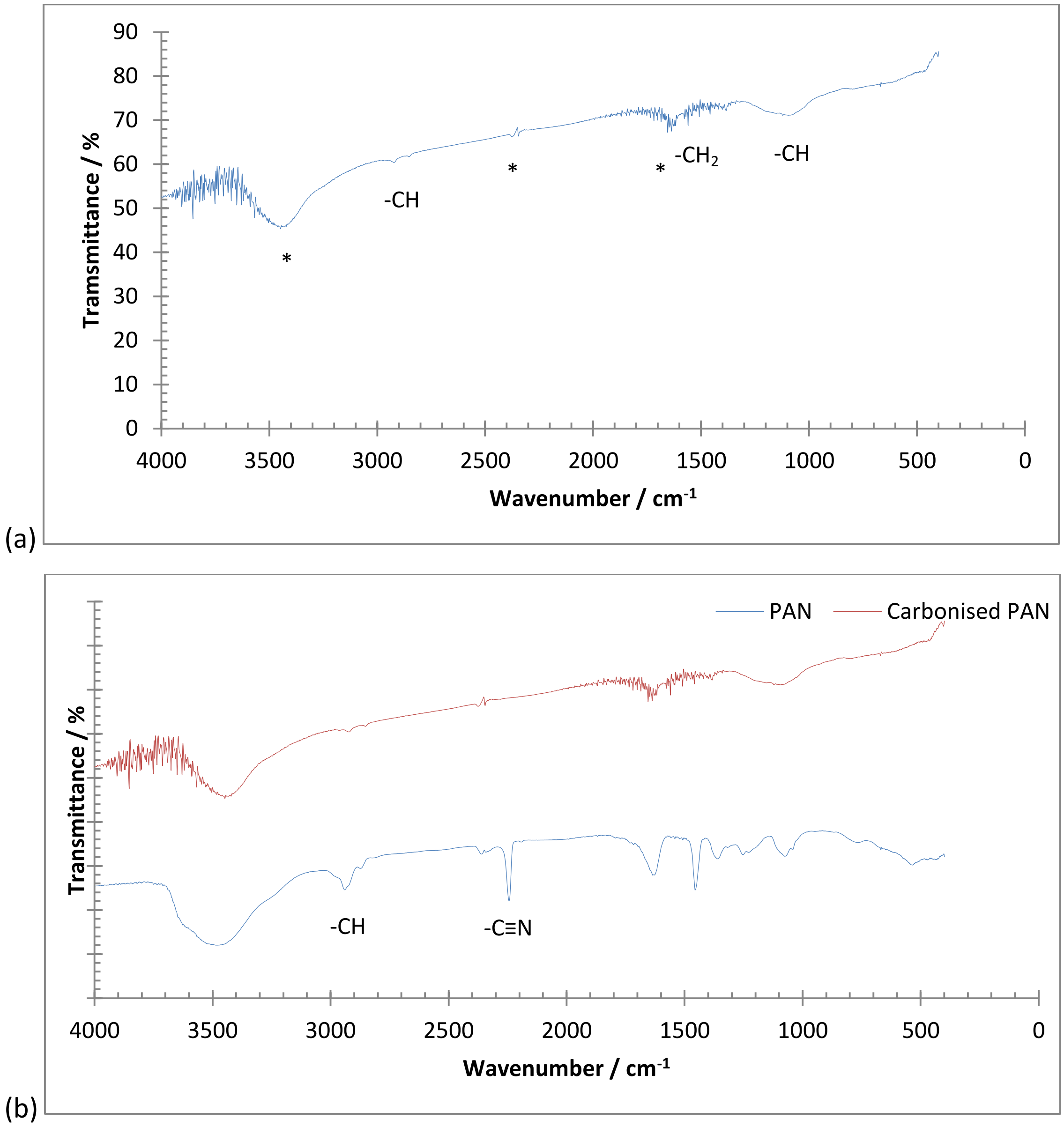

Figure 6.16: The FTIR spectrum of: (a) carbonised PAN fibres; and (b) PAN and carbonised PAN fibres.

Summary

The wet-spun PAN fibres were successfully carbonised. This can be seen in the dramatic change in the Raman spectrum, indicating the restoration of the sp^2 hexagonal carbon network, the new peak ~ $2\theta = 25$ °, representing the formation of carbon fibres, and the lack of C≡N group in the TGA and FTIR spectra. SEM shows the fibres have retained their porous centre. The nitrile group has been removed from the PAN fibres, allowing for cyclization and ladder formation at high temperatures. This produces the carbon fibre.

This step was performed to compare neat carbon fibres with graphene-functionalised ones. By doing this, the contribution of graphene to the carbon fibres can be assessed. Additionally, the successful carbonisation of PAN shows that the method of carbonisation (specific heat ramping) is successful and should allow for the carbonisation of the PAN-graphene composites, where the characterisation can prove more difficult due to the sp^2 carbon content in the graphene obscuring the formation of new sp^2 carbon content in the fibre.

6.4 Characterisation of the Graphene Carbonised Fibres

The wet-spun PAN-graphene fibres were also carbonised for ultimately testing for electrochemical performance.

Unlike with the pure PAN fibres, the colour change could not be observed as the fibres were already quite dark due to the presence of exfoliated graphite. In order to image the material, the PAN fibres with graphene had to be coated in gold to avoid electron scattering by charging, which distorts the image. This was not the case for the carbonised composite fibres.

Scanning Electron Microscopy

Figure 6.17 shows SEM images of the graphene infiltrated carbon fibres. The original PAN based exfoliated graphite fibres had an extremely ordered surface where occasionally the presence of graphite could be optically identified. The carbonised fibres have a more rough texture. This is due to the decomposition and cyclisation of the PAN which could warp the surface of the carbonised fibres. There are also no places where the graphite can be identified, as the whole fibre is graphitic. The inside of the fibre is less densely porous, with large hollow area. The composite fibres have collapsed as they appear flat during examination. This is due to the removal of the porous structure inside the fibres, which is present in the neat carbon fibre.

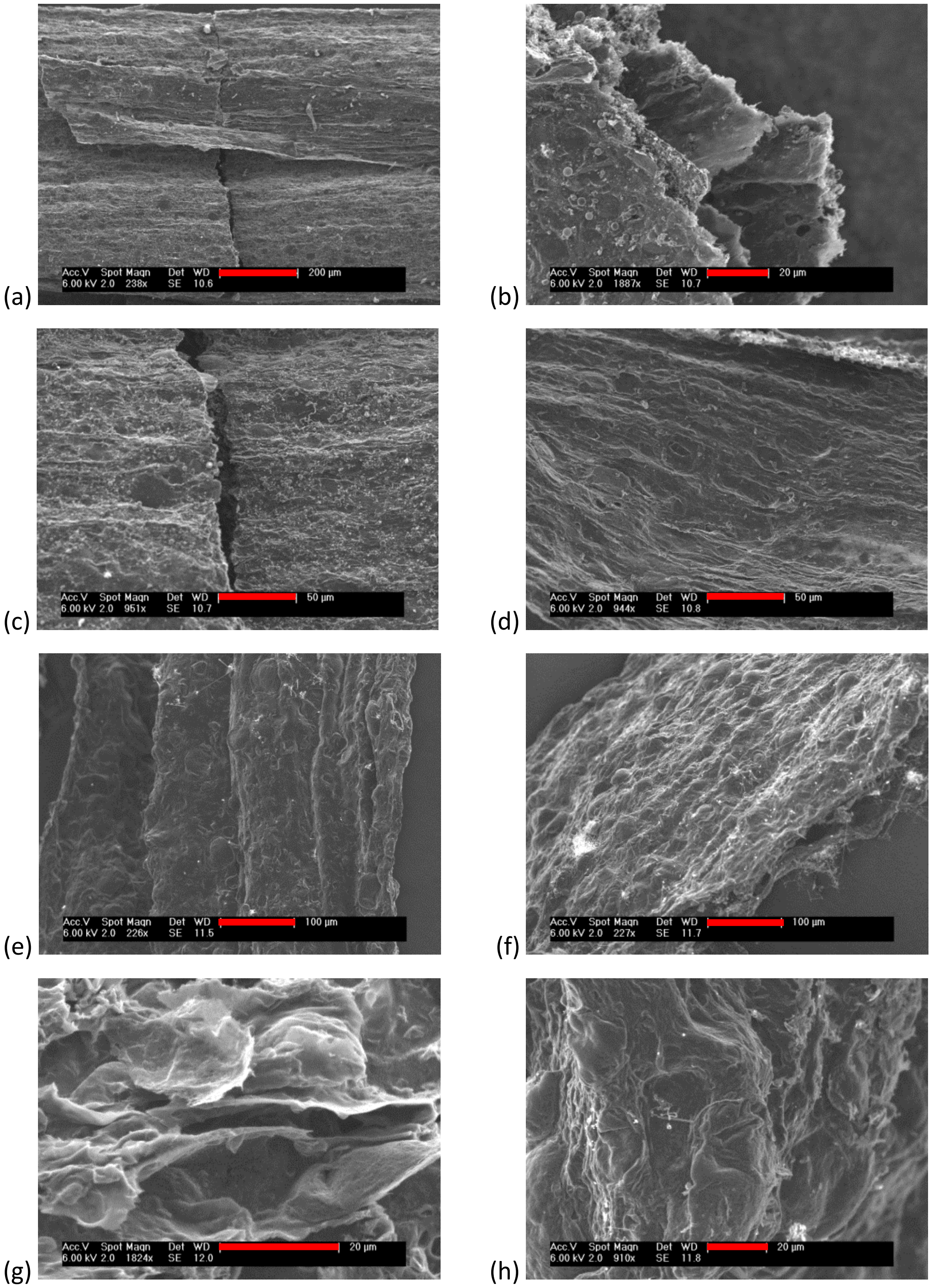

Figure 6.17: SEM images of the carbonised PAN-exfoliated graphite. (a-d) carbonised PAN-399 fibres; (e-h) carbonised PAN-15 µm fibres.

Raman Spectroscopy

Figure 6.18 shows the Raman spectra of the carbonised PAN fibres, with key Raman data in (**Table 6.3**).

The wet-spun carbonised PAN fibres with graphene do not contain the nitrile group PAN peak (2244 cm^{-1}), confirming that the fibres were successfully carbonised. The 2D peak has shifted to a lower wavelength compared to the PAN based-graphene composite fibres. This could suggest that the heat treatment provided additional exfoliation on the graphene in the fibre in an inert atmosphere. When PAN undergoes thermal conversion, gases are released including C≡N and H_2.[123] This could create pressures exceeding the van der Waal forces between the graphitic sheets, exfoliating the graphite further, as seen in graphene oxide.[96] Graphene can also be exfoliated at high temperatures. These processes could exfoliate the fibre in-situ. The presence of exfoliated graphite has increased the I_{2D}/I_G ratio in relation to the carbonised fibres. The peak at ~2910 cm^{-1} is due to the D + G band and not the PAN -CH_2 peak at ~2935 cm^{-1}.

There is a large difference in the D/G ratio between the fibres. The neat carbon fibre has the highest D/G ratio meaning there are smaller / more carbon sites. The addition of the exfoliated graphite reduces this ratio, causing the number of defect sites to be reduced. The crystallite size was again calculated using the Cancado formula (**Equation 15**).[233] For the carbonised-399 graphite the crystallite size was 36.7 nm, while for the carbonised PAN-15 µm graphite the crystallite size was 21.8 nm. For the original carbonised material the crystallite size is 17.9 nm, suggesting that the crystallite size has increased when graphene has added for both species. This suggests graphene acts as a nucleating agent increasing the crystallinity of the fibre.

Sample	D Peak / cm^{-1}	G Peak / cm^{-1}	2D Peak / cm^{-1}	D+G Peak / cm^{-1}	I_D/I_G	I_{2D}/I_G
Carbonised PAN	1323.7 ± 0.7	1583.9 ± 1.2	2617.7 ± 1.6	2903.3 ± 1.6	1.41	0.06
Carbonised	1330.8 ±	1585.5 ±	2647.3 ±	2910.5 ± 10.6	0.92	0.23

15 µm	2.7	3.6	20.3			
Carbonised 399	1329.2 ± 3.5	1578.6 ± 3.3	2655.8 ± 5.1	2915.5 ± 7.7	0.51	0.51

Table 6.3: A table showing the peak positions of the major bands in the carbonised fibres, and graphite carbon fibre composites.

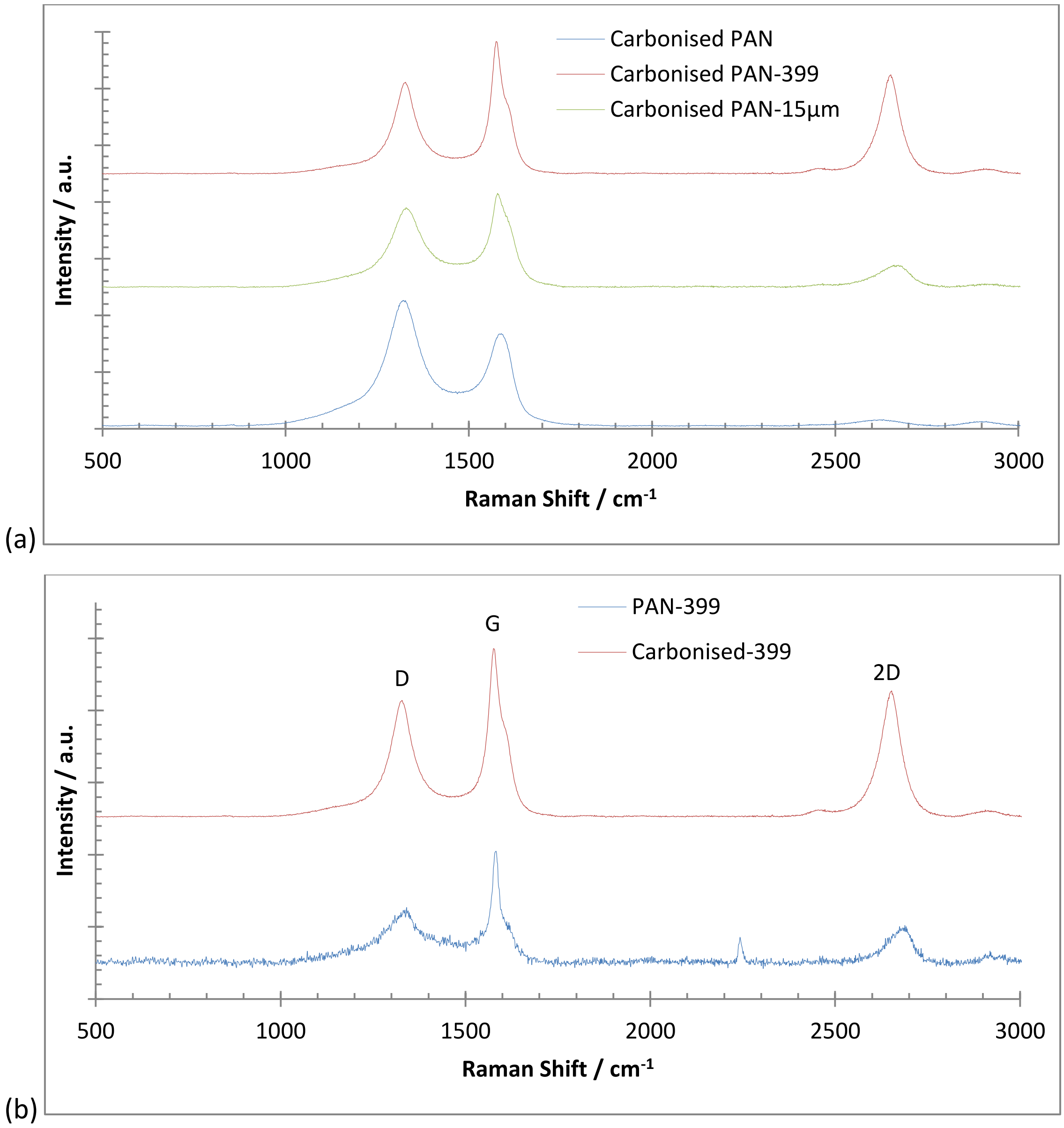

Figure 6.18: Example Raman spectra of: (a) the carbonised wet-spun PAN, PAN-15 µm, and PAN-399; and (b) the un-carbonised and carbonised PAN-399 fibre. Note: the PAN-399 spectra needed to be multiplied by a factor of 10 to make the peaks comparable in height for the carbonised-399 for comparison.

Polarised Raman was also performed on the material (**Figure 6.19**). This spectrum shows the normalised intensity of the Raman peaks is high from 30 ° to 70 ° and 100 ° to 170 °, while it falls off from 0 ° to 20 °, 80 ° to 90 ° and at 180 °. This suggests the material has some sort of polarity, which is due to the alignment of the graphite flakes within the fibre. This is caused by the wet spinning process. There is a uniaxial flow during extrusion into the coagulation bath. This changes the random alignment of the sheets, to make them oriented with the fibre axis. This is also facilitated by with quick coagulation, quickly aligning the sheets.

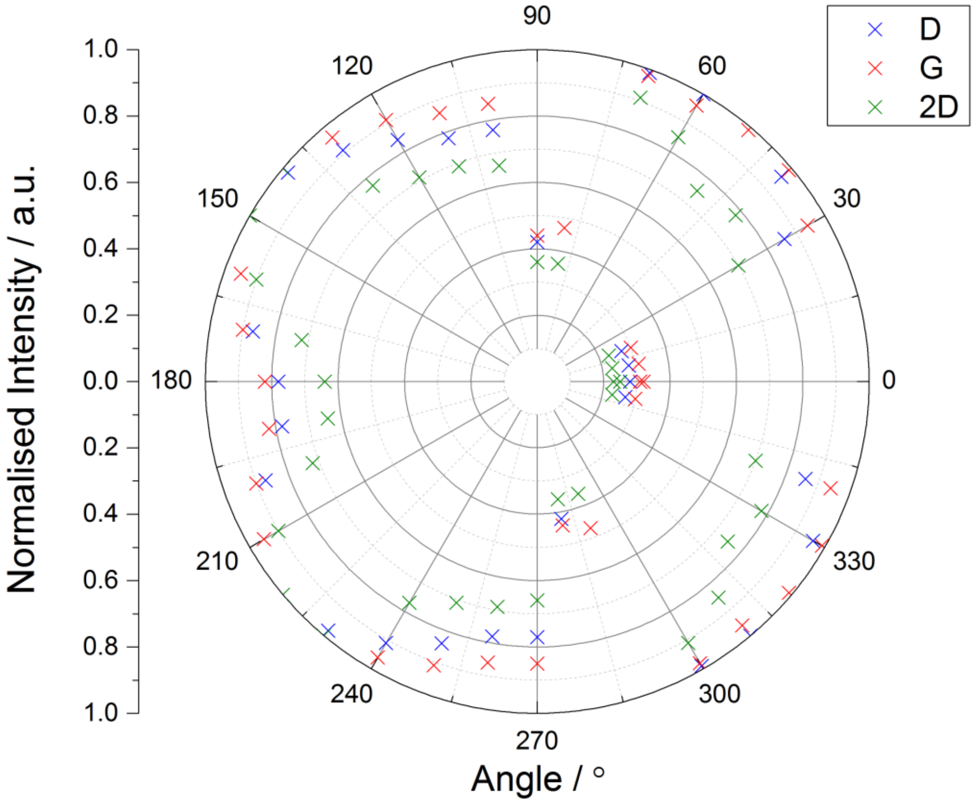

Figure 6.19: Polarised Raman spectrum from 0 to 180 ° of 5x exfoliated 15 µm graphite carbon fibre.

X-Ray Diffraction

Figure 6.20 shows the XRD patterns for the carbonised 5x electrochemically exfoliated graphite fibre. The most notable change from the pure carbon fibres is the new peak at ~2θ = 26 °, which is from the exfoliated graphite. These appear at 2θ = 26.56 ± 0.15 ° for the 399-carbon fibre and 2θ = 26.37 ± 0.03 ° for the 15 µm-carbon fibre. These confer to a d-spacing of 3.44 and 3.45 Å respectively. In comparison to the PAN based graphite infiltrated fibres, there is a new peak at 2θ = 25 °, due to the formation of the hexagonal structure of the carbon fibre. This appears at 2θ = 24.87 ± 0.35 ° for the 399-carbon fibre and 2θ = 25.01 ± 0.05 ° for the 15 µm-carbon fibre, which pertains to a d-spacing of 3.34 Å and 3.44 Å respectively.

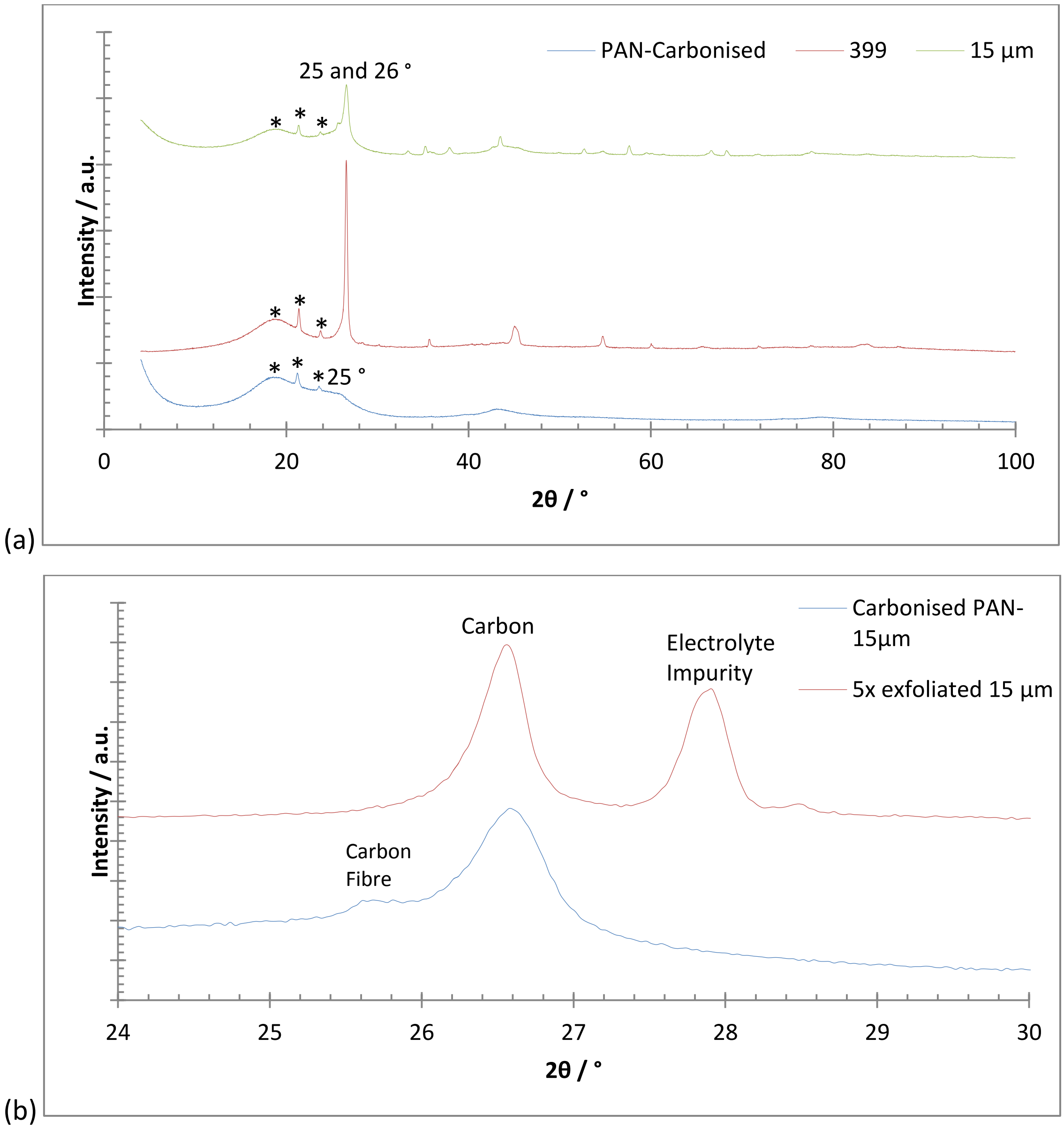

Figure 6.20: The XRD patterns for: (a) the carbonised-PAN and the PAN with electrochemically exfoliated 399 and 15 µm graphite; and (b) the XRD pattern of the carbonised 15 µm-PAN fibre and initial graphite used (5x aluminium cage electrochemically exfoliated 15 µm graphite) with an focus on the peak at 2θ = 25 ° and 26 °.

Thermal Gravimetric Analysis

Figure 6.21 is the TGA spectra for the carbonised fibre composites, while the data can be viewed in **Table 6.4**.

The fibres undergo two mass loss events at ~ 500 °C and 700 °C, finally finishing at ~ 850 °C. These spectra are typical for carbon fibre as the previous heat treatment has removed all functional groups prone to loss, meaning there are fewer mass loss events that the PAN fibre and composites.[230] The carbonised 399 fibre has an additional slope which is not present in the other carbonised fibres. This slope in the 399-carbonised fibre also appears in the PAN-399 fibre. This slope at 700 °C indicates more reactions happening during heating, which are likely due to impurities in the fibre from the electrolyte in the electrochemically exfoliated 399. These electrolyte impurities will decompose at higher temperatures, due to the stability of the electrochemically synthesised composites. The mass loss event that occurred in the PAN based precursor at ~ 270 °C due to the loss of some nitrile groups, does not happen here as these nitrile groups have gone during the stabilisation step. The next mass loss event – the ladder formation at ~ 400 °C is likewise absent. The end temperature is higher than the PAN based precursors due the stabilisation of the hexagonal sp^2 carbon structure. The end temperature is also higher than the pure carbonised PAN fibres, again suggesting the addition of exfoliated graphite stabilises the fibre against thermal decomposition.

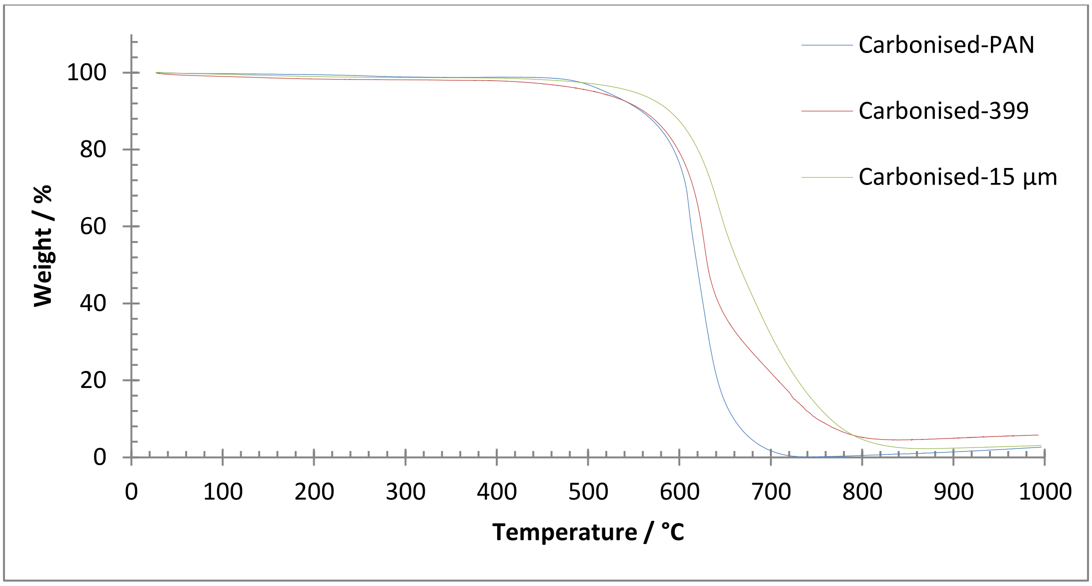
Carbonised-PAN
Carbonised-399
Carbonised-15 µm
Weight / %
0
20
40
60
80
100
0
100
200
300
400
500
600
700
800
900
1000
Temperature / °C

(a)

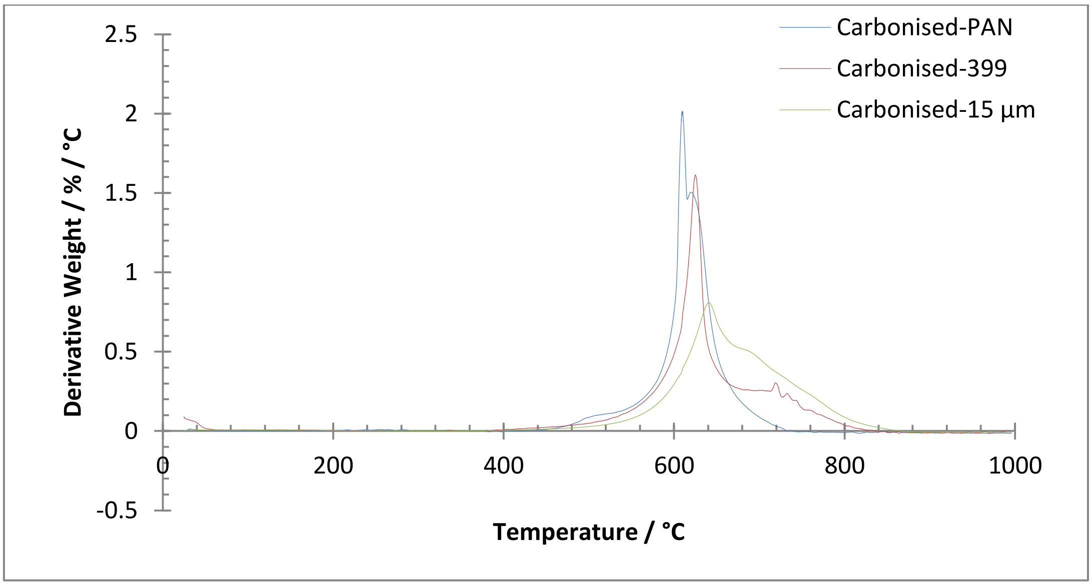
Carbonised-PAN
Carbonised-399
Carbonised-15 µm
Derivative Weight / % / °C
2.5
2
1.5
1
0.5
0
-0.5
0
200
400
600
800
1000
Temperature / °C

(b)

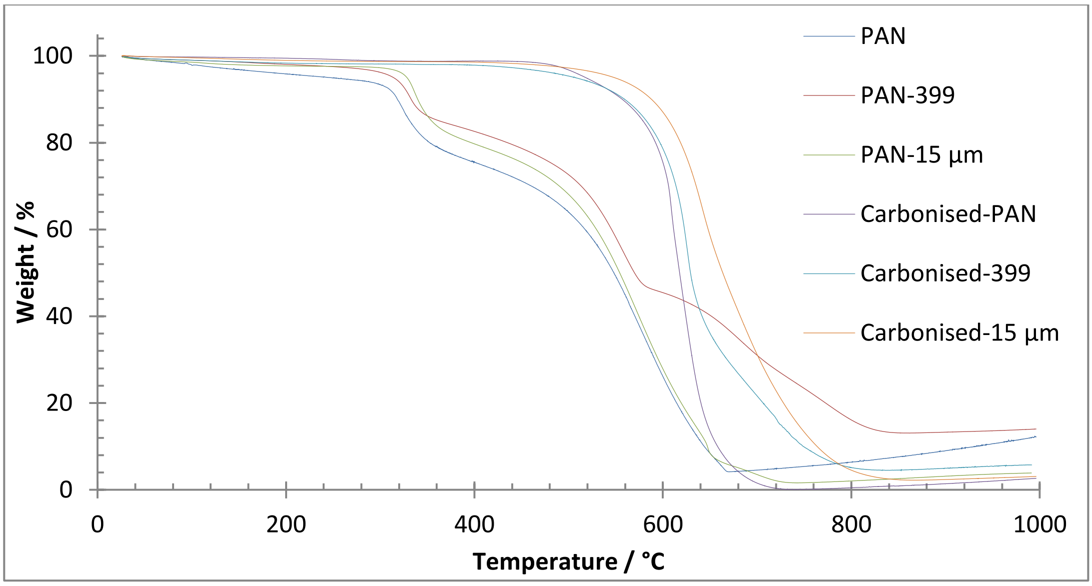
PAN
PAN-399
PAN-15 µm
Carbonised-PAN
Carbonised-399
Carbonised-15 µm
Weight / %
0
20
40
60
80
100
0
200
400
600
800
1000
Temperature / °C

(c)

Figure 6.21: TGA spectra of the carbonised composite fibres. (a) the carbonised fibres weight-loss curve; (b) the derivative (temperature) weight-loss curve; and (c) the carbonised and un-carbonised PAN fibres.

Carbonised Sample	First Event / °C	Final Event / °C	Final Event End / %	End Mass / %
PAN	464.6 ± 5.5	536.6 ± 5.5	734.8 ± 1.8	5.4 ± 3.8
15 µm - PAN	489.0 ± 7.3	685.9 ± 1.8	866.0 ± 1.8	3.3 ± 0.3
399 - PAN	548.2 ± 3.6	787.5 ± 3.6	890.5 ± 3.6	4.6 ± 3.0

Table 6.4: Table of TGA data for the carbonised fibres.

Infra-Red Spectroscopy

FTIR was performed to analyse the functional groups in the material (**Figure 6.22**). The spectra contain all the relevant carbon fibre and graphite peaks which appear at 2933 cm^{-1} for aromatic C-H (stretch), 1630 cm^{-1} for aromatic C=C (bend), and 1150 cm^{-1} for =C-H (bend), and 792 cm^{-1} for the aromatic C-H (bend). The prominent peak at 2244 cm^{-1} for the PAN is no longer present, confirming the loss of the nitrile (C≡N) group.

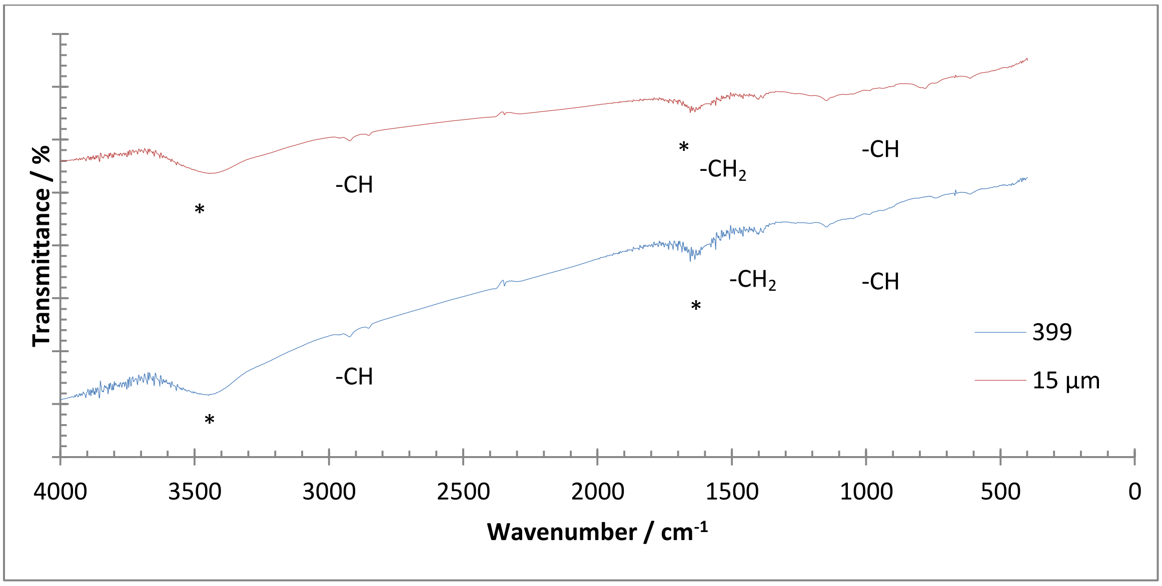

Figure 6.22: FTIR spectra for the carbonised exfoliated graphite fibres. The '*' refer to impurities from the KBr disc.

Summary

The PAN-exfoliated graphite composite fibres were successfully carbonised to form carbon fibres. This was confirmed with Raman spectra showing no peak at ~ 2244 cm^{-1} due to the C≡N group in the PAN, the XRD patterns which have a new peak ~ 2θ = 25 ° due to the formation of carbon fibres, and the TGA and FTIR spectra which indicate no presence of the C≡N group, signifying carbonisation was performed successfully. This nitrile loss, like with the carbon fibres, is due to cyclization and ladder formation in order to form the carbonaceous sp^2 network. As these fibres were synthesised successfully, the next step is to assess whether the addition of graphene to the PAN, and the subsequent carbonisation, was successful in creating fibres which can be used for super-capacitors.

The Raman spectra can give an indication of the % yield of graphene (< 10 layers) in the composite carbon fibres. In the precursor fibres the yield was estimated as ~ 10 % for both 399 and 15 µm fibres. In the carbonised product the yield is estimated as ~ 30 % for both fibres, due to the shape, height, and position of the 2D peak in the spectra. This increase is possibly due to the evolution of gas (C≡N and H_2) and heat providing additional exfoliation of the exfoliated graphite. As the graphene sheets are dispersed throughout the fibre with the PAN, gas evolution could provide additional mechanical exfoliation as seen in graphene oxide. In a review on PAN heat treatment they show that the nitrogen gases evolve more from the inside of the fibre than the surface. This could be the cause of the exfoliation.[123, 237]

6.5 Electrochemical Performance of the Wet-spun Fibres

The electrochemical performance for all the wet-spun fibres was recorded, including CV analysis, galvanostatic performance, impedance, and stability to degradation. The electrode was created by fixing 20 mg of fibre to two titanium current collectors with silver paint separated by a filter paper. A 6 M potassium hydroxide (KOH) electrolyte was added, and the electrode was sealed with insulating tape and binder clips.

Cyclic Voltammetry and Galvanostatic Discharge

Figure 6.23 and **Figure 6.24** show example CV and galvanostatic discharge curves for the fibres. The carbonised-399 and both the 15 µm fibres display the same peaks in the electrochemical exfoliation at ~ 0.7 V and ~ 0.9 V in the anodic charging sweep and ~ 0.85 V and ~ 0.7 V in the cathodic discharging sweep. These are due to the oxidation of Ag to Ag^+, oxidation of Ag^+ to Ag^{2+}, reduction of Ag^{2+} to Ag^+, and reduction of Ag^+ to Ag respectively. The silver is present as a current collector for the fibres, which were aligned onto the silver surface.

The shape of the CV curves changes upon carbonisation to a more larger and rectangular curve. However, there is still resistance in the material, as shown by the sloping of the curves at the corners. The 15 µm carbon fibre had the smallest change in curve window size, while also sporting the smallest change in capacitance. However the shape of this curve window is the closest to a rectangle, discounting the silver peaks, indicating it was the best EDLC.

The galvanostatic charge-discharge curves are not perfectly linear also indicating the fibre is not a perfect EDLC capacitor. Each fibre has a relatively large IR drop of ~ 0.2 V. This indicates high amounts of voltage leakage in the electrode set-up, which will lead to resistance in the fibres.

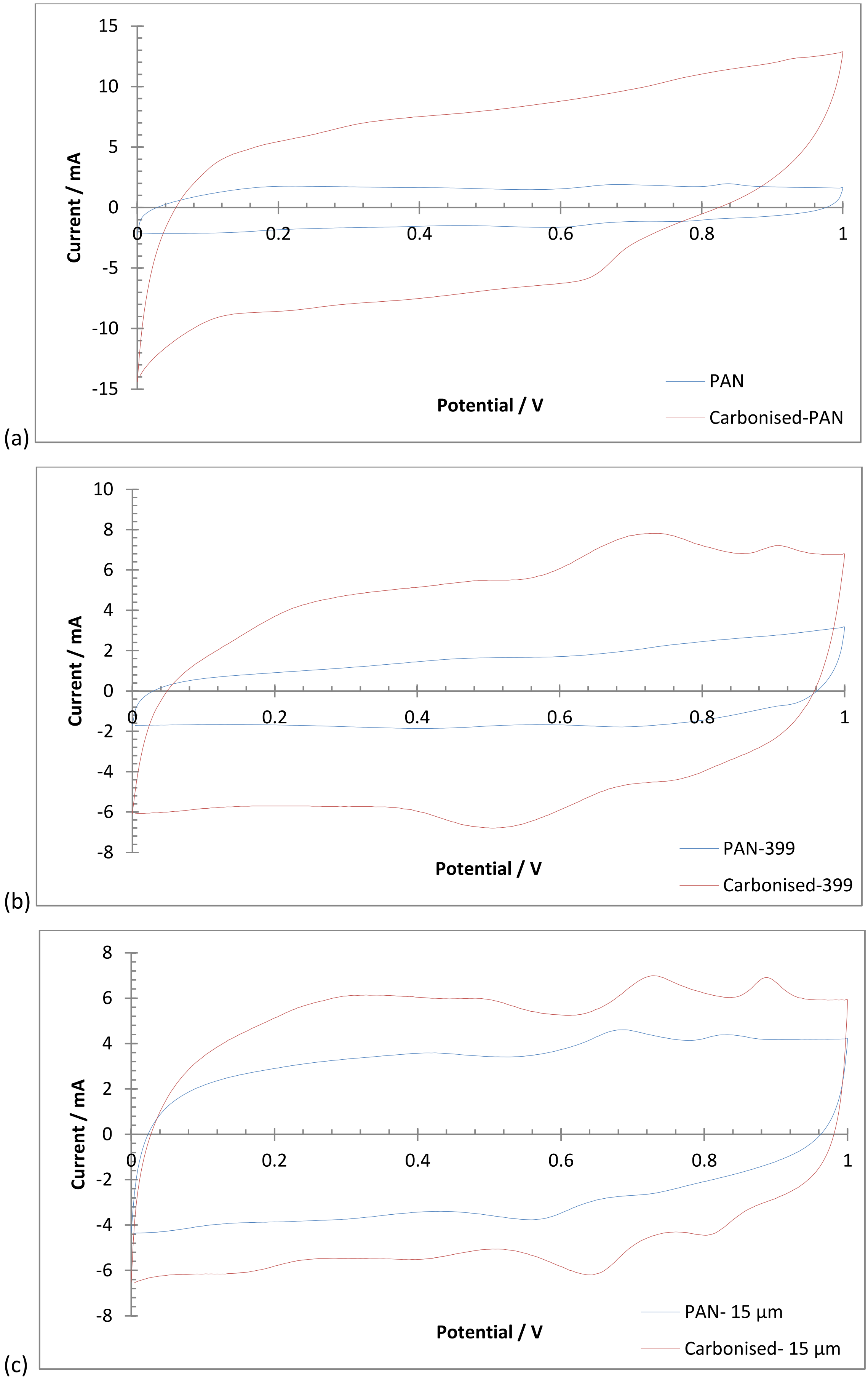
(a)
Current / mA
15
10
5
0
-5
-10
-15
0
0.2
0.4
0.6
0.8
1
Potential / V
PAN
Carbonised-PAN
(b)
Current / mA
10
8
6
4
2
0
-2
-4
-6
-8
0
0.2
0.4
0.6
0.8
1
Potential / V
PAN-399
Carbonised-399
(c)
Current / mA
8
6
4
2
0
-2
-4
-6
-8
0
0.2
0.4
0.6
0.8
1
Potential / V
PAN- 15 µm
Carbonised- 15 µm

Figure 6.23: CV scans of the PAN and carbonised-PAN fibres taken at 100 mV s^{-1}. (a) pure PAN; (b) 5x exfoliated by the aluminium cage methods 399; (c) 5x exfoliated by the aluminium cage methods 15 µm.

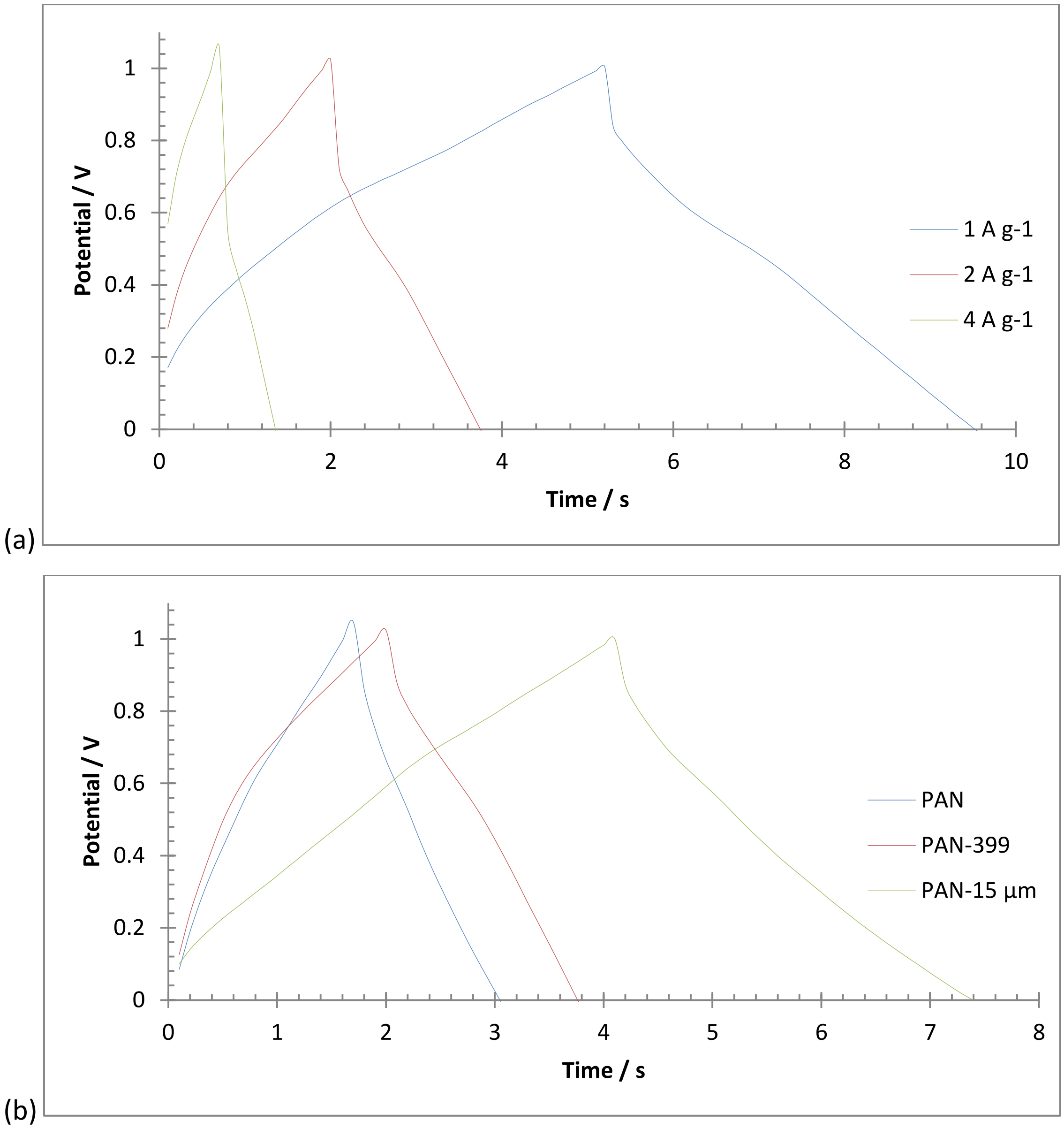

(c)

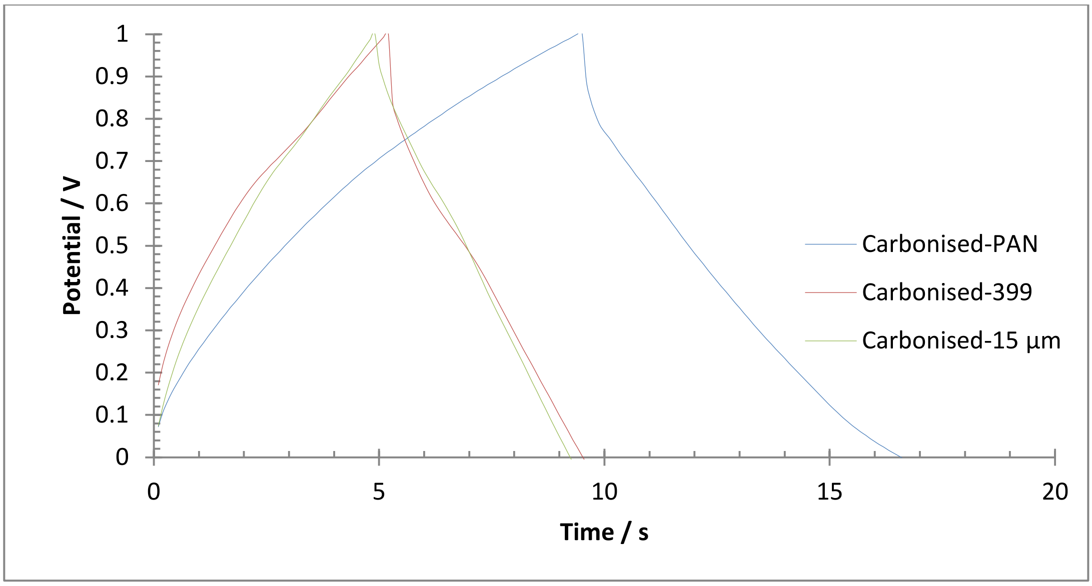

Figure 6.24: Galvanostatic charge-discharge curves for the fibres: (a) the 399 graphite carbon fibre at different scan rates; (b) the PAN fibres at 1 A g^{-1}; and (c) the carbonised-PAN fibres at 1 A g^{-1}.

Capacitance of the PAN Based Fibres

Figure 6.25 and **Table 6.5** show the specific capacitance of the PAN-exfoliated graphite fibre composites**.** The capacitance of the fibres increased after carbonisation for all the fibres, due to changing the PAN fibre from insulating to conducting. This was particularly prevalent in the carbonised PAN material which sported a 560 % or 800 % increase in capacitance upon carbonisation. Additionally the carbonised material has the highest capacitance of all the PAN-based materials. There is, however, a large difference in the capacitance of the carbonised-PAN, with a capacitance of 46.5 F g^{-1} measured at 20 mV s^{-1} by cyclic voltammetry and 27.5 F g^{-1} measured by galvanostatic discharge at 20 mA. Typically, a slower current / potential sweep will ensure further electrolyte penetration, EDL site formation, and thus a higher capacitance. This is evidenced by the carbonised-PAN, however the carbon fibre exhibits a stark difference between the fast and slow charging. This gap is likely further accentuated due to the highly porous nature of the carbonised-PAN. The electrolyte will need to penetrate further into the fibre in order to achieve efficient EDL formation, thus at different sweep speeds the effect is more pronounced.

The addition of exfoliated graphite increases the capacitance of the PAN based fibres. However the capacitance of these fibres is low at ~ 6 Fg^{-1} and ~ 13 F g^{-1} for the 399 and 15 µm aluminium cage exfoliated graphite respectively. This is larger than the capacitance obtained from the 399 and 15 µm initial graphite at 2 F g^{-1} and 2.5 F g^{-1} respectively, but lower than that of the exfoliated graphite at 14 F g^{-1} and 20 F g^{-1} respectively. As the fibres are only comprised of 10 % exfoliated graphite, this suggests the graphite has retained its exfoliation, giving a higher capacitance.

Upon carbonisation, exfoliated graphite infiltration has reduced the capacitance of the fibres. This means the pure carbonised PAN fibre performs as a better capacitor than the exfoliated graphite, and the addition of exfoliated graphite inhibits the extent of EDL formation, reducing the capacitance. This could be seen in the addition of exfoliated graphite, which did not properly disperse with the PAN in DMF. This is due to minute amounts of electrolyte in the dispersion from the electrochemical exfoliation. This is present even after extensive washing. This inhibits the dispersion of the graphene, as seen in Cooper *et al*.[238]

In a paper by Wang *et al.* the capacitance of carbon cloth, with and without the addition of porous graphene was characterised. The porous graphene was added via the electrophoretic deposition of graphene oxide. They calculated the capacitance of the whole material in a two electrode system, a scan rate of 5 mV s^{-1}, and an electrolyte of 1 M H_2SO4 to be 11.8 F g^{-1} for the porous graphene carbon cloth and 1.35 F g^{-1} for the neat carbon cloth. The capacitance results obtained in this research project are far larger than the results obtained here. This is possibly due to the porous microstructure of the carbon fibre, which allows for the formation of many EDL sites.[239]

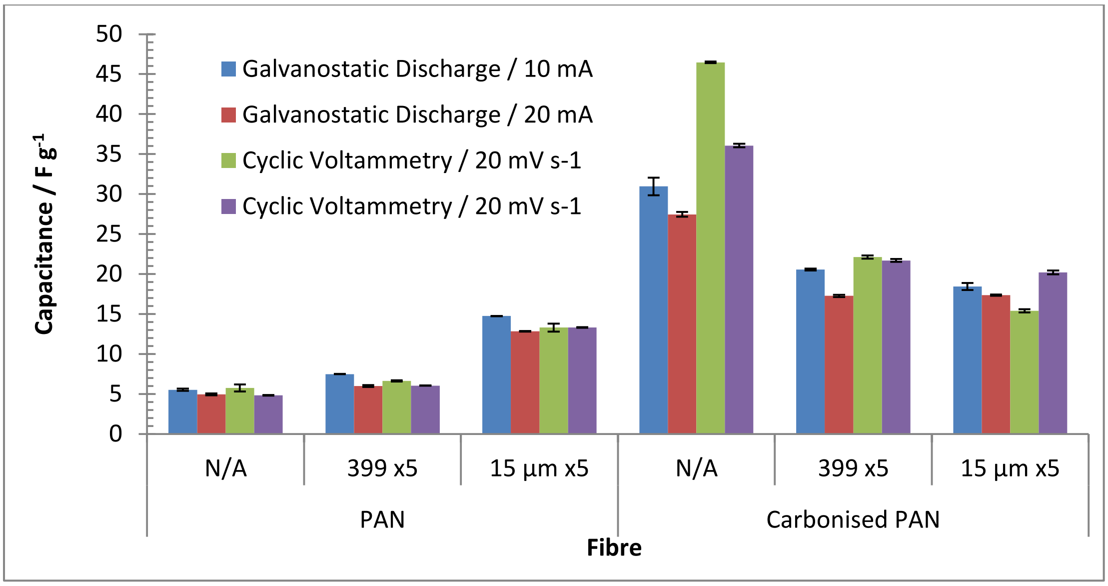

Figure 6.25: Graphitic representation of the capacitance obtained from the PAN and carbonised PAN graphene infiltrated fibres.

Sample	Exfoliation	Galvanostatic Discharge / mA		Cyclic Voltammetry / mV s^{-1}	
		10	20	20	40
PAN	N/A	5.5 ± 0.1	4.9 ± 0.1	5.8 ± 0.4	4.8 ± 0.0
	399 x5	7.5 ± 0.0	6.0 ± 0.1	6.3 ± 0.1	6.0 ± 0.0
	15 µm x5	14.8 ± 0.0	12.8 ± 0.0	13.3 ± 0.5	13.3 ± 0.0
Carbonised PAN	N/A	31.0 ± 1.1	27.5 ± 0.3	46.5 ± 0.1	36.1 ± 0.2
	399 x5	20.6 ± 0.1	17.3 ± 0.1	22.1 ± 0.2	21.7 ± 0.2
	15 µm x5	18.4 ± 0.5	17.4 ± 0.1	15.4 ± 0.2	20.2 ± 0.2

Table 6.5: Capacitance (in F g^{-1}) of PAN-exfoliated graphite fibre composites and their associated carbonised versions using two different analysis techniques.

Figure 6.26 and **Table 6.6** show how the capacitance changes at increasing scan rates. For the carbonised PAN fibre, as the scan rate increase by a factor of twenty, the resultant capacitance is just 40 % of the original capacitance. This is comparable to the exfoliated graphite infiltrated nickel foam. As the scan rate increases, the ease at which the fibre charges decreases, resulting in difficulty creating EDL sites and a reduced capacitance.

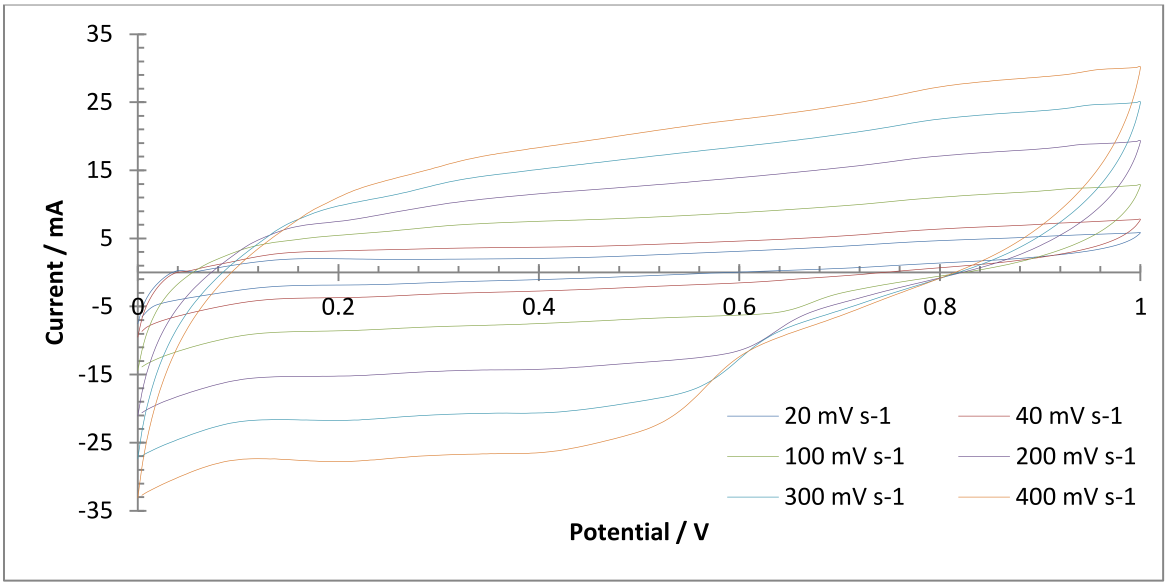

Figure 6.26: CV curves of the carbonised-PAN fibre at increasing scan rates.

Scan Rate / mV s^{-1}	Specific Capacitance / F g^{-1}
20	46.5 ± 0.1
40	36.1 ± 0.2
100	22.8 ± 0.1
200	23.3 ± 0.0
300	20.8 ± 0.0
400	19.0 ± 0.0

Table 6.6: The specific capacitance for the carbonised PAN at different scan rates.

Stability to Charge Cycling

Figure 6.27 and **Table 6.7** show the capacitance retention of the PAN-based fibres after 2000 charge-discharge cycles. The results show that the carbonised fibres are the most stable to degradation, retaining the highest percentage capacitance of the fibres. This is likely due to the stabilisation of the carbon fibres during carbonisation. The formation of the sp^2 structure allows for the creation of a stable framework, which will reduce the deformation of the fibre, reducing the capacitance. The combination of the carbon fibre and 15 µm graphite gave the highest capacitance retention, likely due to the highly stable graphite and carbon fibre. In the PAN fibres the capacitance decreases due to the resistance introduced to the system, collapse of structure after multiple charging cycles which can also cause the material to leave the current collector.

The increase in capacitance after charge cycling has previously been seen in work on MoS_2-graphene composites.[220] This increase in capacitance is most likely from the in-situ exfoliation of the carbon fibre, increasing the active surface area of the fibre (and thus the capacitance).

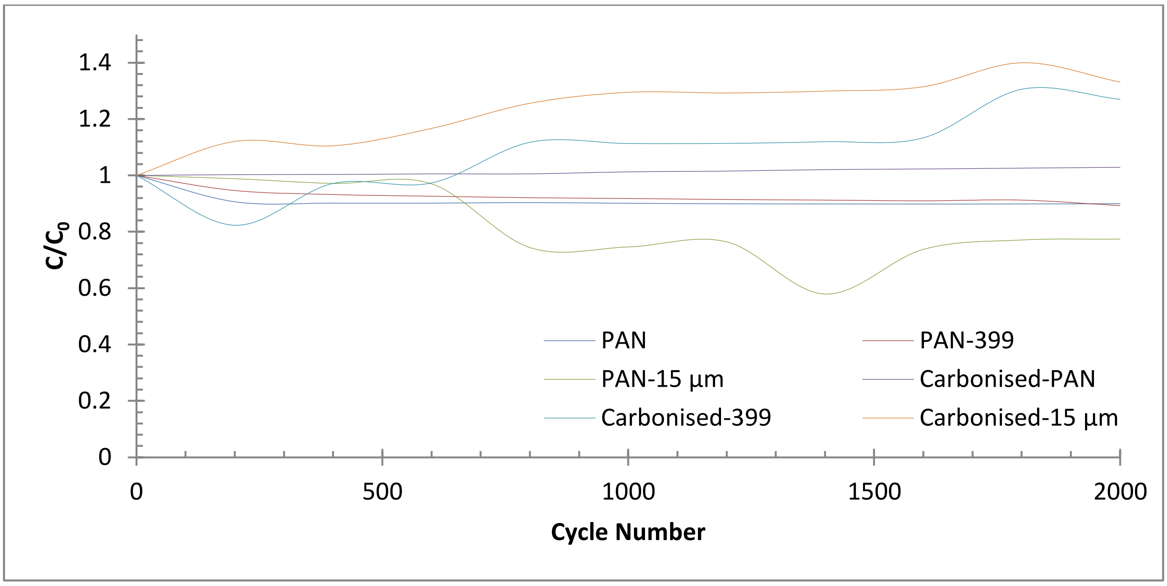

Figure 6.27: Example capacitance change from the initial capacitance across 2000 charge-discharge cycles for the PAN and carbonised exfoliated graphite fibres.

Sample	Exfoliated Graphite	Capacitance Retention / %
PAN	N/A	90.0
	399 x5	89.3
	15 µm x5	77.4
Carbonised PAN	0	102.9
	399 x5	127.0
	15 µm x5	133.1

Table 6.7: Capacitance retention after 200 charge-discharge cycles at 10 A g^{-1}.

Impedance Spectroscopy

Figure 6.28 shows example impedance spectra for the PAN-based fibres. In the high frequency range (100 – 10000 Hz), all fibres show capacitive behaviour. This is shown by the vertical slope in all spectra. At low frequencies (0.01 – 100 Hz) all carbonised fibres only exhibit part of the classic semi-circle which represents charge-transfer resistance. This resistance is exhibited due to the large fibres making poor contact to the electrodes. The carbonised PAN fibres all show a better impedance result than the PNA fibres, although the PAN fibres show better capacitive behaviour. This is represented by the plot being closer to the imaginary impedance axis.

The phase angle shift for the PAN fibres reached > 70 ° which is close to the ideal 90 ° for ideal capacitive behaviour. At a phase shit of -45 ° the fibres give a time constant of 27 ms, 27 ms, 12 ms, 0.79 s, 5.7 s, and 1.0 s for the PAN, PAN-399, PAN-15µm, carbonised-PAN, carbonised-399, and carbonised-15 µm fibres respectively. The rapid response of the PAN fibres is likely due to their porous structure which creates a large surface area for electrolyte penetrations. Upon carbonisation, the carbonised composite fibres lack this porous structure, which inhibits the formation of EDL sites.

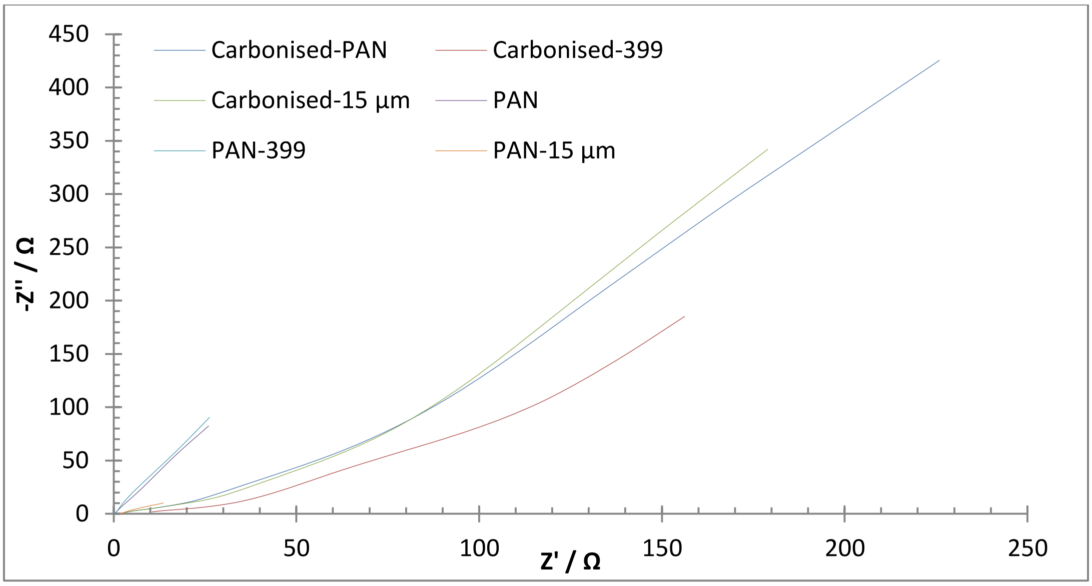
Carbonised-PAN
Carbonised-399
Carbonised-15 µm
PAN
PAN-399
PAN-15 µm
450
400
350
300
250
200
150
100
50
0
-Z'' / Ω
0
50
100
150
200
250
Z' / Ω

(a)

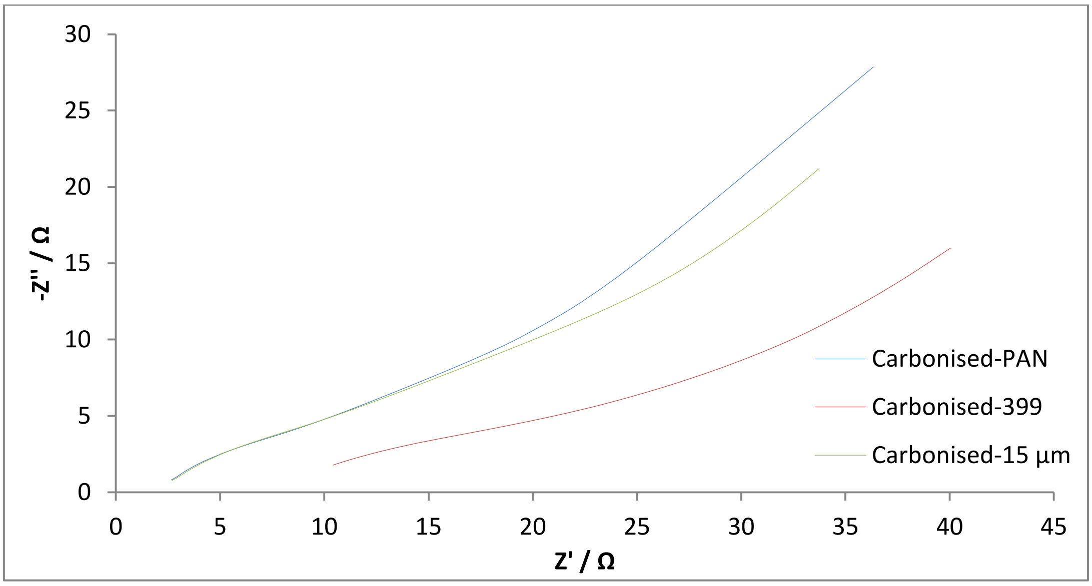
30
25
20
15
10
5
0
-Z'' / Ω
0
5
10
15
20
25
30
35
40
45
Z' / Ω
Carbonised-PAN
Carbonised-399
Carbonised-15 µm

(b)

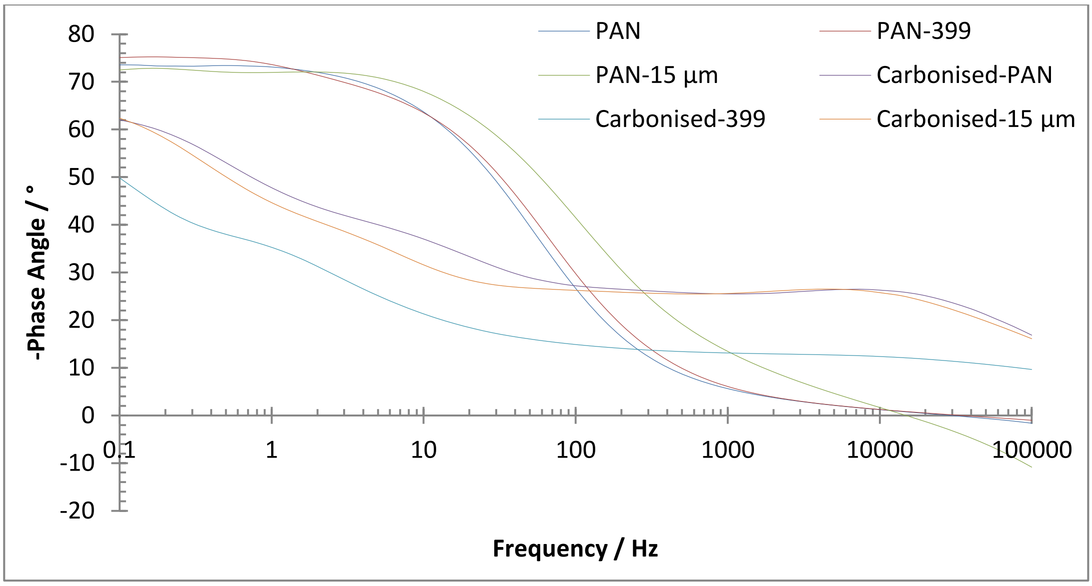
PAN
PAN-399
PAN-15 µm
Carbonised-PAN
Carbonised-399
Carbonised-15 µm
80
70
60
50
40
30
20
10
0
-10
-20
-Phase Angle / °
0.1
1
10
100
1000
10000
100000
Frequency / Hz

(c)

Figure 6.28: Example impedance spectra for the PAN based fibres. (a) Nyquist plots; (b) a closer look at the 'semi-circle' portion of the curve; and (c) Bode plots of the PAN based fibres.

Energy and Power Density

Figure 6.29 and **Table 6.8** show the energy and power density of the fibres was characterised using the same equations used in the previous section. The carbonised PAN composite fibres all have a higher energy density than the un-carbonised fibres, while that all have comparable power densities. The higher energy densities are due to carbonisation which generates an sp^2 carbon lattice which increases the conductivity of the fibres and allows for formation of an EDL. The similar power densities are due to fibrous nature of all the fibres, which allows for a set number of EDL sites.

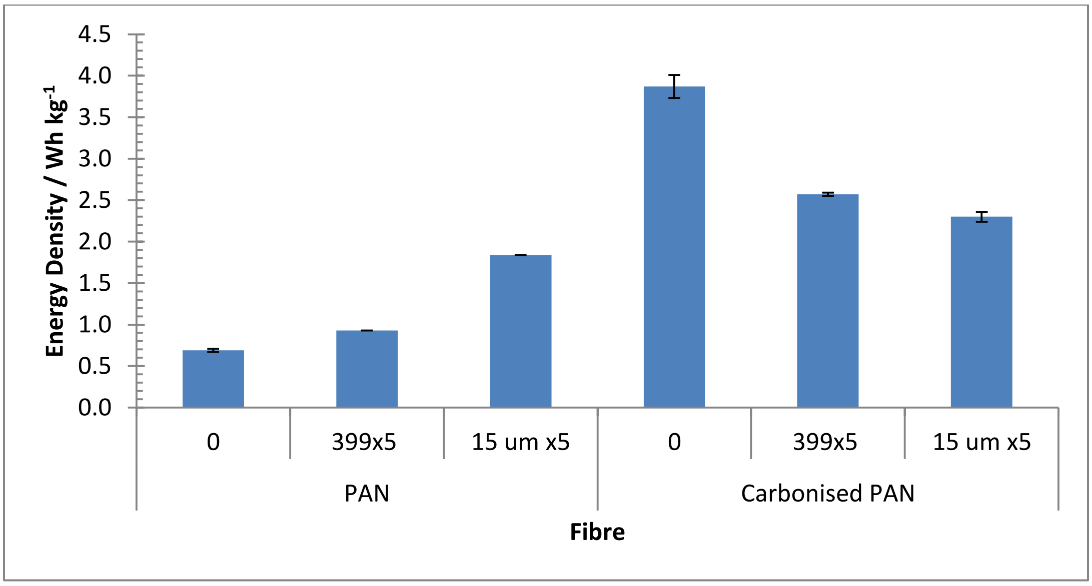

(a)

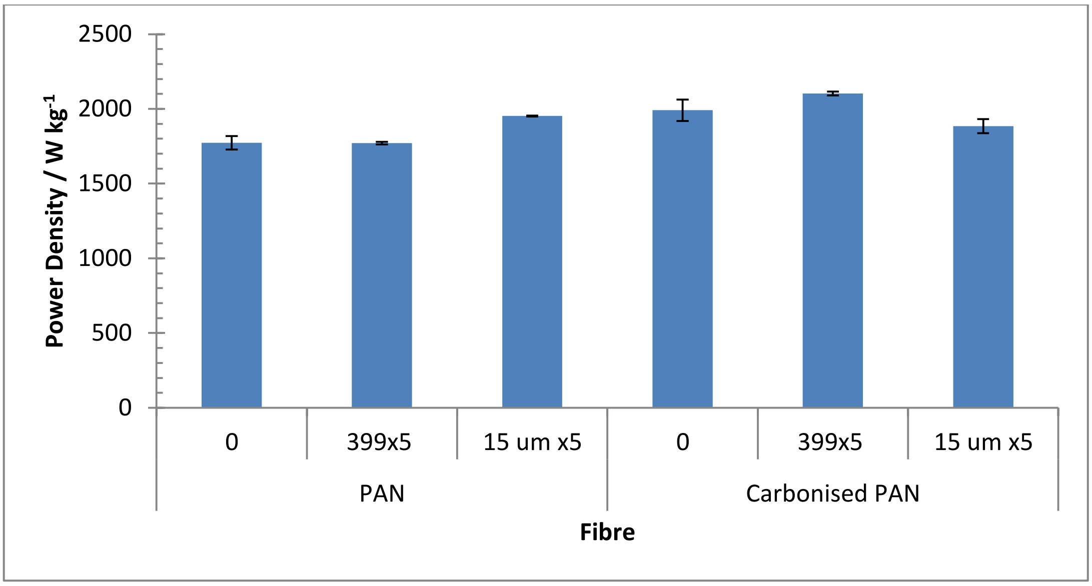

(b)

Figure 6.29: (a) Energy; and (b) Power density of the PAN and carbonised PAN graphene infiltrated fibres.

Sample	Exfoliation	Energy Density / Wh kg^{-1}	Power Density / W kg^{-1}
PAN	N/A	0.69 ± 0.02	1774 ± 45
	399 x5	0.93 ± 0.00	1771 ± 8
	15 µm x5	1.84 ± 0.00	1952 ± 3
Carbonised PAN	N/A	3.87 ± 0.14	1990 ± 71
	399 x5	2.57 ± 0.02	2102 ± 13
	15 µm x5	2.30 ± 0.06	1885 ± 46

Table 6.8: Table of calculated energy and power densities of the PAN and carbonised PAN based fibres using the 10 mA galvanostatic discharge curve.

6.6 Comments on the use of Graphene-Carbon Fibres for Electrochemical Applications

The spinning of PAN-based graphene fibres proves PAN can act as a solid template for the spinning of graphene. At low concentrations of PAN the fibres were not able to be spun, often breaking apart upon handling. This would not make them good for capacitor applications, where the whole fibre needs to be attached to the electrode.

The addition of the exfoliated graphite to this fibre greatly reduced the capacitance. Further separating the exfoliated graphite via settling, to get smaller/thinner flakes, may increase the capacitance of the fibres, as thinner exfoliated graphite could provide a higher capacitance. However the capacitance of the fibres is comparable to the nickel foam capacitance, with the highest capacitance delivered by the carbonised PAN fibre.

The electrochemically exfoliated graphite has been shown to have residual impurities from the exfoliation. This is seen in the XRD, which contains peaks relating to aluminium, TEA-HCl, and LiCl. This greatly reduces the dispersion and stabilisation of the exfoliated graphite in solvents, which could lead to re-stacking of the graphite. This would reduce the capacitance as there would be a poorer peculation of charge carriers and reduced surface area.[238] This may account for the reduced capacitance when the exfoliated graphite was added to the carbon fibre, as the exfoliated graphite did improve the capacitance of the PAN precursor fibres.

Though the carbonisation was successful, the fibres still need to be graphitized in order to properly align the graphitic crystals in the carbon fibres. This is turn would increase the strength of the fibres and the conductivity, which would increase the capacitance of the fibres. This would need to take place at temperatures much higher than the limits furnace used, up to 2500 °C. This could increase the cost for fibre manufacture, but for the correct applications (mechanical), the graphitization of the fibre would be essential.

It has been observed that some groups report capacitances where the fibre has been milled and pressed into current collectors, or only very small amounts (< 5 mg) of fibre has been tested, which would not give an accurate representation of the capacitance of the whole fibre.[240] In this project the capacitance of the fibres was assessed with large amounts of fibre used in a fibre form. This would be the way the fibre would be used in bulk super-capacitor applications.

7 Wet-spinning of graphene oxide fibres as a route towards graphene fibres

In the previous chapter, graphene-polyacrylonitrile (PAN) composite fibres were used a precursor for producing fibres for flexible electrodes in supercapacitors. Herein, an alternative approach is taken to produce fibres which have a much higher graphene content (up to 33 %). Graphene oxide (GO) is very hydrophilic and can form strong interactions to other GO sheets through hydrogen-bonding, dipole-dipole bonding and π-π stacking. These interactions make GO highly suitable for coagulation fibre spinning with the resultant fibre being subsequently reduced to yield a graphene fibre. Thus, GO was first synthesised from flake graphite using an adapted Hummer's method. Performing the wet-spinning of GO and PAN ultimately did not create continuous fibres, with the fibre breaking and dispersing in solution. Thus another polymer was sought in order to accurately compare the fibres. Cellulose acetate was first chosen as the template polymer, but after many trails it was found to be immiscible with the GO. The produced fibres were non-uniform in their size and concentration of GO. Polyvinyl alcohol (PVA) was ultimately chosen as the template polymer due to its ease of synthesis, ability to be wet-spun (which is well documented), and the fact it can be carbonised, allowing for a fibre which is wholly carbon and forms electrical double layers to store energy. These fibres were then reduced and used directly as a super-capacitor electrode.

Graphene fibres derived from GO have previously been sought after for use in mechanical and reinforcement applications due to the high mechanical strength of GO (Young's modulus 207.6 GPa[78]) and flexibility of fibres. However, since the start of this research project, GO is now being used for electrochemical applications, particularly as capacitors due to the inherent capabilities of GO for capacitors.

7.1 Characterisation of the initial graphite

Flake graphite is the most common graphite used for GO synthesis, as it can produce large GO flakes with a high surface area. Thus, for the GO synthesis, the natural flake graphite 'Graphexel 2369' was used.

Scanning Electron Microscopy

Scanning electron microscopy (SEM) was employed to view the flakes at a detailed level (**Figure 7.1**), and ‘Image J’ was used to resolve the size and distribution of the graphite flakes (**Figure 7.2**). The flakes are large, with an average size of 418.4 ± 147.9 µm (n = 100 flakes) and relatively few flakes below 200 µm in diameter. The flakes were flat, with long straight edges and very little additional debris on the surface. These flakes are much larger than the graphite used for the electrochemical exfoliation to produce graphene (~ 30 µm). (Smaller flakes were used for the electrochemical exfoliation process due to the restrictions of the diffusional path length of the intercalants in the graphite.)

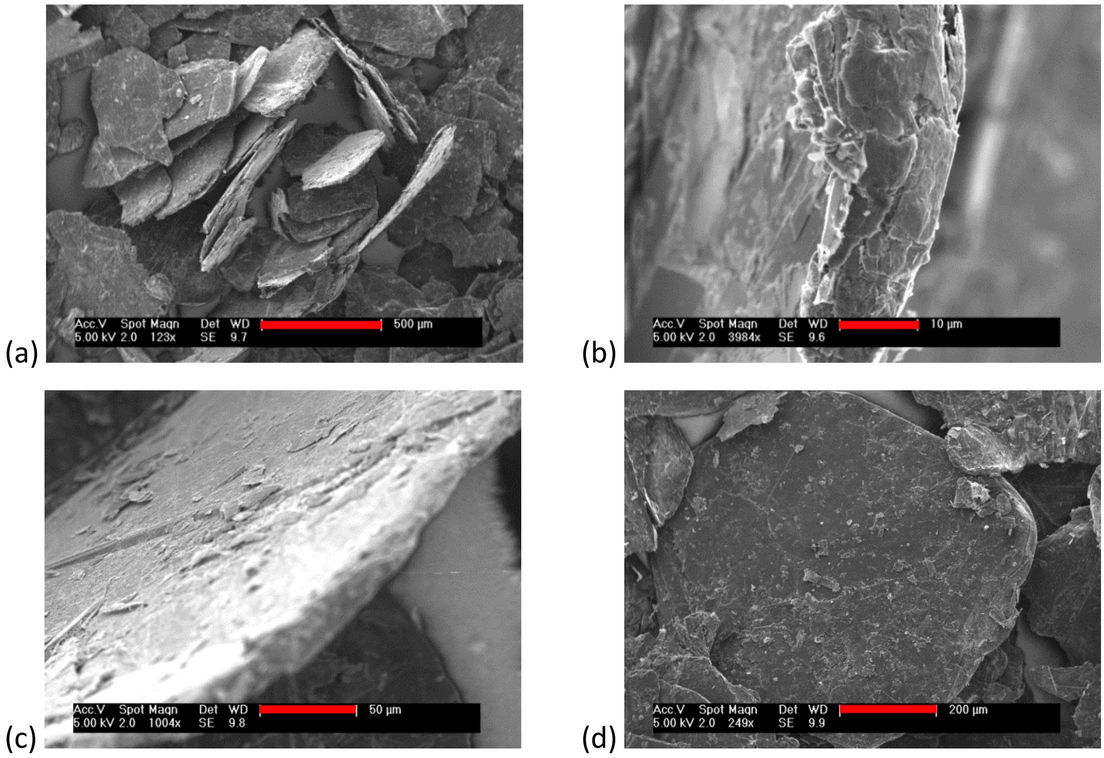

Figure 7.1: SEM images of the starting graphite (Graphexel 2369). (a) assorted graphite flakes; (b) the edge of the flakes; (c) the smoothness of the flakes; and (d) the surface of the graphite flakes.

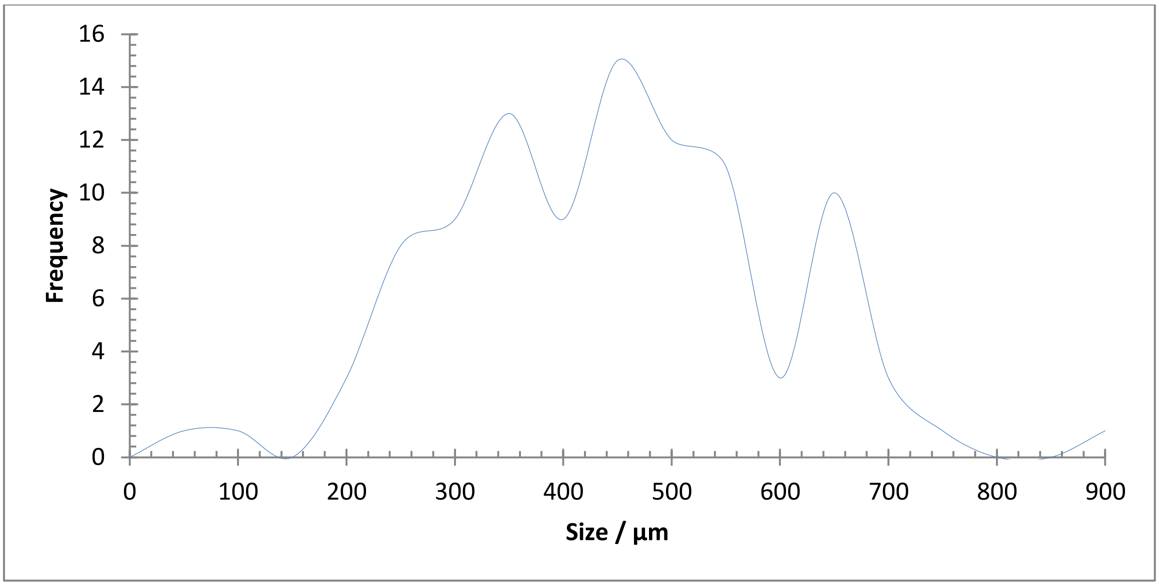

Figure 7.2: The size distribution histogram for the Graphexel 2369 flake graphite over 100 different graphite flakes. BIN size: 50 µm.

Raman Spectroscopy

Raman spectroscopy was employed to characterise the starting flake graphite and for a comparison when oxidation and reduction experiments have taken place (**Figure 7.3**). The characteristic graphite peaks were present at 1332.1 ± 1.9 cm^{-1}, 1581.7 ± 0.5 cm^{-1}, and 2685.1 ± 3.3 cm^{-1}, corresponding to the D, G, and 2D bands respectively. The D peak was noticeably absent from most of the Raman spectra. This indicates that the flake graphite is defect free, due to the large size of the graphite particles and ABA stacking of the material (also shown in the shape of the 2D band). The I_D/I_G was calculated, using spectra in which it appears, as 0.06, while the I_{2D}/I_G was 0.44.

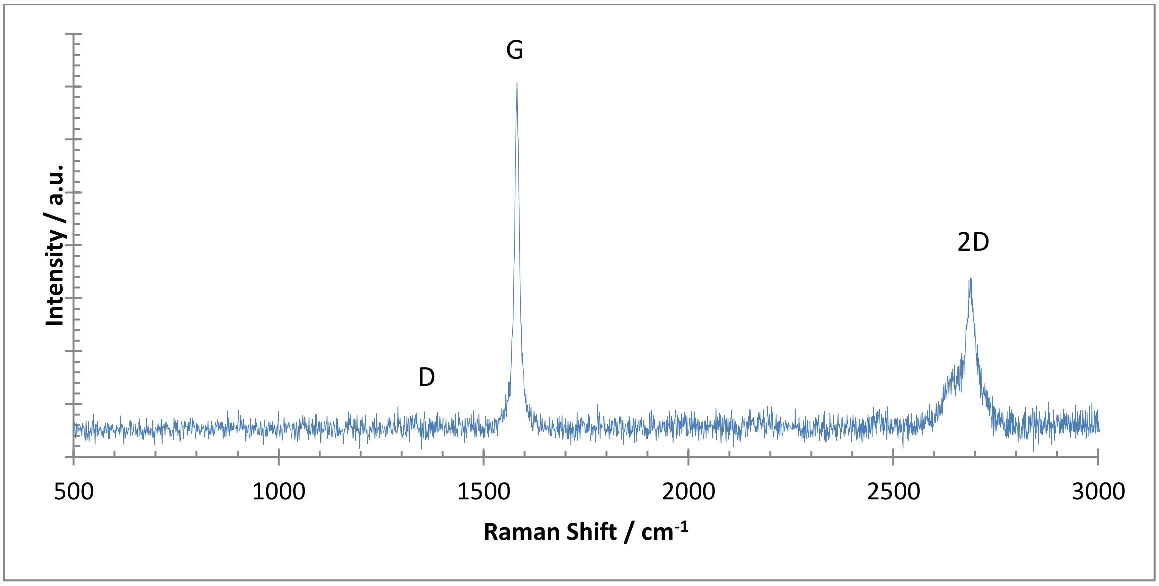

Figure 7.3: An example Raman spectrum of the Graphexel 2369 graphite used for the synthesis of GO. This typical spectrum shows no D band.

X-Ray Diffraction

X-ray diffraction (XRD) was used to analyse the d-spacing in the material**.** The spectrum (**Figure 7.4**) contains no anomalous peaks, with the largest peak (~ 2θ= 26 °) corresponding to the 00.2 plane in graphite, while the second largest peak (~ 2θ= 42 °) designated as the 00.4 plane in graphite. The 00.2 peak appears at 2θ = 26.66 ± 0.07 °, which corresponds to a 00.2 d-spacing of 3.34 ± 0.01 Å, which is in-line with other graphite materials. The FWHM of the peak was 2θ = 0.15 ± 0.02 °, showing the material highly ordered. Using the Scherrer equation the crystalite size was calculated as 21.0 nm.

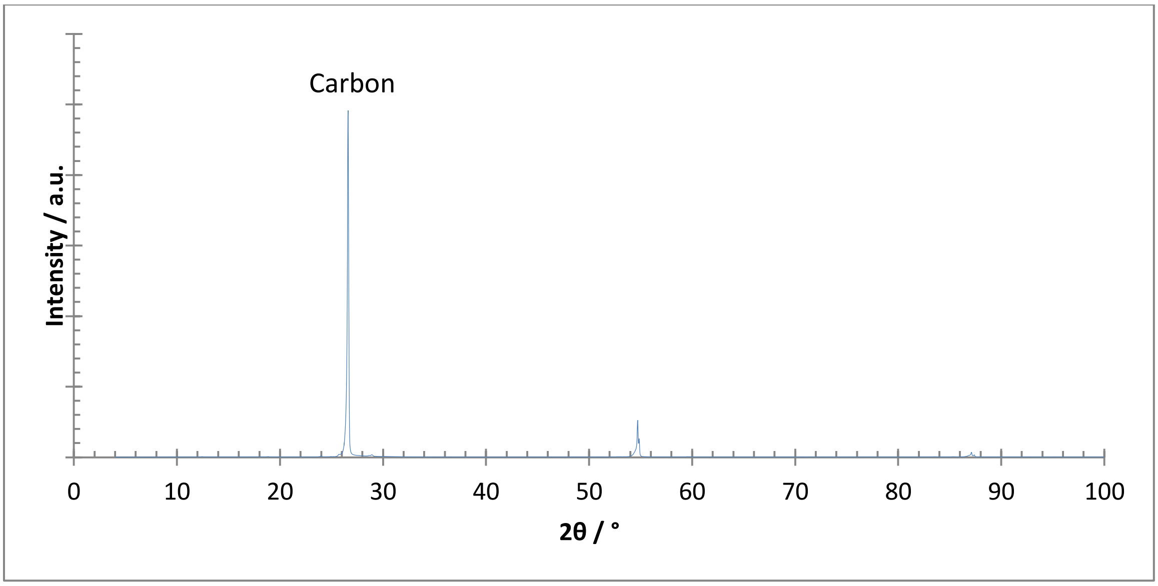

Figure 7.4: XRD pattern of initial graphite Graphexel 2369, showing the classic graphite peak at ~ 2θ = 26 °.

Thermal Gravimetric Analysis

Thermal gravimetric analysis (TGA) was used to ascertain the composition and thermal decomposition profile (**Figure 7.5**) of the graphite. The spectrum shows the material does not undergo significant weight loss until 611.8 ± 2.9 °C. Up until this temperature the weight loss was only ~ 2 %. This oxidative weight loss is due to the burning of the graphitic regions in the graphite. This value was much higher than the four grades of graphite used for electrochemical exfoliation, meaning this grade of graphite was very ordered and difficult to break apart. The material undergoes the fastest decomposition at 943.9 ± 7.1 °C, also at a higher temperature than the previous graphite grades used. In addition the end point of the TGA is not seen, as the weight loss was recorded up to 1000 °C. This confirms that the graphite is highly ordered and has a low surface area, as if more points of the material were subject to the atmosphere, the material will undergo a faster thermal decomposition.

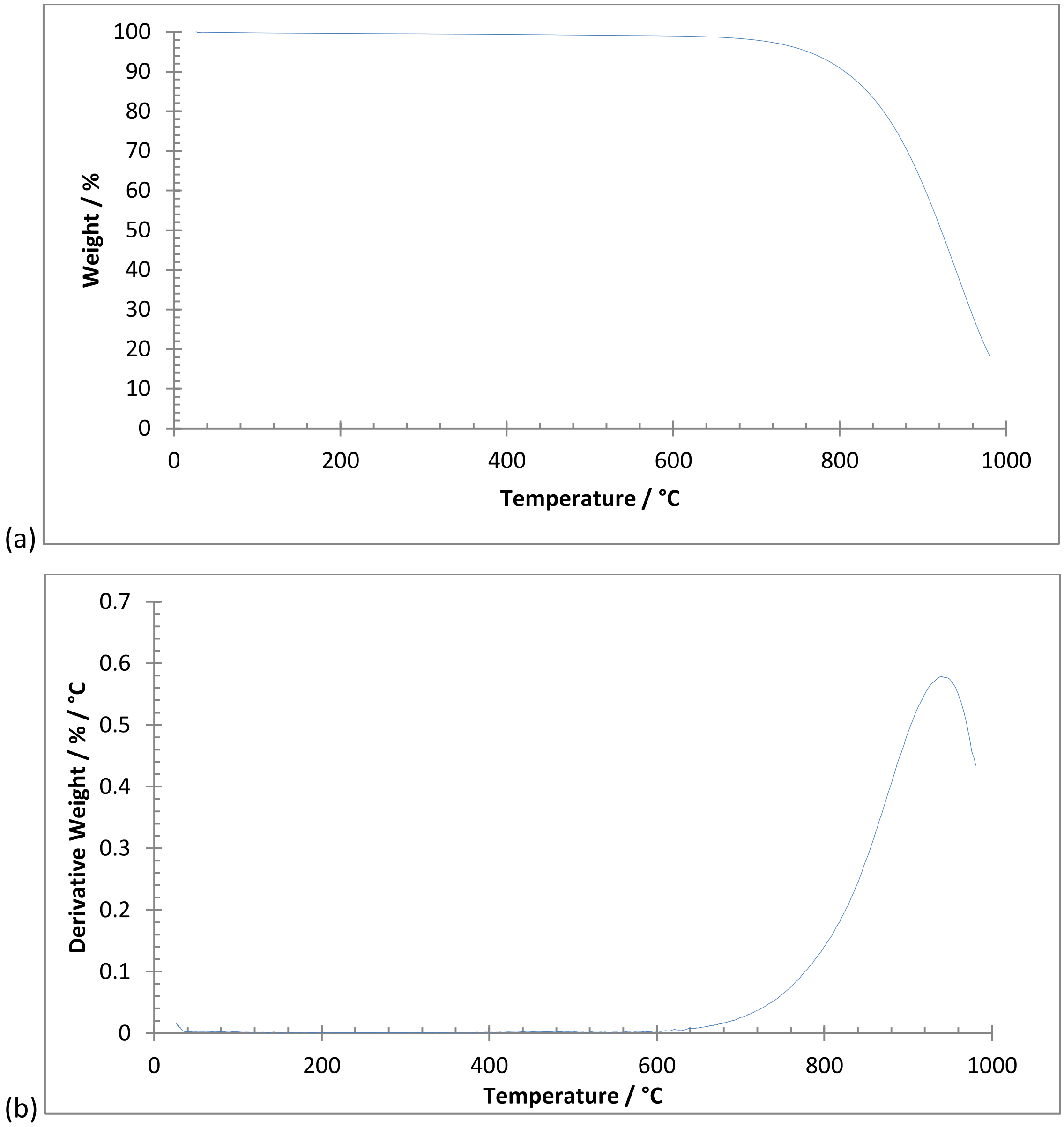

Figure 7.5: TGA profile up to 1000 °C for the Graphexel 2369 flake graphite in air. (a) the weight-loss curve; and (b) the derivative (temperature) weight-loss curve.

Infra-Red Spectroscopy

Infra-red spectroscopy (FTIR) was performed to assess the functionality of the graphite (**Figure 7.6**), which shows peaks which can be attributed to graphite. The peak that appears at 852 cm^{-1} is due to an aromatic C-H group (bend), 1591 cm^{-1} is due to aromatic C=C (bend), and 2966 cm^{-1} is due to an aromatic C-H (stretch) though it is partly masked by the OH group in hydroscopic KBr from 3000 – 4000 cm^{-1}.

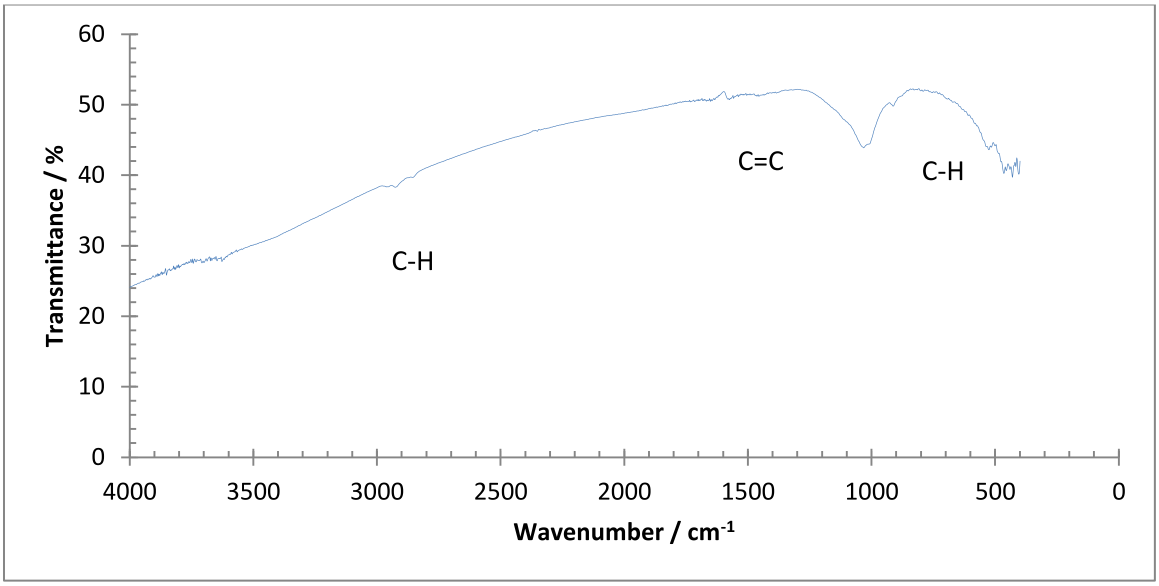

Figure 7.6: FTIR spectrum of Graphexel 2369, showing no anomalous peaks.

Summary

The SEM, Raman, and XRD results indicate that the Graphexel 2369 graphite is large with a strict crystalline ABA structure. The TGA and FTIR results indicate no additional functionality in the graphite. This graphite can be referred to as 'flake' graphite, for it is large and flat, which would allow for larger GO flakes from graphite after oxidation. This is essential for supercapacitor manufacture, where smaller rGO flakes will form a less percolating network and introduce more resistance in the device. Additionally, characterising the starting material will allow for a more robust characterisation of the oxidised GO by comparison.

7.2 Characterisation of the Synthesised Graphene Oxide

GO was synthesised from an adapted Hummer's method[213], using the graphite characterised in the previous section. Presented in this section is the characterisation of the synthesised GO.

When it came to spinning the GO in order to form fibres, it was found that using freeze-dried GO would not allow for continuous fibre formation. However, fibres were spun continuously from GO that had not been freeze-dried. Thus the GO material was stored at a concentration of 3 mg mL^{-1} in water. It was observed that the resultant GO solution was stable in water for over 2 years without sediment forming, indicating the highly hydrophilic nature of the material.

Scanning Electron Microscopy

SEM was used to see how the morphology (Figure 7.7) and size (Figure 7.8) of the flakes had changed after exfoliation.

The topography of the GO particles has changed from the large strict rectangular flakes of the graphite to fragments with disordered edges and graphitic debris. The GO flakes have edges which look torn and crumpled compared to the initial graphite. This is likely from the oxidation reaction which tears the flakes up by the removal of the sp^2 sites and introduction of oxygen-containing functional groups. The particles are no longer in a strict rectangular shape, with a variety of profiles and sizes.

The synthesised GO has a small distribution of flake sizes, with the majority of the flakes < 1 µm in diameter. The average size of over 100 measured flakes was calculated as 1.18 ± 1.52 µm. This relatively homogeneous solution will allow for an even distribution of the flakes throughout a fibre. This could in turn strengthen the fibre, as it would allow for a more crystallised and ordered product. Overall the average size of the flakes has reduced by approximately 2 orders of magnitude, from 418.42 µm to 1.18 µm. This can again be attributed to the oxidation breaking up the graphite, via the formation of sp^3 sites and oxygen-containing functional groups.

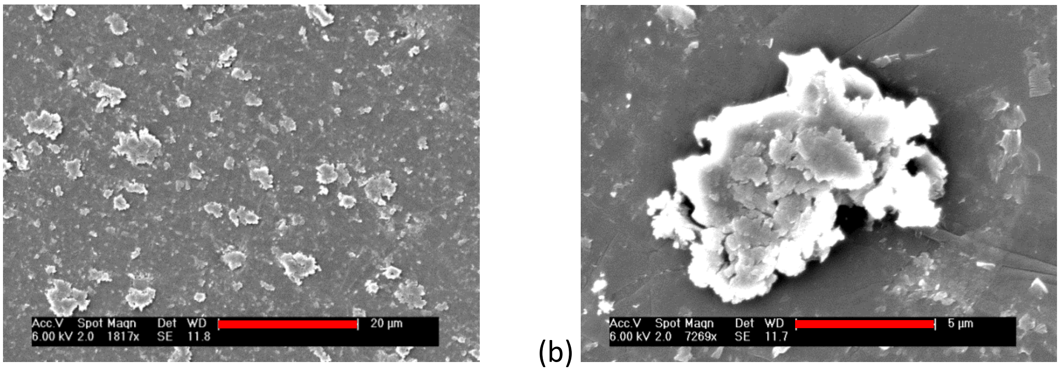

(a) (b)

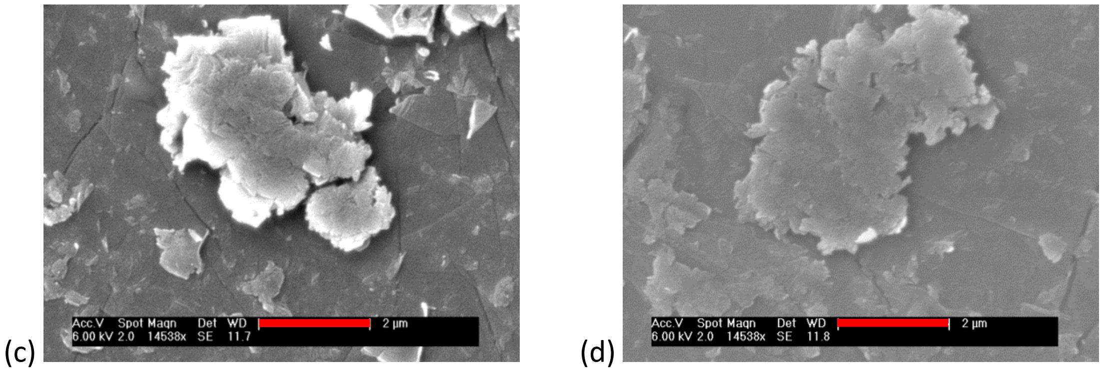

Figure 7.7: SEM images of the synthesised GO flakes. (a) assorted GO flakes; (b-d) large GO flakes, with debris on the surface and surrounding areas.

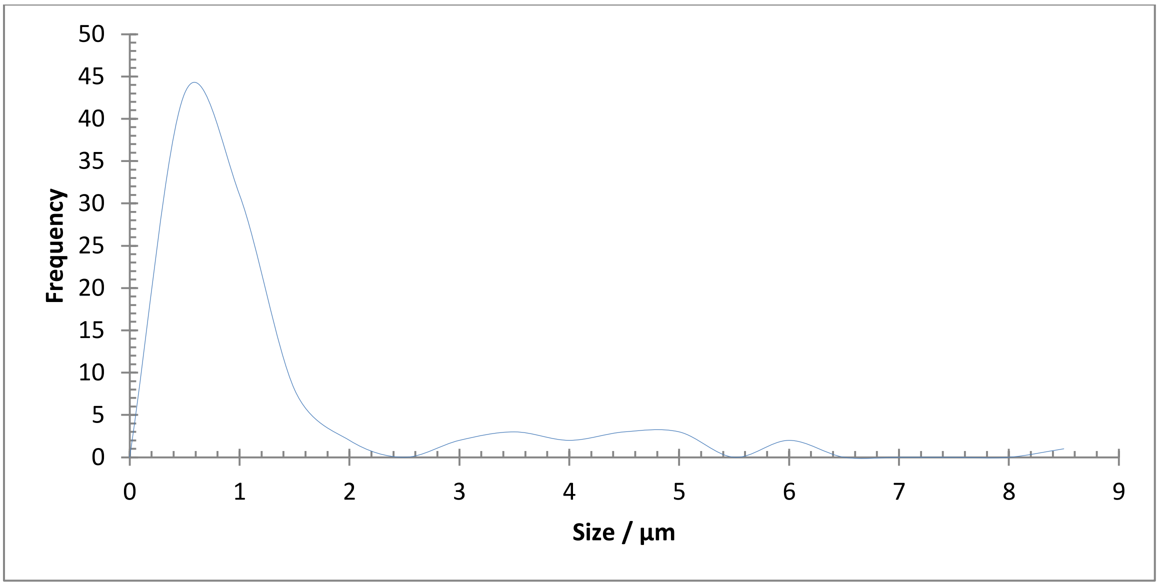

Figure 7.8: The size distribution of 100 GO particles in a histogram measured using 'Image J'. BIN size: 0.5 µm.

Raman Spectroscopy

Raman analysis was performed to ensure the graphite had been suitably oxidised (**Figure 7.9**). The Raman spectrum of the oxidised graphite shows 4 distinct peaks at 1341.2 ± 0.5 cm^{-1}, 1594.5 ± 0.7 cm^{-1}, 2625.2 ± 21.9 cm^{-1}, and 2950.2 ± 12.7 cm^{-1}, which can be attributed to the D, G, 2D, and D + G bands respectively.

Like in graphite the D band at ~ 1350 cm^{-1} appears due to A_{1g} broadening which occurs due to disorder. In the initial graphite this band was not present for most of the spectra, while in the GO it is the most prominent peak in the spectrum. This has occurred due to oxidation breaking apart the material, causing the presence of more defect edges in the Raman laser spot. The peak at ~ 1600 cm^{-1} is due to the sp^2 carbon resonance causing a first order scattering of the E_{2g} mode in the GO. The peak is smaller compared to the D peak with the I_D/I_G ratio of 1.26 (the I_D/I_G ratio of the initial graphite was 0.06). This further confirms the presence of smaller particles in the material. The peak at ~ 2600 cm^{-1} is due to the double resonance of the E_{2g} peak, which is an overtone of the D band. The peak is softened due to the damage in the material structure. This damage is in the form of sp^3 defects and oxygen-containing functional groups, which reduces the concentration of sp^2 sites, thus reducing the intensity this classical sp^2 peak. The I_{2D}/I_G ratio is 0.06, and the width is 179.4 ± 36.5 cm^{-1}. Another peak also appears at ~ 2930 cm^{-1}, which is due to a D+G band. This band occurs in more prominent in GO due to the low intensity of all other bands.

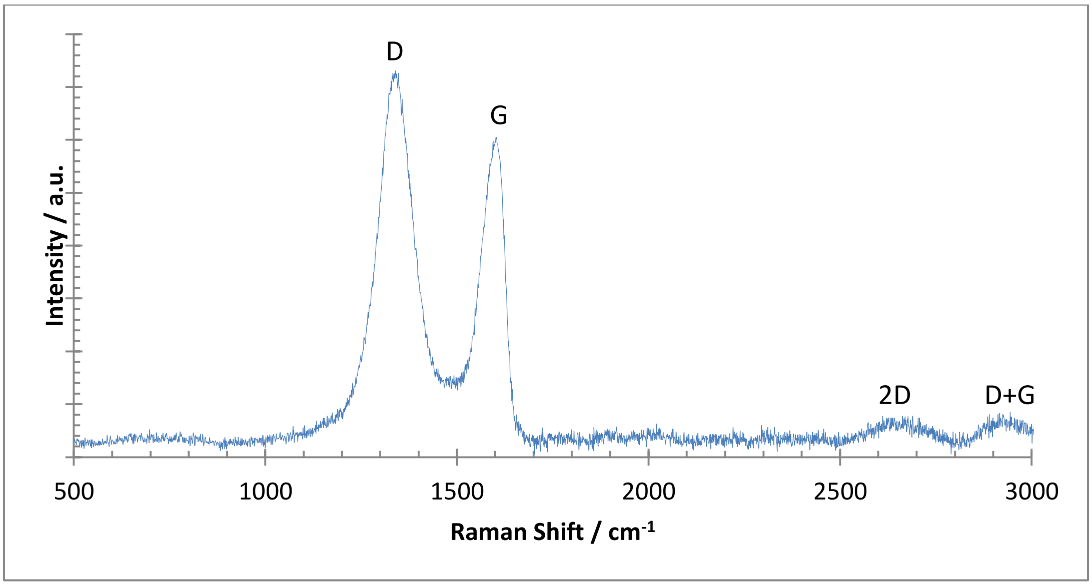

(a)

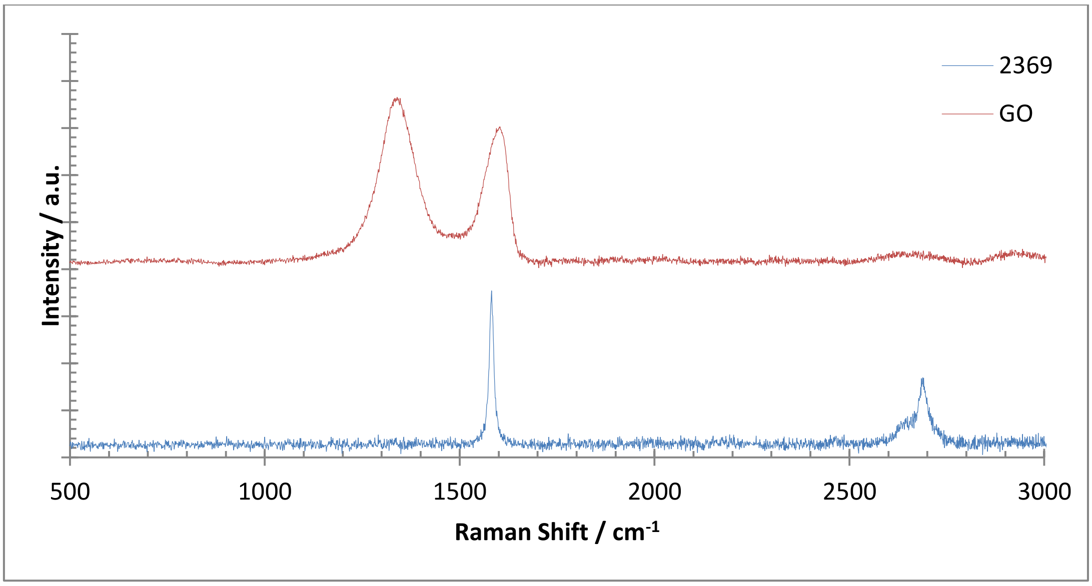

(b)

Figure 7.9: (a) GO Raman spectrum, showing the 4 Raman active bands, D, G, 2D, and D + G; and (b) the Raman spectra for the initial graphite used (Graphexel 2369) and the synthesised GO.

X-Ray Diffraction

The XRD pattern of the synthesised GO (**Figure 7.10**) shows a very significant change from the initial graphite XRD pattern. The oxidised graphite has a sharp peak at 2θ = 11.01 ± 0.15 °, which corresponds to the (00.2) d-spacing of 8.17 ± 0.30 Å, and a FWHM of 2θ = 0.43 ± 0.01 °. This increase in d-spacing is due to the oxygen containing functional groups on the surface, which separate the sheets and inhibit the vdW forces to restacking. The FWHM of the peak is nearly 4x larger than that of the initial graphite. This indicates the presence of a significant amount of material that is < 0.1 µm large. Additionally the spectrum has a large background, commonly associated with amorphous material being imaged. This is likely due to the disordered stacking of the GO flakes. The crystlite size was calculated as 22.1 nm, which is in line with the initial graphite.

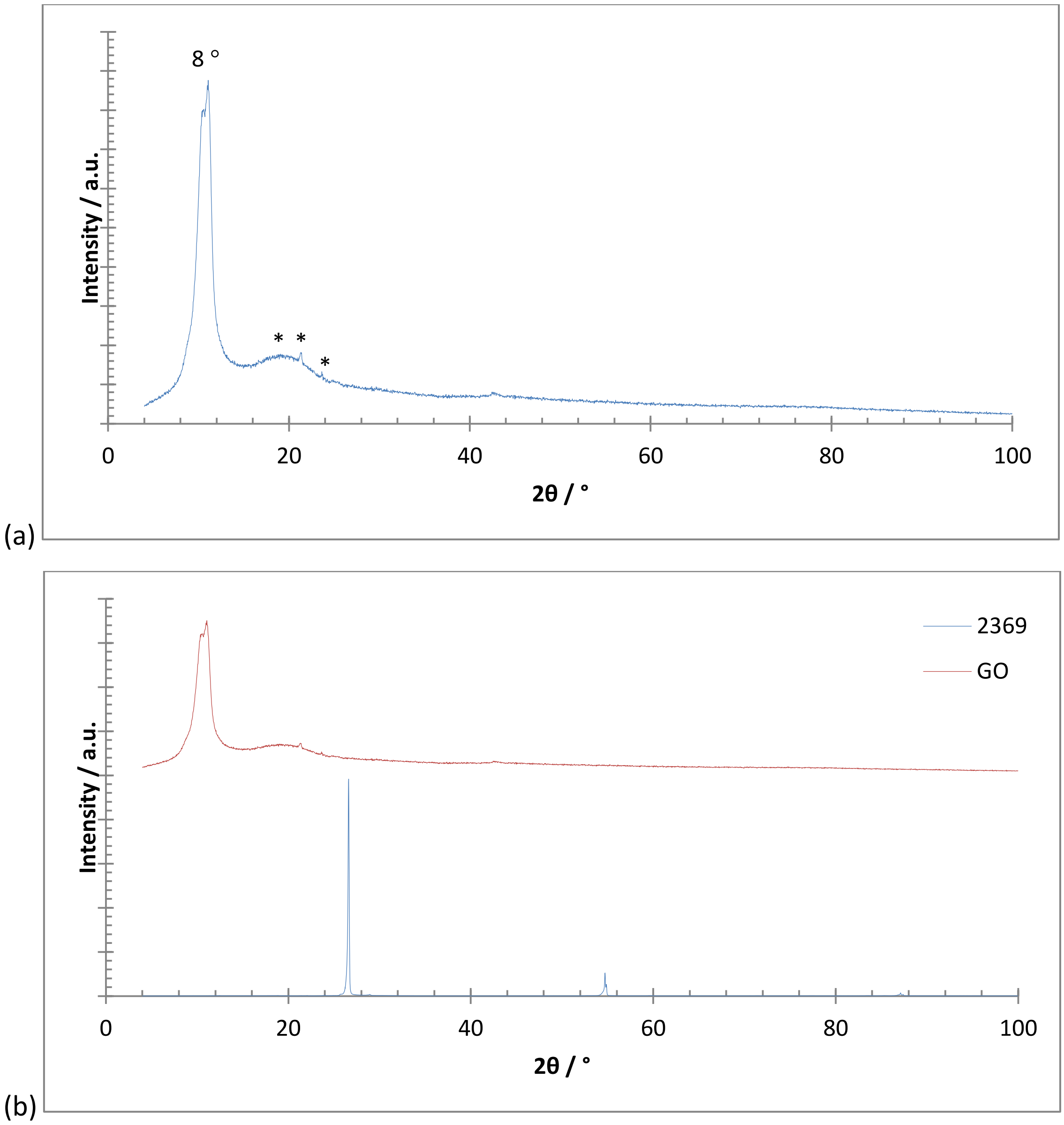

Figure 7.10: The XRD patterns of: (a) the synthesised GO, which shows a large peak at ~ 2θ = 11 °; and (b) the initial graphite used and the oxidised product. Due to the far lower intensity of the GO XRD pattern, the data was multiplied in order for comparisons to be made. '*' is used to mark signals relating to the zero-background holder.

Thermal Gravimetric Analysis

Figure 7.11 is the TGA curve of the synthesised GO. The thermal decomposition curve of the GO has far more weight loss events than the initial graphite product. These weight loss events also occur at lower temperatures than the initial graphite. This is due to the relatively thermally unstable oxygen-containing functional groups, which will leave the GO at high temperatures. Additionally, as the TGA was carried out in air, sp^3 and other defect regions will oxidise, breaking apart the GO, which could not happen in the graphite as it is strictly an sp^2 material.

The slight mass loss of 10 wt.% up to 100 °C is due to adsorbed water on the GO. The sharp mass loss (~ 25 %) which starts at 148.5 ± 4.0 °C is due to the loss of oxidative debris on the GO. The second sharp mass loss (~ 40 %) which occurs at 456.1 ± 19.3 °C is due to the burning off of the damaged graphitic regions in the GO.

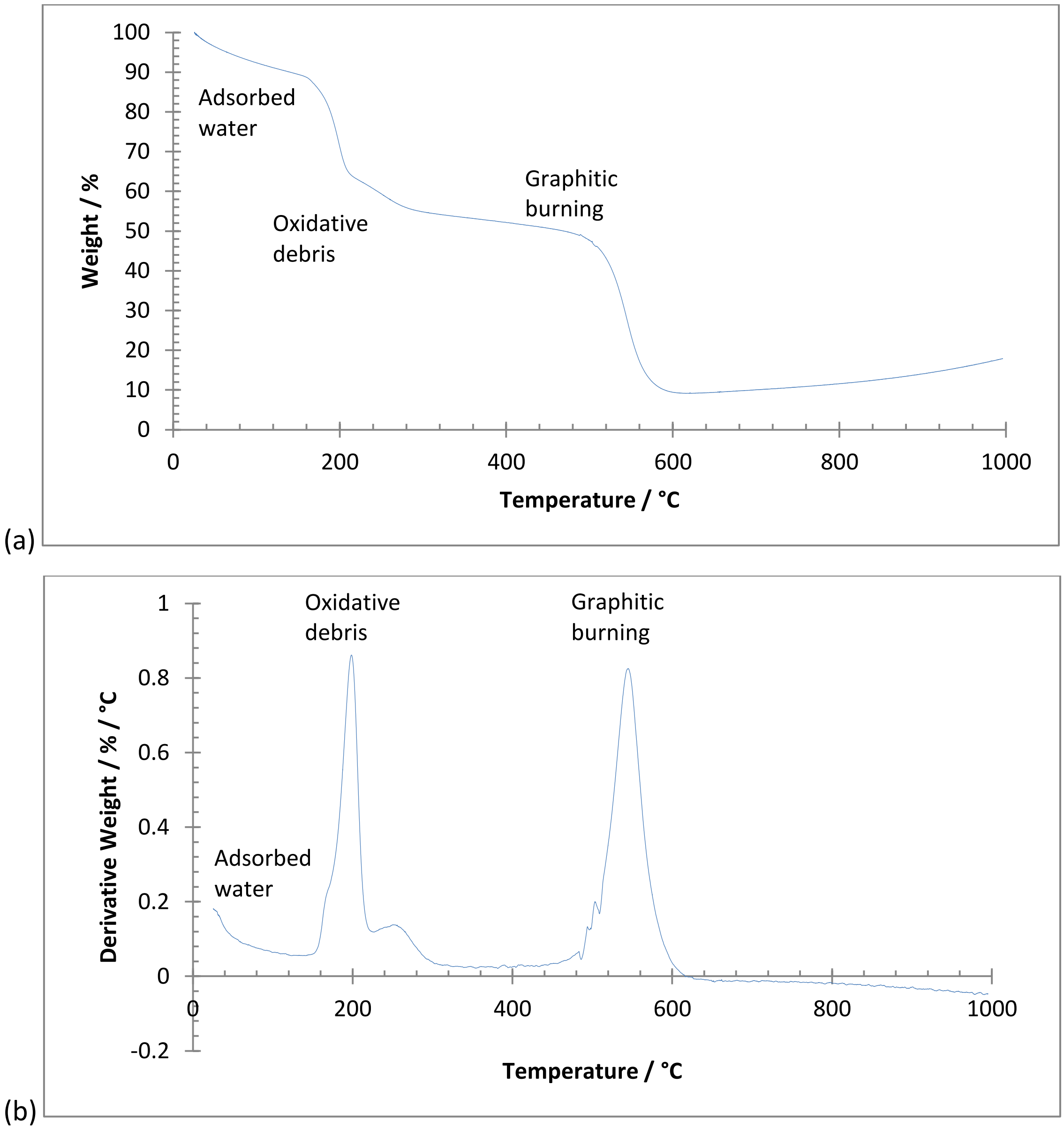

Figure 7.11: TGA curve of the synthesised GO up to 1000 °C in an air atmosphere. (a) the weight-loss curve; and (b) the derivative (temperature) weight-loss curve.

Infra-Red Spectroscopy

An FTIR spectrum (**Figure 7.12**) of the GO shows an increase in the number of functional groups in the material, which is indicative of oxidation. These oxygen containing functional groups appear as peaks from 1000 cm^{-1} to 1800 cm^{-1}. As there are many possible groups, it can be hard to define each peak; however, the definable peaks are characterised below. The peak at 1226 cm^{-1} appears due to epoxide (-C-O, stretch), the peak at 1052 cm^{-1} appears due to alkyoxy (C-O, stretch). The peak at 1726 cm^{-1} is a C=O (stretch). The peaks from 1500 cm^{-1} to 1700 cm^{-1} are due to hydroxides (O-H, stretch), ketone and carboxyl groups (C=O, stretch), and aromatic carbon (C=C, stretch). From ~3000 cm^{-1} to 3700 cm^{-1}, there is a broad peak attributed to H_2O (in part from the KBr), alcohol and acid groups.

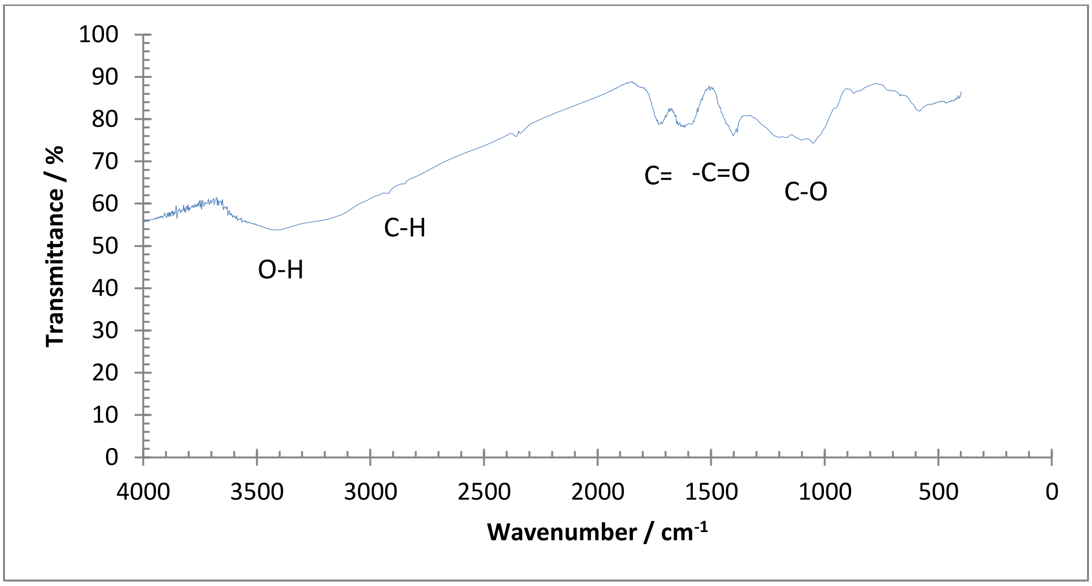

(a)

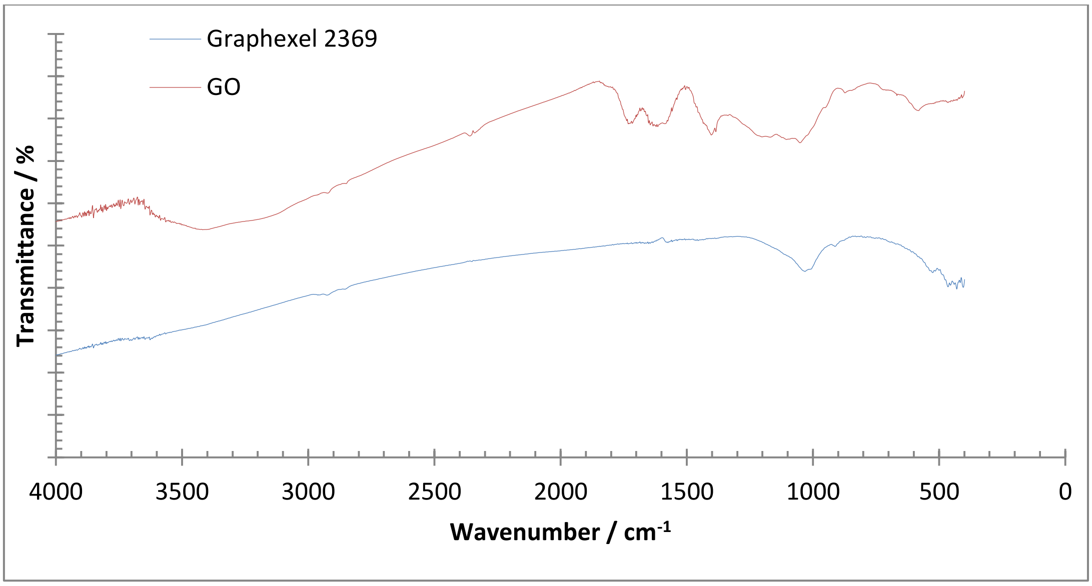

(b)

Figure 7.12: FTIR spectra of: (a) the synthesised GO, showing the material contains many oxygen-containing functional groups; and (b) the synthesised GO and starting graphite Graphexel 2369, showing increased functionality in the oxidised material.

Absorption Spectroscopy

The ultra violet-visible (UV-vis) absorbance spectrum of GO (**Figure 7.13**) from 200 to 800 nm shows two significant peaks at 230 nm and 302 nm. The peak at 230 nm is due to a C-C π- π* transition, while the peak at 302 nm is due to C=O n- π* transition. This confirms the presence of oxygen in the material, which allows for the absorbance of light.

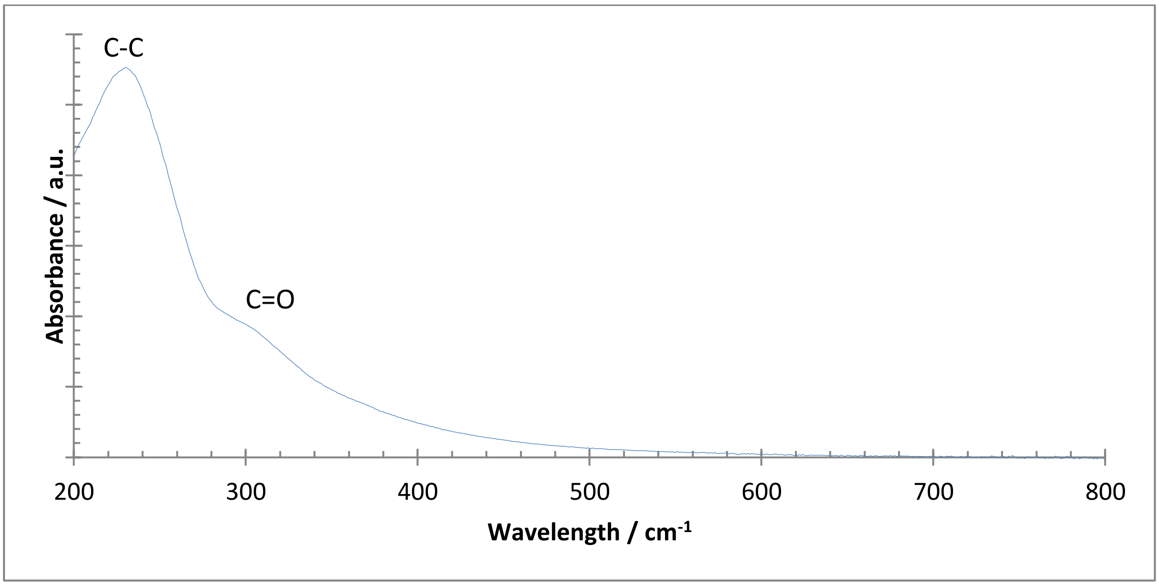

Figure 7.13: The UV-vis spectrum of GO, showing 2 distinct peaks at 230 and 302 nm, which are characteristic of the GO absorbance spectrum.

Atomic Force Microscopy

The thickness of the synthesised GO was measured by atomic force microscopy (AFM) (**Figure 7.14**). Most of the GO found was monolayer, with stacking of more layers present in more concentrated areas. The section height profile, (**Figure 7.15**) which crosses over two pieces of GO has two defined steps, one from the silicon substrate to the monolayer GO, and another from monolayer GO to bilayer GO. This can be confirmed via the height of the steps. The first step from silicon to the GO is around 1.18 nm. This is in-line with the thickness of monolayer GO (1 – 1.2 nm).[241] The second step is around 0.60 nm which is in-line with bilayer GO (2 nm).

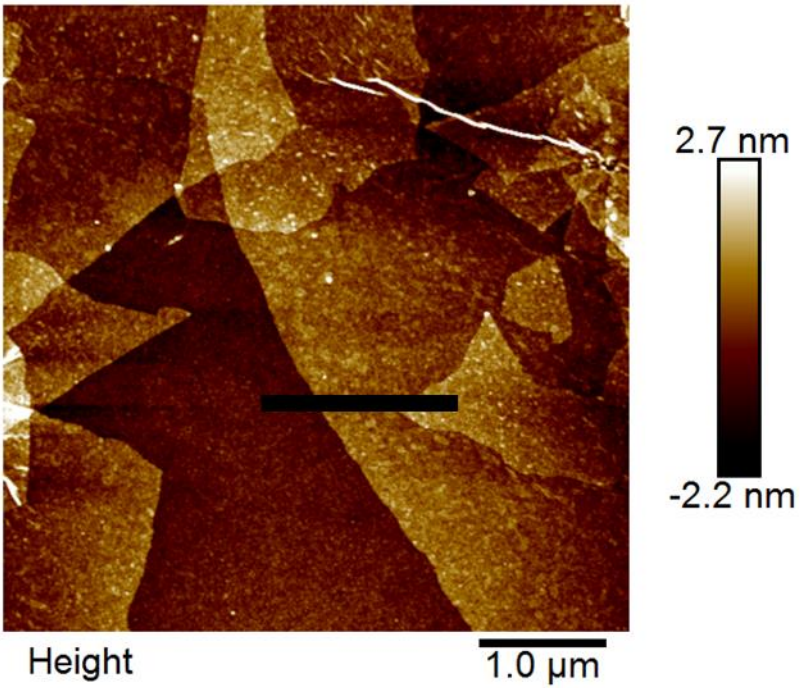

Figure 7.14: AFM image of GO on a silicon substrate. The dark brown area in the middle is the silicon substrate surface, while the more orange areas are the GO. The black bar represents the section profile shown in Figure 7.15.

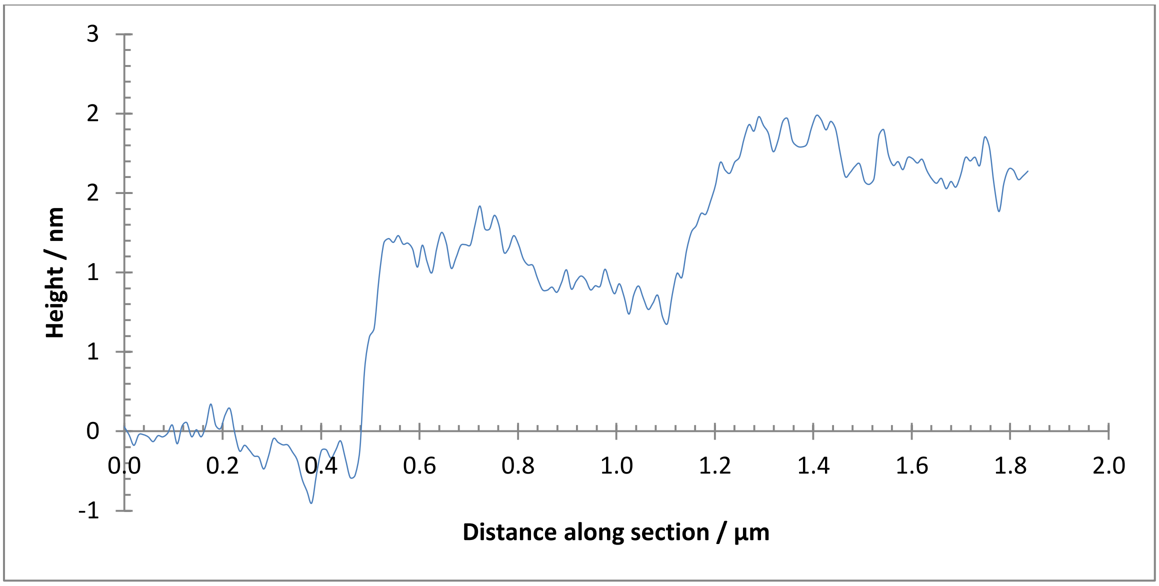

Figure 7.15: A height map along a section shown in Figure 7.14. The section shows two steps, from the silicon substrate to monolayer GO and from monolayer GO to bilayer GO.

Summary

GO characterisation reveals that the initial graphite has increased in functionality and has been damaged to produce smaller flakes, which are indicative of oxidation. SEM and Raman, show the graphite has reduced in size upon oxidation. FTIR and TGA show the product has been functionalised, with XRD showing this functionalisation has increase the d-spacing between the graphitic planes. UV-vis shows the GO now has an absorbance peak due to the presence of oxygen and AFM shows the mono-layer GO is of the correct thickness. Having successfully synthesised and characterised GO, the next step is to see if the reduction can also be successful. Following this the formation of fibres from this GO will allow for fibre reduction to create rGO fibres, which can be used as a supercapacitor electrode.

7.3 Characterisation of the Reduced Graphene Oxide

The reduction of GO is common for applications that require an un-functionalised graphene-like material. In this work, the GO was reduced to check if the reduction method was successful, which could then be applied to the reduction of the wet-spun GO fibres.

Tests were performed on multiple reduction methods. The most common method to reduce GO is the hydrazine method, however this method introduced nitrogen functionalisation, and as a comparison to the electrochemically synthesised graphene this was not favourable. Thermal reduction at 200 °C and 600 °C gave reduced graphene oxide (rGO) that still contained a high concentration of oxygen functionality. The ascorbic acid reduction of GO at room temperature also gave a functionalised product, however the ascorbic acid reduction at 95 °C for 24 hours thoroughly reduced the GO. This method was then used for the reduction of the GO fibres, with the characterisation of the rGO powder in this section.

Scanning Electron Microscopy

SEM (**Figure 7.16**) was performed to analyse the size distribution (**Figure 7.17**) of the rGO particles. The average size of the rGO particles was found to be 28.0 ± 17.6 µm. This suggests the rGO particles have increased in size when compared to the original GO particles. The average size particles has increased due to the lack of oxidative debris in the GO SEM images. The GO SEM showed a large amount of debris which was under 0.5 µm in size. This debris would be washed away during the reduction process through the filter paper which had a pore size of 1.1 µm. This is shown in the size distribution, where there is little material present under 0.5 µm in size. Additionally restoring the sp^2 domains in the rGO will increase the interactive forces between the sheets (van der Waals and π-π stacking). This will cause the re-stacking of sheets after reduction increasing the particle size. When compared to the original graphite the rGO particles are still smaller, which indicates the reduction has been successful, with smaller flakes and thinner sheets obtained. The topography of the particles has changed from the disordered GO flakes to the more regulated rGO. There are less sheets with torn and defect edges, however the flakes are not strictly rectangular like in the initial graphite.

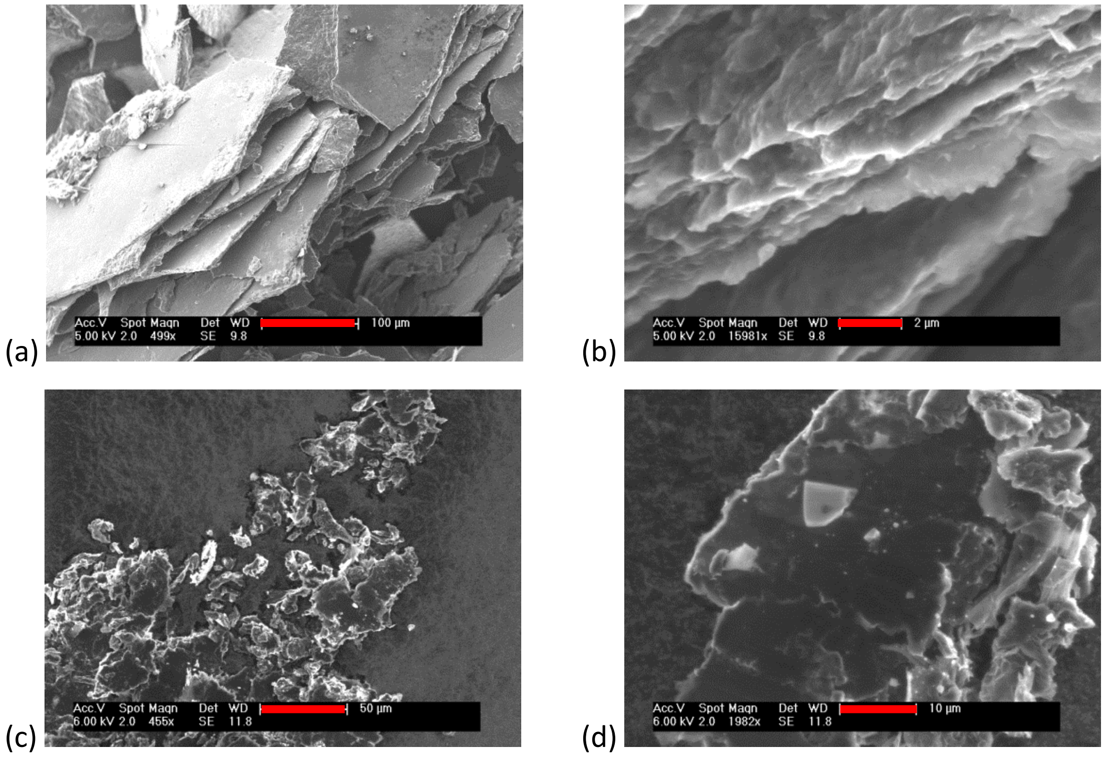

Figure 7.16: SEM images of the synthesised rGO particles. (a-b) highly ordered and large rGO flakes; and (c-d) an example of more disordered rGO flakes.

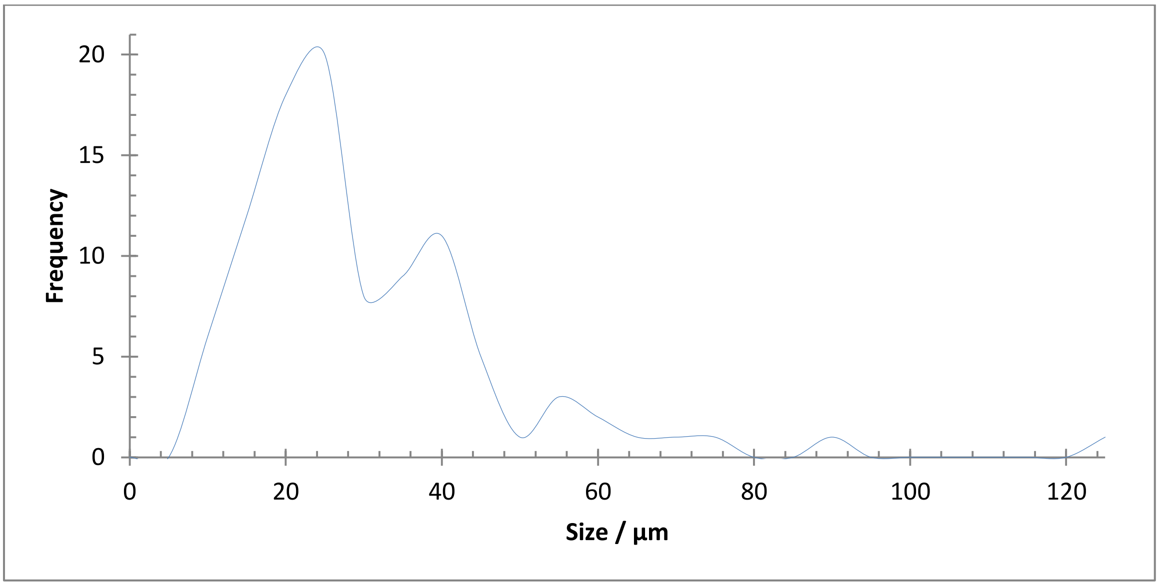

Figure 7.17: The size distribution of 100 rGO flakes as a histogram. BIN size: 5 µm.

Raman Spectroscopy

The Raman spectrum (**Figure 7.18**) and peak position / height (**Table 7.1**) for the rGO suggest the reduction of GO has been successful. The rGO Raman spectra contained all the relevant peaks at 1332.5 ± 0.4 cm^{-1}, 1592.4 ± 1.5 cm^{-1}, 2637.4 ± 2.2 cm^{-1}, and 2922.2 ± 4.4 cm^{-1}, which represent the D, G, 2D, and D+G bands of sp^2 hexagonal carbon respectively.

Compared to GO the 2D band has shifted to a higher wavenumber (from 2625.2 cm^{-1} to 2637.4 cm^{-1}), the I_D/I_G ratio has increased (from 1.26 to 1.44), and the 2D band has sharpened (from 179.4 cm^{-1} to 137.2 cm^{-1}). These are all indicative of reduction.[242] The increase in the I_D/I_G ratio means that there is a decrease in the average size of the sp^2 domains. This is due to the development of new graphitic domains, which are smaller than in the precursor GO.[79] The reduction of the I_{2D}/I_G ratio and the shift to a higher magnitude shows there is more graphitization in the sample than before.[242]

Sample	2D Peak Position / cm^{-1}	I_D/I_G	I_{2D}/I_G	2D Width / cm^{-1}
Initial Graphite	2685.1 ± 3.3	0.06	0.44	48.7 ± 15.9
GO	2625.2 ± 21.9	1.26	0.07	179.4 ± 36.5
rGO	2637.4 ± 2.2	1.44	0.04	137.2 ± 7.4

Table 7.1: A table of Raman spectroscopic data for the different graphene oxide related materials used in this PhD project. These materials are Graphexel 2369, the Hummer's method synthesised GO, and the ascorbic acid reduced rGO.

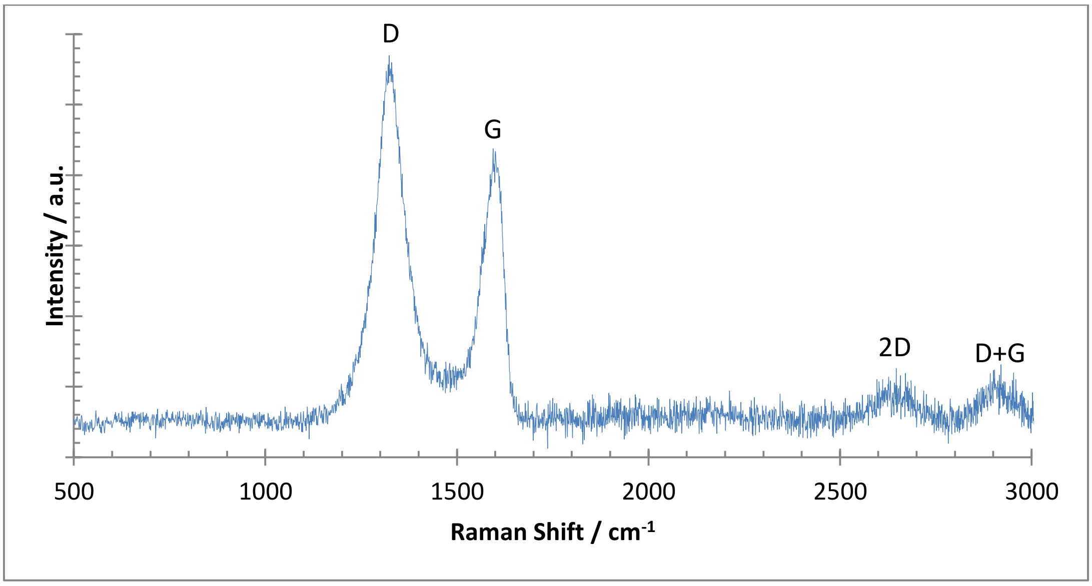

(a)

(b)

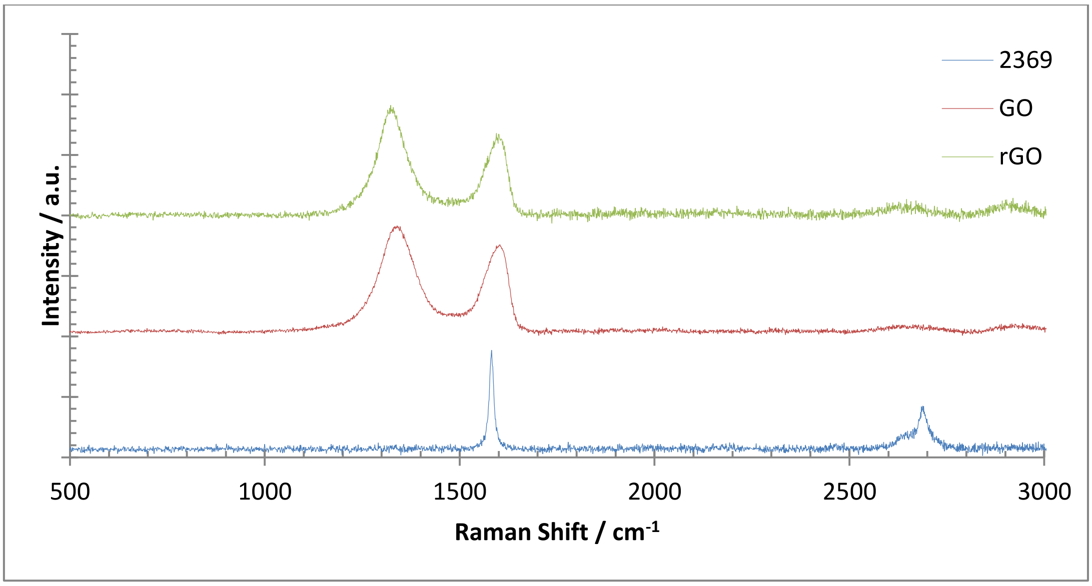

Figure 7.18: The Raman spectra of: (a) a representative Raman spectrum of the rGO sample, showing all the relevant peaks; and (b) a comparison of the Raman spectra for the Graphexel 2369, GO, and rGO materials. The I_D/I_G has clearly increased during reduction.

X-Ray Diffraction

The XRD pattern (**Figure 7.19**) for the rGO reveals the rGO has gained some of the crystallinity of graphite back and the 00.2 d-spacing has reduced. After reduction the powder was washed thoroughly with water to remove the ascorbic acid. This is shown in the XRD pattern with no additional peaks which could have been attributed to ascorbic acid.

The rGO has a broad peak at 2θ = 25.33 ± 0.10 °, which pertains to a hexagonal carbon (00.2) d-spacing of 3.44 ± 0.15 Å. This reduction has brought the d-spacing in line with the most common (00.2) diffraction peak in graphite which has a d-spacing of 3.35 Å (2θ = 26.6 °). This shows clear reduction, as the d-spacing has reduced from 8.17 Å to 3.44 Å. This reduction in the spacing between the sheets is caused by the removal of the oxygen-containing functional groups, which keep the graphitic sheets separate. The FWHM of the material was 2θ = 1.30 ± 0.00 °, which is far larger than the obtained 2θ = 0.43 ± 0.01 ° for GO, suggesting the crystallite size has reduced. This is due to the shrinking of the sp^2 domains after reduction. This has been confirmed using the Scherrer equation which gave a size of 0.11 nm. This value is far lower than the values for the initial graphite and GO (21.0 nm and 22.1 nm respectively), again confirming the creation / shrinking of new sp^2 domains.

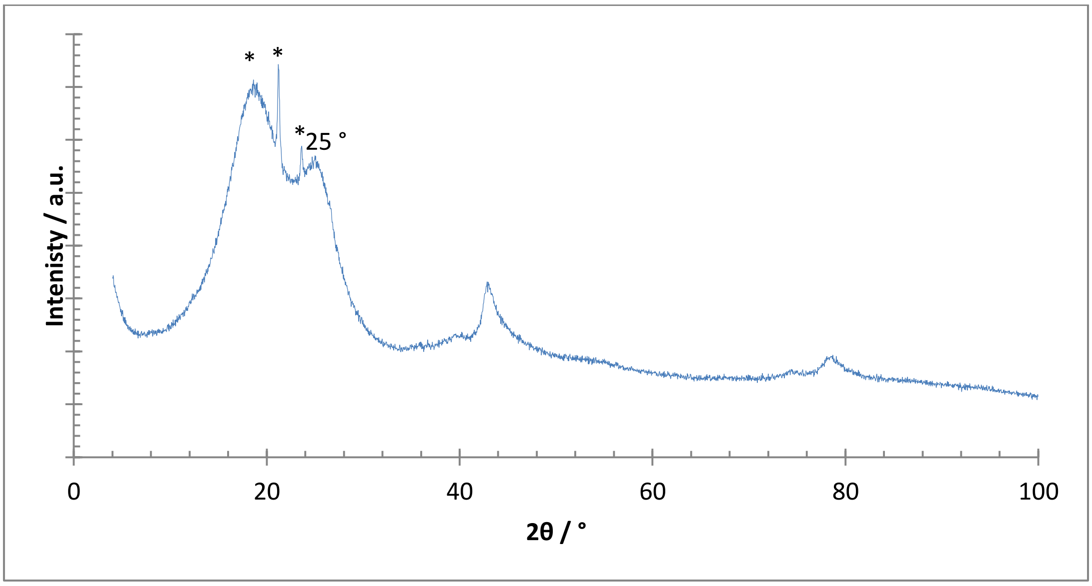

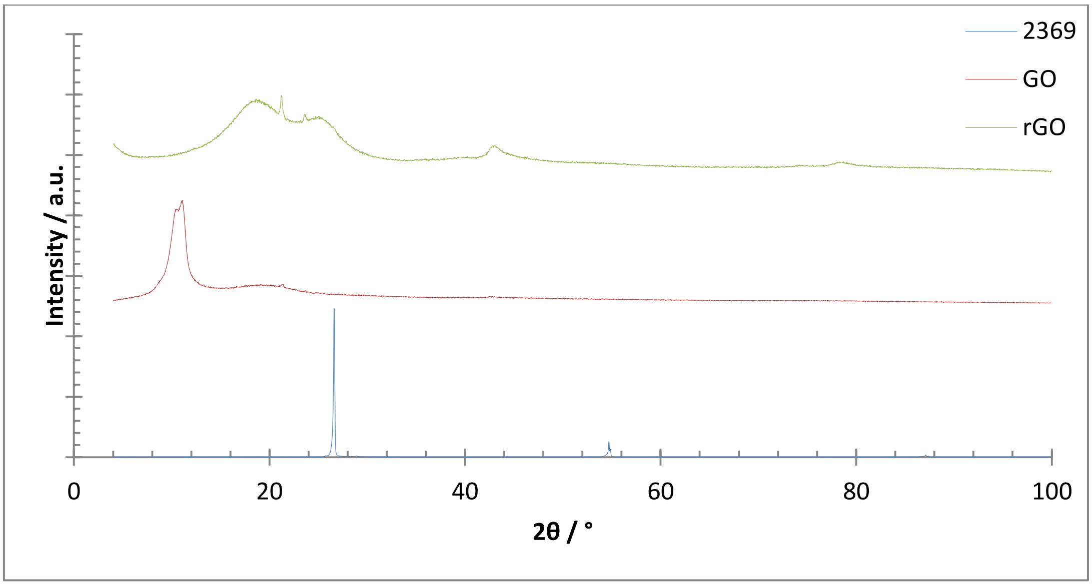

Figure 7.19: XRD pattern showing: (a) an example XRD pattern of rGO, showing the broad peak at 2θ = 25 °; and (b) the XRD patterns of Graphexel 2369, GO, and rGO. The GO and rGO data have been manipulated compared to the initial graphite to ensure the peaks can be seen. The '*' denotes signals from the zero-background holder.

Thermal Gravimetric Analysis

Figure 7.20 shows the TGA curve of the rGO powder. Reduction has taken place, as seen by the change in the thermal decomposition curve shape. There is one significant mass loss event (~ 75 %) which occurs from 462.0 ± 12.7 °C to 687.2 ± 58.2 °C. This event is due to the burning off of the graphitic regions in the rGO. This also occurs in GO at a similar temperature (456.1 °C). The slight mass loss which starts at room temperature (~ 25 %), like GO, is due to the loss of adsorbed water molecules and lingering oxidative debris on the rGO. rGO has been shown to retain some of the hydrophilicity of GO. This mass loss is much less pronounced than the initial GO, suggesting the rGO has far fewer oxygen containing groups than the initial GO, confirming reduction has taken place. The rGO did not perform as the initial graphite also confirming residual oxygen-containing functional groups in the rGO. The lower temperature initialisation of the major weight loss at ~ 450 °C compared to ~ 600 °C for the initial graphite means there are sp^3 defects still present in the rGO too. This mass loss event occurs at a temperature comparable to the non-flake graphite used for the electrochemical exfoliation.

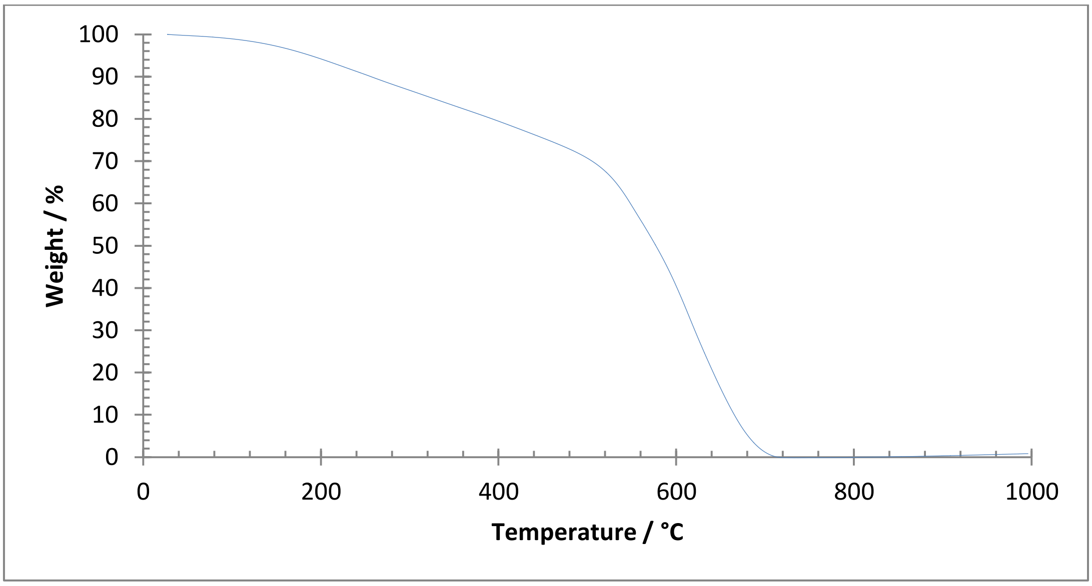

(a)

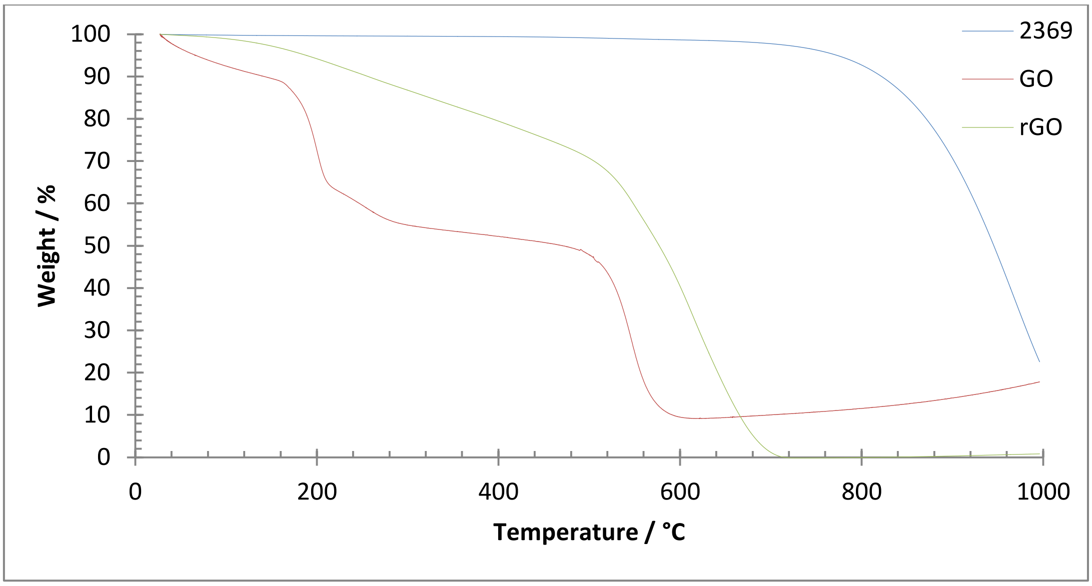

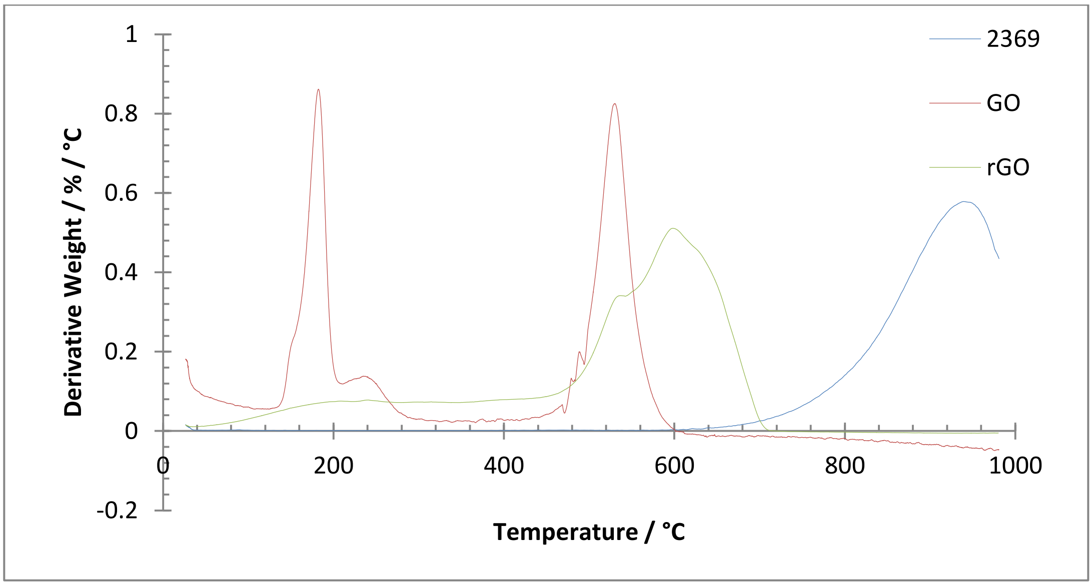

Figure 7.20: TGA curves for: (a) the weight-loss curve for the rGO powder; (b) the initial graphite (2369), GO, and rGO; and (c) the derivative (temperature) weight-loss curve for the graphite (2369), GO, and rGO.

Infrared Spectroscopy

The FTIR spectrum of the rGO (**Figure 7.21**) shows reduced functionality when compared to the GO spectrum. This confirms successful reduction. Peaks in the rGO appear at 836 cm^{-1} due to aromatic C-H (bend), 1579 cm^{-1} due to aromatic C=C (bend), and 2885 cm^{-1} due to aromatic C-H (stretch). Additional peaks appear at 1200 cm^{-1} and 1101 cm^{-1}. These are most likely due to residual oxygen-containing defects (C-O, stretch) in the rGO. The large broad peak from 3300 – 3600 cm^{-1} is due to the KBr. It may have a contribution from residual O-H groups, however the magnitude of the peak is reduced compared to the GO, and is more in line with the initial graphite.

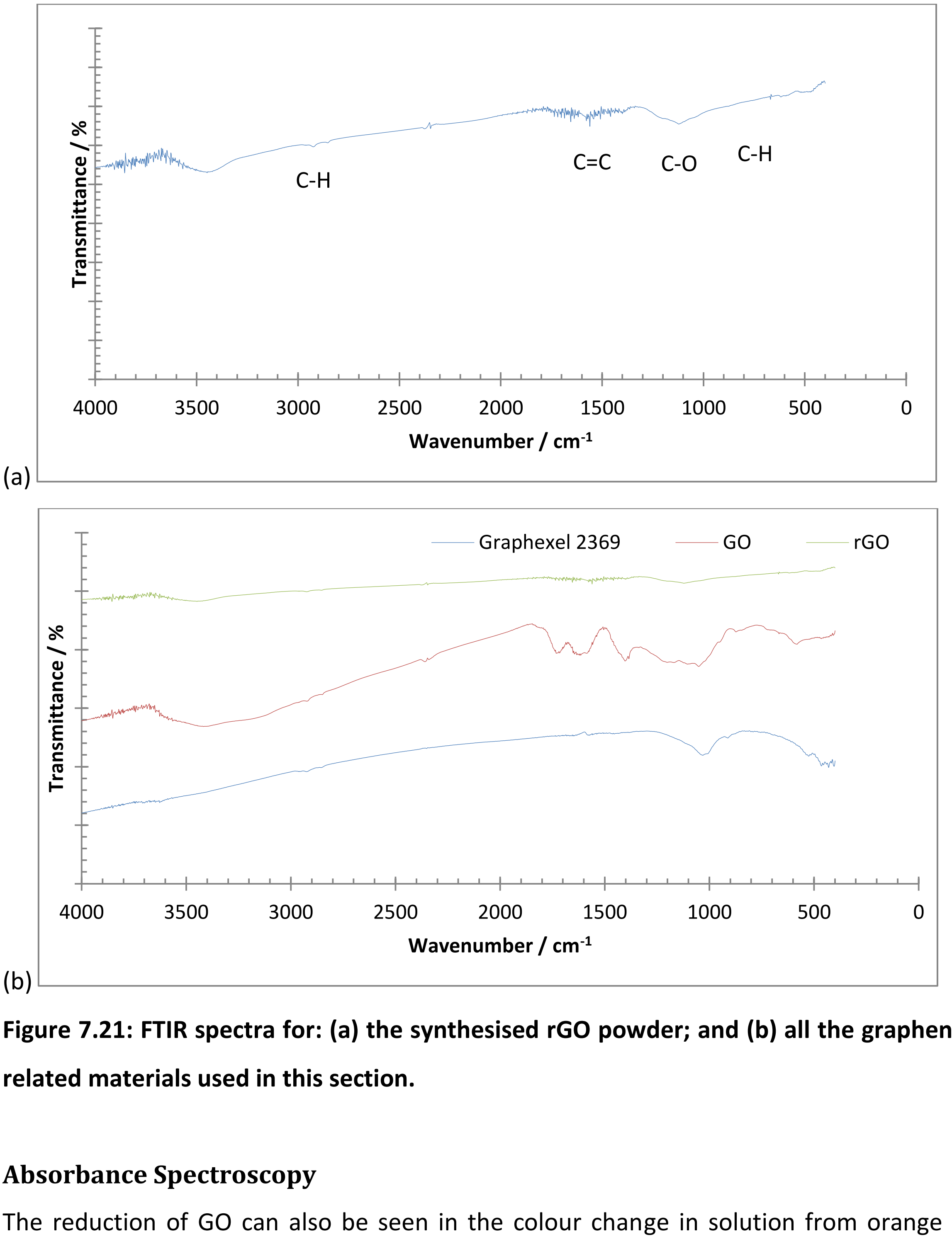

Figure 7.21: FTIR spectra for: (a) the synthesised rGO powder; and (b) all the graphene-related materials used in this section.

Absorbance Spectroscopy

The reduction of GO can also be seen in the colour change in solution from orange to black, which can be assessed using absorbance spectroscopy (**Figure 7.22**). The peak at 230 nm has undergone a red-shift to 284 nm, while the peak at 300 nm is no longer present. There is also an increase in absorbance under 300 nm.

The peak at 302 nm, while originally due to the C=O n- π^* transition is gone due to the lack of oxygen in the material. The peak at 230 nm has shifted due to a C-C π- π^* transition, however there is still a slight peak at 225 nm, meaning there are residual defects from the GO in the rGO. The increase in absorption under 300 nm is most likely due to the aromaticity of the material being restored, meaning the material absorbs more of the spectrum.

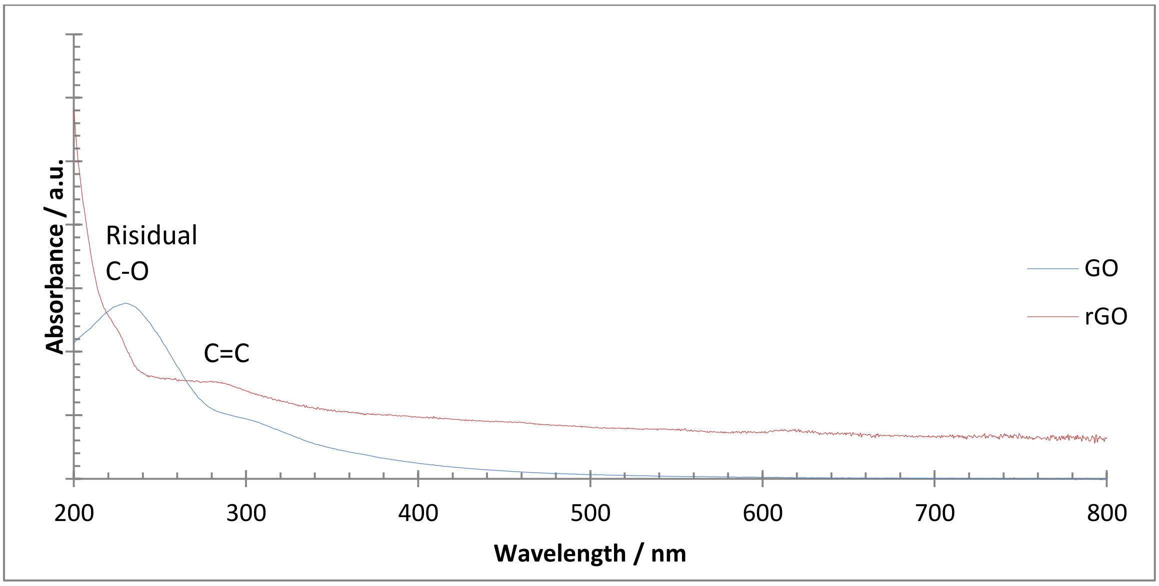

Figure 7.22: UV-Vis spectrum of GO and rGO solutions, from 200 to 800 nm, showing the change in absorbance for the powders. The labels on the graph relate to the rGO sample.

Summary

The Raman, XRD, TGA, and FTIR analysis reveal the rGO has much less functionality than the initial GO, though more than the initial graphite used for oxidation. This can be expected for reduction, with the retention of some residual oxygen-containing functional groups. The overall decrease in functionality confirms the reduction was successful. Absorbance and Raman spectroscopy reveal the hexagonal sp^2 conjugation has been partially restored. This will allow for the fast transfer of charge carriers in the rGO, which is essential for capacitors. Additionally restoring the sp^2 network will allow for EDL sites to be formed when charging, increasing the capacitance of the fibre. As this reduction has been successful, the reduction can be applied to future GO fibres in order to get supercapacitor fibres.

7.4 Graphene Oxide-PVA Composite Fibre Characterisation

Fibres were spun from a dope of GO and PVA in water, into a coagulation bath of ethanol, water, and $CaCl_2$. The characterisation of these fibres is shown in the next section. Notation for the PVA-GO (and subsequent PVA-rGO) fibres is in the form of a '%'. For instance a stock 1 % solution of PVA was made from 0.19 g of PVA and 20.50 g of water. Mixed 1:1 v/v with GO (20 mg mL^{-1}), in this example ~ 5 mL each, the resultant mixture would contain 46 mg of PVA and 100 mg of GO. Thus the fibre has a PVA:GO ratio of 0.46:1. **Table 7.2** shows the real proportion of PVA:GO for the other fibre concentrations, up to 10 % PVA-GO fibres.

Fibre / PVA %	PVA:GO Ratio
0.5	0.46
1	0.98
5	4.67
10	8.43

Table 7.2: A table showing the notation used to the PVA % in GO fibres.

It was observed that, during spinning, pure GO fibres would often break and fall apart. This occurred mostly when handling the fibres after coagulation. When the PVA template polymer was used, even at 0.5 %, the fibres held together far better, and could be easily handled and transferred for electrode testing. They could also be spun continuously without breakage. At 10 % PVA-GO fibres, the fibres became much harder to spin, due to the viscosity of the solution, which would clog the needles resulting in the stalling of the syringe pump. The spun fibres were also thicker as the concentration of PVA increased, likely due to the increase in viscosity of the solution.

Scanning Electron Microscopy

SEM was used to analyse the topography and fibre diameters (**Figure 7.23**). An examination of the two extremes showed that the wet-spun pure PVA fibres had a very smooth surface; while the wet-spun GO fibres had a have a very rough textured surface. The rough surface of the GO fibres comes from the ordered GO sheets which have to assemble to create the fibre. This results in crumpling during self-assembly. As the concentration of PVA in the wet-spun PVA-GO fibres increases the surface becomes smoother, as the GO sheets are assembled into a fibre with the PVA coating them. Additionally the average size of the fibres increased as the concentration of PVA increased, from 359.8 ± 31.1 µm for 0.5 % PVA-GO fibre, to 699.3 ± 109.6 µm for the 10 % PVA-GO fibre.

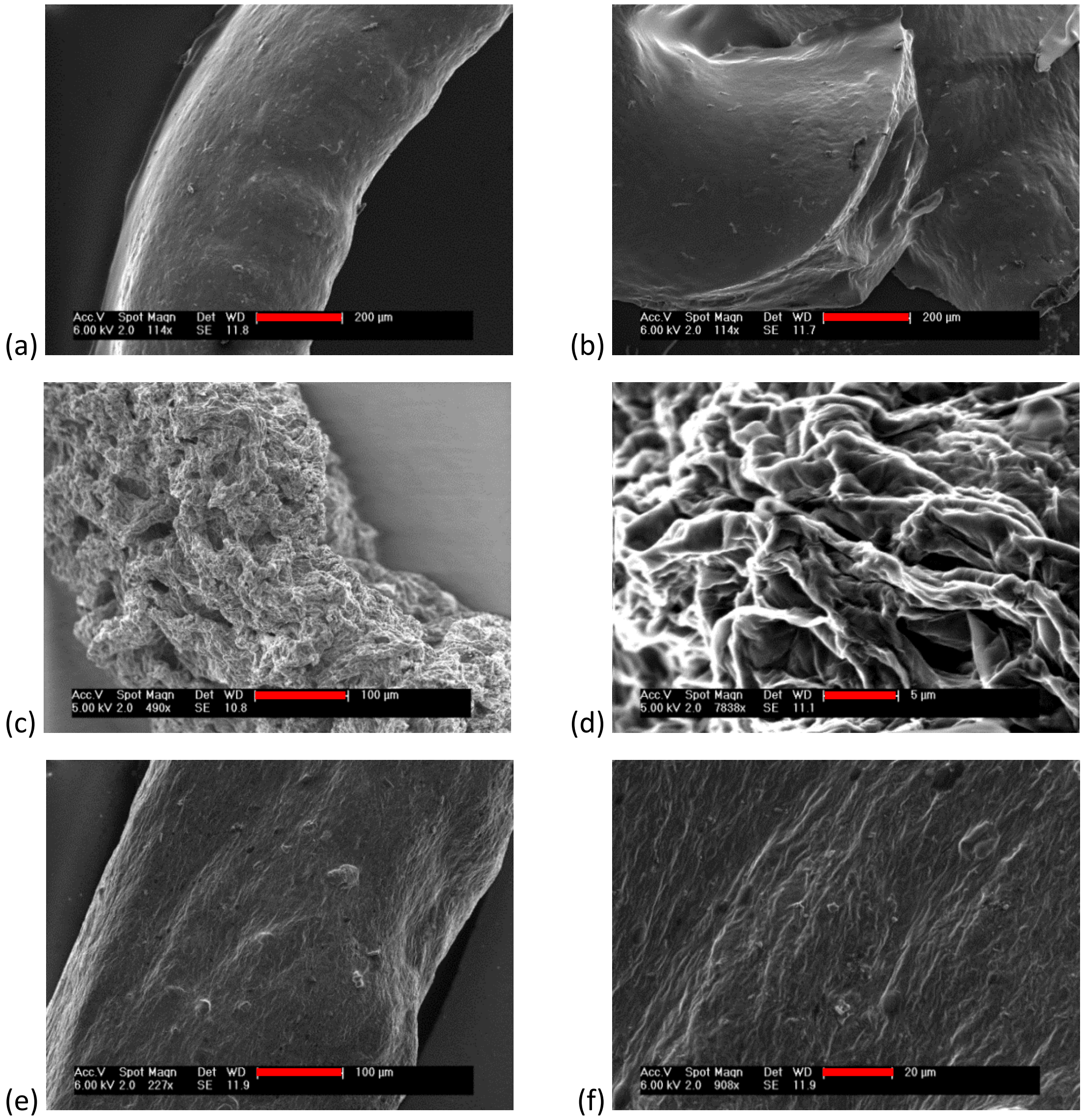

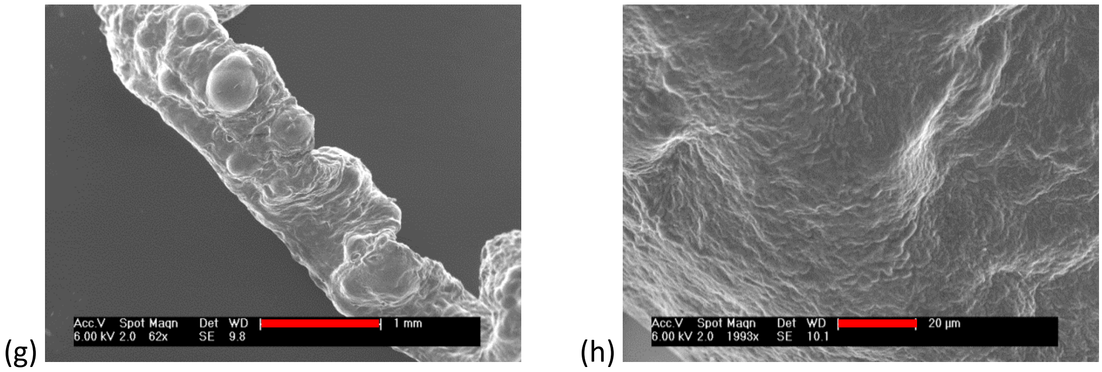

Figure 7.23: Various SEM images of the wet-spun PVA-GO fibres. (a-b) pure PVA fibre; (c-d) concentrated GO fibre; (e-f) 0.5 % PVA fibre; and (g-h) 10 % PVA fibre.

Raman Spectroscopy

The Raman spectrum of the GO fibre (**Figure 7.24**) was taken to ensure the GO was dispersed throughout the fibre. The most prominent bands for all concentrations of fibre appear, with the positions shown for the 1 % PVA-GO fibre. There are five distinct peaks in the spectrum, four of which are due to GO which appear at 1338.4 ± 0.3 cm^{-1}, 1599.2 ± 0.4 cm^{-1}, 2649.1 ± 6.0 cm^{-1}, 2935.3 ± 5.1 cm^{-1}, which correspond to the D, G, 2D, and D + G bands respectively. The 2D width is 180.9 ± 31.4 cm^{-1}, I_D/I_G = 1.15, and I_{2D}/I_G 0.06. There is a single peak corresponding to the PVA in the spectra which appears at ~ 1100 cm^{-1}. The Raman spectrum of pure PVA features far more bands, which in the fibre are masked by the high intensity GO peaks.

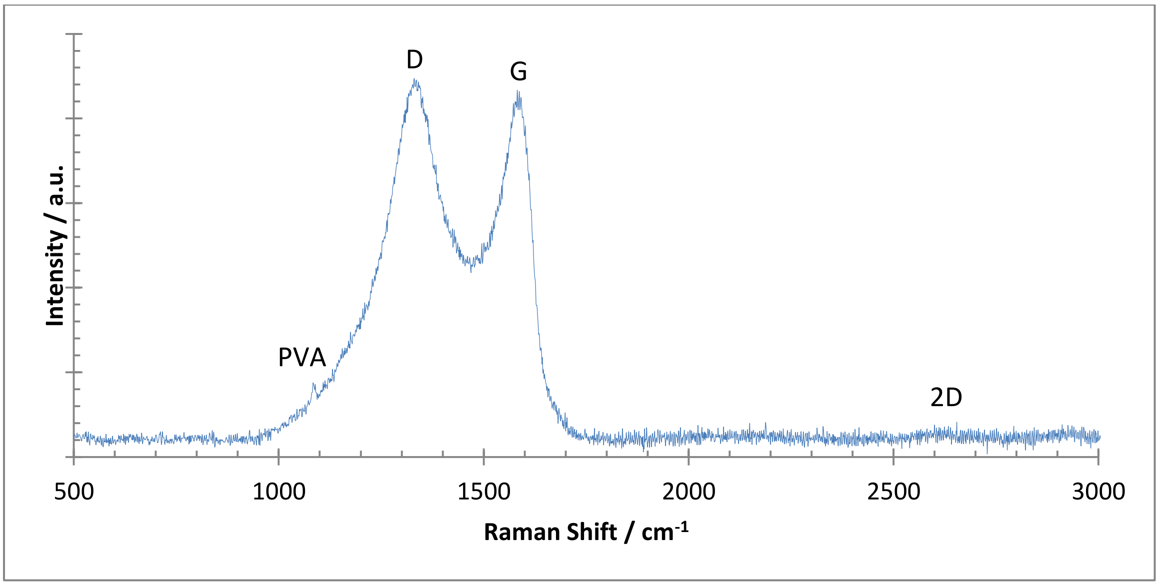

Figure 7.24: Raman spectrum of the graphene oxide / PVA composite fibre showing all the peaks associated with GO, and an additional peak at 1100 cm^{-1} for PVA.

X-Ray Diffraction

The XRD pattern of an example PVA-GO fibre (**Figure 7.25**) shows the fibre is highly amorphous. This can be seen from the very wide peaks in the spectrum, due to the X-rays being scattered in many different directions. This occurred in in all PVA-GO fibre concentrations. The amorphous nature of the spectrum means the d-spacing of the fibres cannot be analysed as there is no coherent stacking of the GO particles. This is true for the PVA as well, as a large peak should appear ~ 2θ = 20 °.

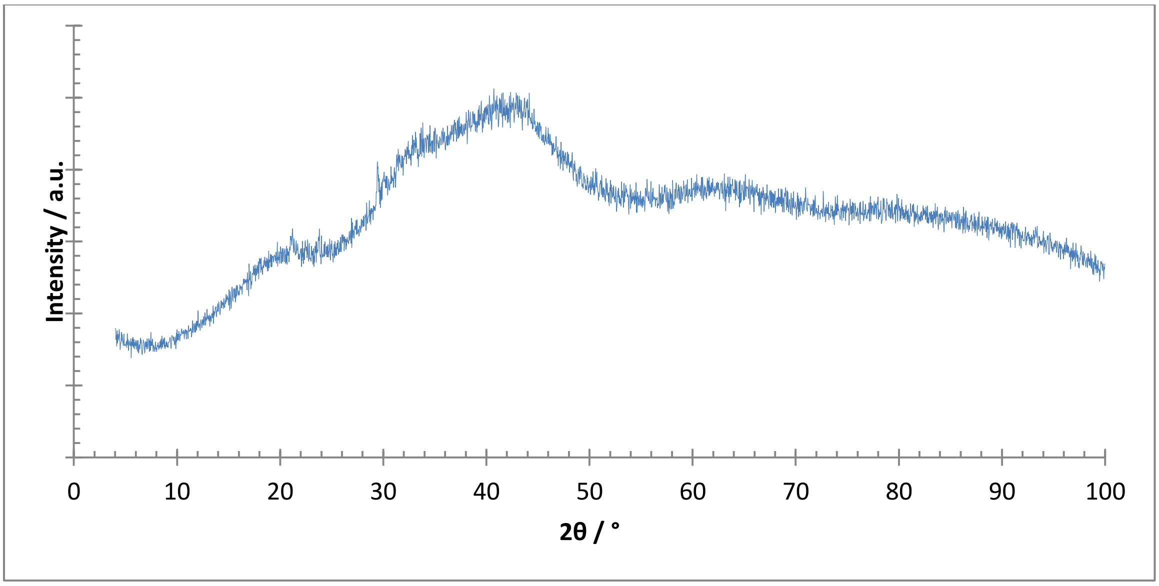

Figure 7.25: XRD pattern of the GO PVA fibre showing the wide peaks, which confirms the amorphous nature of the fibre.

Thermal Gravimetric Analysis

Thermal gravimetric analysis in air was performed to ascertain the composition of the material, along with the decomposition profile of the PVA-GO fibre (**Figure 7.26**).

The initial mass loss (~ 25 %) from 0 °C to 100 °C is due to adsorbed water leaving the fibre. The next mass loss (~ 25 %) which happens at 136.6 ± 5.1 °C is due to the loss of oxidative debris on the surface of the fibre. The next mass loss (~ 10 %) at 456 ± 9.0 °C occurs due to the burning off of the graphitic regions in the GO, and the carbonisation of

PVA. The final mass loss event (~ 20 %) at 731.8 ± 10.3 °C is due to the final burring off of the graphitic regions in the GO fibre, which occurs later than that of the GO as it is stabilised in the fibre.

(a)

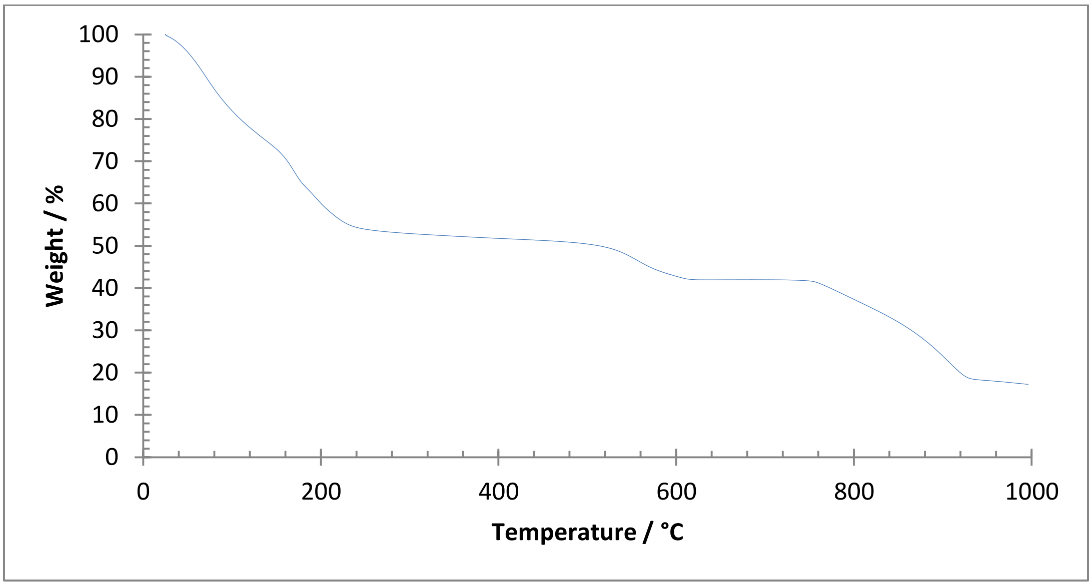

(b)

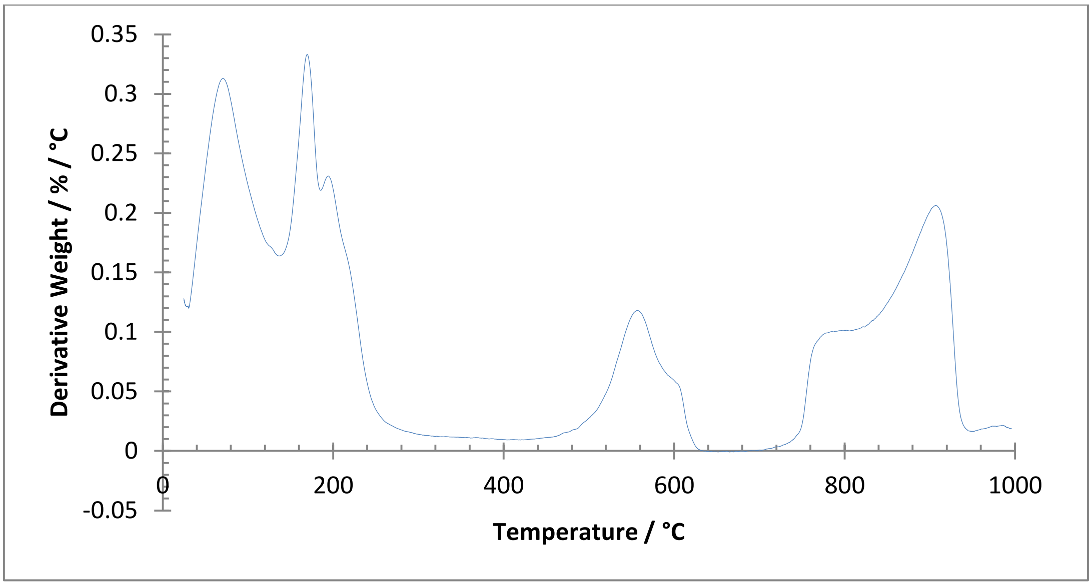

Figure 7.26: TGA curve of the 1 % PVA-GO fibre from 0 to 1000 °C in an air atmosphere. (a) the weight-loss curve ; and (b) the derivative (temperature) weight-loss curve.

Infra-Red spectroscopy

FTIR spectroscopy was performed to verify the functionality of the GO fibre (**Figure 7.27**). The sharp peaks show there is still much functionality in the material. Peaks appear at 1623 cm^{-1} due to a carbonyl group (C=O, stretch), 1432 cm^{-1} due to an aromatic C=C (stretch), 1133 cm^{-1} due to an epoxide C-O (stretch), 1095 cm^{-1} due to an alcohol C-O (stretch), 850 cm^{-1} due to an aromatic C-H (bend), 2956 cm^{-1} due to an aromatic C-H (stretch), and a very broad peak at 3446 cm^{-1}, which is due to the alcohol and acid groups, in conjunction with the hydroscopic KBr (-O-H, stretch).

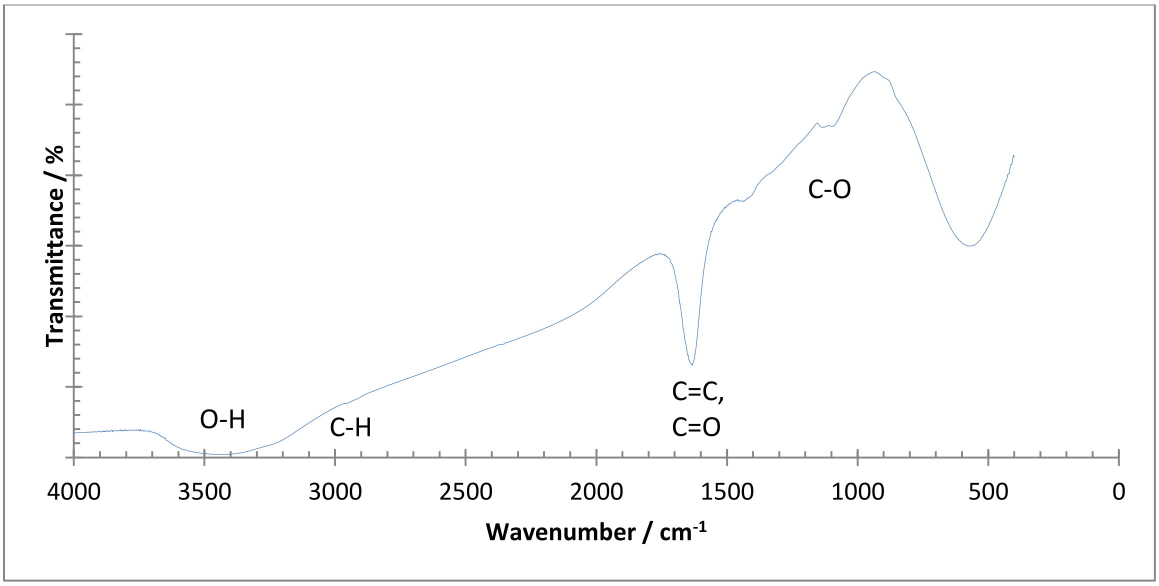

Figure 7.27: FTIR spectrum of the GO fibre, showing much functionality.

Summary

The fibres retain the functionality of the GO, with the addition of the PVA after coagulation. This is shown in the Raman, XRD, FTIR, and TGA spectroscopy. No additional sources of contamination are present. SEM shows the fibres are composed of a rough surface at higher concentrations of GO and the XRD results indicate the fibre is amorphous. This makes these fibres ideal for continuing examination via reduction and carbonisation.

7.5 Reduced Graphene Oxide-PVA Fibre Characterisation

The GO-PVA fibres were reduced and characterised for use as a super-capacitor electrode. It can be assumed that the greater the extent of reduction, the higher the capacitive performance of the fibres will be.

In order to reduce the GO fibres, the fibres were refluxed at 95 °C for 24 hours in an ascorbic acid solution. The initial solution was clear, with the fibres easily stirred without breakage. As the reaction progressed the clear colourless ascorbic acid solution gradually turned orange, then dark brown, and finally black. This is due to dispersion of the GO in the fibres into solution. In this solution the GO would have also been reduced. After reduction and washing, it was noted that the fibres were far more brittle. This is likely due to the weaker forces which bind the sheets together compared to GO.

Scanning Electron Microscopy

SEM images of the rGO-PVA fibres were taken to assess how to topography and size of the fibres had changed after reduction (**Figure 7.28**).

While at higher concentrations of PVA the GO-PVA fibres had a smooth surface, the rGO-PVA fibres had a rough surface. The loss of functional groups on the surface of the GO will result in rGO flakes which are further apart than they were in the GO-PVA fibre, resulting in crumpling to retain their shape. The average size of the fibres decreased after reduction with the 10 % PVA-rGO fibre going from 699.3 ± 109.6 µm to 485.3 ± 149.1 µm, the 1 % PVA-rGO fibre going from 660.5 ± 335.1 µm, to 435.1 ± 174.2 µm. This is most likely due to the loss of functional groups, and the dispersion of GO into solution during reduction.

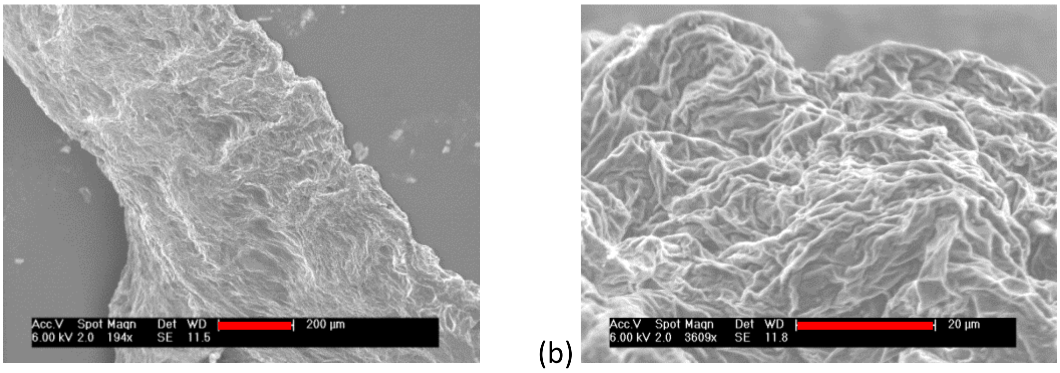

(a) (b)

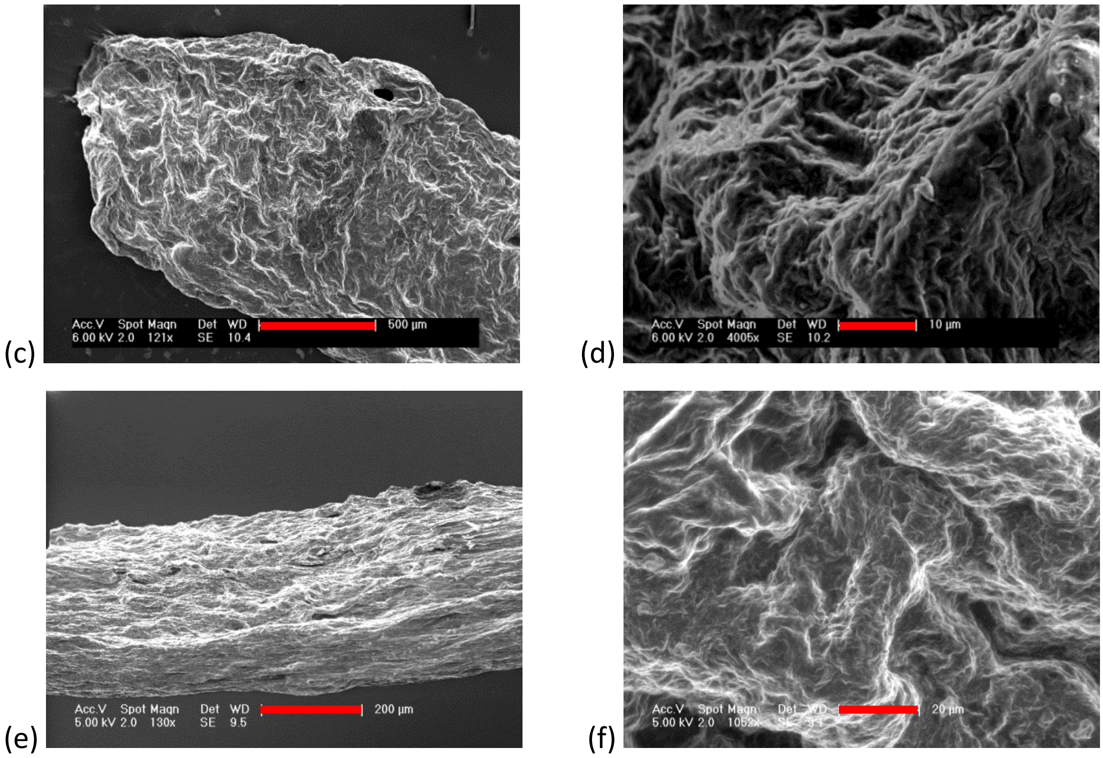

Figure 7.28: SEM images of rGO fibres. (a-b) 0.5 % PVA rGO fibre; (c-d) 5 % PVA-rGO fibre; and (e-f) 10 % PVA-rGO fibres.

Raman Spectroscopy

Raman spectroscopy of the rGO-PVA fibres was performed to ensure the GO in the fibres was reduced using peak shape (**Figure 7.29**) and position (**Table 7.3**).

Like with the reduction of GO platelets the I_D/I_G ratio increases, in this case from 1.08 to 1.25. The higher concentration of defects is due to the formation of new sp^2 sites from the sp^3 sites and oxygen-containing groups in the GO fibre, confirming the reduction reaction has been successful. The 2D band has shifted to a higher wavenumber, from 2618 cm^{-1} to 2629 cm^{-1}, which is also indicative of reduction. The 2D band has also sharpened (from 179.4 cm^{-1} to 137.2 cm^{-1}). The I_{2D}/I_G ratio has reduced, which is also indicative of reduction, as there is more graphitisation than before. The PVA peak at ~ 1100 cm^{-1} is no longer present. This is possibly due to the more intense D peak overshadowing the PVA peak, or the loss of PVA during reduction, which would reduce the intensity of this peak.

Sample	PVA Peak / cm^{-1}	D Peak / cm^{-1}	G Peak / cm^{-1}	2D Peak / cm^{-1}	D+G Peak / cm^{-1}	I_D/I_G	I_{2D}/I_G
GO-PVA Fibre	1084.2 ± 1.3	1331.4 ± 3.7	1582.3 ± 4.4	2617.6 ± 9.8	2910.0 ± 6.7	1.08	0.024
rGO PVA Fibre	Not Present	1330.1 ± 4.5	1583.6 ± 4.0	2629.5 ± 5.0	2909.9 ± 3.1	1.25	0.019

Table 7.3: Raman data that could be used to ascertain whether reduction has been successful for the 1 % GO-PVA fibre before and after reduction.

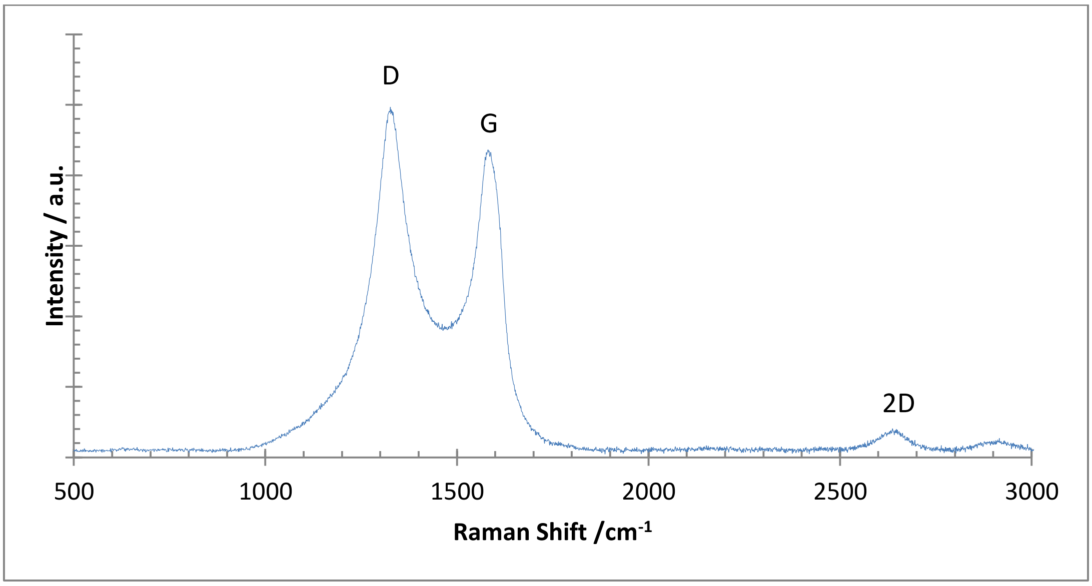

(a)

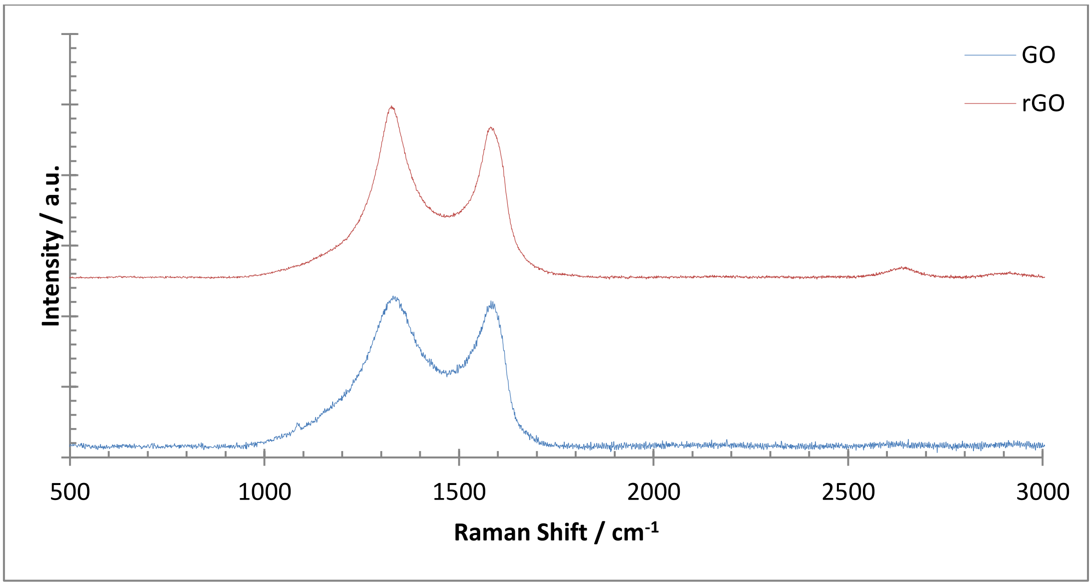

(b)

Figure 7.29: Raman spectra for the: (a) the 1 % PVA-rGO fibre; and (b) a comparrsion of the 1 % PVA-GO and 1 % PVA-rGO fibre.

The orientation of the GO in the fibres was analysed using polarised Raman spectroscopy. A singular spot on the fibre was analysed at 10 ° integers from 0 ° to 180 °. A graph of the normalised intensity of the peaks against the degree of polarisation was made (**Figure 7.30**)**.** The normalised intensity of the Raman signals varies according to the polarised light. This can be seen from the high proportion of intensity from ~10 ° to 20 ° and ~150 ° to 180 °, while there is a much lower relative intensity from ~70 ° to 100 °. The conclusion is that the GO flakes are aligned in the wet-spun GO fibre. This is due to the same reasons as the alignment of the graphitic flakes in the carbon fibre. The spinning mechanism which extrudes through a uniaxial flow into the coagulation bath aligns the random arrangement of the graphitic sheets with the fibre axis. Alignment of the sheets will help facilitate the peculation of electrical charge through the fibre enhancing its electrical properties in fibre form. Good alignment will also provide better mechanical characteristics, due to increased interactive forces between the sheets.

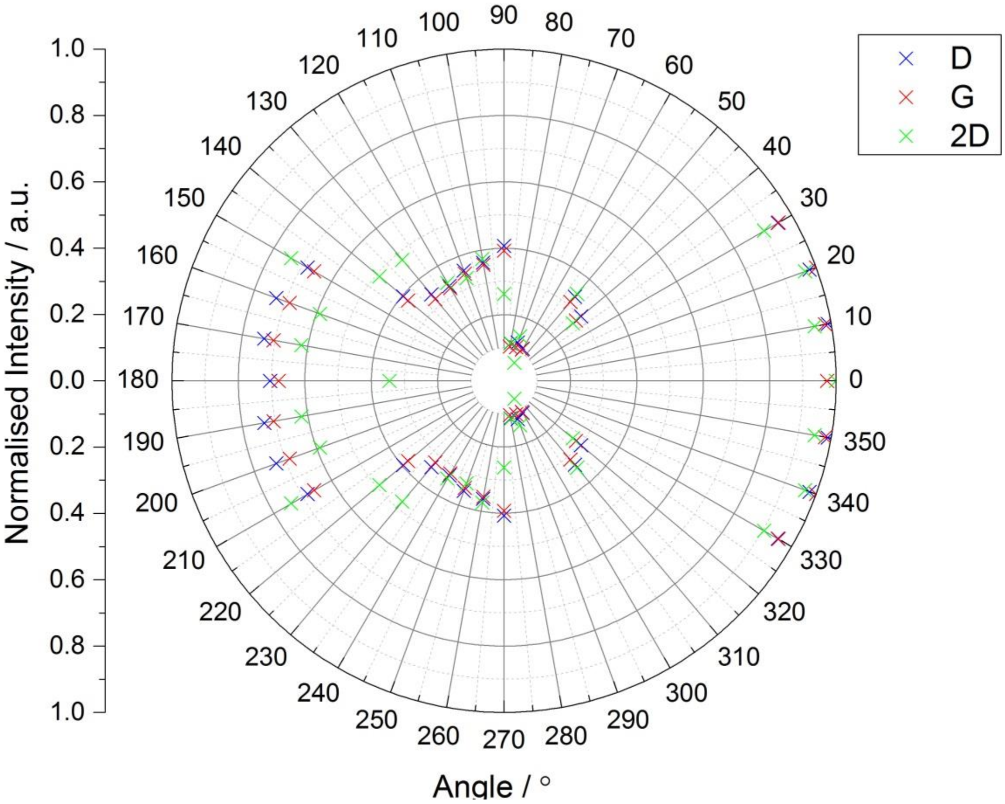

Figure 7.30: Polarised Raman spectrum from 0 – 180 ° for the 1 % PVA-rGO fibre, created using 'OriginPro 9.2'.

X-Ray Diffraction

The XRD patterns show the fibres have been reduced with a large new peak at 2θ = 25.38 ± 0.35 °, which confers to a d-spacing of 3.59 Å, and a FWHM of 0.32 °(**Figure 7.31**). The PVA-rGO fibre still shows some amorphous nature, indicated by the larger background than other patterns, however there are more clearly defined peaks than with the PVA-GO fibre. This is due the removal of the oxygen-containing functional groups, which affords better alignment of the graphitic sheets. This spacing is larger than the spacing in the rGO powder and may be due to the retention of some oxygen-containing functional groups on the fibre. The powder is likely more reduced as it has a higher surface area to volume ratio, increasing the potential for reduction when compared to the reduction of the fibre.

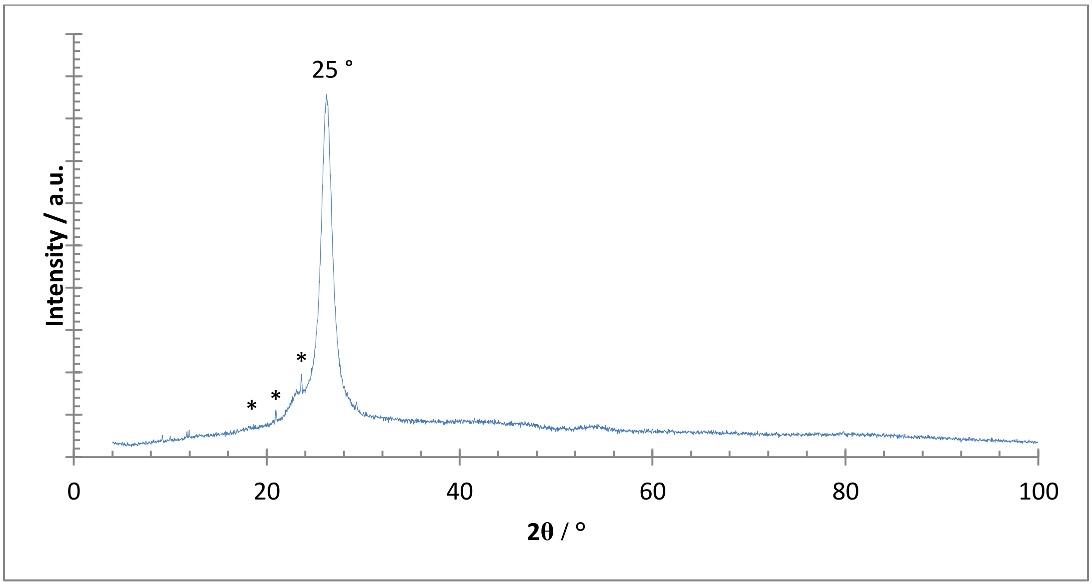

(a)

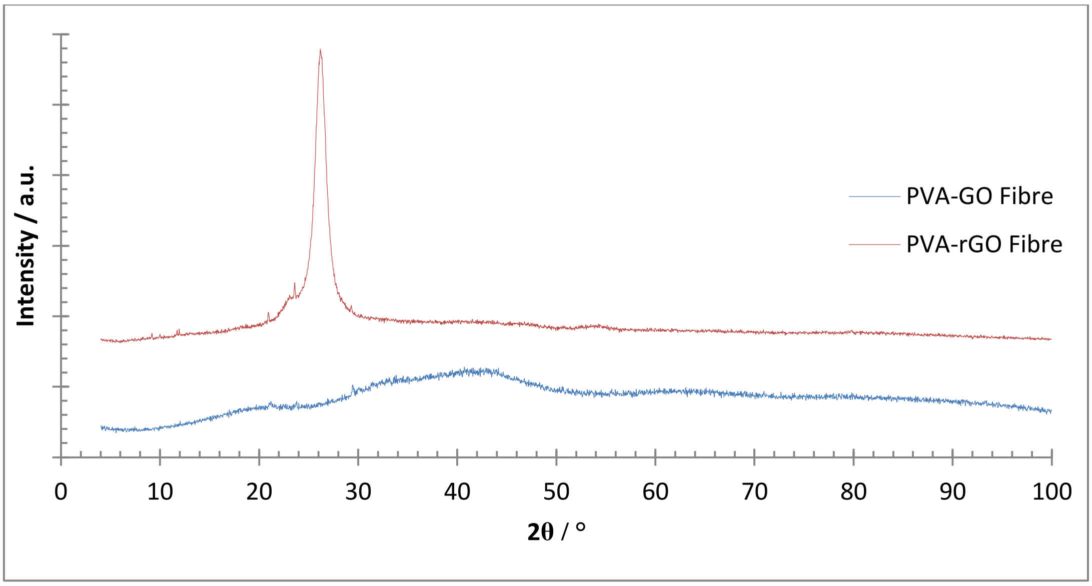

(b)

Figure 7.31: XRD pattern of: (a) the 1 % PVA-rGO fibre; and (b) the 1 % PVA-GO and 1 % PVA-rGO fibre.

Thermal Gravimetric Analysis

TGA was performed to ascertain the functionality and decomposition profile of the fibre (**Figure 7.32**). The results below are for the 1 % PVA-rGO fibre, which was similar to the other fibre concentrations.

The decomposition profile of the rGO fibre has far fewer instances of increased decomposition. While the GO fibre had a large mass (~ 25 %) loss up to 100 °C, the rGO fibre has a very small mass loss of ~ 5 %. This is due to the rGO not containing many hydrophilic groups which could adsorb water from the atmosphere. The GO fibre has a mass loss event at ~ 150 °C due to the oxidative debris on the GO. This does not occur in the rGO fibre. The first large mass loss (~ 30 %) at 275.0 ± 2.6 °C in the rGO fibre is due to the decomposition of PVA. PVA is also responsible for the slight drop at 435.1 ± 2.6 °C. This occurs until 518.8 ± 6.4 °C, where the graphitic regions in the rGO are burned off resulting in a large drop in weight for the fibre (~ 60 %).

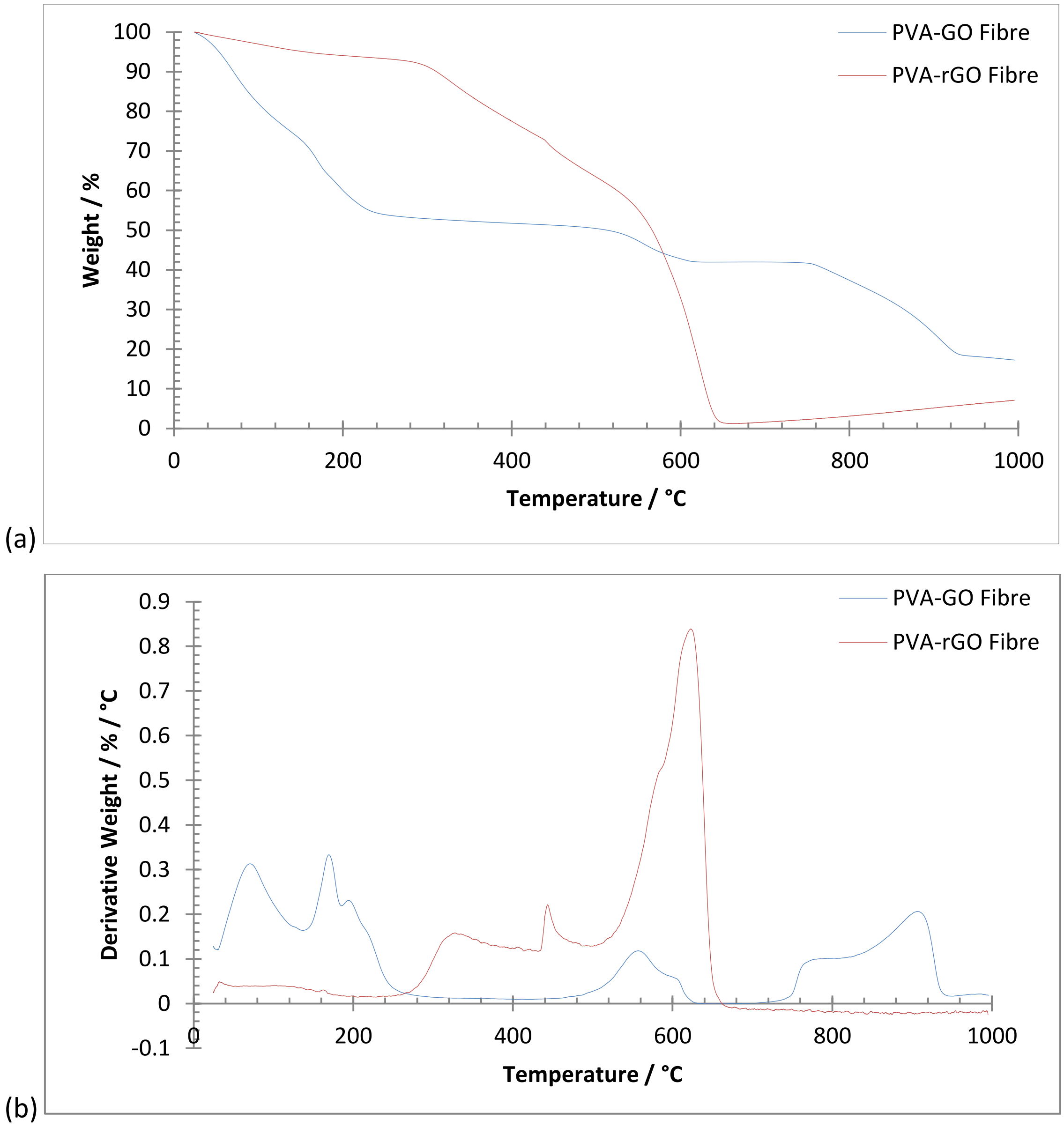

Figure 7.32: TGA spectrum of the 1 % PVA-rGO and 1% PVA-GO fibre. (a) the weight-loss curve; and (b) the derivative (temperature) weight-loss curve.

Infra-Red Spectroscopy

FTIR was used to see the extent of reduction in the rGO fibre (**Figure 7.33**). Peaks appear from the aromatic rGO carbon structure at 848 cm^{-1} due to aromatic C-H (bend), 1591 cm^{-1} due aromatic C=C (bend), and 2910 cm^{-1} due to aromatic C-H (stretch). Additional peaks appear at 1151 cm^{-1} and 1124 cm^{-1}, most likely due to residual function groups including alkoxy (C-O, stretch) and 3373 cm^{-1} due to the hydroscopic KBr. This means the fibre, like the rGO before it, still retains some oxygen functionality, though not to the extent of the GO fibre.

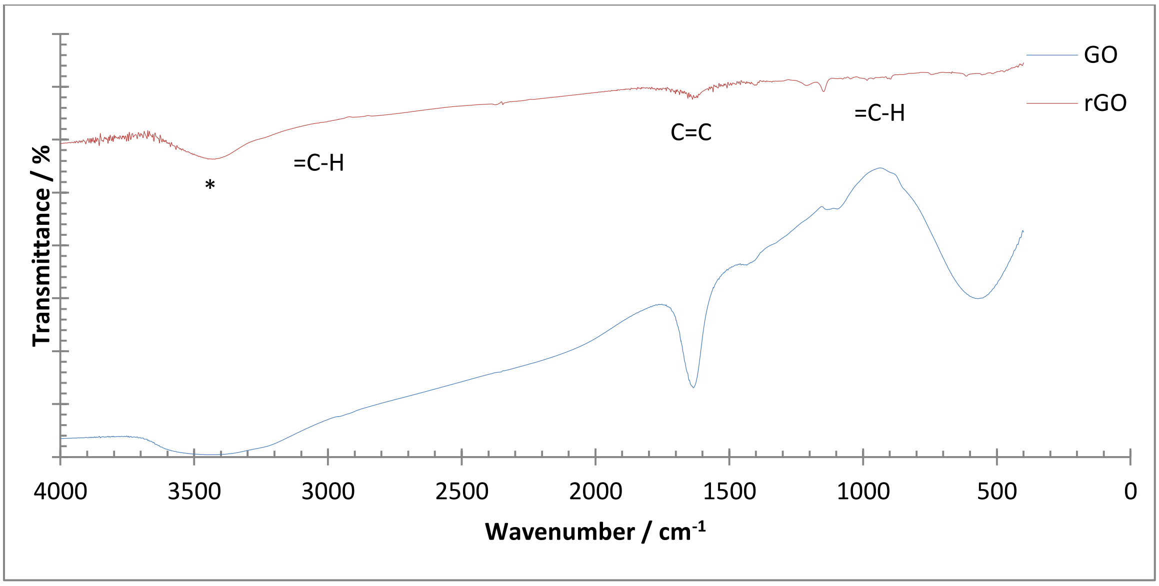

Figure 7.33: FTIR spectra of the 1 % PVA-GO and 1 % PVA-rGO fibres. There is far less functionality in the rGO fibre.

Carbonisation of the rGO-PVA fibres

In order to reduce the weight of the PVA-rGO fibres, thus to hopefully increase the gravimetric capacitance (F g^{-1}) the PVA in the fibre was carbonised. SEM showed that the carbonised fibres have increased porosity, shown by the number of large hollow bumps in the fibre. These appear due to the expansion of PVA during heating, which has distorted the shape of the fibre. When the PVA was not fully carbonised, the PVA leaves the fibres in spherical form. This is facilitated by the vacuum during SEM imaging, as these were not seen before the fibres were imaged. The loss of PVA was confirmed using SEM (**Figure 7.34**) and the weight change after carbonisation.

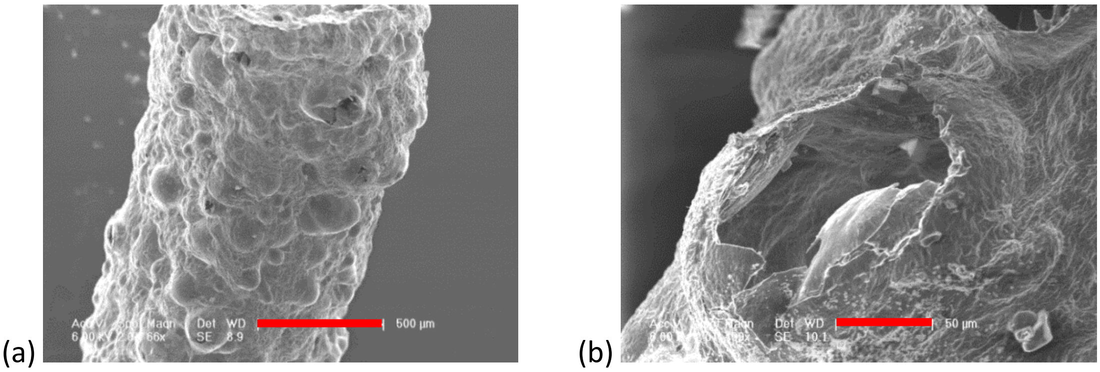

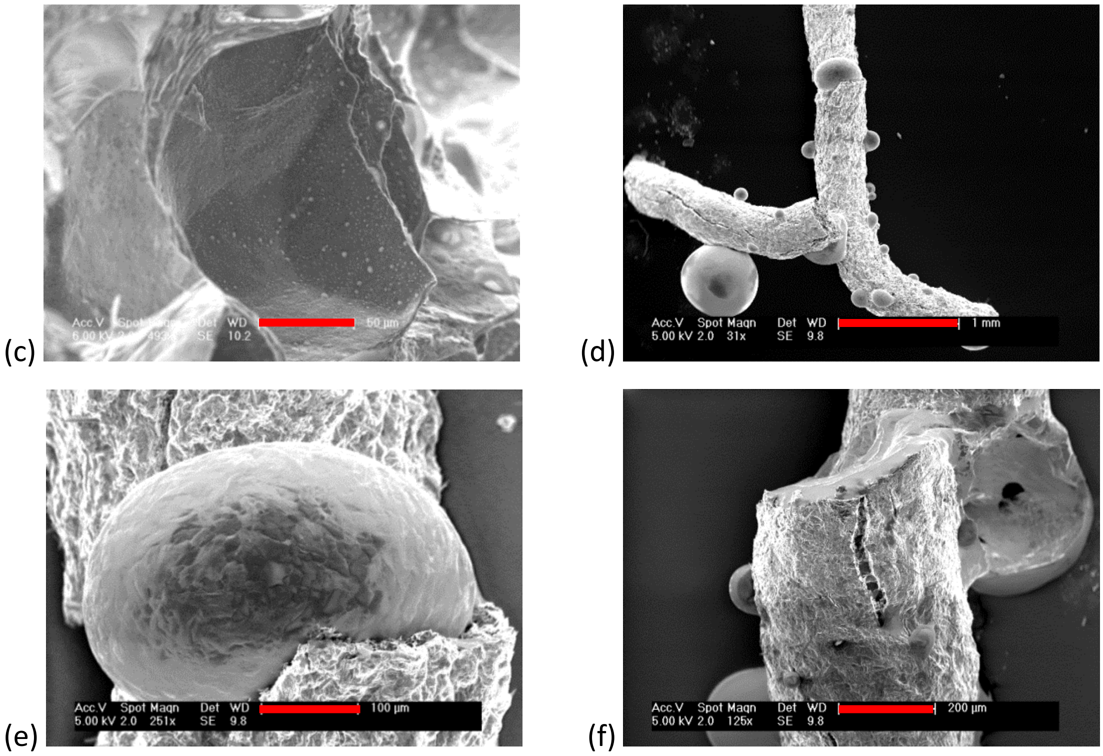

Figure 7.34: Carbonised fibres in an effort to remove the PVA from the PVA-rGO fibres. (a-c) 10 % PVA-rGO fibre with the PVA removed; (d-f) incomplete removal of the PVA from the 0.5 % PVA-rGO fibres.

Summary

The characterisation shows that the fibres were successfully reduced. The Raman and XRD patterns confirm the restoration of the sp^2 structure, while the TGA and FTIR spectra indicate there are far fewer functional groups in the fibre. XRD and SEM indicate no ascorbic acid crystals which would contaminate the fibre. The main aim of reduction is the reformation of the sp^2 structure. This is due to the removal of the oxygen-containing functional groups on the rGO, which allows for the restoration of the conjugated network through the formation of new carbon sp^2 bonds from sp^3 functional groups. This allows for the formation of more EDL sites, as the fibre now has a higher proportion of carbon in it, which will contribute towards the overall capacitance of the fibre. Due to this successful reduction, the fibres can now be tested for their supercapacitor properties.

7.6 Electrochemical Performance of PVA-rGO Fibres

The super-capacitor performance of the rGO fibres was assessed using cyclic voltammetry, galvanostatic discharge, and impedance, with the results shown below.

Supercapacitor Performance

Like with the exfoliated graphite infiltrated nickel foam and carbon fibres, the super-capacitor performance was assessed using two different methods, CV and galvanostatic discharge.

Figure 7.35 shows example CV curves. The shapes of the curves are not perfect rectangles. Rather they are curved which shows they have severe resistance in them. This is most likely caused by the residual defects on the surface of the rGO. However, the silver redox peaks common in the graphite exfoliation CV curves are not present, suggesting the fibres are forming electrical double layers (EDLs). There an extremely large difference in the CV shape for GO and rGO. The rGO curve is much more open with a wide window, showing the conductivity of the rGO has improved, due to the successful reduction of the GO. The response to the voltage reversal at 1 V and 0 V is slow, which indicates that there is a mediocre electrochemical performance. The rGO curve shows cathodic peaks at 0.38 V and 0.24 V. These reactions relate to silver redox reactions, as seen in the carbon fibre electrodes. These pronounced peaks appear largely in the rGO, which is due to the powder nature of the sample, which causes more contact with the silver, allowing for more redox reactions to occur.

Figure 7.36 shows example galavostatic discharge curves. The charge-discharge curves are mostly triangular, which means they are performing EDL competently. However as the shapes are not perfectly triangular there are some pseudo-capacitive reactions happening in the fibres. This could be from insufficient reduction of the GO, leaving oxygen-containing functional groups on the rGO fibre. These would inhibit the EDL formation, introducing resistance into the electrode. At a charge of 1 A g^{-1}, the fibres show a small IR drop of ~ 0.1 V.

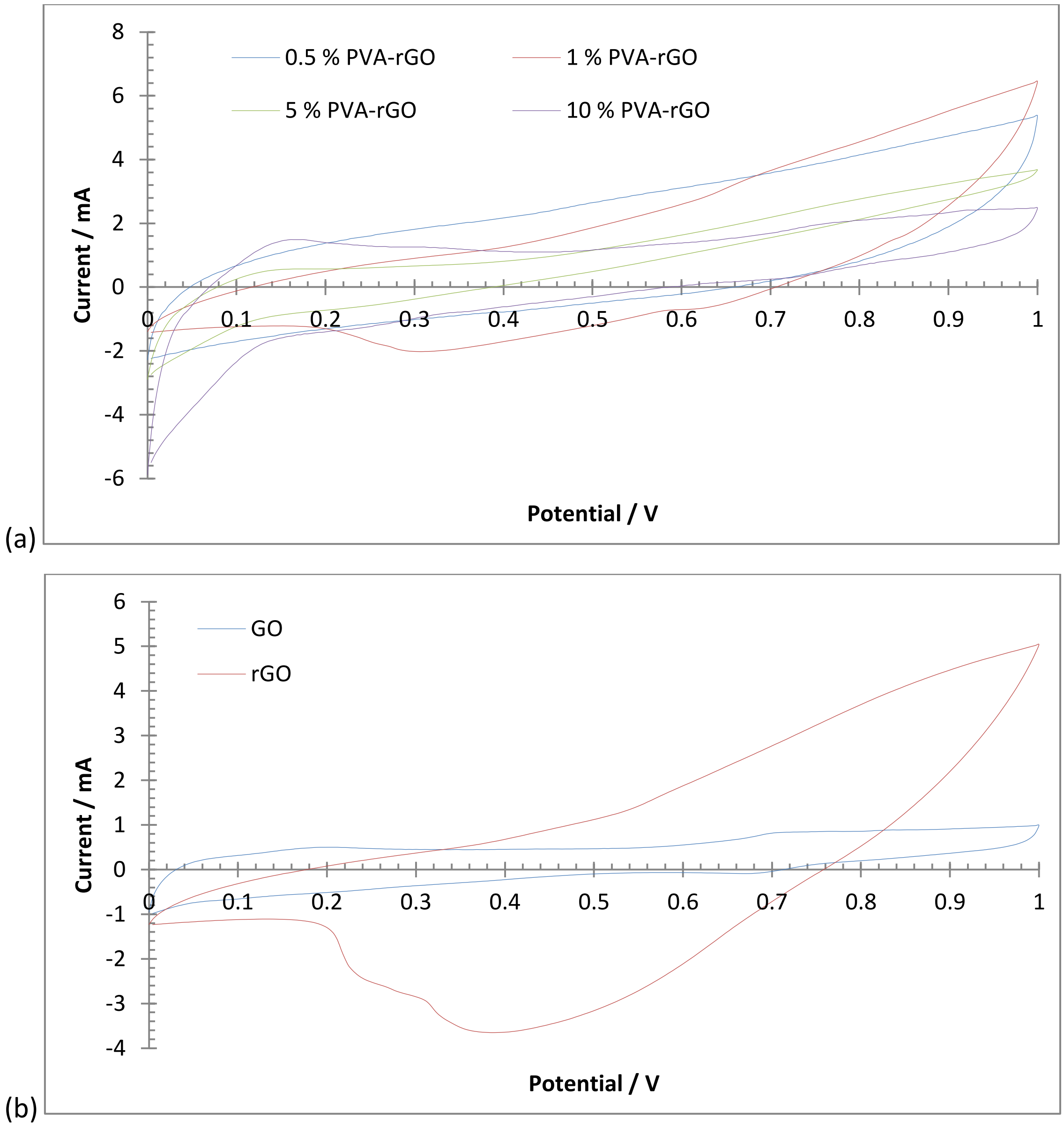

Figure 7.35: CV curves of the rGO fibres. (a) the rGO fibre capacitors at 20 mV s^{-1} ; (b) the GO and rGO CV curves at 20 mv s^{-1}.

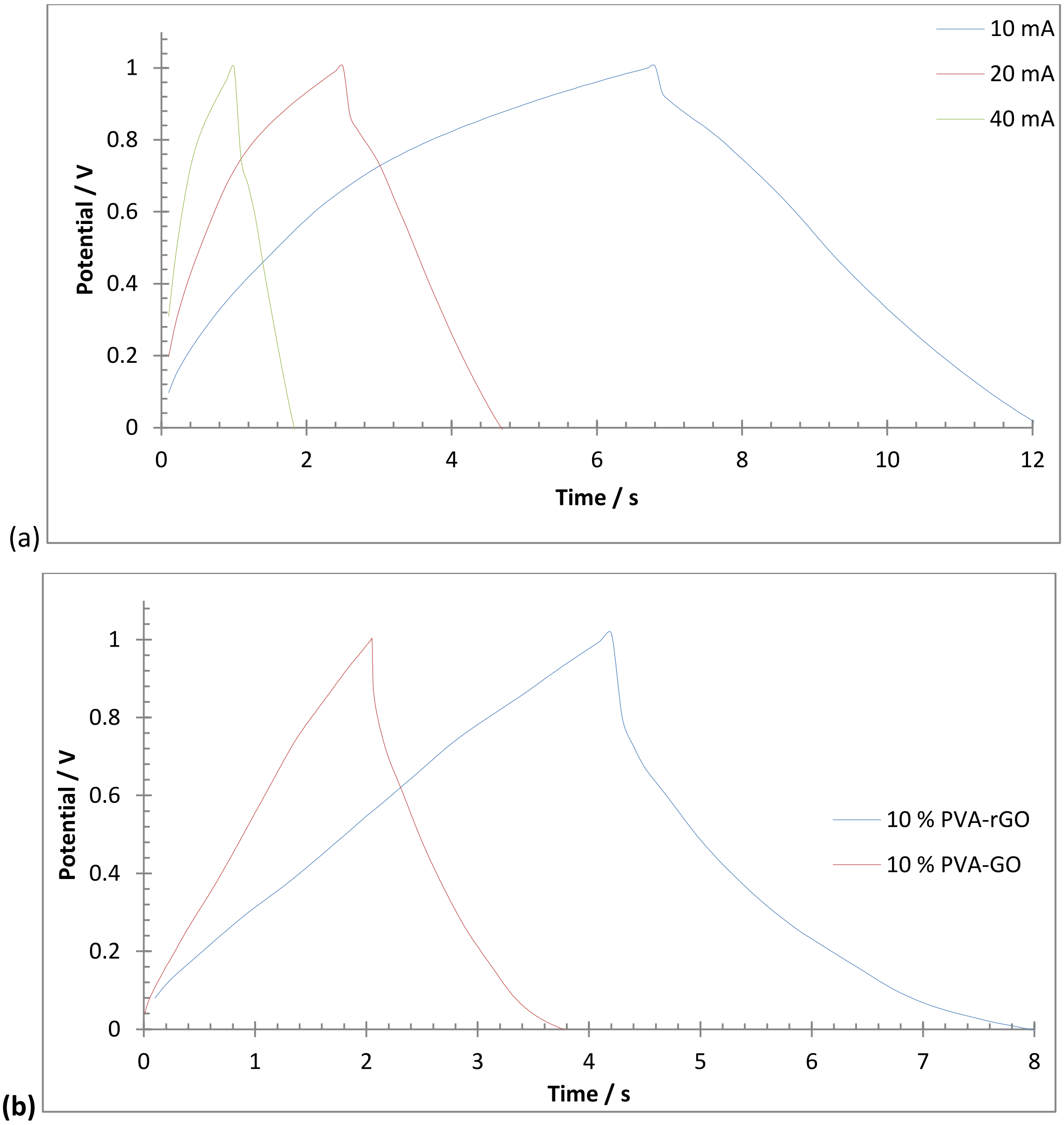

Figure 7.36: Galvanostatic charge-discharge curves rGO fibres. (a) the 0.5 % PVA-rGO fibres at three charge-discharge rates; (b) the 10 % PVA-rGO and 10 % PVA-GO galvanostatic charge-discharge curves at a constant current of 10 mA.

Capacitance of the Fibres

Figure 7.37 and **Table 7.4** show the capacitance of the rGO fibres. The calculations show that as the PVA content of the rGO fibres increases, the capacitance of the fibres decreases. Though this PVA has been carbonised, the product does not contribute to capacitance as much as the rGO material in the fibres, which results in a reduced capacitance for the fibres which have a higher PVA content. Additionally when the fibre was carbonised, it may not have become as porous, which would allow for more EDLs to be formed, as to counteract the beneficial contribution of rGO, resulting in a higher capacitance. The higher content PVA fibres also had larger diameters, which resulted in a lower surface area, meaning less EDLs can form.

There is a marked difference in the capacitance of the 1 % and 5 % PVA-rGO fibres when considering the two methods, galvanostatic discharge and cyclic voltammetry. The galvanostatic results show the capacitance of the fibres is very low, while the cyclic voltammetry results are in line with the other fibres. This could be due to the fibres discharging very quickly, as they have a high power density than the other fibres.

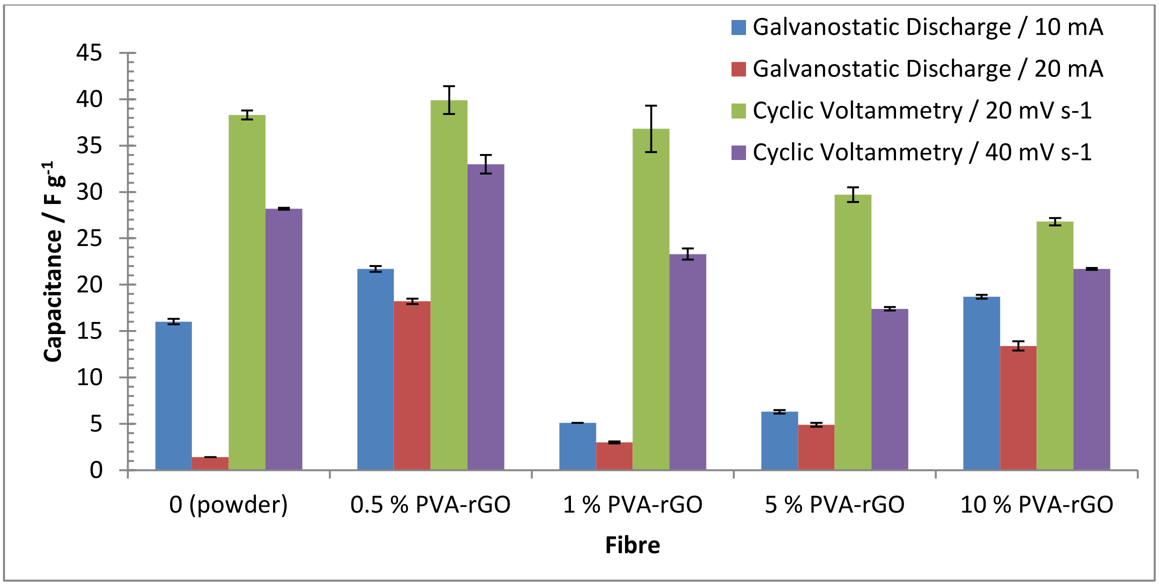

Figure 7.37: Column graph representing the capacitance of the rGO fibres using two different analytical techniques.

PVA-rGO Fibre / %	Galvanostatic Discharge / mA		Cyclic Voltammetry / mV s^{-1}	
	10	20	20	40
0 (Powder)	16.0 ± 0.3	1.4 ± 0.0	38.3 ± 0.5	28.2 ± 0.1
0.5	21.7 ± 0.3	18.2 ± 0.3	39.9 ± 1.5	33.0 ± 1.0
1	5.1 ± 0.0	3.0 ± 0.1	36.8 ± 2.5	23.3 ± 0.6
5	6.3 ± 0.2	4.9 ± 0.2	29.7 ± 0.8	17.4 ± 0.2
10	18.7 ± 0.1	13.4 ± 0.5	26.8 ± 0.4	21.7 ± 0.1

Table 7.4: Capacitance (in F g^{-1}) of rGO fibres at different concentrations and using two different calculation methods.

Scan rate stability

Figure 7.38 and **Table 7.5** show how the capacitance of an rGO fibre changed as the scan rate was increased. The results show that as the scan rate increases, the capacitance reduces dramatically. In this example, when the scan rate is increased by a factor of twenty, the capacitance is only 15 % of what it was originally. When the scan rate is increased the material is charged more quickly. This requires more sites of charging, thus porosity. Unlike the carbon fibres and the nickel foam, these fibres are not porous. This means there is less contact with the electrolyte. Thus when the fibre is charged at a fast rate, EDLs take time to form, which would mean as there are less places for EDLs the capacitance of the fibre reduces.

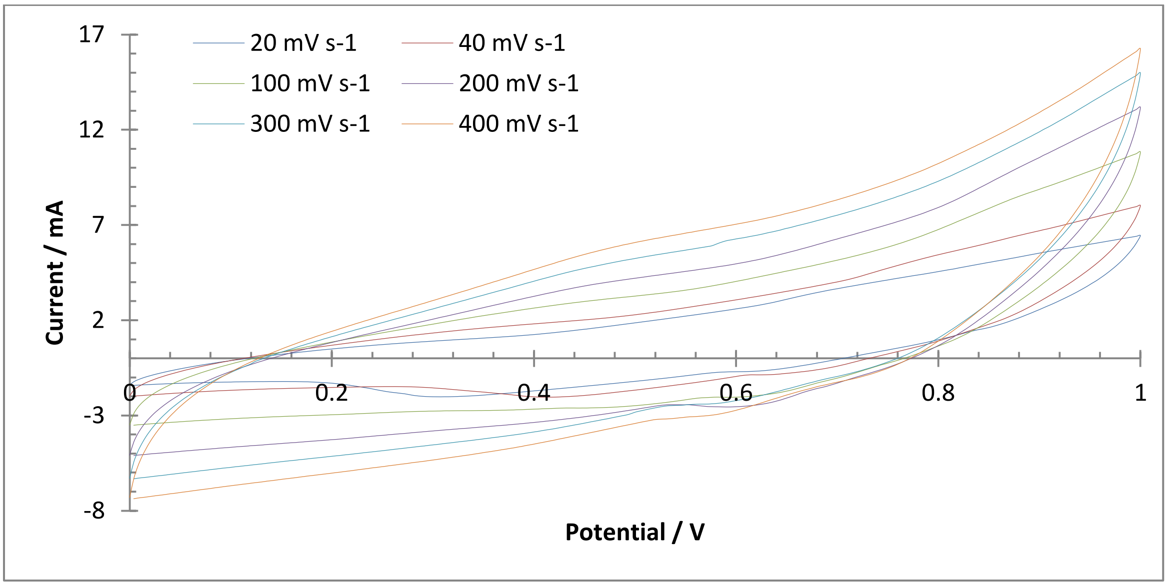

Figure 7.38: CV scans of the 1 % PVA-rGO fibres in a KOH electrolyte at increasing scan rates.

Scan Rate / mV s^{-1}	Average Specific Capacitance / F g^{-1}
20	36.8 ± 2.5
40	23.3 ± 0.6
100	13.0 ± 0.5
200	8.3 ± 0.1
300	6.6 ± 0.0
400	5.6 ± 0.1

Table 7.5: The calculated specific capacitance of the 1 % PVA-rGO fibres in a KOH electrolyte at different scan rates.

Charge Cycling Stability

The cycle life of the PVA-rGO fibres was characterised by the stability towards many charge-discharge cycles. The results are shown below in **Table 7.6**. The fibre with the highest capacitance retention was the 10 % PVA-rGO fibre. This may be due to the number of contact sites the fibres has with the electrolyte, allowing for deeper penetration. The 5 % PVA-rGO follows, though it is very close to the 0 % PVA-rGO powder, and 0.5 % PVA-rGO fibre. It could be said that the PVA content (or after carbonisation, the left over material) stabilises the fibre against the continuous charge-discharge cycles damaging the fibre. The 1 % PVA-rGO fibre bucks the trend sporting a significantly lower capacitance retention than the other fibres. This may be due to electrolyte leakage, as it plateaus after many charge-discharge cycles.

The 0.5 % PVA-rGO fibres initially fall in capacitance (400 charge-discharge cycles) compared to the initial capacitance, but gradually regain capacitance to a reasonable overall capacitance loss of 11.3 % after 2000 charge-discharge cycles. As the capacitance is only taken every 200 cycles, anomalies like this can occur, with the next recording (600 charge-discharge cycles) more in line with the final capacitance and expected curve shape. Likewise the 5 % PVA-rGO fibres exhibited abnormal behaviour, where the early recordings have a far larger capacitance than the initial capacitance, which then peters out to a more expected curve via a loss in capacitance over charge-discharge cycling. This initial increase in capacitance is likely due to more efficient electrolyte penetration during the early charge-discharge cycles, which allows more EDLs to be formed, increasing the capacitance. The other rGO fibre samples largely remain steady over time in terms of either capacitance reduction or retention.

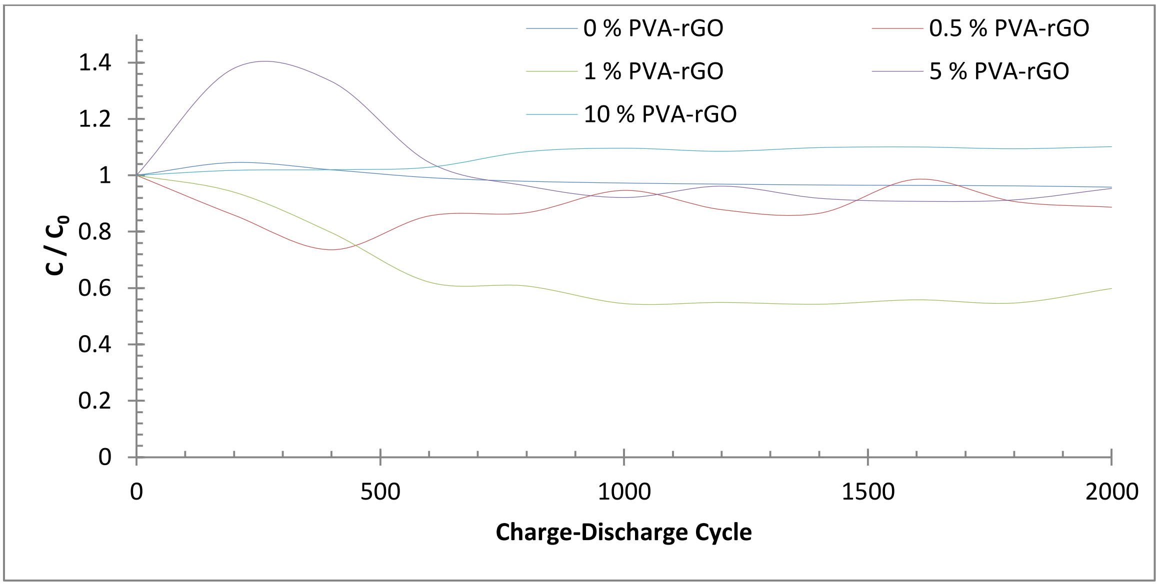

Figure 7.39: Retention of capacitance for the 1% rGO fibre charged at 10 A g^{-1} over 2000 charge cycles.

PVA-rGO Fibre / %	Capacitance Retention / %
0 (Powder)	96.1
0.5	88.7
1	59.8
5	95.4
10	110.2

Table 7.6: Capacitance retention after 2000 charge-discharge cycles at 10 A g^{-1} for the rGO-based samples.

Flexibility and Bending Times

The flexibility of the PVA-GO fibres was assessed by measuring the capacitance of the fibre after many bending cycles. The fibres were bent to 180 ° (**Figure 7.41** is a guide) and **Figure 7.40** shows example CV curves for the 10 % GO fibre, with **Table 7.7** outlining the calculated capacitance of the fibres before and after bending. After 1000 bending cycles, the fibres retain ~ 75 % of the original capacitance at both concentrations of PVA. This suggests that the mechanical stability of the fibres is due to the GO and not the PVA. It was noted however, the bending cycles had to be repeated more often on the lower concentration GO fibres, due to breaking of the fibre while bending. The higher concentration GO fibres did not break during the bending cycles. This is due to the high concentration of PVA, which binds the GO together, reducing breakage.

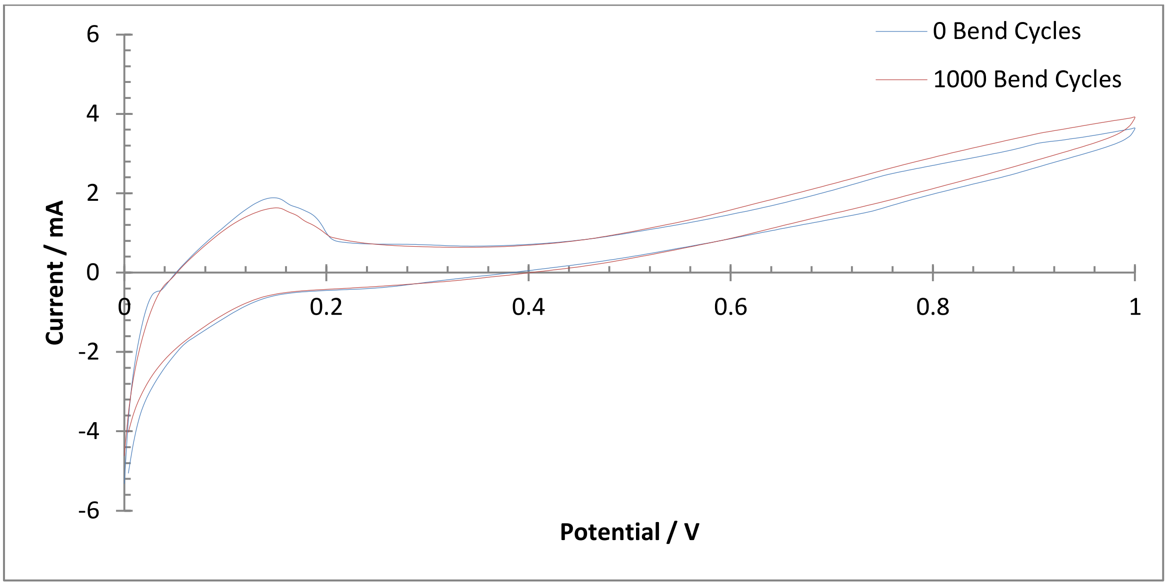

Figure 7.40: 10% GO fibre after 0 and 1000 bend cycles CV curves at 20 mV s^{-1}.

Sample	Initial Capacitance / F g^{-1}	Capacitance after 1000 bending cycles / F g^{-1}
0.5 % PVA-GO	3.1 ± 0.0	2.3 ± 0.0
10 % PVA-GO	7.1 ± 0.2	5.2 ± 0.2

Table 7.7: The change in capacitance upon 1000 bending cycles in 6 M KOH electrolyte, calculated from the 20 mV CV curve.

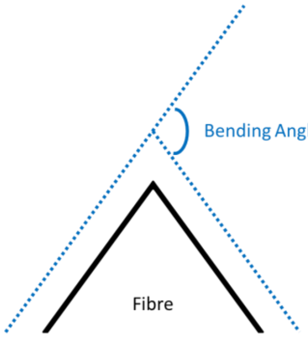

Figure 7.41: Schematic of the bending of the fibre to create a capacitance calculation

Impedance Spectroscopy

Figure 7.42 shows example impedance spectra in the form of Nyquist plots and Bode plots for the rGO fibres. All the fibres had a line tending on vertical showing they all had some form of EDL capacitance. Overall the fibres perform as worse capacitors as the concentration of PVA in the fibres increases. The ESR was slightly more than capacitors created from nickel foam and carbon fibre, with resistance ranging from 0.5 – 3 Ω. This may be due to the large fibre size creating poor connections to the electrode when compressed.

The sample which behaves most like an EDLC is the rGO powder. In the Nyquist plot this curve is the most vertical and gives a larger response than the fibre curves and in the Bode plot, the 0.1 Hz frequency is closest to the ideal -90 ° phase angle. At -45 °, where the resistive and capacitive impedances are equal, the rGO powder gives a time constant of 0.60 s. This rapid response is due to the powder form having a large accessible surface area, which facilitates ion transport.

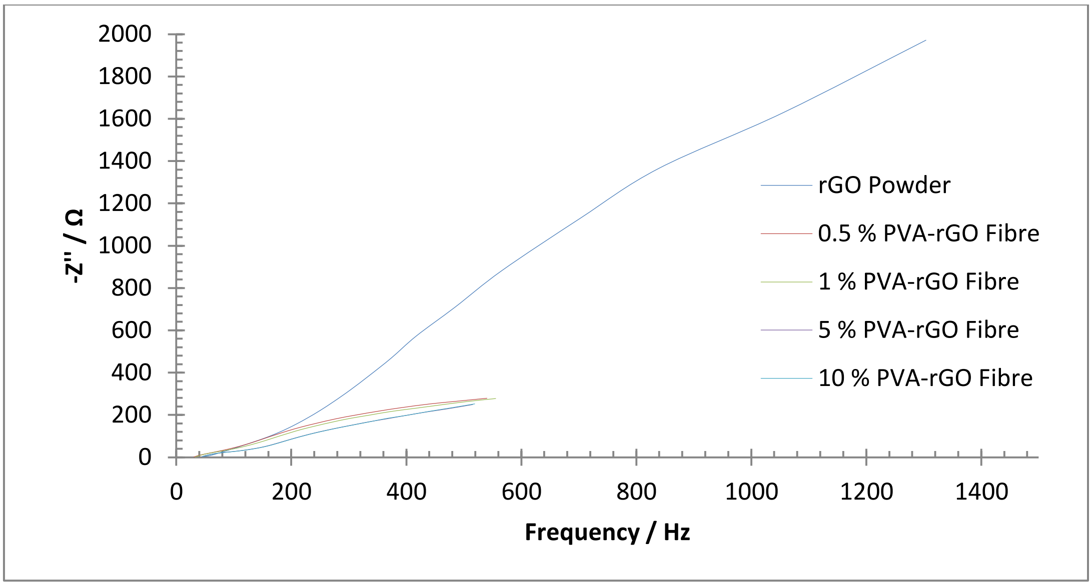

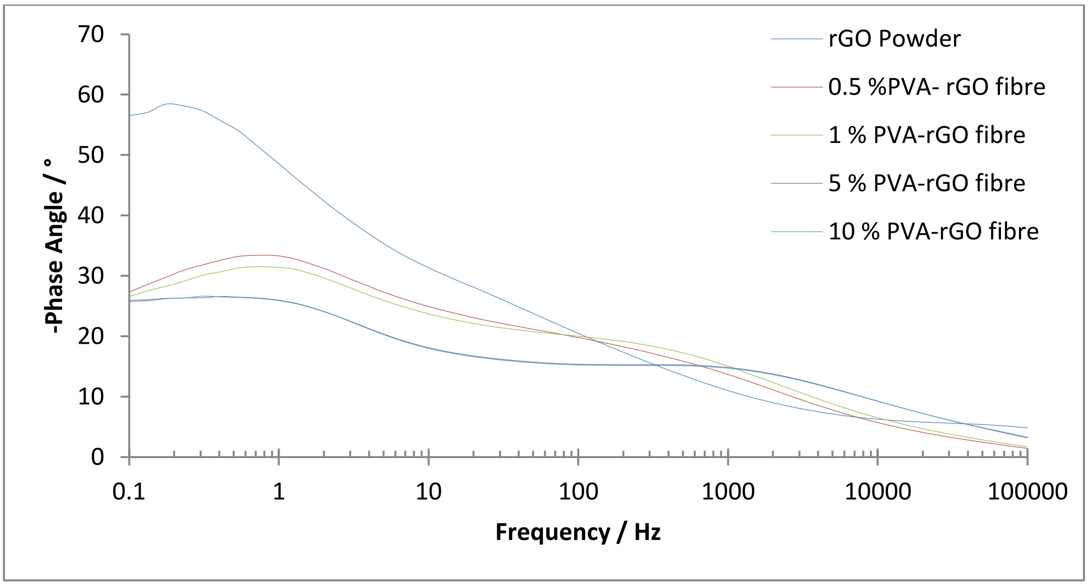

Figure 7.42: Example impedance spectra for the PVA-rGO fibres used in this chapter. (a) a Nyquist plot with a real (Z') and imaginary impedance (-Z'') axis; and (b) a Bode plot from 0.1 to 100000 Hz.

Energy and Power Density

Figure 7.43 and **Table 7.8** show the energy and power densities of the graphene oxide related fibres. The energy density of the rGO fibres are comparable except for the 1 % and 5 % rGO fibres. This is due to the calculation which uses the galvanostatic discharge curve, which for these fibres resulted in a markedly lower capacitance that for the cyclic voltammetry calculation method. The power density of the rGO fibres are comparable to each other. They slightly increase as the PVA content increases. This could be due to more sites of contact with the electrolyte which would increase the surface area of the material, allowing for a faster charge-discharge. The power density of the 0 % rGO is the highest due to the fact that it is in a powder form, and thus has the most contact to the electrolyte allowing it to discharge the quickest.

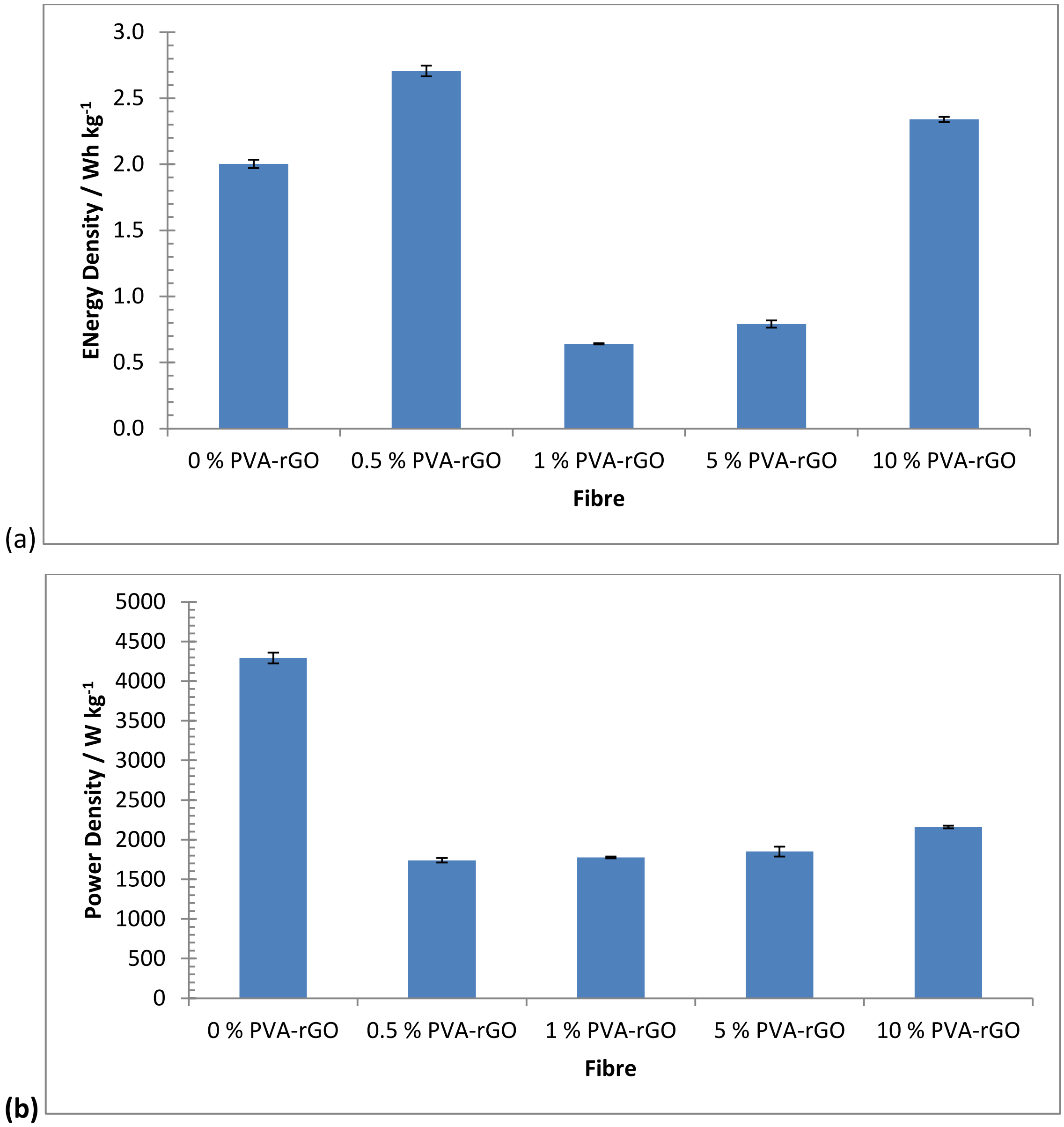

Figure 7.43: The (a) energy density; and (b) power density, of the rGO fibres calculated using the 10 mA galvanostatic discharge slope.

Sample	Specific Energy / Wh kg^{-1}	Specific Power / W kg^{-1}
0 % PVA-rGO	2.00 ± 0.032	4290 ± 68
0.5 % PVA-rGO	2.71 ± 0.042	1740 ± 27
1 % PVA-rGO	0.64 ± 0.0043	1776 ± 12
5 % PVA-rGO	0.79 ± 0.027	1850 ± 62
10 % PVA-rGO	2.34 ± 0.020	2160 ± 19

Table 7.8: Table of specific energy and power of the graphene oxide related materials calculated using the 10 mV galvanostatic discharge curve.

Conclusions

GO was successfully synthesised and wet-spun to form fibres. These were then successfully reduced, and a good capacitance was obtained. These fibres gave the best capacitance of all the materials in the PhD project.

The dope used for the wet-spinning of GO fibres was used in a bulk form. No form of size selection was performed, via force settling, to ensure only few to monolayer GO was used for the spinning. This was done to ensure high quantities of product. At low concentrations of GO, the fibres would not spin efficiently, often breaking apart upon handling. At higher concentrations (20 mg mL^{-1}) the fibres were transferrable and allowed for electrode formation.

In the literature fibre supercapacitors are often expressed in F cm^{-1}. However for the rGO fibres it was chosen to express the capacitance as a gravimetric capacitance (F g^{-1}). This is for efficient comparisons to the exfoliated graphite carbon fibres and exfoliated graphite infiltrated nickel foam. The same could be said for the electrolyte used. Solid electrolytes, like PVA-H_3PO_4, can provide a way for the fibres to an all solid state supercapacitor. It was deemed unnecessary for the fibres in this project, as an all solid state supercapacitor would not bind well to the nickel foam electrodes and the stability to bending could not be tested.

Many different dope and coagulation baths solvents were investigated, but it was found that the best combination was a PVA composite dope and an ethanol-water-$CaCl_2$ bath.

Spinning into baths with more concentrated water resulted in fibres which would ripple, possibly due to surface tension at the syringe point. High concentrations of $CaCl_2$ would result in disjointed fibres and hole formation. This was due to the escalated coagulation, which inhibits the smooth spinning of the fibres.

The reduction in capacitance for the 1 % and 5 % PVA-rGO fibres measured by galvanostatic discharge remains unexplained. This is surprising given the regular capacitance calculated using CV. This may be due to the high power density of these fibres, or differences in reduction potential.

The reduction of the GO was successful using ascorbic acid. Commonly in the literature, hydrazine is used. However as a comparison to earlier work on exfoliated graphite hydrazine could not be used as they would introduce nitrogen functionalities.

PVA was used as a template polymer at much research has been performed on the polymer. PVA proves the ideal polymer to spin with due to the ease of mixing with GO, with hydrogen bonds facilitating mixing. Additionally the removal of PVA via carbonisation ultimately increases the gravimetric capacitance of the fibres.

Chartarrayawadee *et al*. have assessed the capacitance of ascorbic acid reduced rGO. They calculated the capacitance as 63 F g^{-1}, which again is larger than the results in this chapter. For the synthesis of the electrodes, the rGO was electrophoretically deposited on glassy carbon substrates. This would ensure the maximum amount of contact with the electrode, and is far better than using rGO as a powder.[243]

8 Conclusions and Recommendations

8.1 Conclusions

Graphene Infiltration of Nickel Foam

The electrochemical exfoliation of graphite was performed on four different graphite samples using two different methods (pellet and aluminium cage). The smaller graphite grades (Graphexel 399 and xGnP 15 µm) were more easily exfoliated than the larger graphite grades (Graphexel 197 and xGnP 25 µm). This was confirmed through Raman spectroscopy and scanning electron microscopy (SEM). The pellet method exfoliation did not reduce the average particle size of the graphite below 30 µm indicating an upper limit of exfoliation, with the exfoliated graphite containing a wide distribution of particle sizes. Additionally Raman spectroscopy indicated that full exfoliation had not occurred. This is likely due to the short exfoliation duration, as the pellet fell from the power supply early into the exfoliation procedure. The aluminium cage method allowed for a longer exfoliation time pushing the exfoliation to completion. This is shown by the change in the graphite size and large shift of the 2D peak in Raman spectroscopy to a lower wavenumber. SEM showed the pellet exfoliated graphite had many smaller particulates present with agglomeration, while the aluminium exfoliated graphite was purer but contained residue from the aluminium and electrolyte. The yield of graphene for the electrochemically exfoliated graphite (mainly calculated using Raman spectroscopy) was lower for the pellet electrode (197: 0 %, 399: 20 %, 15 µm: 20 %, and 25 µm: 20 %) than the aluminium cage electrode (197: 20 %, 399: 25 %, 15 µm: 30 %, and 25 µm: 20 %). This also shows that the smaller initial graphite sizes (399 and 15 µm) were exfoliated better (produced a larger yield of graphene in the final product) than the larger initial graphite (197 and 25 µm). Upon assessing the specific capacitance, it was confirmed that exfoliation increased the capacitance of all graphite samples for both methods. This is in line with the increased graphene yield after exfoliation. In general the aluminium cage exfoliated graphite possessed a higher capacitance than the pellet exfoliated graphite, and that the previously processed graphite was more easily exfoliated than the natural graphite. Conversely the best capacitance was achieved from the pellet exfoliated XG sciences 25 µm graphite, at 26 F g^{-1}, though the pellet exfoliated graphite in general performed worse than the aluminium cage exfoliated graphite. (**197: (P)** 9.5 Fg^{-1} vs **(A)**

15.4 Fg^{-1}; **399: (P)** 12.6 Fg^{-1} vs **(A)** 12.7 Fg^{-1}; **15 µm: (P)** 24.1 Fg^{-1} vs **(A)** 27.4 Fg^{-1}; **25 µm: (P)** 26.5Fg^{-1} vs **(A)** 19.5 Fg^{-1}). Electrochemical exfoliation increased the capacitance and energy density of all the samples compared to the initial graphite. The cycle lives of the products were all reasonable with at least 70 % retention of capacitance after 2000 charge cycles. Compared to current state-of-the-art capacitors like the graphene film by Lui et al.[244] the capacitance obtained from the nickel foam electrodes in this research are far lower. Liu et al. report a bi-layer graphene yield of 54 % from the electrochemical exfoliation of graphite, which is far higher than the few layer graphene yield of 20 % acquired from the electrochemical exfoliation performed during this research. They state that “Bilayer graphene flakes are dominant in the final product by using sonication during the electrochemical exfoliation process, while without sonication the product contains a larger percentage of four-layer graphene flakes.” The electrochemical exfoliation of graphene requires sonication (or reduction if using anodic exfoliation) in order to further exfoliate the graphene sheets. In turn, this is likely the biggest cause for the reduced capacitance compared to the best in literature, as the graphene species obtained in this research require further exfoliation. However the niche of this project is to synthesise a graphene capacitor via (cathodic) electrochemical exfoliation without additional exfoliation techniques. The presence of many-layer graphene to graphite species for the supercapacitor will reduce the charge transfer speed, introduce large amounts of resistance, and reduce the amount of area which can form EDLs (while also increasing the weight of the device reducing the capacitance in terms of F g^{-1}).

Carbon Fibre Infiltration

The wet-spinning technique was developed from scratch by first observing success with electrospinning. The dope concentration / composition, needle aperture, and applied voltage were all finely tuned in order synthesise these fibres. However, during carbonisation, the thin fibres (in a mat) were prone to rapid decomposition to form a powder rather than a fibre. In order to make larger fibres, which would allow for successful carbonisation, the wet-spinning technique was proposed. Again, bath concentration / composition, dope concentration / composition, template polymer, and needle aperture needed to be adjusted in order to successfully synthesise the fibres. Where the dope was too concentrated (in terms of exfoliated graphite), the fibres would not form due to the small needle aperture; where the dope was too dilute, the fibres could not be continuously formed. After the successful synthesis of the fibres, the carbonisation also proved successful, which allowed for high-throughput production of the carbon fibres and graphene-functionalised carbon fibres. The capacitance of the fibres all increased upon carbonisation; however it was found that the addition of exfoliated graphite reduced the capacitance of the carbonised fibre. The highest capacitance was obtained from pure carbon fibres at 47 F g^{-1}, while carbon fibre-graphene composites had a capacitance of 22 F g^{-1}. This was most likely due to the collapse of the porous network in the neat carbon fibres with the addition of the exfoliated graphite. This would reduce the electrolyte penetration and number of EDL sites to form. The microstructure of the un-carbonised PAN composite fibres reveals the exfoliated graphite contributed to the porous network, and also the surface and walls of the fibre, which is still present in the carbonised fibre. The capacitance for the exfoliated graphite PAN fibres was comparable to the exfoliated graphite on porous nickel foam (8 F g^{-1} and 15 F g^{-1} respectively for the 399 and 15 µm graphite). This gives an indication that the spinning process did not adversely affect the exfoliation of the graphite. While the PAN fibres were not stable to charge cycling, the carbonised composite fibres were, with a ~ 30 % increase in capacitance after 2000 charge cycles. This could be due to in-situ exfoliation or deeper penetration of the electrolyte into the fibre allowing for more EDLs to be formed. Compared to current research on graphene in carbon fibre, the fibres performed far better than the research performed by Wang et al.[239] They achieved a capacitance of 1.35 F g^{-1}, while the graphene functionalised carbon fibre gave capacitances of 22 and 20 F g^{-1} for the 5x aluminium cage exfoliated 399 and 15 µm graphite respectively. This increase in capacitance is likely due to the highly porous structure of the carbon fibre, even though it has collapsed.

Reduced Graphene Oxide Fibre

The spinning of graphene oxide (GO) to form fibres and subsequent reduction was another route to obtain graphene based fibres. Using knowledge and experience gained from the wet-spinning of PAN, the spinning of GO was also successful. Again this proved difficult at first, mainly due to the dope concentration, where fibres spun from the dope quickly dissipated when handled. This was eventually solved by dramatically increasing the concentration of the dope, in order for the continuous spinning of the GO dope. In this work, it was demonstrated that these flexible fibres perform well in energy storage. At higher concentrations of GO, there is a marked increase in the capacitance of the material, due to the reduced graphene oxide (rGO) as the base for electric double layer (EDL) formation. It was also seen that the topography of the higher concentration rGO fibres were rougher allowing for more EDL sites to be formed. The best capacitance performance was achieved by 0.5 % PVA-rGO at 39.9 F g^{-1}. Other concentrations of rGO in the PVA-rGO fibres showed similar results, with 38.3 F g^{-1} for the rGO powder, 36.8 F g^{-1} for the 1 % PVA-rGO fibre, 29.7 F g^{-1} for the 5 % PVA-rGO fibre, and 26.8 F g^{-1} for the 10 % PVA-rGO fibre. The carbonised PVA did not have an as good contribution to the capacitance as the reduced graphene oxide, however, in terms of capacitance retention after 2000 charge-discharge cycles, the fibres with the most PVA proved to hold onto capacitance the most, even increasing in capacitance. Current research by the Aboutalebi group [154] shows graphene yarn capacitors can reach up to 400 F g^{-1}. The fibres created in this project show a capacitance an order of magnitude lower at 40 F g^{-1}. In Aboutalebi et al.'s work, the graphene fibre is spun from a liquid crystalline GO dope. These liquid crystals allow the formation of a more ordered structure, which can facilitate the formation of the fibre. Additionally the long range ordering, from the liquid crystal, aligning the GO flakes, allows for a stronger, more resilient fibre.[111] The reduction technique was also different in that they used annealing at 200 °C, while in this project the reduction technique was ascorbic acid. Though no residual ascorbic acid was found on the fibre, through SEM, IR, and XRD, contaminants can reduce the capacitance of the fibre. Annealing provides a 'cleaner' option to reduce the graphene fibre, as no addition chemicals are used. Additionally the annealing can produce gaseous molecules, which can further separate the sheets, allowing for a higher surface area. The reduced capacitance of the GO fibres created in this project, compared to the literature, is likely a result of the GO fibre synthesis, and the inefficient reduction of the rGO. The fibre synthesis allows for turbostratcic GO flakes in the fibre, which reduces the amount of sheet packing in the fibre and the percolating network, and inefficient reduction allows for more oxygen-containing functional groups on the surface of the rGO will reduce the electrical conductivity and density of the EDL sites.

Figure 8.1 shows an amended Ragone plot previously shown in the literature review with the samples synthesised placed on it. The power and energy density of these materials is far less than that of the materials found in the literature. This suggests that the electrode design needs improving, in order to successfully increase the contact between the sample and current collector. Additionally, the electrochemical exfoliation of graphite needs to be improved, in order to achieve a higher concentration of graphene in the exfoliated product.

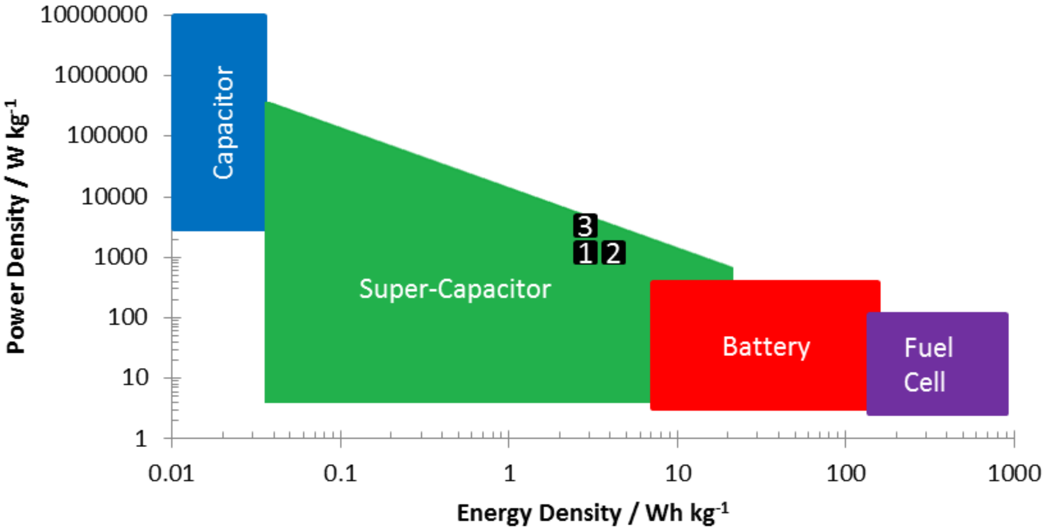

Figure 8.1: Modified Ragone plot of the best performing, in terms of energy density and power density, super-capacitors created using three different methods, electrochemically exfoliated graphite infiltration, carbonised wet-spun PAN, and reduced wet-spun GO fibres. 1: 5x exfoliated 15 µm graphite by the aluminium cage method; 2: carbonised PAN fibre; 3: 0.5 % PVA-rGO fibre.

8.2 Recommendations

One of the fundamental issues with this project was cell design. The presence of silver paint created redox peaks in some of the CV plots. To ensure the electrochemical exfoliation of the materials only comes from the active material to be analysed, removing the silver paint is crucial. Coin cells could be created for the analysis of the materials, which are often used for electrochemical analysis and in commercial applications. Coin cells are manufactured in an inert atmosphere, ensuring no oxygen can interfere in the electrochemical analysis. There are also springs, which ensure efficient contact of the active materials to the separator and current collectors. This makes sure the EDLs and charge transfer reactions occur instantaneously.

The electrochemical exfoliation of the graphite successfully produced FLG. The aluminium cage electrodes produced a higher yield of this material. However the product contains many impurities, like aluminium, lithium and hydroxides. These proved difficult to wash away, even after many washing cycles with water and acid. The main purpose of the aluminium electrode compared to the pellet electrode was to increase in the surface area of the electrode. This allows for the exfoliation of more graphite at a time, while ensuring more graphite is in contact with the electrode to be exfoliated. To further increase this surface area of the working electrode, the graphite could be placed into a wire cage or metal sieve (with pores in the µm range) like electrode. This would increase the contact of the electrode to the graphite, while also size selecting the graphite flakes ensuring the larger graphite pieces are also exfoliated. This could promote the exfoliation of the natural graphite Graphexel 197, and the processed XG sciences 25 µm graphite, as the largest difference from the Graphexel 399 and XG Sciences 25 µm graphite was the size of the graphite particles.

The mechanism of the electrochemical exfoliation process was not fully explored during this project, though the movement of the ions through graphite was previously been explored by Cooper *et al*. In this work they measured the TEA ions intercalating into graphite, and leaving the graphite.[72] To identify the reactions happening during exfoliation, a CV measurement could be performed within the limits of the potential, ensuring the reaction is complete.

Other concerns were that during exfoliation it was noted that occasionally the electrolyte would degrade. This resulted in reduced intercalation due to the electrolysis of DMSO. Additionally the pellet electrode would fall almost instantly into solution. Increasing the concentration of the binder (gum arabic) could solve this problem, however one fault of the pellet method is the pressing of the graphite into a small disc at high pressures. Gum arabic has also been reported as a separator for graphite, which would increase the yield of graphene in the product. Chabot *et al.* have previously synthesised almost defect free graphene (0.5 mg mL^{-1}) via sonication with gum arabic.[245]

For the carbon fibre work, graphitization of the fibres was not performed. This is a process where the PAN precursors are heated up to > 2500 °C. Graphitization can further increase the graphitic content in a carbon fibre, thus it would increase the strength, and electrochemical performance of the fibres. While PAN was used as a template polymer for the graphene, other polymers like cellulose acetate could be used. Cellulose can be converted to carbon fibre via graphitisation, and can also be activated using KOH. PAN creates toxic gases as by-products (HCN), while cellulose fibres are more environmentally friendly for carbon fibre manufacture.[246]

There are distinct differences between the production of the final graphene fibre for the carbon fibre and rGO fibre products. However, in terms of real time, both methods have a similar production time. Both precursors are able to produce graphene fibres continuously via wet-spinning; however they both have different steps which will inhibit the fast production of the fibres. For carbon fibres the electrochemical exfoliation of graphite takes more time, while the carbonisation extends the production time for the carbon fibres. For the rGO fibres, the synthesis of GO takes a long time, and additional reduction steps are required for the creation of graphene fibres. The microstructure of the carbon fibres and graphene fibres are different too. The wet spun graphene fibres are mostly comprised of well-aligned sheets along the fibre axis. These are in alignment along the fibre axis which allows for better electrical conductivity, both electrical and thermal, as there is less space between the crystal sizes, as the sheets are large and aligned. The microstructure of carbon fibre makes it that carbon fibre is made of nano-graphite crystals, which are grown in 3D. These can be aligned but grow perpendicular to the fibre axis. These small crystals will cause some miss alignment, and hamper the conductivity through the fibre. Conductivity is primarily controlled by grain boundaries. The addition of graphene to the carbon fibre will help alleviate some of these problems. The polarised Raman shows that the sheets are aligned which improves the electrical conductivity. [109]

9 References

1. Agency, I. E. Renewables to lead world power market growth to 2020. https://www.iea.org/newsroomandevents/pressreleases/2015/october/renewables-to-lead-world-power-market-growth-to-2020.html (accessed 18/10/2016).
2. Miller, J. R.; Burke, A. F., Electrochemical capacitors: Challenges and opportunities for real-worldapplications. *Electrochemistry Society Interface* **2008,** *17*, 53-57.
3. Kotz, R.; Carlen, M., Principles and applications of electrochemical capacitors. *Electrochimica Acta* **2000,** *45* (15-16), 2483-2498.
4. Salgarkar, R. Graphene Market by Type. http://www.marketsandmarkets.com/PressReleases/graphene.asp (accessed 20/07/16).
5. Ceskaa Global Market for Supercapacitor: 2015-2020. https://www.ceskaa.com/shop/energy-and-power/global-market-for-supercapacitor-report-2015-2020/ (accessed 20/07/16).
6. The Nobel Prize in Physics 2010. http://www.nobelprize.org/nobel_prizes/physics/laureates/2010/index.html (accessed 24/02/14).
7. Number of articles published on graphene in 2016. http://apps.webofknowledge.com/Search.do?product=WOS&amp;SID=S1U16ivXm8DBrHMuQEo&amp;search_mode=GeneralSearch&amp;prID=cc1c58f9-7350-48f3-97e1-9be2c127c2b7 (accessed 02/05/17).
8. Partoens, B.; Peeters, F. M., From graphene to graphite: Electronic structure around the K point. *Phys. Rev. B* **2006,** *74* (7), 11.
9. Bacon, G. E., THE INTERLAYER SPACING OF GRAPHITE. *Acta Crystallographica* **1951,** *4* (6), 558-561.
10. Zacharia, R.; Ulbricht, H.; Hertel, T., Interlayer cohesive energy of graphite from thermal desorption of polyaromatic hydrocarbons. *Physical Review B* **2004,** *69* (15), 7.
11. Kim, D. S.; Kwon, H.; Nikitin, A. Y.; Ahn, S.; Martin-Moreno, L.; Garcia-Vidal, F. J.; Ryu, S.; Min, H.; Kim, Z. H., Stacking Structures of Few-Layer Graphene Revealed by Phase-Sensitive Infrared Nanoscopy. *Acs Nano* **2015,** *9* (7), 6765-6773.
12. Geim, A. K.; Novoselov, K. S., The rise of graphene. *Nature Materials* **2007,** *6* (3), 183-191.
13. Popov, I. A.; Bozhenko, K. V.; Boldyrev, A. I., Is graphene aromatic? *Nano Research* **2012,** *5* (2), 117-123.
14. Casiraghi, C., Raman spectroscopy of graphene. In *Spectroscopic Properties of Inorganic and Organometallic Compounds: Techniques, Materials and Applications*, 1st ed.; Yarwood, J.; Douthwaite, R.; Duckett, S. B., Eds. Royal Soc Chemistry: Cambridge, 2012; Vol. 43, pp 29-56.
15. Wallace, P. R., THE BAND THEORY OF GRAPHITE. *Physical Review* **1947,** *71* (9), 622-634.
16. Shafraniuk, S., Chapter 1: Chiral Fermions in Graphene. In *Graphene: Fundamentals, Devices, and Applications*, 1st ed.; Singapore Pan Stanford Publishing: Singapore, 2015; pp 29-66.
17. Das Sarma, S.; Adam, S.; Hwang, E. H.; Rossi, E., Electronic transport in two-dimensional graphene. *Reviews of Modern Physics* **2011,** *83* (2), 407-470.
18. Castro Neto, A. H.; Guinea, F.; Peres, N. M. R.; Novoselov, K. S.; Geim, A. K., The electronic properties of graphene. *Reviews of Modern Physics* **2009,** *81* (1), 109-162.

19. Novoselov, K. S.; Geim, A. K.; Morozov, S. V.; Jiang, D.; Zhang, Y.; Dubonos, S. V.; Grigorieva, I. V.; Firsov, A. A., Electric field effect in atomically thin carbon films. *Science* **2004,** *306* (5696), 666-669.

20. Lee, C.; Wei, X. D.; Kysar, J. W.; Hone, J., Measurement of the elastic properties and intrinsic strength of monolayer graphene. *Science* **2008,** *321* (5887), 385-388.

21. Rogers, J. A.; Someya, T.; Huang, Y. G., Materials and Mechanics for Stretchable Electronics. *Science* **2010,** *327* (5973), 1603-1607.

22. Stoller, M. D.; Park, S. J.; Zhu, Y. W.; An, J. H.; Ruoff, R. S., Graphene-Based Ultracapacitors. *Nano Letters* **2008,** *8* (10), 3498-3502.

23. Nair, R. R.; Blake, P.; Grigorenko, A. N.; Novoselov, K. S.; Booth, T. J.; Stauber, T.; Peres, N. M. R.; Geim, A. K., Fine structure constant defines visual transparency of graphene. *Science* **2008,** *320* (5881), 1308-1308.

24. Park, H.; Chang, S.; Jean, J.; Cheng, J. J.; Araujo, P. T.; Wang, M. S.; Bawendi, M. G.; Dresselhaus, M. S.; Bulovic, V.; Kong, J.; Gradecak, S., Graphene Cathode-Based ZnO Nanowire Hybrid Solar Cells. *Nano Letters* **2013,** *13* (1), 233-239.

25. Wu, J. B.; Agrawal, M.; Becerril, H. A.; Bao, Z. N.; Liu, Z. F.; Chen, Y. S.; Peumans, P., Organic Light-Emitting Diodes on Solution-Processed Graphene Transparent Electrodes. *Acs Nano* **2010,** *4* (1), 43-48.

26. Reina, A.; Jia, X. T.; Ho, J.; Nezich, D.; Son, H. B.; Bulovic, V.; Dresselhaus, M. S.; Kong, J., Large Area, Few-Layer Graphene Films on Arbitrary Substrates by Chemical Vapor Deposition. *Nano Letters* **2009,** *9* (1), 30-35.

27. Deprez, N.; McLachlan, D. S., THE ANALYSIS OF THE ELECTRICAL-CONDUCTIVITY OF GRAPHITE POWDERS DURING COMPACTION. *Journal of Physics D-Applied Physics* **1988,** *21* (1), 101-107.

28. Yang, W.; Chen, G. R.; Shi, Z. W.; Liu, C. C.; Zhang, L. C.; Xie, G. B.; Cheng, M.; Wang, D. M.; Yang, R.; Shi, D. X.; Watanabe, K.; Taniguchi, T.; Yao, Y. G.; Zhang, Y. B.; Zhang, G. Y., Epitaxial growth of single-domain graphene on hexagonal boron nitride. *Nature Materials* **2013,** *12* (9), 792-797.

29. Dato, A.; Radmilovic, V.; Lee, Z.; Phillips, J.; Frenklach, M., Substrate-free gas-phase synthesis of graphene sheets. *Nano Letters* **2008,** *8* (7), 2012-2016.

30. Wu, Y. P.; Wang, B.; Ma, Y. F.; Huang, Y.; Li, N.; Zhang, F.; Chen, Y. S., Efficient and large-scale synthesis of few-layered graphene using an arc-discharge method and conductivity studies of the resulting films. *Nano Research* **2010,** *3* (9), 661-669.

31. Novoselov, K. S.; Fal'ko, V. I.; Colombo, L.; Gellert, P. R.; Schwab, M. G.; Kim, K., A roadmap for graphene. *Nature* **2012,** *490* (7419), 192-200.

32. Li, X. S.; Cai, W. W.; Colombo, L.; Ruoff, R. S., Evolution of Graphene Growth on Ni and Cu by Carbon Isotope Labeling. *Nano Letters* **2009,** *9* (12), 4268-4272.

33. Chen, W.; Fan, Z. L.; Zeng, G. F.; Lai, Z. P., Layer-dependent supercapacitance of graphene films grown by chemical vapor deposition on nickel foam. *Journal of Power Sources* **2013,** *225*, 251-256.

34. Mattevi, C.; Kim, H.; Chhowalla, M., A review of chemical vapour deposition of graphene on copper. *Journal of Materials Chemistry* **2011,** *21* (10), 3324-3334.

35. Bae, S.; Kim, H.; Lee, Y.; Xu, X. F.; Park, J. S.; Zheng, Y.; Balakrishnan, J.; Lei, T.; Kim, H. R.; Song, Y. I.; Kim, Y. J.; Kim, K. S.; Ozyilmaz, B.; Ahn, J. H.; Hong, B. H.; Iijima, S., Roll-to-roll production of 30-inch graphene films for transparent electrodes. *Nature Nanotechnology* **2010,** *5* (8), 574-578.

36. Kim, K. S.; Zhao, Y.; Jang, H.; Lee, S. Y.; Kim, J. M.; Ahn, J. H.; Kim, P.; Choi, J. Y.; Hong, B. H., Large-scale pattern growth of graphene films for stretchable transparent electrodes. *Nature* **2009,** *457* (7230), 706-710.
37. Wei, D. C.; Liu, Y. Q.; Wang, Y.; Zhang, H. L.; Huang, L. P.; Yu, G., Synthesis of N-Doped Graphene by Chemical Vapor Deposition and Its Electrical Properties. *Nano Letters* **2009,** *9* (5), 1752-1758.
38. Coleman, J. N., Liquid Exfoliation of Defect-Free Graphene. *Accounts of Chemical Research* **2013,** *46* (1), 14-22.
39. Ciesielski, A.; Samori, P. Y., - Graphene via sonication assisted liquid-phase exfoliation. - *Chemical Society Reviews* (- 1), - 381.
40. De, S.; King, P. J.; Lotya, M.; O'Neill, A.; Doherty, E. M.; Hernandez, Y.; Duesberg, G. S.; Coleman, J. N., Flexible, Transparent, Conducting Films of Randomly Stacked Graphene from Surfactant-Stabilized, Oxide-Free Graphene Dispersions. *Small* **2010,** *6* (3), 458-464.
41. Kuilla, T.; Bhadra, S.; Yao, D. H.; Kim, N. H.; Bose, S.; Lee, J. H., Recent advances in graphene based polymer composites. *Progress in Polymer Science* **2010,** *35* (11), 1350-1375.
42. Hennrich, F.; Krupke, R.; Arnold, K.; Stutz, J. A. R.; Lebedkin, S.; Koch, T.; Schimmel, T.; Kappes, M. M., The mechanism of cavitation-induced scission of single-walled carbon nanotubes. *Journal of Physical Chemistry B* **2007,** *111* (8), 1932-1937.
43. Haar, S.; El Gemayel, M.; Shin, Y. Y.; Melinte, G.; Squillaci, M. A.; Ersen, O.; Casiraghi, C.; Ciesielski, A.; Samori, P., Enhancing the Liquid-Phase Exfoliation of Graphene in Organic Solvents upon Addition of n-Octylbenzene. *Scientific Reports* **2015,** *5*, 9.
44. Khan, U.; Porwal, H.; O'Neill, A.; Nawaz, K.; May, P.; Coleman, J. N., Solvent-Exfoliated Graphene at Extremely High Concentration. *Langmuir* **2011,** *27* (15), 9077-9082.
45. Hernandez, Y.; Nicolosi, V.; Lotya, M.; Blighe, F. M.; Sun, Z. Y.; De, S.; McGovern, I. T.; Holland, B.; Byrne, M.; Gun'ko, Y. K.; Boland, J. J.; Niraj, P.; Duesberg, G.; Krishnamurthy, S.; Goodhue, R.; Hutchison, J.; Scardaci, V.; Ferrari, A. C.; Coleman, J. N., High-yield production of graphene by liquid-phase exfoliation of graphite. *Nature Nanotechnology* **2008,** *3* (9), 563-568.
46. Shih, C. J.; Lin, S. C.; Strano, M. S.; Blankschtein, D., Understanding the Stabilization of Liquid-Phase-Exfoliated Graphene in Polar Solvents: Molecular Dynamics Simulations and Kinetic Theory of Colloid Aggregation. *Journal of the American Chemical Society* **2010,** *132* (41), 14638-14648.
47. Smith, R. J.; Lotya, M.; Coleman, J. N., The importance of repulsive potential barriers for the dispersion of graphene using surfactants. *New Journal of Physics* **2010,** *12*, 11.
48. Lotya, M.; King, P. J.; Khan, U.; De, S.; Coleman, J. N., High-Concentration, Surfactant-Stabilized Graphene Dispersions. *Acs Nano* **2010,** *4* (6), 3155-3162.
49. Xu, Z. W.; Li, H. J.; Li, W.; Cao, G. X.; Zhang, Q. L.; Li, K. Z.; Fu, Q. G.; Wang, J., Large-scale production of graphene by microwave synthesis and rapid cooling. *Chemical Communications* **2011,** *47* (4), 1166-1168.
50. Li, N.; Wang, Z. Y.; Zhao, K. K.; Shi, Z. J.; Gu, Z. N.; Xu, S. K., Large scale synthesis of N-doped multi-layered graphene sheets by simple arc-discharge method. *Carbon* **2010,** *48* (1), 255-259.

51. Low, C. T. J.; Walsh, F. C.; Chakrabarti, M. H.; Hashim, M. A.; Hussain, M. A., Electrochemical approaches to the production of graphene flakes and their potential applications. *Carbon* **2013,** *54*, 1-21.

52. Wang, G. X.; Wang, B.; Park, J.; Wang, Y.; Sun, B.; Yao, J., Highly efficient and large-scale synthesis of graphene by electrolytic exfoliation. *Carbon* **2009,** *47* (14), 3242-3246.

53. Abdelkader, A. M.; Kinloch, I. A.; Dryfe, R. A. W., Continuous Electrochemical Exfoliation of Micrometer-Sized Graphene Using Synergistic Ion Intercalations and Organic Solvents. *Acs Applied Materials & Interfaces* **2014,** *6* (3), 1632-1639.

54. Parvez, K.; Li, R. J.; Puniredd, S. R.; Hernandez, Y.; Hinkel, F.; Wang, S. H.; Feng, X. L.; Mullen, K., Electrochemically Exfoliated Graphene as Solution-Processable, Highly Conductive Electrodes for Organic Electronics. *Acs Nano* **2013,** *7* (4), 3598-3606.

55. Chang, L. C.; Hsieh, Y. C.; Chen, Y. M.; Wu, P. W.; Lee, J. F., Fabrication of Graphene by Electrochemical Exfoliation in Alkaline Electrolytes. *Carbon Nanostructures 4 - Fullerenes to Graphene* **2014,** *58* (24), 33-38.

56. Liu, N.; Luo, F.; Wu, H. X.; Liu, Y. H.; Zhang, C.; Chen, J., One-step ionic-liquid-assisted electrochemical synthesis of ionic-liquid-functionalized graphene sheets directly from graphite. *Advanced Functional Materials* **2008,** *18* (10), 1518-1525.

57. Sorokina, N. E.; Maksimova, N. V.; Avdeev, V. V., Anodic oxidation of graphite in 10 to 98% HNO3. *Inorganic Materials* **2001,** *37* (4), 360-365.

58. Hsieh, Y. P.; Chiang, W. Y.; Tsai, S. L.; Hofmann, M., Scalable production of graphene with tunable and stable doping by electrochemical intercalation and exfoliation. *Physical Chemistry Chemical Physics* **2016,** *18* (1), 339-343.

59. Kovtyukhova, N. I.; Wang, Y.; Berkdemir, A.; Cruz-Silva, R.; Terrones, M.; Crespi, V. H.; Mallouk, T. E., Non-oxidative intercalation and exfoliation of graphite by Brønsted acids. *Nat Chem* **2014,** *6* (11), 957-963.

60. Lu, X. Y.; Zhao, C., Controlled electrochemical intercalation, exfoliation and in situ nitrogen doping of graphite in nitrate-based protic ionic liquids. *Physical Chemistry Chemical Physics* **2013,** *15* (46), 20005-20009.

61. Zeng, F. W.; Sun, Z. H.; Sang, X. G.; Diamond, D.; Lau, K. T.; Liu, X. X.; Su, D. S., In Situ One-Step Electrochemical Preparation of Graphene Oxide Nanosheet-Modified Electrodes for Biosensors. *Chemsuschem* **2011,** *4* (11), 1587-1591.

62. Li, P.; Bae, S. H.; Zan, Q. Y.; Kim, N. H.; Lee, J. H., One-step process for the exfoliation and surface modification of graphene by electrochemical method. *Multi-Functional Materials and Structures Iii, Pts 1 and 2* **2010,** *123-125*, 743-746.

63. Parvez, K.; Wu, Z. S.; Li, R. J.; Liu, X. J.; Graf, R.; Feng, X. L.; Mullen, K., Exfoliation of Graphite into Graphene in Aqueous Solutions of Inorganic Salts. *Journal of the American Chemical Society* **2014,** *136* (16), 6083-6091.

64. Kwon, J.; Lee, S. H.; Park, K. H.; Seo, D. H.; Lee, J.; Kong, B. S.; Kang, K.; Jeon, S., Simple Preparation of High-Quality Graphene Flakes without Oxidation Using Potassium Salts. *Small* **2011,** *7* (7), 864-868.

65. Bizeto, M. A.; Shiguihara, A. L.; Constantino, V. R. L., Layered niobate nanosheets: building blocks for advanced materials assembly. *Journal of Materials Chemistry* **2009,** *19* (17), 2512-2525.

66. Viculis, L. M.; Mack, J. J.; Mayer, O. M.; Hahn, H. T.; Kaner, R. B., Intercalation and exfoliation routes to graphite nanoplatelets. *Journal of Materials Chemistry* **2005,** *15* (9), 974-978.

67. Zhou, M.; Tang, J.; Cheng, Q.; Xu, G. J.; Cui, P.; Qin, L. C., Few-layer graphene obtained by electrochemical exfoliation of graphite cathode. *Chemical Physics Letters* **2013,** *572*, 61-65.

68. Xu, M. W.; Sun, H. T.; Shen, C.; Yang, S.; Que, W. X.; Zhang, Y.; Song, X. P., Lithium-assisted exfoliation of pristine graphite for few-layer graphene nanosheets. *Nano Research* **2015,** *8* (3), 801-807.

69. Huang, H.; Xia, Y.; Tao, X. Y.; Du, J.; Fang, J. W.; Gan, Y. P.; Zhang, W. K., Highly efficient electrolytic exfoliation of graphite into graphene sheets based on Li ions intercalation-expansion-microexplosion mechanism. *Journal of Materials Chemistry* **2012,** *22* (21), 10452-10456.

70. Zhong, Y. L.; Swager, T. M., Enhanced Electrochemical Expansion of Graphite for in Situ Electrochemical Functionalization. *Journal of the American Chemical Society* **2012,** *134* (43), 17896-17899.

71. Sirisaksoontorn, W.; Adenuga, A. A.; Remcho, V. T.; Lerner, M. M., Preparation and Characterization of a Tetrabutylammonium Graphite Intercalation Compound. *Journal of the American Chemical Society* **2011,** *133* (32), 12436-12438.

72. Cooper, A. J.; Wilson, N. R.; Kinloch, I. A.; Dryfe, R. A. W., Single stage electrochemical exfoliation method for the production of few-layer graphene via intercalation of tetraalkylammonium cations. *Carbon* **2014,** *66*, 340-350.

73. Dryfe, R. A. W.; Kinloch, I. A. Production of graphene. Sep 13, 2012, 2012.

74. Wang, J. Z.; Manga, K. K.; Bao, Q. L.; Loh, K. P., High-Yield Synthesis of Few-Layer Graphene Flakes through Electrochemical Expansion of Graphite in Propylene Carbonate Electrolyte. *Journal of the American Chemical Society* **2011,** *133* (23), 8888-8891.

75. Suslick, K. S.; Price, G. J., Applications of ultrasound to materials chemistry. *Annual Review of Materials Science* **1999,** *29*, 295-326.

76. He, H. Y.; Klinowski, J.; Forster, M.; Lerf, A., A new structural model for graphite oxide. *Chemical Physics Letters* **1998,** *287* (1-2), 53-56.

77. Lerf, A.; He, H. Y.; Forster, M.; Klinowski, J., Structure of graphite oxide revisited. *Journal of Physical Chemistry B* **1998,** *102* (23), 4477-4482.

78. Suk, J. W.; Piner, R. D.; An, J. H.; Ruoff, R. S., Mechanical Properties of Mono layer Graphene Oxide. *Acs Nano* **2010,** *4* (11), 6557-6564.

79. Stankovich, S.; Dikin, D. A.; Piner, R. D.; Kohlhaas, K. A.; Kleinhammes, A.; Jia, Y.; Wu, Y.; Nguyen, S. T.; Ruoff, R. S., Synthesis of graphene-based nanosheets via chemical reduction of exfoliated graphite oxide. *Carbon* **2007,** *45* (7), 1558-1565.

80. Dreyer, D. R.; Park, S.; Bielawski, C. W.; Ruoff, R. S., The chemistry of graphene oxide. *Chemical Society Reviews* **2010,** *39* (1), 228-240.

81. Hummers, W. S.; Offeman, R. E., PREPARATION OF GRAPHITIC OXIDE. *Journal of the American Chemical Society* **1958,** *80* (6), 1339-1339.

82. Brodie, C., Sur le poids atomique du graphite. *Annales de Chimie et de Physique* **1860,** *59*, 466-472.

83. Staudenmaiser, L., Verfahren zur Darstellung der Graphitsäure. *Ber Dtsch Chem Ges* **1898,** *31* (2), 1481-1487.

84. Wissler, M., Graphite and carbon powders for electrochemical applications. *Journal of Power Sources* **2006,** *156* (2), 142-150.

85. Koch, K. R., Oxidation by Mn207: An impressive demonstration of the powerful oxidizing property of dimanganeseheptoxide. *Journal of Chemical Education* **1982,** *59* (11), 973.

86. Stankovich, S.; Piner, R. D.; Chen, X. Q.; Wu, N. Q.; Nguyen, S. T.; Ruoff, R. S., Stable aqueous dispersions of graphitic nanoplatelets via the reduction of exfoliated graphite oxide in the presence of poly(sodium 4-styrenesulfonate). *Journal of Materials Chemistry* **2006,** *16* (2), 155-158.

87. Becerril, H. A.; Mao, J.; Liu, Z.; Stoltenberg, R. M.; Bao, Z.; Chen, Y., Evaluation of solution-processed reduced graphene oxide films as transparent conductors. *Acs Nano* **2008,** *2* (3), 463-470.

88. Gomez-Navarro, C.; Burghard, M.; Kern, K., Elastic properties of chemically derived single graphene sheets. *Nano Letters* **2008,** *8* (7), 2045-2049.

89. Wharton, P.; Bohlen, D., Hydrazine Reduction of α, β-Epoxy Ketones to Allylic Alcohols. *J. Org. Chem.* **1961,** *26* (9), 3615-3616.

90. Shin, H. J.; Kim, K. K.; Benayad, A.; Yoon, S. M.; Park, H. K.; Jung, I. S.; Jin, M. H.; Jeong, H. K.; Kim, J. M.; Choi, J. Y.; Lee, Y. H., Efficient Reduction of Graphite Oxide by Sodium Borohydride and Its Effect on Electrical Conductance. *Advanced Functional Materials* **2009,** *19* (12), 1987-1992.

91. Moon, I. K.; Lee, J.; Ruoff, R. S.; Lee, H., Reduced graphene oxide by chemical graphitization. *Nature Communications* **2010,** *1*, 6.

92. Kou, L.; Huang, T. Q.; Zheng, B. N.; Han, Y.; Zhao, X. L.; Gopalsamy, K.; Sun, H. Y.; Gao, C., Coaxial wet-spun yarn supercapacitors for high-energy density and safe wearable electronics. *Nature Communications* **2014,** *5*, 3754-3754.

93. Abdolhosseinzadeh, S.; Asgharzadeh, H.; Kim, H. S., Fast and fully-scalable synthesis of reduced graphene oxide. *Scientific Reports* **2015,** *5*, 7.

94. Zhang, J. L.; Yang, H. J.; Shen, G. X.; Cheng, P.; Zhang, J. Y.; Guo, S. W., Reduction of graphene oxide via L-ascorbic acid. *Chemical Communications* **2010,** *46* (7), 1112-1114.

95. Xu, C. Y.; Shi, X. M.; Ji, A.; Shi, L. N.; Zhou, C.; Cui, Y. Q., Fabrication and Characteristics of Reduced Graphene Oxide Produced with Different Green Reductants. *Plos One* **2015,** *10* (12), 15.

96. McAllister, M. J.; Li, J. L.; Adamson, D. H.; Schniepp, H. C.; Abdala, A. A.; Liu, J.; Herrera-Alonso, M.; Milius, D. L.; Car, R.; Prud'homme, R. K.; Aksay, I. A., Single sheet functionalized graphene by oxidation and thermal expansion of graphite. *Chemistry of Materials* **2007,** *19* (18), 4396-4404.

97. Wang, X.; Zhi, L. J.; Mullen, K., Transparent, conductive graphene electrodes for dye-sensitized solar cells. *Nano Letters* **2008,** *8* (1), 323-327.

98. Strong, V.; Dubin, S.; El-Kady, M. F.; Lech, A.; Wang, Y.; Weiller, B. H.; Kaner, R. B., Patterning and Electronic Tuning of Laser Scribed Graphene for Flexible All-Carbon Devices. *Acs Nano* **2012,** *6* (2), 1395-1403.

99. El-Kady, M. F.; Strong, V.; Dubin, S.; Kaner, R. B., Laser Scribing of High-Performance and Flexible Graphene-Based Electrochemical Capacitors. *Science* **2012,** *335* (6074), 1326-1330.

100. Dubin, S.; Gilje, S.; Wang, K.; Tung, V. C.; Cha, K.; Hall, A. S.; Farrar, J.; Varshneya, R.; Yang, Y.; Kaner, R. B., A One-Step, Solvothermal Reduction Method for Producing Reduced Graphene Oxide Dispersions in Organic Solvents. *Acs Nano* **2010,** *4* (7), 3845-3852.

101. Paredes, J. I.; Villar-Rodil, S.; Fernandez-Merino, M. J.; Guardia, L.; Martinez-Alonso, A.; Tascon, J. M. D., Environmentally friendly approaches toward the mass production of processable graphene from graphite oxide. *Journal of Materials Chemistry* **2011,** *21* (2), 298-306.

102. Zhou, M.; Wang, Y. L.; Zhai, Y. M.; Zhai, J. F.; Ren, W.; Wang, F. A.; Dong, S. J., Controlled Synthesis of Large-Area and Patterned Electrochemically Reduced Graphene Oxide Films. *Chemistry-a European Journal* **2009,** *15* (25), 6116-6120.
103. Bai, H.; Li, C.; Wang, X. L.; Shi, G. Q., On the Gelation of Graphene Oxide. *Journal of Physical Chemistry C* **2011,** *115* (13), 5545-5551.
104. Xu, Y. X.; Sheng, K. X.; Li, C.; Shi, G. Q., Self-Assembled Graphene Hydrogel via a One-Step Hydrothermal Process. *Acs Nano* **2010,** *4* (7), 4324-4330.
105. Medeiros, E. L. G.; Braz, A. L.; Porto, I. J.; Menner, A.; Bismarck, A.; Boccaccini, A. R.; Lepry, W. C.; Nazhat, S. N.; Medeiros, E. S.; Blaker, J. J., Porous Bioactive Nanofibers via Cryogenic Solution Blow Spinning and Their Formation into 3D Macroporous Scaffolds. *Acs Biomaterials Science & Engineering* **2016,** *2* (9), 1442-1449.
106. Santos, A. M. C.; Medeiros, E. L. G.; Blaker, J. J.; Medeiros, E. S., Aqueous solution blow spinning of poly(vinyl alcohol) micro- and nanofibers. *Materials Letters* **2016,** *176*, 122-126.
107. Nakajima, T., *Advanced Fiber Spinning Technology*. First Edition ed.; Woodhead Publishing Ltd.: Cambridge, England, 1994.
108. Morgan, H. S., Process for wet-spinning fibers derived from acrylic polymers. Google Patents: 1975.
109. Chen, L.; He, Y. L.; Chai, S. G.; Qiang, H.; Chen, F.; Fu, Q., Toward high performance graphene fibers. *Nanoscale* **2013,** *5* (13), 5809-5815.
110. Xu, Z.; Sun, H. Y.; Zhao, X. L.; Gao, C., Ultrastrong Fibers Assembled from Giant Graphene Oxide Sheets. *Advanced Materials* **2013,** *25* (2), 188-193.
111. Jalili, R.; Aboutalebi, S. H.; Esrafilzadeh, D.; Shepherd, R. L.; Chen, J.; Aminorroaya-Yamini, S.; Konstantinov, K.; Minett, A. I.; Razal, J. M.; Wallace, G. G., Scalable One-Step Wet-Spinning of Graphene Fibers and Yarns from Liquid Crystalline Dispersions of Graphene Oxide: Towards Multifunctional Textiles. *Advanced Functional Materials* **2013,** *23* (43), 5345-5354.
112. Xu, Z.; Gao, C., Graphene chiral liquid crystals and macroscopic assembled fibres. *Nature Communications* **2011,** *2*, 9.
113. Huang, X. D.; Qian, K.; Yang, J.; Zhang, J.; Li, L.; Yu, C. Z.; Zhao, D. Y., Functional Nanoporous Graphene Foams with Controlled Pore Sizes. *Advanced Materials* **2012,** *24* (32), 4419-4423.
114. Mit-uppatham, C.; Nithitanakul, M.; Supaphol, P., Ultratine electrospun polyamide-6 fibers: Effect of solution conditions on morphology and average fiber diameter. *Macromolecular Chemistry and Physics* **2004,** *205* (17), 2327-2338.
115. Vigolo, B.; Penicaud, A.; Coulon, C.; Sauder, C.; Pailler, R.; Journet, C.; Bernier, P.; Poulin, P., Macroscopic fibers and ribbons of oriented carbon nanotubes. *Science* **2000,** *290* (5495), 1331-1334.
116. Lin, X. Y.; Shen, X.; Zheng, Q. B.; Yousefi, N.; Ye, L.; Mai, Y. W.; Kim, J. K., Fabrication of Highly-Aligned, Conductive, and Strong Graphene Papers Using Ultra large Graphene Oxide Sheets. *Acs Nano* **2012,** *6* (12), 10708-10719.
117. Zhang, S. C.; Liu, P. Q.; Jia, E. P.; Zhao, X. S.; Xu, J. J.; Li, C. L., Graphene oxide reinforced poly(vinyl alcohol) composite fibers via template-oriented crystallization. *Journal of Polymer Research* **2016,** *23* (10), 14.
118. Li, Y. J.; Sun, J.; Wang, J. J.; Qin, C. X.; Dai, L. X., Preparation of well-dispersed reduced graphene oxide and its mechanical reinforcement in polyvinyl alcohol fibre. *Polymer International* **2016,** *65* (9), 1054-1062.

119. Xiang, C. S.; Young, C. C.; Wang, X.; Yan, Z.; Hwang, C. C.; Cerioti, G.; Lin, J.; Kono, J.; Pasquali, M.; Tour, J. M., Large Flake Graphene Oxide Fibers with Unconventional 100% Knot Efficiency and Highly Aligned Small Flake Graphene Oxide Fibers. *Advanced Materials* **2013,** *25* (33), 4592-4597.

120. Huang, Y.; Young, R. J., EFFECT OF FIBER MICROSTRUCTURE UPON THE MODULUS OF PAN-AND PITCH-BASED CARBON-FIBERS. *Carbon* **1995,** *33* (2), 97-107.

121. Chung, D., Applied Materials Science: Applications of Engineering Materials in Structural, Electronics, Thermal, and Other Industries. 1st ed.; Chapman & Hall / CRC Press LLC: United States of America, 2001; pp 225-234.

122. Paiva, M. C.; Kotasthane, P.; Edie, D. D.; Ogale, A. A., UV stabilization route for melt-processible PAN-based carbon fibers. *Carbon* **2003,** *41* (7), 1399-1409.

123. Rahaman, M. S. A.; Ismail, A. F.; Mustafa, A., A review of heat treatment on polyacrylonitrile fiber. *Polymer Degradation and Stability* **2007,** *92* (8), 1421-1432.

124. Xu, B.; Wu, F.; Chen, S.; Zhang, C. Z.; Cao, G. P.; Yang, Y. S., Activated carbon fiber cloths as electrodes for high performance electric double layer capacitors. *Electrochimica Acta* **2007,** *52* (13), 4595-4598.

125. Lee, J. K.; An, K. W.; Ju, J. B.; Cho, B. W.; Cho, W. I.; Park, D.; Yun, K. S., Electrochemical properties of PAN-based carbon fibers as anodes for rechargeable lithium ion batteries. *Carbon* **2001,** *39* (9), 1299-1305.

126. Melanitis, N.; Tetlow, P. L.; Galiotis, C., Characterization of PAN-based carbon fibres with laser Raman spectroscopy .1. Effect of processing variables on Raman band profiles. *Journal of Materials Science* **1996,** *31* (4), 851-860.

127. 2016, C. Definition of Farad. http://www.collinsdictionary.com/dictionary/english/farad (accessed 21/10/2016).

128. Rieger, P., The Electrified Interface. In *Electrochemistry*, 2nd ed.; Chapman & Hall: London, UK, 1994; pp 59-108.

129. Banerjee, P.; Perez, I.; Henn-Lecordier, L.; Lee, S. B.; Rubloff, G. W., Nanotubular metal-insulator-metal capacitor arrays for energy storage. *Nature Nanotechnology* **2009,** *4* (5), 292-296.

130. Emmenegger, C.; Mauron, P.; Sudan, P.; Wenger, P.; Hermann, V.; Gallay, R.; Zuttel, A., Investigation of electrochemical double-layer (ECDL) capacitors electrodes based on carbon nanotubes and activated carbon materials. *Journal of Power Sources* **2003,** *124* (1), 321-329.

131. Aue, D. H.; Webb, H. M.; Bowers, M. T., THERMODYNAMIC ANALYSIS OF SOLVATION EFFECTS ON BASICITIES OF ALKYLAMINES - ELECTROSTATIC ANALYSIS OF SUBSTITUENT EFFECTS. *Journal of the American Chemical Society* **1976,** *98* (2), 318-329.

132. Zhong, H.; Xu, F.; Li, Z. H.; Fu, R. W.; Wu, D. C., High-energy supercapacitors based on hierarchical porous carbon with an ultrahigh ion-accessible surface area in ionic liquid electrolytes. *Nanoscale* **2013,** *5* (11), 4678-4682.

133. Frackowiak, E.; Beguin, F., Carbon materials for the electrochemical storage of energy in capacitors. *Carbon* **2001,** *39* (6), 937-950.

134. Qu, D. Y.; Shi, H., Studies of activated carbons used in double-layer capacitors. *Journal of Power Sources* **1998,** *74* (1), 99-107.

135. Liu, C. G.; Yu, Z. N.; Neff, D.; Zhamu, A.; Jang, B. Z., Graphene-Based Supercapacitor with an Ultrahigh Energy Density. *Nano Letters* **2010,** *10* (12), 4863-4868.

136. Rufford, T. E.; Hulicova-Jurcakova, D.; Zhu, Z. H.; Lu, G. Q., Empirical Analysis of the Contributions of Mesopores and Micropores to the Double-Layer Capacitance of Carbons. *Journal of Physical Chemistry C* **2009,** *113* (44), 19335-19343.

137. Chen, T.; Dai, L. M., Carbon nanomaterials for high-performance supercapacitors. *Materials Today* **2013,** *16* (7-8), 272-280.

138. Supercapacitor Back-Up Uninterruptible Power Supplies. https://www.ecopowersupplies.com/supercapacitor-ups (accessed 10/05/17).

139. Burke, A.; Liu, Z.; Zhao, H. In *Present and future applications of supercapacitors in electric and hybrid vehicles*, 2014 IEEE International Electric Vehicle Conference (IEVC), 17-19 Dec. 2014; 2014; pp 1-8.

140. Simon, P.; Gogotsi, Y., Materials for electrochemical capacitors. *Nature Materials* **2008,** *7* (11), 845-854.

141. Groote, S. Tackling KERS in Formula One. http://www.f1technical.net/features/11805 (accessed 17/06/16).

142. Pitcher, G. If the cap fits... http://www.newelectronics.co.uk/article-images/6610%5Cif-the-cap-fits.pdf (accessed 17/06/16).

143. Kaempgen, M.; Chan, C. K.; Ma, J.; Cui, Y.; Gruner, G., Printable Thin Film Supercapacitors Using Single-Walled Carbon Nanotubes. *Nano Letters* **2009,** *9* (5), 1872-1876.

144. Xia, J. L.; Chen, F.; Li, J. H.; Tao, N. J., Measurement of the quantum capacitance of graphene. *Nature Nanotechnology* **2009,** *4* (8), 505-509.

145. Cong, H. P.; Ren, X. C.; Wang, P.; Yu, S. H., Flexible graphene-polyaniline composite paper for high-performance supercapacitor. *Energy & Environmental Science* **2013,** *6* (4), 1185-1191.

146. Mitra, S.; Sampath, S., Electrochemical capacitors based on exfoliated graphite electrodes. *Electrochemical and Solid State Letters* **2004,** *7* (9), A264-A268.

147. Zhang, K.; Mao, L.; Zhang, L. L.; Chan, H. S. O.; Zhao, X. S.; Wu, J. S., Surfactant-intercalated, chemically reduced graphene oxide for high performance supercapacitor electrodes. *Journal of Materials Chemistry* **2011,** *21* (20), 7302-7307.

148. Liang, C. D.; Li, Z. J.; Dai, S., Mesoporous carbon materials: Synthesis and modification. *Angewandte Chemie-International Edition* **2008,** *47* (20), 3696-3717.

149. Wang, H. L.; Casalongue, H. S.; Liang, Y. Y.; Dai, H. J., Ni(OH)(2) Nanoplates Grown on Graphene as Advanced Electrochemical Pseudocapacitor Materials. *Journal of the American Chemical Society* **2010,** *132* (21), 7472-7477.

150. Lonkar, S. P.; Raquez, J. M.; Dubois, P., One-Pot Microwave-Assisted Synthesis of Graphene/Layered Double Hydroxide (LDH) Nanohybrids. *Nano-Micro Letters* **2015,** *7* (4), 332-340.

151. Murugan, A. V.; Muraliganth, T.; Manthiram, A., Rapid, Facile Microwave-Solvothermal Synthesis of Graphene Nanosheets and Their Polyaniline Nanocomposites for Energy Strorage. *Chemistry of Materials* **2009,** *21* (21), 5004-5006.

152. Dong, Z. L.; Jiang, C. C.; Cheng, H. H.; Zhao, Y.; Shi, G. Q.; Jiang, L.; Qu, L. T., Facile Fabrication of Light, Flexible and Multifunctional Graphene Fibers. *Advanced Materials* **2012,** *24* (14), 1856-1861.

153. Meng, Y. N.; Zhao, Y.; Hu, C. G.; Cheng, H. H.; Hu, Y.; Zhang, Z. P.; Shi, G. Q.; Qu, L. T., All-Graphene Core-Sheath Microfibers for All-Solid-State, Stretchable Fibriform Supercapacitors and Wearable Electronic Textiles. *Advanced Materials* **2013,** *25* (16), 2326-2331.

154. Aboutalebi, S. H.; Jalili, R.; Esrafilzadeh, D.; Salari, M.; Gholamvand, Z.; Yamini, S. A.; Konstantinov, K.; Shepherd, R. L.; Chen, J.; Moulton, S. E.; Innis, P. C.; Minett, A. I.; Razal, J. M.; Wallace, G. G., High-Performance Multifunctional Graphene Yarns: Toward Wearable All-Carbon Energy Storage Textiles. *Acs Nano* **2014,** *8* (3), 2456-2466.

155. Bao, L. H.; Li, X. D., Towards Textile Energy Storage from Cotton T-Shirts. *Advanced Materials* **2012,** *24* (24), 3246-3252.

156. Xiao, F.; Song, J. B.; Gao, H. C.; Zan, X. L.; Xu, R.; Duan, H. W., Coating Graphene Paper with 2D-Assembly of Electrocatalytic Nanoparticles: A Modular Approach toward High-Performance Flexible Electrodes. *Acs Nano* **2012,** *6* (1), 100-110.

157. Tai, Z. X.; Yan, X. B.; Lang, J. W.; Xue, Q. J., Enhancement of capacitance performance of flexible carbon nanofiber paper by adding graphene nanosheets. *Journal of Power Sources* **2012,** *199*, 373-378.

158. Ra, E. J.; Raymundo-Pinero, E.; Lee, Y. H.; Beguin, F., High power supercapacitors using polyacrylonitrile-based carbon nanofiber paper. *Carbon* **2009,** *47* (13), 2984-2992.

159. Meng, F. C.; Lu, W. B.; Li, Q. W.; Byun, J. H.; Oh, Y.; Chou, T. W., Graphene-Based Fibers: A Review. *Advanced Materials* **2015,** *27* (35), 5113-5131.

160. Kosynkin, D. V.; Higginbotham, A. L.; Sinitskii, A.; Lomeda, J. R.; Dimiev, A.; Price, B. K.; Tour, J. M., Longitudinal unzipping of carbon nanotubes to form graphene nanoribbons. *Nature* **2009,** *458* (7240), 872-U5.

161. Carretero-Gonzalez, J.; Castillo-Martinez, E.; Dias-Lima, M.; Acik, M.; Rogers, D. M.; Sovich, J.; Haines, C. S.; Lepro, X.; Kozlov, M.; Zhakidov, A.; Chabal, Y.; Baughman, R. H., Oriented Graphene Nanoribbon Yarn and Sheet from Aligned Multi-Walled Carbon Nanotube Sheets. *Advanced Materials* **2012,** *24* (42), 5695-5701.

162. Wang, G. K.; Sun, X.; Lu, F. Y.; Sun, H. T.; Yu, M. P.; Jiang, W. L.; Liu, C. S.; Lian, J., Flexible Pillared Graphene-Paper Electrodes for High-Performance Electrochemical Supercapacitors. *Small* **2012,** *8* (3), 452-459.

163. Choi, B. G.; Yang, M.; Hong, W. H.; Choi, J. W.; Huh, Y. S., 3D Macroporous Graphene Frameworks for Supercapacitors with High Energy and Power Densities. *Acs Nano* **2012,** *6* (5), 4020-4028.

164. El-Kady, M. F.; Kaner, R. B., Scalable fabrication of high-power graphene micro-supercapacitors for flexible and on-chip energy storage. *Nature Communications* **2013,** *4*, 9.

165. Gao, W.; Singh, N.; Song, L.; Liu, Z.; Reddy, A. L. M.; Ci, L. J.; Vajtai, R.; Zhang, Q.; Wei, B. Q.; Ajayan, P. M., Direct laser writing of micro-supercapacitors on hydrated graphite oxide films. *Nature Nanotechnology* **2011,** *6* (8), 496-500.

166. Wang, Y.; Shi, Z. Q.; Huang, Y.; Ma, Y. F.; Wang, C. Y.; Chen, M. M.; Chen, Y. S., Supercapacitor Devices Based on Graphene Materials. *Journal of Physical Chemistry C* **2009,** *113* (30), 13103-13107.

167. Liu, T.; Sreekumar, T. V.; Kumar, S.; Hauge, R. H.; Smalley, R. E., SWNT/PAN composite film-based supercapacitors. *Carbon* **2003,** *41* (12), 2440-2442.

168. Wang, J. C.; Kaskel, S., KOH activation of carbon-based materials for energy storage. *Journal of Materials Chemistry* **2012,** *22* (45), 23710-23725.

169. Wang, J. B.; Yang, X. Q.; Wu, D. C.; Fu, R. W.; Dresselhaus, M. S.; Dresselhaus, G., The porous structures of activated carbon aerogels and their effects on electrochemical performance. *Journal of Power Sources* **2008,** *185* (1), 589-594.

170. Zhu, Y. W.; Murali, S.; Stoller, M. D.; Ganesh, K. J.; Cai, W. W.; Ferreira, P. J.; Pirkle, A.; Wallace, R. M.; Cychosz, K. A.; Thommes, M.; Su, D.; Stach, E. A.; Ruoff, R. S.,

Carbon-Based Supercapacitors Produced by Activation of Graphene. *Science* **2011,** *332* (6037), 1537-1541.

171. Cao, X. H.; Shi, Y. M.; Shi, W. H.; Lu, G.; Huang, X.; Yan, Q. Y.; Zhang, Q. C.; Zhang, H., Preparation of Novel 3D Graphene Networks for Supercapacitor Applications. *Small* **2011,** *7* (22), 3163-3168.

172. Wang, W.; Guo, S. R.; Penchev, M.; Ruiz, I.; Bozhilov, K. N.; Yan, D.; Ozkan, M.; Ozkan, C. S., Three dimensional few layer graphene and carbon nanotube foam architectures for high fidelity supercapacitors. *Nano Energy* **2013,** *2* (2), 294-303.

173. Xu, Y. X.; Chen, C. Y.; Zhao, Z. P.; Lin, Z. Y.; Lee, C.; Xu, X.; Wang, C.; Huang, Y.; Shakir, M. I.; Duan, X. F., Solution Processable Holey Graphene Oxide and Its Derived Macrostructures for High-Performance Supercapacitors. *Nano Letters* **2015,** *15* (7), 4605-4610.

174. Pham, V. H.; Dickerson, J. H., Reduced Graphene Oxide Hydrogels Deposited in Nickel Foam for Supercapacitor Applications: Toward High Volumetric Capacitance. *Journal of Physical Chemistry C* **2016,** *120* (10), 5353-5360.

175. Yang, X. W.; Zhu, J. W.; Qiu, L.; Li, D., Bioinspired Effective Prevention of Restacking in Multilayered Graphene Films: Towards the Next Generation of High-Performance Supercapacitors. *Advanced Materials* **2011,** *23* (25), 2833-2838.

176. Yang, X. W.; Cheng, C.; Wang, Y. F.; Qiu, L.; Li, D., Liquid-Mediated Dense Integration of Graphene Materials for Compact Capacitive Energy Storage. *Science* **2013,** *341* (6145), 534-537.

177. Ke, Q.; Wang, J., Graphene-based materials for supercapacitor electrodes – A review. *Journal of Materiomics* **2016,** *2* (1), 37-54.

178. Liang, J. J.; Huang, Y.; Zhang, L.; Wang, Y.; Ma, Y. F.; Guo, T. Y.; Chen, Y. S., Molecular-Level Dispersion of Graphene into Poly(vinyl alcohol) and Effective Reinforcement of their Nanocomposites. *Advanced Functional Materials* **2009,** *19* (14), 2297-2302.

179. Xu, Z.; Gao, C., Graphene fiber: a new trend in carbon fibers. *Materials Today* **2015,** *18* (9), 480-492.

180. Cheng, H. H.; Liu, J.; Zhao, Y.; Hu, C. G.; Zhang, Z. P.; Chen, N.; Jiang, L.; Qu, L. T., Graphene Fibers with Predetermined Deformation as Moisture-Triggered Actuators and Robots. *Angewandte Chemie-International Edition* **2013,** *52* (40), 10482-10486.

181. Erni, R.; Rossell, M. D.; Kisielowski, C.; Dahmen, U., Atomic-Resolution Imaging with a Sub-50-pm Electron Probe. *Physical Review Letters* **2009,** *102* (9), 4.

182. Knoll, M.; Ruska, E., Das Elektronenmikroskop. *Zeitschrift fur PhysikZeitschrift fur Physik* **1932,** *78* (5-6), 318-399.

183. **The Nobel Prize in Physics 1986**The Nobel Prize in Physics 1986. http://www.nobelprize.org/nobel_prizes/physics/laureates/1986/ (accessed 8/11/16).

184. Goohew, P. J.; Humphreys, F. J., *Chapter 1 – Microscopy with Light and Electrons in Electron Microscopy and Analysis*. 2nd ed.; Taylor and Francis: London, 1988.

185. The Nobel Prize in Physics 1930. http://www.nobelprize.org/nobel_prizes/physics/laureates/1930/ (accessed 19/08/16).

186. Gardiner, D., *Practical Raman Spectroscopy*. 1st ed.; Springer Berlin Heidelberg: Berlin, 1989.

187. Adar, F. Depth Resolution of the Raman Microscope: Optical Limitations and Sample Characteristics. http://www.spectroscopyonline.com/depth-resolution-raman-microscope-optical-limitations-and-sample-characteristics (accessed 19/06/16).

188. Ferrari, A. C., Raman spectroscopy of graphene and graphite: Disorder, electron-phonon coupling, doping and nonadiabatic effects. *Solid State Communications* **2007,** *143* (1-2), 47-57.

189. Yan, J. A.; Ruan, W. Y.; Chou, M. Y., Phonon dispersions and vibrational properties of monolayer, bilayer, and trilayer graphene: Density-functional perturbation theory. *Physical Review B* **2008,** *77* (12), 7.

190. Tuinstra, F.; Koenig, J. L., RAMAN SPECTRUM OF GRAPHITE. *Journal of Chemical Physics* **1970,** *53* (3), 1126-&.

191. Tuinstra, F.; Koenig, J. L., CHARACTERIZATION OF GRAPHITE FIBER SURFACES WITH RAMAN SPECTROSCOPY. *Journal of Composite Materials* **1970,** *4*, 492-&.

192. Mohiuddin, T. M. G.; Lombardo, A.; Nair, R. R.; Bonetti, A.; Savini, G.; Jalil, R.; Bonini, N.; Basko, D. M.; Galiotis, C.; Marzari, N.; Novoselov, K. S.; Geim, A. K.; Ferrari, A. C., Uniaxial strain in graphene by Raman spectroscopy: G peak splitting, Gruneisen parameters, and sample orientation. *Physical Review B* **2009,** *79* (20), 8.

193. Nemanich, R. J.; Solin, S. A., 1ST-ORDER AND 2ND-ORDER RAMAN-SCATTERING FROM FINITE-SIZE CRYSTALS OF GRAPHITE. *Physical Review B* **1979,** *20* (2), 392-401.

194. Nemanich, R. J.; Solin, S. A., Observation of an anomolously sharp feature in the 2nd order Raman spectrum of graphite. *Solid State Communications* **1977,** *23* (7), 417-420.

195. Cancado, L. G.; Pimenta, M. A.; Neves, B. R. A.; Medeiros-Ribeiro, G.; Enoki, T.; Kobayashi, Y.; Takai, K.; Fukui, K.; Dresselhaus, M. S.; Saito, R.; Jorio, A., Anisotropy of the Raman spectra of nanographite ribbons. *Physical Review Letters* **2004,** *93* (4), 4.

196. Malard, L. M.; Pimenta, M. A.; Dresselhaus, G.; Dresselhaus, M. S., Raman spectroscopy in graphene. *Physics Reports* **2009,** *473* (5–6), 51-87.

197. Pimenta, M. A.; Dresselhaus, G.; Dresselhaus, M. S.; Cancado, L. G.; Jorio, A.; Saito, R., Studying disorder in graphite-based systems by Raman spectroscopy. *Physical Chemistry Chemical Physics* **2007,** *9* (11), 1276-1291.

198. Ferrari, A. C.; Meyer, J. C.; Scardaci, V.; Casiraghi, C.; Lazzeri, M.; Mauri, F.; Piscanec, S.; Jiang, D.; Novoselov, K. S.; Roth, S.; Geim, A. K., Raman spectrum of graphene and graphene layers. *Physical Review Letters* **2006,** *97* (18), 4.

199. Malard, L. M.; Nilsson, J.; Elias, D. C.; Brant, J. C.; Plentz, F.; Alves, E. S.; Castro, A. H.; Pimenta, M. A., Probing the electronic structure of bilayer graphene by Raman scattering. *Physical Review B* **2007,** *76* (20), 4.

200. Lespade, P.; Marchand, A.; Couzi, M.; Cruege, F., Caracterisation de materiaux carbones par microspectrometrie Raman. *Carbon* **1984,** *22* (4), 375-385.

201. Reich, S.; Thomsen, C., Raman spectroscopy of graphite. *Philosophical Transactions of the Royal Society a-Mathematical Physical and Engineering Sciences* **2004,** *362* (1824), 2271-2288.

202. Ferrari, A. C.; Robertson, J., Interpretation of Raman spectra of disordered and amorphous carbon. *Physical Review B* **2000,** *61* (20), 14095-14107.

203. Jorio, A.; Lucchese, M. M.; Stavale, F.; Ferreira, E. H. M.; Moutinho, M. V. O.; Capaz, R. B.; Achete, C. A., Raman study of ion-induced defects in N-layer graphene. *Journal of Physics-Condensed Matter* **2010,** *22* (33), 5.

204. Thomsen, C.; Reich, S., Double resonant Raman scattering in graphite. *Physical Review Letters* **2000,** *85* (24), 5214-5217.

205. Tsu, R.; Gonzalez, J.; Hernandez, I., OBSERVATION OF SPLITTING OF E2G MODE AND 2-PHONON SPECTRUM IN GRAPHITES. *Solid State Communications* **1978,** *27* (5), 507-510.

206. Saito, R.; Jorio, A.; Souza, A. G.; Dresselhaus, G.; Dresselhaus, M. S.; Pimenta, M. A., Probing phonon dispersion relations of graphite by double resonance Raman scattering. *Physical Review Letters* **2002,** *88* (2), 4.

207. Jorio, A.; Saito, R.; Dresselhaus, G.; Dresselhaus, M., Summary of Raman Spectroscopy on sp ^{2} Nanocarbons. In *Raman spectroscopy in graphene related systems*, Dresselhaus, M. S.; Jorio, A., Eds. Wiley-VCH: Weinheim, Germany, 2011; pp 327-334.

208. Nguyen, T. A.; Lee, J. U.; Yoon, D.; Cheong, H., Excitation Energy Dependent Raman Signatures of ABA- and ABC-stacked Few-layer Graphene. *Scientific Reports* **2014,** *4*, 5.

209. The Nobel Prize in Physics 1915. https://www.nobelprize.org/nobel_prizes/physics/laureates/1915/ (accessed 03/02/17).

210. Lotya, M.; Hernandez, Y.; King, P. J.; Smith, R. J.; Nicolosi, V.; Karlsson, L. S.; Blighe, F. M.; De, S.; Wang, Z. M.; McGovern, I. T.; Duesberg, G. S.; Coleman, J. N., Liquid Phase Production of Graphene by Exfoliation of Graphite in Surfactant/Water Solutions. *Journal of the American Chemical Society* **2009,** *131* (10), 3611-3620.

211. Zhao, C. M.; Zheng, W. T.; Wang, X.; Zhang, H. B.; Cui, X. Q.; Wang, H. X., Ultrahigh capacitive performance from both Co(OH)(2)/graphene electrode and K3Fe(CN)(6) electrolyte. *Scientific Reports* **2013,** *3*, 6.

212. Chen, W.; Fan, Z. L.; Gu, L.; Bao, X. H.; Wang, C. L., Enhanced capacitance of manganese oxide via confinement inside carbon nanotubes. *Chemical Communications* **2010,** *46* (22), 3905-3907.

213. Rourke, J. P.; Pandey, P. A.; Moore, J. J.; Bates, M.; Kinloch, I. A.; Young, R. J.; Wilson, N. R., The Real Graphene Oxide Revealed: Stripping the Oxidative Debris from the Graphene-like Sheets. *Angewandte Chemie-International Edition* **2011,** *50* (14), 3173-3177.

214. Shin, M. K.; Lee, B.; Kim, S. H.; Lee, J. A.; Spinks, G. M.; Gambhir, S.; Wallace, G. G.; Kozlov, M. E.; Baughman, R. H.; Kim, S. J., Synergistic toughening of composite fibres by self-alignment of reduced graphene oxide and carbon nanotubes. *Nature Communications* **2012,** *3*, 8.

215. Baskin, Y.; Meyer, L., LATTICE CONSTANTS OF GRAPHITE AT LOW TEMPERATURES. *Physical Review* **1955,** *100* (2), 544-544.

216. Zhao, W. Z.; Lu, Y. G.; Jiang, J. Q.; Hu, L. Y.; Zhou, L. X., The effect of gamma-ray irradiation on the microstructure and thermal properties of polyacrylonitrile fibers. *Rsc Advances* **2015,** *5* (30), 23508-23518.

217. Aurbach, D.; Gofer, Y., Nonaqueous electrochemistry. New York : Marcel Dekker: New York, 1999; pp 137-208.

218. Coker, E. N. *The oxidation of aluminum at high temperature studied by Thermogravimetric Analysis and Differential Scanning Calorimetry*; Albuquerque, New Mexico, 2013.

219. Pollak, E.; Geng, B. S.; Jeon, K. J.; Lucas, I. T.; Richardson, T. J.; Wang, F.; Kostecki, R., The Interaction of Li+ with Single-Layer and Few-Layer Graphene. *Nano Letters* **2010,** *10* (9), 3386-3388.

220. Bissett, M. A.; Kinloch, I. A.; Dryfe, R. A. W., Characterization of MoS2-Graphene Composites for High-Performance Coin Cell Supercapacitors. *Acs Applied Materials & Interfaces* **2015,** *7* (31), 17388-17398.

221. Almeida, E. C.; Baldan, M. R.; Rosolen, J. M.; Ferreira, N. G., Impedance characteristics of the diamond/carbon fiber electrodes for electrical double-layer capacitor. *Diamond and Related Materials* **2008,** *17* (7-10), 1529-1533.

222. Taberna, P. L.; Simon, P.; Fauvarque, J. F., Electrochemical characteristics and impedance spectroscopy studies of carbon-carbon supercapacitors. *Journal of the Electrochemical Society* **2003,** *150* (3), A292-A300.

223. Wang, Y.; Wu, Y. P.; Huang, Y.; Zhang, F.; Yang, X.; Ma, Y. F.; Chen, Y. S., Preventing Graphene Sheets from Restacking for High-Capacitance Performance. *Journal of Physical Chemistry C* **2011,** *115* (46), 23192-23197.

224. Deng, S. K.; Berry, V., Wrinkled, rippled and crumpled graphene: an overview of formation mechanism, electronic properties, and applications. *Materials Today* **2016,** *19* (4), 197-212.

225. Zang, J. F.; Cao, C. Y.; Feng, Y. Y.; Liu, J.; Zhao, X. H., Stretchable and High-Performance Supercapacitors with Crumpled Graphene Papers. *Scientific Reports* **2014,** *4*, 7.

226. Wu, L. Q.; Li, W. W.; Li, P.; Liao, S. T.; Qiu, S. Q.; Chen, M. L.; Guo, Y. F.; Li, Q.; Zhu, C.; Liu, L. W., Powder, Paper and Foam of Few-Layer Graphene Prepared in High Yield by Electrochemical Intercalation Exfoliation of Expanded Graphite. *Small* **2014,** *10* (7), 1421-1429.

227. Liu, Z.; Xu, Z.; Hu, X. Z.; Gao, C., Lyotropic Liquid Crystal of Polyacrylonitrile-Grafted Graphene Oxide and Its Assembled Continuous Strong Nacre-Mimetic Fibers. *Macromolecules* **2013,** *46* (17), 6931-6941.

228. Seyedin, S.; Romano, M. S.; Minett, A. I.; Razal, J. M., Towards the Knittability of Graphene Oxide Fibres. *Scientific Reports* **2015,** *5*, 12.

229. Song, Z. Y.; Hou, X. X.; Zhang, L. Q.; Wu, S. Z., Enhancing Crystallinity and Orientation by Hot-Stretching to Improve the Mechanical Properties of Electrospun Partially Aligned Polyacrylonitrile (PAN) Nanocomposites. *Materials* **2011,** *4* (4), 621-632.

230. Saha, B.; Schatz, G. C., Carbonization in Polyacrylonitrile (PAN) Based Carbon Fibers Studied by ReaxFF Molecular Dynamics Simulations. *Journal of Physical Chemistry B* **2012,** *116* (15), 4684-4692.

231. Chieu, T. C.; Dresselhaus, M. S.; Endo, M., RAMAN STUDIES OF BENZENE-DERIVED GRAPHITE FIBERS. *Physical Review B* **1982,** *26* (10), 5867-5877.

232. Knight, D. S.; White, W. B., CHARACTERIZATION OF DIAMOND FILMS BY RAMAN-SPECTROSCOPY. *Journal of Materials Research* **1989,** *4* (2), 385-393.

233. Cancado, L. G.; Takai, K.; Enoki, T.; Endo, M.; Kim, Y. A.; Mizusaki, H.; Jorio, A.; Coelho, L. N.; Magalhaes-Paniago, R.; Pimenta, M. A., General equation for the determination of the crystallite size L-a of nanographite by Raman spectroscopy. *Applied Physics Letters* **2006,** *88* (16), 3.

234. Yusof, N.; Rana, D.; Ismail, A. F.; Matsuura, T., Microstructure of polyacrylonitrile-based activated carbon fibers prepared from solvent-free coagulation process. *Journal of Applied Research and Technology* **2016,** *14* (1), 54-61.

235. Ryu, Z. Y.; Rong, H. Q.; Zheng, J. T.; Wang, M. Z.; Zhang, B. J., Microstructure and chemical analysis of PAN-based activated carbon fibers prepared by different activation methods. *Carbon* **2002,** *40* (7), 1144-1147.

236. Shin, H. K.; Park, M.; Kang, P. H.; Choi, H. S.; Park, S. J., Preparation and characterization of polyacrylonitrile-based carbon fibers produced by electron beam irradiation pretreatment. *Journal of Industrial and Engineering Chemistry* **2014,** *20* (5), 3789-3792.
237. Laffont, L.; Monthioux, M.; Serin, V.; Mathur, R. B.; Guimon, C.; Guimon, M. F., An EELS study of the structural and chemical transformation of PAN polymer to solid carbon. *Carbon* **2004,** *42* (12-13), 2485-2494.
238. Abdelkader, A. M.; Cooper, A. J.; Dryfe, R. A. W.; Kinloch, I. A., How to get between the sheets: a review of recent works on the electrochemical exfoliation of graphene materials from bulk graphite. *Nanoscale* **2015,** *7* (16), 6944-6956.
239. Wang, S. Y.; Pei, B.; Zhao, X. S.; Dryfe, R. A. W., Highly porous graphene on carbon cloth as advanced electrodes for flexible all-solid-state supercapacitors. *Nano Energy* **2013,** *2* (4), 530-536.
240. Deng, L. B.; Young, R. J.; Kinloch, I. A.; Abdelkader, A. M.; Holmes, S. M.; De Haro-Del Rio, D. A.; Eichhorn, S. J., Supercapacitance from Cellulose and Carbon Nanotube Nanocomposite Fibers. *Acs Applied Materials & Interfaces* **2013,** *5* (20), 9983-9990.
241. Park, S.; Ruoff, R. S., Chemical methods for the production of graphenes. *Nature Nanotechnology* **2009,** *4* (4), 217-224.
242. Yang, D.; Velamakanni, A.; Bozoklu, G.; Park, S.; Stoller, M.; Piner, R. D.; Stankovich, S.; Jung, I.; Field, D. A.; Ventrice, C. A.; Ruoff, R. S., Chemical analysis of graphene oxide films after heat and chemical treatments by X-ray photoelectron and Micro-Raman spectroscopy. *Carbon* **2009,** *47* (1), 145-152.
243. Chartarrayawadee, W.; Moulton, S. E.; Too, C. O.; Kim, B. C.; Yepuri, R.; Romeo, T.; Wallace, G. G., Facile synthesis of reduced graphene oxide/MWNTs nanocomposite supercapacitor materials tested as electrophoretically deposited films on glassy carbon electrodes. *Journal of Applied Electrochemistry* **2013,** *43* (9), 865-877.
244. Liu, J. Z.; Notarianni, M.; Will, G.; Tiong, V. T.; Wang, H. X.; Motta, N., Electrochemically Exfoliated Graphene for Electrode Films: Effect of Graphene Flake Thickness on the Sheet Resistance and Capacitive Properties. *Langmuir* **2013,** *29* (43), 13307-13314.
245. Chabot, V.; Kim, B.; Sloper, B.; Tzoganakis, C.; Yu, A. P., High yield production and purification of few layer graphene by Gum Arabic assisted physical sonication. *Scientific Reports* **2013,** *3*, 7.
246. Dumanli, A. G.; Windle, A. H., Carbon fibres from cellulosic precursors: a review. *Journal of Materials Science* **2012,** *47* (10), 4236-4250.